Fuzzy Nanostructure Formation in Fusion Relevant Conditions

by

Patrick McCarthy

UNIVERSITY OF LIVERPOOL

Department of Electrical Engineering and Electronics

Thesis submitted in accordance with the requirements of the University of Liverpool for the degree of Doctor of Philosophy

September 2019

Declaration

I hereby declare that this thesis is my own work and further sources of information have been used other than the references cited. Neither this thesis nor any part of it have been submitted to any other university or institution for the application of another degree or qualification.

Signed: _____ _____

(P.McCarthy) Date

Abstract

Fuzzy nanostructure formation is a phenomenon unique to helium ion exposure of certain metal surfaces. The growth of fuzzy nanostructures causes a change in the morphology of the surfaces they form on, producing a porous network of interlocking tendrils that can change mechanical, optical, and thermal properties of the material. Although many metals can exhibit this behaviour after helium ion irradiation, one of the most heavily researched materials for its formation of surface fuzz is tungsten. The observation of fuzzy tungsten formation has become a concern for the operation of nuclear fusion devices, where wall materials are composed near entirely of tungsten, and helium ash is inherent in reactors as a by-product in hydrogenic fusion reactions. In the next generation of fusion devices, known as ITER, the formation conditions required to produce fuzzy tungsten are likely to occur, making understanding its growth an aspect for the realisation of fusion power. For this reason, it is vital to research the growth of fuzzy tungsten to interpret better its formation conditions and characteristics, as well as its behaviour in fusion like environments.

In this thesis a literature review provides the current knowledge of fuzzy tungsten research, including its observed formation conditions, its effects on the surfaces it forms on, and potential theories on its growth process. The production of fuzzy nanostructures on other materials, as well as tungsten, and observations of fuzzy tungsten growth inside current fusion devices, are described. The experimental results in this thesis, arranged into three chapters, are as follows. The first chapter comprises a characterisation of the experimental apparatus used, with subsequent chapters describing two investigations into fuzzy tungsten formation under fusion like conditions.

Fuzzy tungsten was grown in the presence of mixed-species plasmas, containing a large percentage of helium (90 - 95 %) and a small amount of a known impurity (5 - 10%), to observe the effects of plasma impurity on its growth. The plasma impurities chosen for this study, nitrogen (N_2), neon (Ne), and argon (Ar) are likely to be used in fusion devices as a way of regulating the heat fluxes to plasma-facing components in a fusion device. In the impurity percentage ranges used, results from SEM observations indicated that impurity in the helium plasma caused an overall reduction in the fuzzy layer thickness. The effects of sputtering on the fuzzy layer surfaces were more significant for both heavier impurity species and higher concentrations. Using higher percentages (7.5 to 10 %) of N_2 or Ar, fuzzy tungsten growth was near wholly terminated. At 5 % impurity (N_2, Ne and Ar), the fuzzy W layer thickness was reduced by a factor of 3 relative to a sample of fuzzy W produced under a 100 % He plasma at the same ion fluence. Mass loss measurements

confirmed SEM findings that heavier atomic mass impurities produced a larger sputtering effect on the fuzzy tungsten surfaces. The measured sputtering yields for each fuzzy surface were reduced relative to bulk sputtering yield values, indicating a higher tolerance of fuzzy surfaces to ion sputtering. Fuzzy tungsten layer thicknesses were compared to an analytical model describing the growth rates of fuzzy tungsten in erosive regimes. The model predicted similar levels of fuzzy tungsten growth, as was seen in the experiments carried out. Larger fuzzy nanostructures named Nano-Tendril Bundles were observed to grow, in addition to general fuzzy tungsten layers, when impurity species were present in the helium plasma. The surface temperature and apparent sputtering yield limits for their formation are presented.

Simultaneous deposition of tungsten on to tungsten surfaces transitioning to fuzz is shown to cause an acceleration in the growth rate of fuzz. The results from this study showed that enhanced growth rates of fuzzy tungsten were dependent on both the surface temperature and tungsten atom-to-helium ion arrival rate ratio. For the same helium ion exposure, an increase in the sample temperature (from 1050 to 1150 K) lead to a six-fold increase in the fuzzy layer thickness. Increasing the tungsten atom-to-helium ion arrival rate ratio over the full range produced a two-fold increase in the thickness. High-resolution surface microscopy probed both the inner structure of fuzzy tungsten fibre layers, with electron diffraction showing the polycrystalline nature of fuzz. The magnetron results are compared directly with fuzzy tungsten layers grown in NAGDIS II, a plasma device operating in completely deposition-free conditions, providing a similar range of helium ion fluences, ion energies, and sample temperatures. The comparisons showed that a lower incubation fluence and an enhanced growth rate of fuzz was produced in the magnetron system. A similar enhancement in fuzzy molybdenum growth rates, when coupled with molybdenum deposition, was observed.

Acknowledgements

I would first like to thank my PhD supervisor Professor James Bradley for his kind and continued guidance during the course of my time here. It has been an absolute pleasure to have had this opportunity, and I am very grateful for his help during my studies. A thank you must also be extended to the University of Liverpool and ESPRC who funded this studentship, as well as the Fusion CDT for the introductory courses at the beginning of this PhD which helped to improve (or indeed establish) my knowledge of fusion research.

I must send huge thanks to Dr David Donaghy for his expertise and patience in teaching me how to work the experimental rig, as well as his cheery help when things tended to break! I'm hugely thankful for the time Dr Matt Bilton and Dr Karl Dawson have spent teaching me how to operate many of the surface analysis devices I have used in this study. To Gareth Blacoe and Mark Burnley, who have also spent large amounts of their time building or re-assembling things for me to use during my studies, I am more than grateful.

From my time spent with the group at Nagoya University, I would like to thank Dr. Shin Kajita and Dogyun Hwangbo for an incredible experience, not only to work with them but also to enjoy their company. However, the less said about karaoke the better.

To the number one technological plasma lunch, quiz and darts team (Mike, Aaron, Youssef, Brandon, Felix, Pete, Steph, Matt S, Matt B, Carl, Mo, Kirsty, Mark, James, David, Ella, Martin, other Mike, Marcus, Tom, Brenno...and the rest), I need to give a huge thank you. You have all helped to make the last four years such a great experience. I am also very thankful for the support given to me by Phil and Jill in stores, as well as Lindsey who has sorted out all of my travel requests.

Lastly, to my long term friendship partners (Joe, Ashley, Danny, Aji, Jay, Johnny C, Jaime, The Moff (Ste M), Cooko, Adam Buxton and Cornballs) and family (Mum, Dad, Mike, Sarah, Craig, Aoife) I just want to say thank you so much for all you have done for me over the last four years (and to be fair, long before that). It would have been nigh on impossible to have completed this without all of your lovely love and support. Thanks again.

Publications

The research performed during the course of this PhD has, so far, resulted in the following publications

- **P.McCarthy**, D. Hwangbo, M. Bilton, S. Kajita and J. W. Bradley, "Enhanced Fuzzy Tungsten Growth in the Presence of Tungsten Deposition", *Nuclear Fusion*, **60**, 026012, (2020)
- D. Hwangbo, S. Kajita , N. Ohno, **P.McCarthy**, James W. Bradley and H. Tanaka, "Growth of nano-tendril bundles on tungsten with impurity-rich He plasmas",*Nuclear Fusion*, **58**, 096022, (2018)

Conferences

The conferences which research has been presented at will now be listed

- The 17$^{\text{th}}$ International Conference on Plasma-Facing Materials and Components for Fusion Applications (**Poster Presentation**) - Eindhoven, The Netherlands, 20 - 24$^{\text{th}}$ May 2019
- 46$^{\text{th}}$ IOP Plasma Physics Conference (**Poster Presentation** - 1st Prize) - Loughborough University, UK, 23-26$^{\text{th}}$ April 2019
- Plasma Surface Engineering (**Poster Presentation**) – Garmisch-Partenkirchen, Germany, 24-27$^{\text{th}}$ September 2018
- LRC Materials Discovery Symposium (**Poster Presentation**) – University of Liverpool, Liverpool, 3-4$^{\text{th}}$ September 2018
- Culham PhD Showcase (**Poster Presentation** – 1st Prize) – Culham, UK, 7-8$^{\text{th}}$ July 2018
- 45th IOP Plasma Physics Conference (**Oral Presentation**) – Queens University, Belfast, 9-13$^{\text{th}}$ April 2018
- KSTAR Conference 2018 (**Oral and Poster Presentation**) – Muju, Korea, 21–23$^{\text{rd}}$ February 2018

Nomenclature

This list describes various abbreviations and symbols that feature throughout this thesis

Fusion Devices and Experimental Apparatus

Alcator C-Mod An experimental tokamak that operated between 1991 and 2016 at the Massachusetts Institute of Technology (MIT) Plasma Science

ASDEX U An experimental tokamak, featuring a tungsten divertor and first wall, at the Max-Planck-Institut für Plasmaphysik in Germany

COMPASS Experimentak tokamak located at the Institute of Plasma Physics of the Academy of Sciences of the Czech Republic

DIII-D Operated by General Atomics for the U.S. Department of Energy, this is the DIII-D tokamak national fusion research facility.

EDX Energy-Dispersive X-ray Analysis

FIB Focussed Ion Beam

IR Infra-Red

ITER The next generation of experimental magnetic confinement fusion devices known as tokamaks. Latin for *'the way'*, it is hoped it will be the first fusion device to produce up to 10x as much energy as is put in.

JET Joint European Torus, an experimental magnetic confinement fusion device located at the Culham Centre for Fusion Energy in Oxfordshire, UK

LPD Linear Plasma Device

MSD Magnetron sputtering device

NAGDIS II NAGoya DIvertor Simulator

PFC Plasma Facing Component

QCM Quartz Crystal Microbalance

RGA Residual Gas Analysis

SEM Scanning Electron Microscope

TEM Transmission Electron Microscope

Notation

ϵ emissivity

Γ Flux density, the number of particles that reach a surface per area per second, in units of m^{-2} s^{-1})

λ_D Debye length, the measure of scale over which mobile charge carriers can screen out electric fields that are produced in plasmas.

Φ Fluence of particles (equivalent to the flux density multiplied by time), in units of m^{-2}

eV Electron Volt, the energy equivalent to the work done by an electron accelerating from rest through an electric potential difference of 1 volt

n Particle density, in units of m^{-3}

p Porosity

T_e Electron Temperature, the average temperature of electrons within a plasma, in units of eV.

V_f Floating Potential, the potential at which the combination of both positive and negative charges to a surface placed in a plasma are zero (V)

V_p Plasma Potential, the potential that the bulk plasma is at (V)

BSE Backscattered electron

CFC Carbon-fibre composite

D Fick's law Diffusion co-efficient, in units of m^2 s^{-1}

E_s Surface binding energy, the energy required to remove one atom from the top of material surface, in units of electron volts eV

E_{th} Sputtering threshold energy, the energy required to remove one atom from a surface due to a sputtering event, in units of eV

h Fuzzy layer thickness, commonly in units of micrometers (μm)

I Current, rate of flow of electrical charges, in units of Amperes (A)

m_i mass of an ion, in units of kg

SE Secondary electron

t time, the amount of plasma exposure in seconds, in units of seconds (s)

V Voltage, the difference in electrical potential between two points, in units of volts (V)

Physical Constants

ϵ_0 permittivity of free space, equivalent to 8.85 x 10^{-12} F m^{-1}

e charge of an electron, equivalent to 1.602 x 10^{-19} C

k_B Boltzmann constant, equivalent to 1.38 x 10^{-23} kg

m_e mass of an electron, equivalent to 9.11 x 10^{-31} kg

Contents

List of Figures

List of Tables

Chapter 1

Introduction

1.1 Plasma

Plasma is one of the four fundamental states of matter. It is formed when a gas attains enough energy to be ionised, causing the removal of electrons from their constituent atoms, eventually resulting in an approximately equivalent number of positively charged ions and negatively charged electrons to be produced. This condition of the equivalence in the numbers of electrons and ions is called *quasineutrality*, and it is useful in clarifying the difference between gas and plasma states.

It has often been said that 99 % of all matter in the universe is in a plasma state. For viewers on earth, there are many varied examples of plasmas in the observable universe. The sun, the star at the centre of our solar system, and all other stars are almost entirely made up of plasma. Moving toward the earth's outer atmosphere, plasmas are produced due to interactions of the solar wind and the magnetosphere resulting in the Aurora Borealis. Even lightning bolts and simple neon lights found in shop windows are all forms of plasma.

Plasma discharges have been shown to have many applications for society, notably in space travel, medical applications, the semiconductor industry and energy production. For these purposes, plasmas may be produced using different processes, depending on the application they are required for. The simplest method to form an experimental plasma is to use two conducting electrodes and apply a voltage between them. Assuming the voltage applied is high enough, electrical breakdown can occur in the gases between the electrodes, and this allows a current to be conducted by the intermediate gas. The voltage required to produce electrical breakdown can be dependent on the gas pressure and distance between the two electrodes, and in most cases can be described by Paschen's law [1] .

Generally, experimental plasmas can be separated into two categories based on the pressure at which the discharge is produced; atmospheric pressure or low pressure plasmas. Atmospheric pressure plasma discharges, produced at a pressure near to one atmosphere, typically involve the application of voltages in the range of hundreds of volts to several kilovolts to form a plasma [2]. Due to the nature of atmospheric pressure plasma the set up is relatively simple, with no requirement for vacuum vessels to carry out experiments. Currently, atmospheric pressure plasmas are being investigated for their potential uses in a

variety of industrial and biomedical applications, notably in the production of surface coatings for material surfaces, as well as surface cleaning of surgical equipment [2]. Applications of these discharges for the capture of carbon dioxide is also a research field of interest [3]. In the case of a low pressure plasma, vacuum systems (chambers and pumps) are used to reduce the pressure of gas between two electrodes (and the system as a whole). Low pressure discharges can be formed for a number of different experimental set ups, examples include inductively and capacitively coupled plasmas, cascade arc and magnetron (glow discharge, HIPIMS) plasmas. The degree of ionisation and temperature of the plasma can distinguish each type of low pressure discharge produced. Ionisation rates within low pressure plasmas can vary from a few percent, such as in glow discharges, to tens of percent in cascade arc discharges. The temperature of the plasma is usually given, for both electron and ions, in terms of the electron volt (eV), with the difference between the relative temperatures of electrons and ions defining where the plasma is thermal or non-thermal. In plasmas where electrons have far greater temperatures than ions, with the electron temperature usually equivalent to several eV (of the order 10, 000 K) and the ion temperature around room temperature ($\sim$ 273 K), the plasma is said to be non-thermal. For a thermal plasma, the temperature of the ions is much larger than in non-thermal plasmas, and considered to be equivalent to the temperature of the electrons (i.e both ions and electrons on the eV scale).

Thermal plasmas are possible to be produced experimentally, however large magnetic fields are required to contain the particles so as to trap charged particles. As charged particles are confined, the rates of interaction between charged and neutral gas particles are enhanced, increasing the overall ionisation and temperature of the plasma. An example of a thermal plasma with high rates of ionisation is the core of the sun, which is known to exhibit nuclear fusion processes due to the high temperatures (many keV) of the plasma within. On earth, nuclear fusion is being actively pursued due to the large amounts of energy production that can be harvested from it. It is hoped that the energy production can be harnessed in electricity generation, and possibly replace the ubiquity of fossil fuel use.

1.2 Nuclear Fusion

Nuclear fusion is the process where two light atomic nuclei are combined to produce a heavier nucleus. The mass defect between the produced heavier nucleus and the original atomic nuclei determines the amount of energy that can be released in the reaction. Typically in fusion reactions, energy can be released in the form of other particles. Due to the large energy release possible in fusion reactions, fusion power has become an attractive proposition to replace the energy provided by the burning of fossil fuels on earth. For fusion to occur in practice, the nuclei involved in the reaction must be energetic enough to overcome the repulsion of the coulomb barrier due to their respective positively charged protons, thus allowing the short range, attractive nuclear force to bring them together.

Within the sun's core, the large mass and gravitational pull acts to confine hydrogenic

gases to high densities and temperatures ($\sim 10^7$ K). These conditions allow the core of the sun to produce the fusion of hydrogen (H) to helium (He) through proton-proton reactions. The force of gravity is however a very weak force compared to the forces of nuclear physics, and plasma confinement is only achieved due to the heavy mass of gases within the core. Whereas gravity can be used to produce fusion in the sun and stars, it will not be possible for the much smaller plasmas that will be used for fusion processes in a reactor. Furthermore, the fusion power density in the core of the Sun is low ($\sim$ 270 watts per cubic meter) compared to the megawatts per cubic meter required for a commercial power plant [4]. Therefore, larger plasma densities and temperatures, confined within a small volume, must be achieved to provide viable nuclear fusion in a reactor.

In the proton-proton reaction, its initial stages are known to be slow, mainly due to the initiation by the weak nuclear force to convert a proton into a neutron. To remove this slow first stage in terrestrial fusion reactors, fusion reactions will start with deuterium (D) at the initial stage of the reaction. Various approaches of fusion of D particles are summarised in figure 1.1, including the probability for a fusion reaction to occur given the energy of the particles. Each fusion reaction is unique, and as such has a cross section ascribed to it, σ, which denotes the likelihood of the Coulomb barrier repulsion to be overcome. With current engineering projections, the most promising fusion reaction being pursued in fusion devices is the deuterium (D) and tritium (T) reaction. The reaction is included below:

$$D + T \rightarrow He\,(3.5MeV) + n\,(14.1MeV) \tag{1.1}$$

The benefits of the D-T fusion reaction are best summarised as follows. It will require the lowest temperature of the three reactions in figure 1.1, and the fuels required in the reaction are either naturally abundant (deuterium exists in sea water) or can be produced as a by product of the fusion reaction. Tritium has a short half life (12.32 years), and so a method for production would be required to make fusion commercially viable in the future. Since neutrons are already produced in the D-T reaction, breeding of tritium will take place by using blankets of lithium in the walls [5]. It is known that lithium and a neutron can interact to produce tritium as,

$$D + T \rightarrow^4 He + n \tag{1.2}$$

$$^6Li + n \rightarrow^4 He + T \tag{1.3}$$

$$^7Li + n \rightarrow^4 He + T + n \tag{1.4}$$

The tritium produced would then be fed back into replenish the plasma of its spent tritium. The breeding ratio is required to be at least 1, and higher ratios may needed to account for any tritium retained in the walls of a fusion reactor [6]. Coupled with the benefits for tritium replenishment, neutrons will contain significant amounts of kinetic energy after the D-T fusion reaction. The energy of the neutrons will therefore be required to be extracted in some way, and it is thought that through the heat transfer of neutrons to the blankets

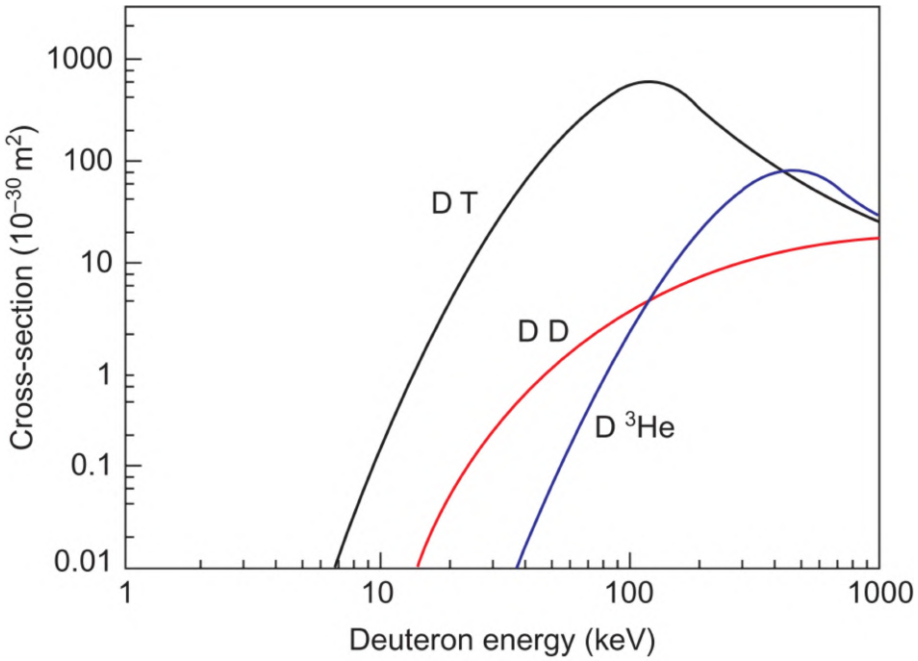

Figure 1.1: The cross sections σ for typical fusion reactions against the ion energy (temperature). The data for three different potential fusion reactions are included (D + T, D + D and D + ^{3}He). Taken from [4]

in the wall, this heat can be extracted. By positioning water pipes around a the outer surfaces of the reactor, the heat transfer from the blanket and wall regions can heat the water to produce steam, facilitating the production of electricity in a similar way to current commercial energy production.

Despite the relatively low temperatures required for D-T fusion compared to other reactions described in figure 1.1, extremely large temperatures ($\sim 10^8$ K) will be necessary to produce fusion. Auxiliary heating methods will therefore be required to reach this temperature range initially. The production of charged alpha particles (^{4}He), released as a byproduct in the D-T reaction, will eventually provide sufficient energy to heat the plasma and maintain the fusion reaction. However, He accumulation above certain limits within the D-T plasma is a concern for the optimisation of fusion power [7]. The production of fusion power is heavily dependent on the plasma (D-T) density and the confinement time, as well as the plasma temperature, therefore finding a balance between these three parameters is believed to be key to the success of fusion devices.

1.3 Nuclear Fusion Devices

In producing sustainable energy from nuclear fusion, a state of *ignition* must be reached. Fusion ignition is the point at which a nuclear fusion reaction becomes self-sustaining i.e. the energy lost to the surroundings is exceeded by the energy retained in the plasma. This occurs when the energy released by the fusion reactions heats the fuel (D-T) faster than it can be cooled. At this stage external heating mechanisms would no longer be required. To ignite a D-T plasma, certain conditions are required. The Lawson Criterion

was introduced by John Lawson [8] describing the interplay between the plasma density (n_e), the energy confinement time (τ_e) and the ion temperature (in keV), with the product of these quantities being shown to be important in production of ignition. For D-T fusion to reach ignition and operate for large amounts of time, the criterion is summarised as:

$$n_i T \tau_e \geq 3 \cdot 10^{21} \frac{\text{keV} \cdot s}{m^3} \tag{1.5}$$

There are two main methods that are currently being investigated to meet the Lawson criterion for D-T fusion, magnetic confinement fusion (MCF) and inertial confinement fusion (ICF). In ICF, high powered lasers are used to compress a pellet of D-T fuel. At the outermost layer of the pellet, a shock wave is produced that travels throughout the fuel compressing the pellet. The density and temperature inside the pellet increase to such a level that ignition is achieved, all before the pellet is vaporised. MCF involves confining hot plasmas with strong magnetic fields (on the order of several Tesla). In MCF, the prevalent devices used for this purpose are the tokamak and the stellerator, with both using contrasting magnetic field configurations. In the tokamak, toroidal and poloidal magnetic fields create a torus (donut) shaped magnetic field to confine plasma. The toroidal field is generated by currents in the external magnetic coils, and the poloidal field is supported by a toroidal plasma current. A large solenoid in the centre of the set up is ramped to inductively generate this plasma current, which enhances plasma confinement. Stellerators on the other hand uses a complicated field coil arrangement which creates the magnetic field solely. In the absence of large currents being generated, stellerators can often operate without plasma disruptions, produced as a result of the plasma current becoming too large.

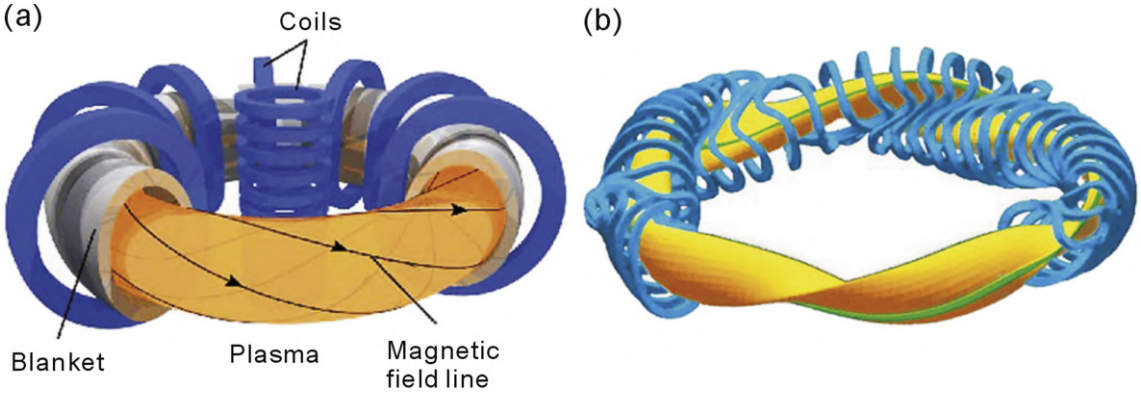

Figure 1.2: Magnetic field coil arrangements in a) Tokamaks and b) Stellerators. Taken from [9]

In tokamaks, the plasma current has two functions. As well as generating the poloidal magnetic field, it heats the plasma ohmically. The plasma temperature that can be achieved via this process is significantly large ($\sim$ 50 million degrees), but it is still less than that required for ignition. Other processes that can be used to provide heating in tokamak plasma include neutral beam injection (NBI), electron cyclotron resonant heating (ECRH) and ion cyclotron resonant heating (ICRH). In NBI, high energy neutral beams will be injected into the plasma, flowing through it unaffected by the magnetic fields, with the

beam's particles transferring their energy to the plasma through collisions. In ECRH and ICRH, the frequency of gyration of the plasma particles is matched to electromagnetic waves, producing resonant heating of the particles. To date, steady state operation of a fusion plasma has not been demonstrated with any configuration of MCF device or with any heating method. The aim in the near future will be to produce large amounts of energy from the chosen fusion reaction type, far surpassing the initial energy input. The large tokamak ITER, Latin for '*the way*', is the next generation of experimental fusion reactors to help realise this goal. Utilising the tokamak device, and the heating methods previously mentioned, it is planned that this device will lead to net energy production through nuclear fusion. The reactor will be the largest fusion reactor ever built, capable of the largest net gain (q), estimated to be around 10, in fusion energy seen in any experiment so far.

1.4 ITER

The ITER tokamak is a future experimental tokamak which will be the culmination of a multi billion euro international effort to build a fusion device that produces a large net gain in fusion energy. ITER will be larger than any previous tokamak, creating various issues related to its design and construction. ITER will use a large array of superconducting magnets to produce the toroidal magnetic fields for confinement (~ 5.3 T), with the vacuum vessel twice as large and sixteen times the weight ($\sim 50,000$ tonnes in total) as any previous tokamak [4]. It will measure 19 meters horizontally (with an inner diameter of 6 meters) and 11 meters in vertical height. To reach q ~ 10, 500 MW of fusion power will be produced, with roughly 400 MW of the fusion power to be removed from the plasma by neutrons. In the initial experimental campaigns of ITER where no D-T fusion is to be tested, no alpha particles will be produced hence additional plasma heating will be required. The present guidelines for ITER are to initially operate with 73 MW of additional plasma heating, consisting of 33 MW of neutral beam injection, 20 MW of ion cyclotron heating, and 20 MW of electron cyclotron heating. Various options are being studied where the additional plasma heating could be increased up to 130 MW at a later stage. For more details on the specifics of the ITER construction and design see the resources within [4].

In figure 1.3 a cross section of the vacuum vessel to be used in ITER is provided. The inner walls of the vessels will be covered with the blanket modules, which capture the high energy neutrons produced by the fusion reactions whilst also shielding the superconducting magnets and vessel itself. In ITER, the energy deposited by the neutrons will cause heating of the blanket, so cooling systems will be used to remove this excess heat. In a commercial fusion power plant, this heat will eventually be used for energy production. The access ports, indicated on figure 1.3, provide access paths for diagnostics and plasma heating systems during plasma operation, and during maintenance the ports will act as access routes for remote handling tools to replace blanket and divertor components.

Located at the bottom of the vacuum vessel is the divertor. The divertor itself will

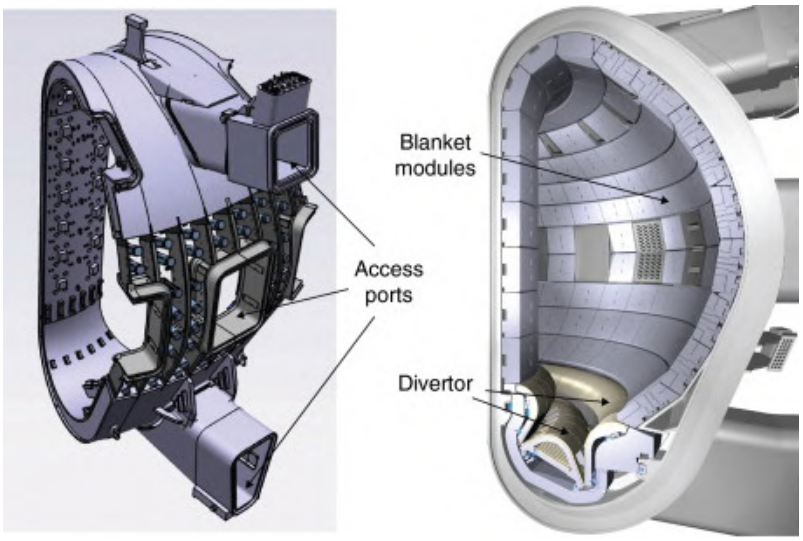

Figure 1.3: The ITER vacuum vessel. Taken from [4]

be made up of separate cassettes (54 in total) for easy removal during any required maintenance. These cassettes (see image 1.6) have three plasma facing areas, and due to the magnetic field line configuration in ITER, two will be where magnetic field lines intersect with the divertor. This will mean ions and electrons which are guided by the fields from the boundary of the plasma to the divertor will deposit their considerable kinetic energies at these points. In ITER 10 MW m^{-2} is predicted as the steady operational limit of plasma facing components (PFCs), and an upper limit of 20 MW m^{-2} is predicted for transient energetic events [10]. During steady state operation, the particle fluxes (x 10^{24}) and heat loads ($>$ 10 MW m^{-2}) will be large enough to require active water cooling of the cassettes [11].

There are only a small selection of materials which could be used as plasma facing components in the divertor, with tungsten (W) currently chosen to be present in most of the PFCs within the ITER divertor [10], [11]. The divertor is a critical component in the stable operation of ITER, so experimental testing of W under fusion like conditions is necessary.

1.4.1 Tungsten Components in ITER

In the initial designs for ITER, carbon fibre composites (CFCs) were to be used in the divertor of the reactor as PFCs. However, findings by Loarer *et al.* showed that in various tokamaks all over the world (JET, ASEDEX-Upgrade, TEXTOR and Tore Supra), which were all designed with ITER in mind, significant hydrogenic fuel retention occurred due C deposits within the reactors [12]. Extrapolating to ITER, they concluded that the T inventory limit, a safety requirement for operation of ITER with a legal limit of 350 g at any one time, would be reached at ITER within less than 100 discharges. The JET ITER-Like Wall (ILW) experiment, which contained a mixture of beryllium (Be) and W in its plasma facing components demonstrated a significant reduction in T retention ($\sim$ factor

of 10) compared to CFC components, hence the choice to replace C with a W divertor in ITER was made [13]. A similar level of reduction ($\sim$ 5 times) in the tritium retention in W relative to CFC components was also seen in ASDEX Upgrade [14].

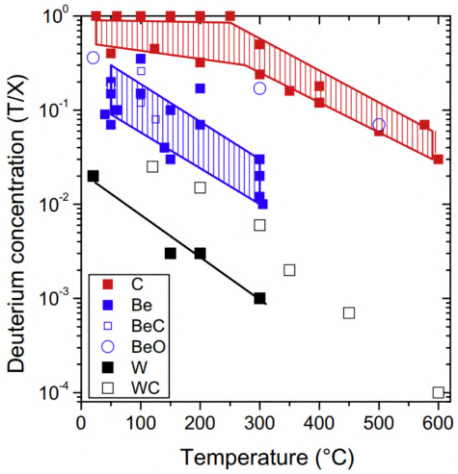

Figure 1.4: T retention against temperature for C, Be and W wall materials. Taken from [15]

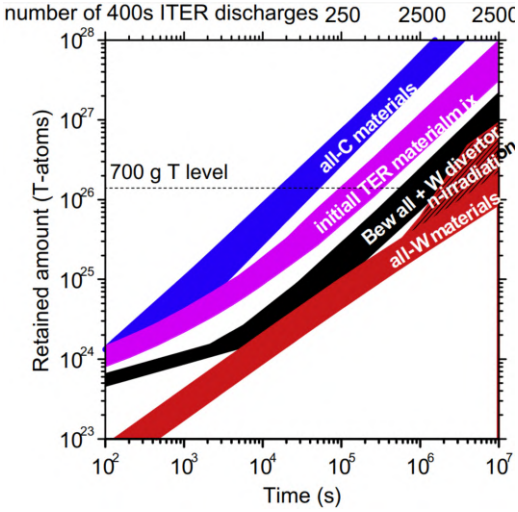

Figure 1.5: T retention vs Time for different divertor material candidates. Tests completed in the JET tokamak. Taken from [15]

Following the observations in [12], the initial operation of ITER was to use CFC components within its divertor for the non-active experiments involving D or He plasmas (hence no T production), and then replace the divertor cassettes for an all W divertor for active campaigns (using D-T plasmas). In the report by Pitts *et al.* in 2013 it was deemed simpler to begin ITER with an all W divertor [10]. Similar to the initial CFC components design, cassettes of W, with dimensions of 12 x 28 x 28 mm will be used. In total 54 cassettes are expected to compose the ITER divertor made up of consecutive chains of W monoblocks bonded to copper-chromium-zirconium (CuCrZr) cooling tubes [16], [17] (shown in figure 1.6).

During plasma operation, the engineering requirements for the divertor monoblocks

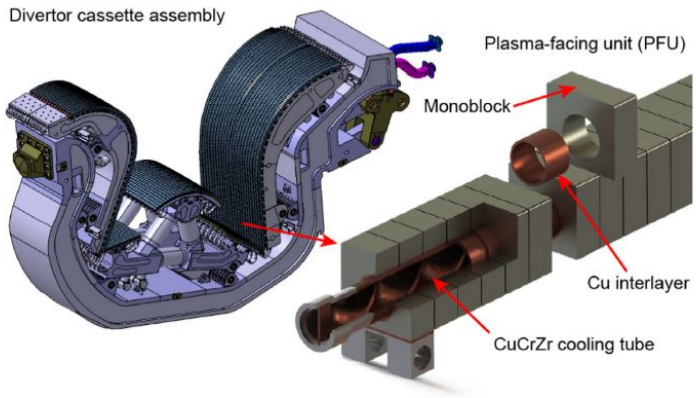

Figure 1.6: Images of the ITER cassettes and monoblocks expected to be used in the divertor.

specify they will be able to handle exposures for 5000 heat load cycles of 10 s duration at 10 MW m^{-2}, in addition to 300 cycles of 10 s at 20 MW m^{-2} [18]. In addition, shaping and tilting of the monoblock chains will be implemented, designed to protect the leading edges of monoblocks which, due to the glancing angle of the magnetic field lines in tokamaks, can lead to hot spots appearing [17], [18]. These hot spots can reach temperatures close to the recrystallisation of W ($\sim$ 1600 K [19]), with recrystallised W surfaces known to be susceptible to macro-crack formation [20]. Much of the heat transferred to the W divertor in ITER will be as a result of large fluxes of energetic particles. These particle fluxes, consisting of H and He, are also of interest due to likelihood of surface morphology changes as they interact with W. In addition, should the particles have enough energy sputtering processes may occur which could remove wall material [21].

The interactions between H ions with W surfaces have been observed to lead to surface morphology changes both through the production of surface blistering [22], [23] and small nanostructure formation [24], [25]. The mechanisms that lead to these formations (blisters, nanostructures) are still a part of ongoing discussion, but generally they are attributed to the aggregation of H in defects within the W lattice and the subsequent production of high pressure bubbles. Eventually rupturing of these bubbles in the near surface region forms blisters on the surface [26]. An example of these nanostructures on W at H fluxes relevant to the ITER divertor ($\sim 10^{24}$ m^{-2} s^{-1}) is shown figure 1.7. Presented through scanning electron microscope (SEM) images, Xu *et al.* observed the formation of surface nanostructures after total H ion fluences of 7 x 10^{26} m^{-2}, ion energies of 38 eV and surface temperatures of 423 K. The nanostructures themselves are shown in the bottom of figure 1.7, where cross-sectional SEM imaging indicated bubbles and porous structures beneath the W surface. [27].

He ions are also known to produce forms of surface blistering [28] and nanostructure formation [29] after implantation into W surfaces. In the next section, the effects of He ion irradiation on W components will be discussed.

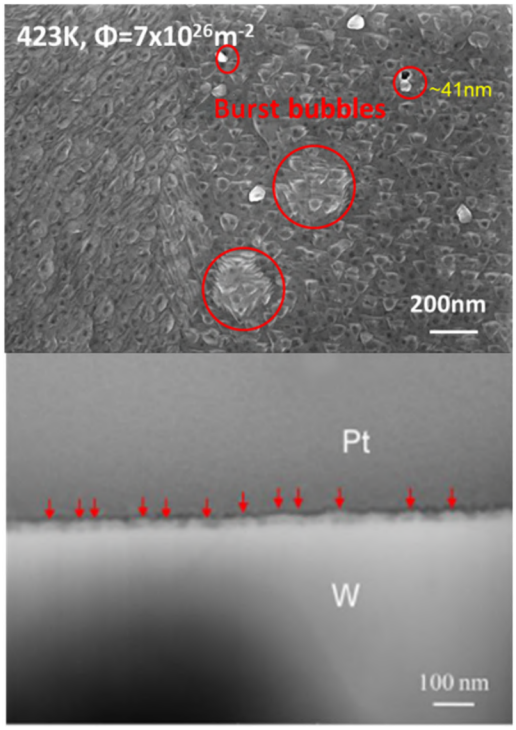

Figure 1.7: In the top image, plasma-induced nanostructures appear in addition to blisters for a H fluence of 7 x 10^{26} m^{-2} and a surface temperature of 423 K. In the bottom image a cross-section of the same sample is shown, where nanobubbles can be observed. Reproduced from [24].

1.5 Helium Ion Irradiation of Tungsten Components

Helium, released as a by product of the D-T fusion reaction (equation 1.1), has been an issue for the steady state operation of fusion reactors for many years [7], [30]–[32]. To satisfy the Lawson criterion (1.5) sufficient confinement of the plasma must occur, however if the confinement is too great and large amounts of He are retained in the plasma, dilution of the D-T plasma can occur. Subsequently, the overall density of D and T is reduced, meaning the value given by equation 1.5 may be reduced below the condition for ignition. A method of removing excess He, known as He ash, from the core plasma is therefore required. The current methods for particle removal in tokamaks are to use cryopumping systems located in the divertor region of the reactor. Pumps will flush out charged particles (He, D, T) which have escaped the confinement in the core. When they reach the edge regions of the plasma, they can be transported to the divertor through the scrape off layer (SOL) of the plasma, and removed via pumping ducts located there (see figure 1.3). At the same time fresh D and T gas will be used to replenish the core plasma and maintain the densities of D and T to mitigate the production of He. In ITER, the fluxes of energetic He particles predicted for the divertor are on the order of 10^{21} m^{-2} s^{-1} for D-T fusion campaigns, and increasing to 10^{22} - 10^{23} m^{-2} s^{-1} for pure He discharges [33].

In both cases, the neutral pressure will have an impact on the relative fluxes; for larger pressures, the fluxes are reduced, with the fluxes increasing as the neutral pressures in these regions decreases [33]. It has been the subject of many reports over the last thirty years to

expose W components to expected fusion-like fluxes of He to better understand the changes to the material this can induce. It is well known that although He may be insoluble in W, it can move quickly through W lattices and will often be trapped at any defects (vacancies, interstitials, dislocations) that may exist [30]. Over time, and with repeated trapping, He accumulates forming clusters which precede high pressure He bubble formation [34]. Bubble formation can lead to a variety of modifications to the materials surface depending on the fluence of He particles (equivalent to the flux multiplied by time), the energy of the He particles and the surface temperature of the W during the plasma exposure. In figure 1.8 an overview of the surface temperature dependence on the induced morphology changes in W, as a result of He irradiation, is provided.

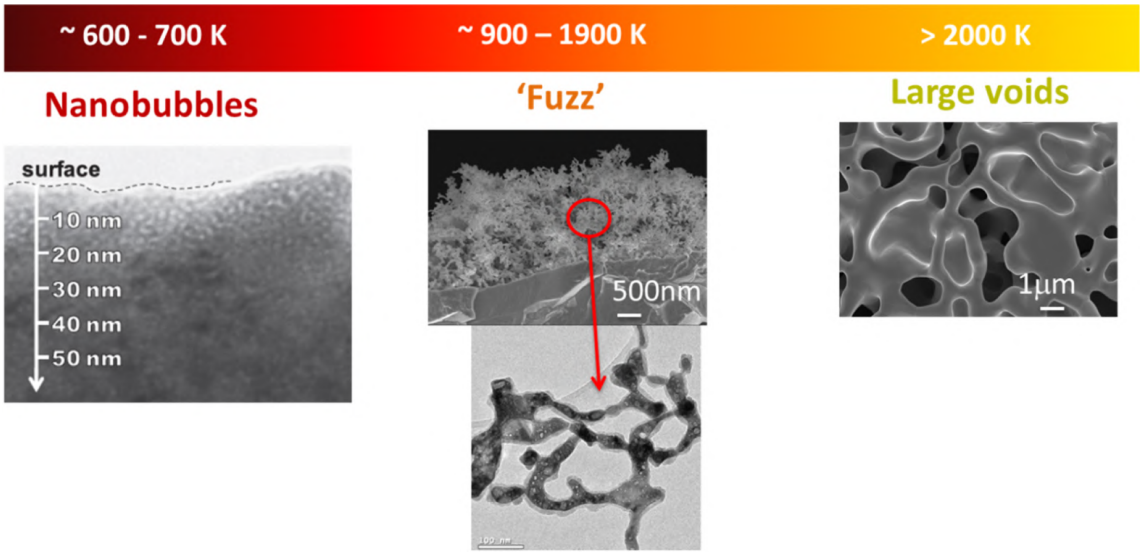

Figure 1.8: The different observations of surface morphology produced due to He bubble accumulation in W, over a temperature range. Taken from [33]

The low (i.e 500 K - 1000 K) and high (> 2000 K) temperature ranges on figure 1.8 indicate nano-bubble or void formation is possible for He ion irradiation on W at these conditions [35], [36]. In the intermediate temperature range (900 - 1900 K), surface nanostructures are produced on W surfaces. These nanostructures, known colloquially as 'fuzz' are of significant interest because of their potential formation in ITER, with the threshold conditions for their formation likely to be met in parts of the divertor. In figure 1.9 the temperature and ion energy profiles predicted for the ITER divertor are shown [33]. It has been demonstrated in previous reports ([37], [38]) that W nanostructures can be formed upon W surfaces when the following conditions are met: surface temperatures of 1000 - 2000 K, He ion energies of greater than 10 eV and He ion fluences of $> 2 \times 10^{24}$ m^{-2}. The predicted surface temperatures and ion energies (plotted as a function of the neutral pressure adjacent to the divertor in figure 1.9) indicate a region (shaded red) across the outer vertical divertor target where the conditions for nanostructure formation are satisfied. Given the predicted fluxes of He for the ITER divertor (see figure 1.10), it will take around 1 hour to produce W nanostructures in the ITER divertor (assuming pulse lengths of 400 s [39]). Due to likelihood of fuzz to grow in ITER's divertor, further research into W nanostructure

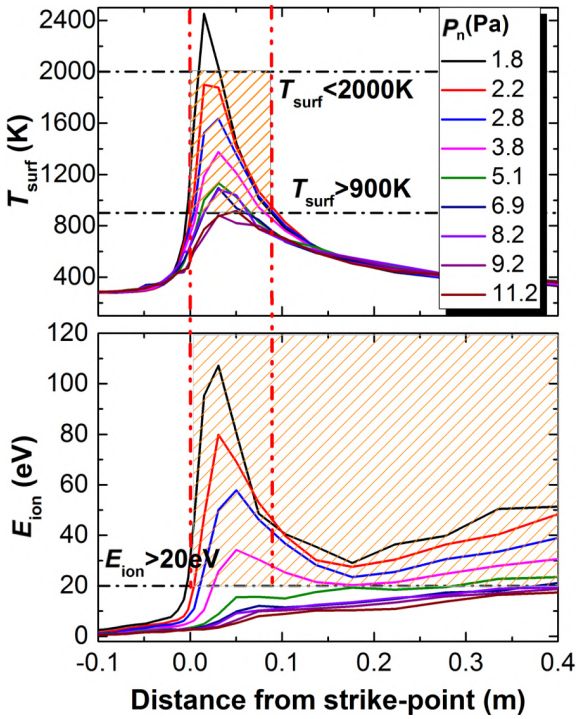

Figure 1.9: The temperature and ion energy profiles predicted for different neutral pressure at the ITER outer vertical divertor target, made using the SOLPS - 4.3 simulation. Taken from [33]

growth under fusion like conditions is required. There has long been concerns about the embrittlement on W surfaces after He irradiation [40], however W nanostructure formation poses new questions, as currently little is known about the positive and negative effects it could have on ITER's operation. For this reason, research to understand the nature of his phenomenon and it's evolution in fusion-like conditions must be carried out. In the following chapter a literature review of fuzzy W growth will be provided.

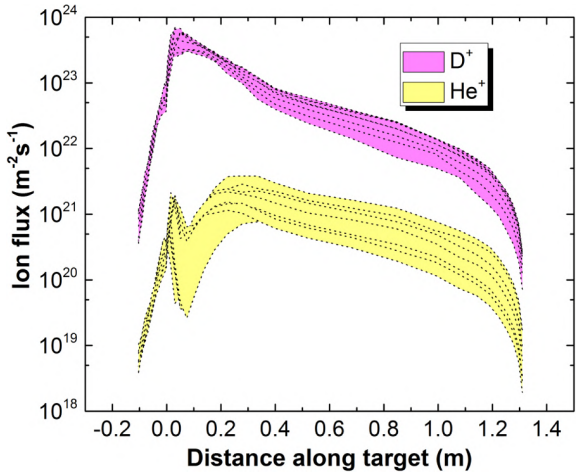

Figure 1.10: H and He flux profile predicted for the outer target of the ITER divertor [33].

Chapter 2

Literature Review

Over the following chapter, a literature review of the research on fuzzy tungsten (W) formation will be provided, highlighting the current knowledge in this particular field. Because of its current technical relevance to future magnetic fusion devices, the focus of this review is predominantly on fuzzy W formation, although fuzzy nanostructure formation has been observed on a range of metals and alloys besides W. The literature review will discuss the threshold conditions required for fuzzy W production, its formation theories, the consequences of fuzz growth for fusion reactors, and the growth of fuzz on other metallic surfaces. A description of the physics behind magnetron sputtering devices will be presented, and finally plasma physics concepts relevant to the current research will be discussed.

2.1 Fuzzy Tungsten Formation

2.1.1 Physical Description and Discovery

Fuzzy W is a surface morphology produced after He ion irradiation of heated W surfaces. The morphologies produced consist of networks of interlocking tendrils, growing at near random orientations from the surface they form on. Tendrils typically have diameters of between 10 - 50 nm [41], [42] and can grow to different vertical heights from the surface, depending on the exact experimental conditions (surface temperature, irradiation time [43]) or metal surface composition [44]. Generally, fuzzy W layers have been observed to grow to thicknesses in the range of 100s of nm to several μm [38], [43], [45]. As fuzzy W layers are formed, a decrease in the optical reflectivity of the surface has been shown to occur (to $\sim 1\%$ [46]), and this can act as a confirmation that nanostructure formation has occurred on the surface. As an illustration of this, in figure 2.1) two samples are compared; a) a pristine untreated W sample and b) a W sample after treatment with He plasma. The sample in 2.1b) is considerably darker than that shown in a), giving an indication hat fuzz has been formed on the surface. Moreover, fuzzy W layers can be characterised by their highly porous nature, with the porosity measured to be between 90 - 99 % [38], [47], implying a large amount of unoccupied space between the nanotendrils and internal bubble structure. The elemental composition of fuzzy W layer has also been studied using energy

dispersive X-ray (EDX) analysis [29], [43], with the resulting spectra (see figure 2.3a) and c)) indicating fuzzy W structures were made up of solely W (although trace impurities within the experimental device were observed in figure 2.3c)). Due to the nanoscale sizes of tendrils, the structures which comprise a fuzzy W layer cannot be seen with the naked eye. Scanning electron microscopes (SEMs) are generally used in the literature to image fuzzy W layers (examples given within the references [37], [42], [43], [45]).

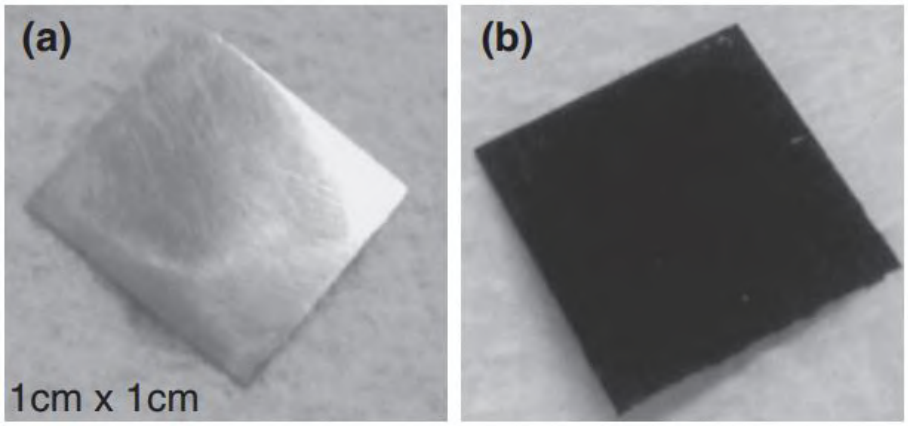

Figure 2.1: An image of a pristine W sample (a) and a fuzzy sample (b). Taken from [46].

Although He ion implantation into W has been investigated for many years, fuzzy W formation is only a fairly recent observation. The earliest reports of the darkening of W surfaces after helium plasma treatment were made by several authors [28], [48]–[50] in experiments using the NAGoya university DIvertor Simulator (NAGDIS II), a linear plasma device (LPD) capable of producing high density plasma discharges ($\sim 10^{20}$ m^{-3}), consistent with those anticipated for the divertor region in ITER. The first study to confirm the growth of fibre-form nanostructure formation was made by Takamura *et al.* [29] in [29], where W coated graphite samples were heated to a range of temperatures (1250 - 1600 K) and treated with low energy (12 eV) helium ions for high ion fluence exposures (3.5 x 10^{27} m^{-2}). Their conclusion based on their SEM imaging, shown in figure 2.2, described surface morphologies as being of a "submicron fine structure, resulting in optical blackening of the surface".

Subsequent investigations to the study by Takamura *et al.* were made by the team of Baldwin *et al.* in the PISCES laboratory at the University of California. Using similar conditions to those described in [29], investigations into the temperature [43], plasma species [47] and W grade effects [45] on fuzzy W growth were undertaken. After SEM identification of the surface nanostructures on W in [45], the authors Baldwin and Doerner were the first to describe the surface structures as fuzz. Fuzzy W is generally the accepted term to describe the nanostructures that are formed after He irradiation on W surfaces, however nanostructure formation [51] or fibre-form formation [52] is still used by authors.

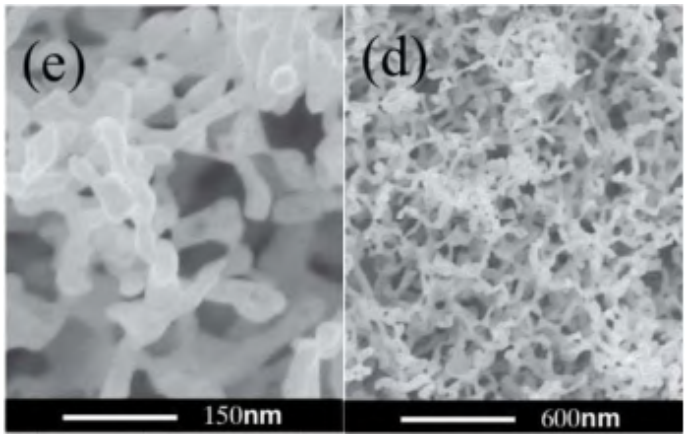

Figure 2.2: Image showing nanostructure formation on a W sample as seen through a field emission SEM, with scale bars indicated on each image. Taken from [29].

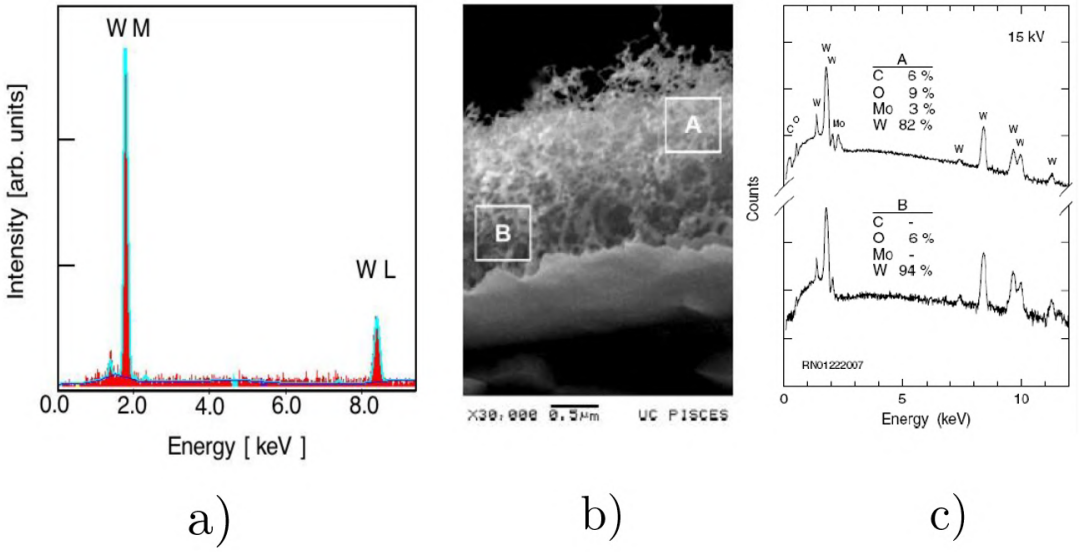

Figure 2.3: a) Shows the EDX spectra from a fuzzy W surface, taken from [29]. In image b) an SEM image of the sample indicating two areas of interest on the fuzzy W layer, A and B, is shown. The EDX spectra from A and B is shown in c), indicating the presence of W as well as small impurities within the experimental device. Image b) and c) used from [43].

2.1.2 Formation Conditions

The production of fuzzy W is dependent on three main experimental parameters; the surface temperature, the incident He ion energy and the He ion fluence (found from the flux of He ions multiplied by the time of exposure in seconds). The ranges of each parameter, verified through experimentation, that can lead fuzzy W formation will now be described.

Surface Temperature of W

Seminal papers by Kajita *et al.* [37] and Baldwin [43] *et al.* first introduced the idea of a temperature and He ion energy dependence for fuzzy W growth. In figure 2.4, the culmination of many investigations conducted on NAGDIS II and within the PISCES

laboratory showed the ranges of surface temperature and He ion energy which had been observed to produced fuzzy W. Overall, it is generally accepted that a temperature window of 1000 - 2000 K is required to form fuzzy W, however exceptions have been observed by Nishijima *et al.* where fuzz-like structures (shown in figure 2.5) were produced at surface temperatures of 2300 K. In addition, SEM imaging from Tokunaga *et al.*'s study in [53] shows what appears to be fuzz growth on the surface. In their report He ions had energies of 19 keV, and surface temperatures were well in excess of 2000 K at 2600 K. This may indicate some interplay between extremely large surface temperatures and He ion energies on the threshold conditions for fuzz growth, but generally the temperature range of 1000 - 2000 K is accepted for fuzzy W formation.

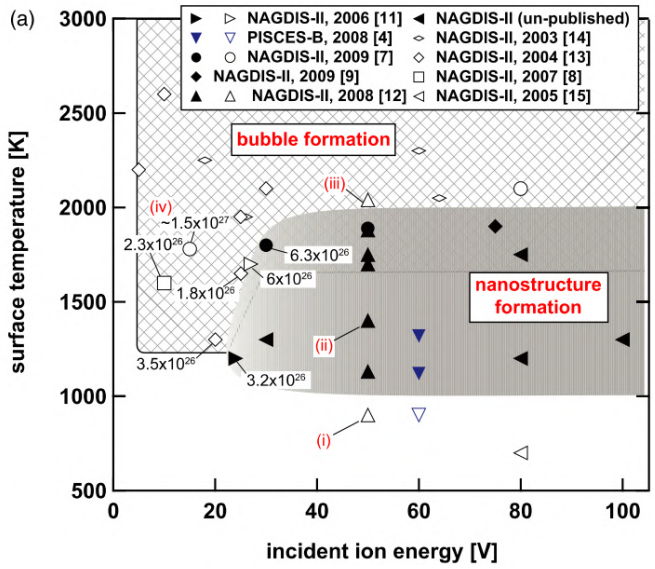

Figure 2.4: Graph to show the observed boundary conditions of the W surface temperature and He ion energy on the formation of fuzzy W. Taken from [37].

2.1.3 He Ion Energy

The minimum He ion energy required to grow fuzz is likely to depend on the surface barrier potential energy of W. In reports by Ullmaier *et al.* [54] the surface barrier potential of W was calculated to be ~ 6 eV, which agreed well with later findings by Nishijima *et al.* where He bubble formation was not seen in W surfaces when the He ion energy was < 5 eV. The most recent study by Thompson *et al.* showed that an ion energy threshold value of ~ 9.0 eV was required for He retention in W to occur [55]. Additionally, it is likely that at lower energies (i.e. < 20 eV) He ions do not penetrate the surface; a result of their reflection coefficient increasing as the He ion energy is reduced [21]. This implies that larger He ion fluences would be required to form fuzz if He ion energies less than ~ 10 eV are used in experiments. Where fuzzy W was produced using ion energies of 12 eV in [50], a fluence of He ions of 3.5 x 10^{27} m^{-2} was used to grow the fuzzy layer, perhaps agreeing with this

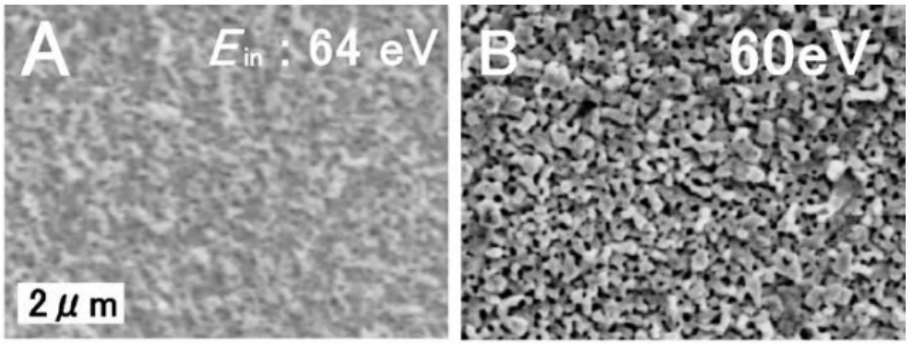

Figure 2.5: An SEM image of fuzz formed at a high W surface temperature (2300 K) and high He ion fluences ($\sim 10^{26}$ m^{-2}), taken from [28].

inference.

High energy He ions (keV) have also been shown to produce fuzzy structures on W surfaces [42], [53], [56]–[58], despite a larger sputtering rate of the surface likely to occur due to high energy of the impinging ions [21]. In the work by Meyer *et al.* in [57], it was demonstrated that for incident He ion energies of 8 keV, He plasma could lead to the production of surface nanostructures, which were near indistinguishable from fuzzy W typically produced in linear plasma devices at lower ion energies ($<$ 100 eV). The only observable difference found in [57] was that the diameter of fuzzy tendrils produced using keV ion energies had greater mean cross sections than fuzz produced by lower ($<$ 100 eV) ion energies. This observation of larger diameter fuzzy tendrils has been shown in the SEM images of fuzzy W grown under keV ion energies in other studies [42], [53], [58]. A comparison between the tendrils of fuzzy W layers in [42] (figure 2.6) showed that the tendril diameter increased from ∼20 nm with a He ion energy of 50 eV to ∼150 nm when the ion energy increased to 12 keV.

The upper He ion energy threshold for fuzzy W growth, which is an area seldom investigated, was shown to be between 100 KeV and 250 KeV in a study by Bannister *et al.* [60]. To date this study has used the largest He ion energies to attempt to grow fuzzy W, with 100 KeV producing fuzz but ion energies of 250 KeV leading to no fuzz growth. Bannister *et al.* also showed that larger W surface temperatures ($>$ 1200 K) were required to form fuzzy W in the higher ion energy range ($>$ keV), something which was also observed in other studies where keV ion energies were used [58]. In addition, at non-normal angles, the orientation of fuzz growth has been shown to be strongly dependent on the incident He ion energy [58]. In figure 2.7 two different ion energies, 10 keV and 218 eV respectively, were used to grow fuzzy W, with the incident beam angle being non-normal to the surface. It can be seen from figures 2.7a and b, where the incident ion energy is 10 keV and ion beam orientation is given as 43 ° to the surface, the angle at which tendrils in the fuzzy layer are observed to grow at is related to the angle at which the incident ions implant into the surface. When the He ion energy is much lower (218 ev) in figures 2.7c and d, the fuzzy W layer is less affected by the changes in incidence of the He ions, and tendrils seem to grow in more random orientations as is usually observed.

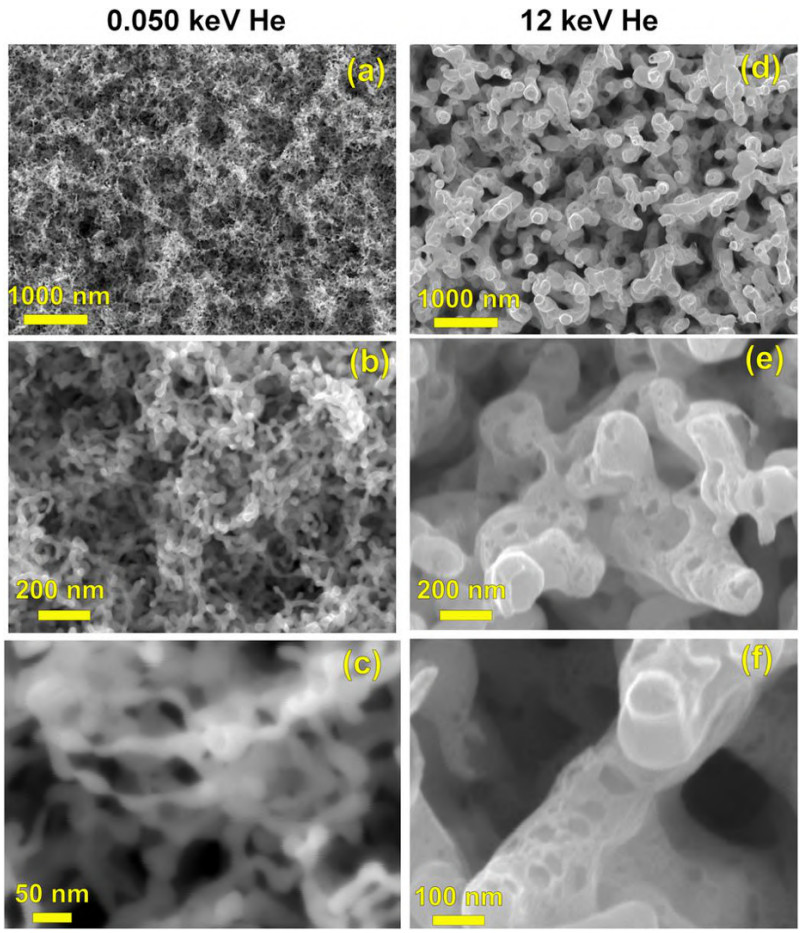

Figure 2.6: Fuzzy W surfaces formed using helium ion energies of 50 eV (a),b),c)) and 12 KeV (d),e),f), and viewed using SEM imaging. Taken from [59]

Time of Exposure

In early investigations on fuzzy W growth, the thickness of fuzzy W layers was observed to increase linearly with the square root of the exposure time [43]. In, [43], W fuzz was grown for increasing lengths of time at two different surface temperatures (1120 K and 1320 K) and at low energies He ion energies (<100 eV). In figure 2.8, the cross-sectional SEM imaging is shown from the study in [43], demonstrating the enhancement in the fuzzy layer thickness as the exposure time increased. On closer inspection, by plotting the thickness of the produced fuzzy W layer against the square root of the exposure time ($t^{1/2}$) Baldwin *et al.* demonstrated a near linear dependence between the two parameters (see figure 2.9 a). From these observations, Baldwin *et al.* established the growth law for a fuzzy layer thickness h as:

$$h(t) = \sqrt{2Dt} \tag{2.1}$$

where h is the thickness of the fuzzy layer, D is the Fick's law diffusion coefficient for one dimensional mass transfer, and t is the experimental exposure time. This dependence of the thickness of the fuzzy layer on $t^{1/2}$ was observed in subsequent investigations [37],

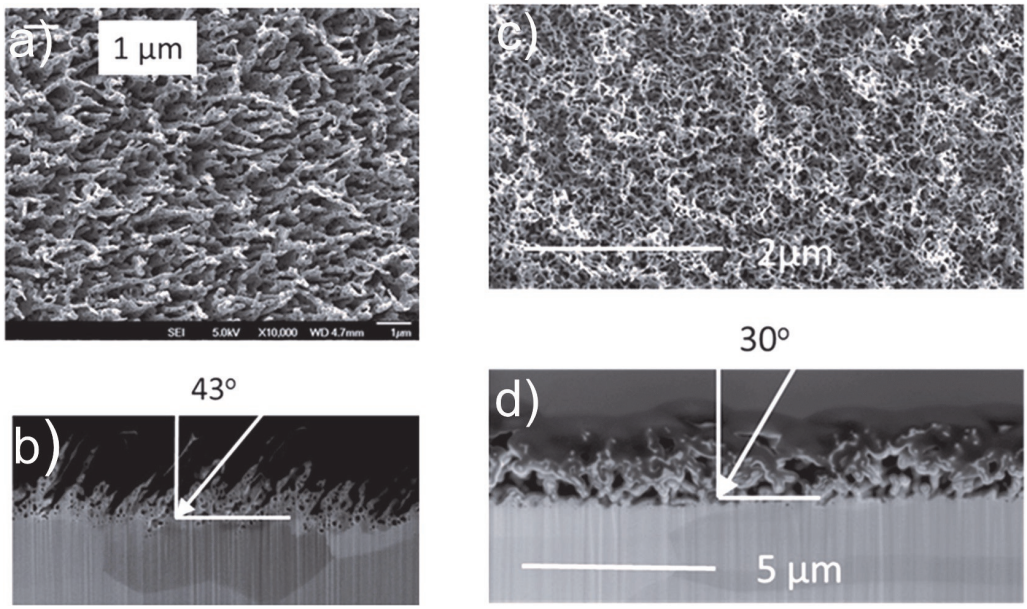

Figure 2.7: Fuzzy W formation at non-normal angles of incidence for very large (10 keV) and intermediate (218 eV) He ion energies. Image taken from [58].

[61]–[63].

However, in the report by Kajita *et al.* [62] an interval between the start of the He plasma exposure and the first appearance of fuzz growth was shown to exist. This minimum time or 'incubation' period (see figure 2.9 b)) was believed to be necessary for a sufficient He loading of the W surface, whereby He bubble formation and fuzzy W tendrils can then be produced. It is important to mention that in [62], Kajita *et al.* recast the growth law of equation 2.1 to be in terms of the He ion fluence in place of the time of the exposure. Subsequent findings by Petty *et al.* produced an adapted form of equation 2.1 and introduced the concept of an incubation fluence Φ_0, similar to that given by Kajita *et al.* in [62], allowing calculations of the expected fuzzy layer thickness h for a given He fluence, Φ, to be made [38] . The growth law of equation 2.1 was recast as,

$$h(\Phi) = \left(C(\Phi - \Phi_0)\right)^{\frac{1}{2}} \tag{2.2}$$

where C is a temperature dependent constant, equivalent to $2D/\Gamma$ where Γ is the incident He ion flux to the surface. The temperature constant C has since been calculated in various reports [38], [43], [44] for a W surface temperature range of 1120 to 1400 K.

In [38], the incubation fluence Φ_0 was shown to be equivalent to 2.5 x 10^{24} m^{-2}, however it is noteworthy that there have been observations of a dependence of Φ_0 on the incident He ion beam parameters, including the initial He ion energy [64], impurity concentration [38] and the initial He ion flux [44], [65]. Fluctuations in Φ_0 have also been shown for variations in the surface properties of the W, including the initial grain structure [66] and the crystallinity [60], [67]. In the study of Meyer *et al.*, Φ_0 was observed to be as low as 2 - 4 x 10^{23} m^{-2} for He ion energies of 218 eV and W surface temperatures at 1300 K [64]. A further reduction in Φ_0 was also reported by Garrison *et al.* in [68], where W surface

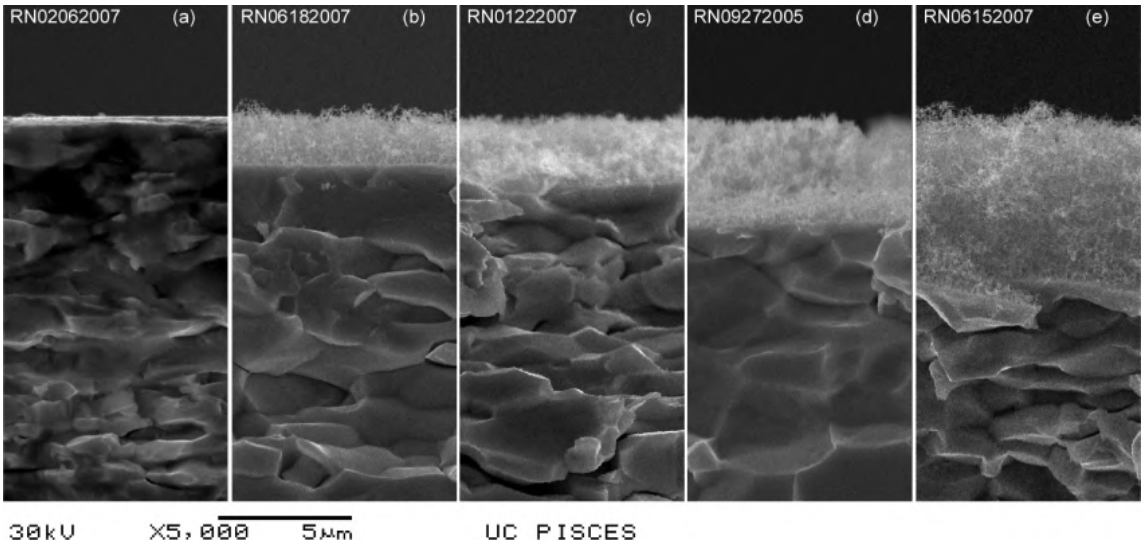

Figure 2.8: Cross-sectional SEM images of W surfaces exposed to pure He plasma for exposures times of increasing amounts of time. From left to right (a) 300 s, (b) 2000 s, (c) 4300 s, (d) 9000 s and (e) 20000 s. Samples were held at surface temperatures of 1120 K, and the He ion flux was equivalent to $\sim$ (4–6) x 10^{22} m^2 s^1 in order to maintain the constant fixed target temperature. Taken from [43].

morphologies, consistent with the early stages of fuzzy W growth, were observed after a He ion fluence of $\sim$ 8 x 10^{22} m^{-2}. In [68], very large He ion energies (30 keV) were used.

Conversely, at lower ion energies of $\sim$ 40 eV, Fiflis *et al.* reported an incubation fluence of 5 x 10^{25} m^{-2}, much larger than the incubation fluences observed by other authors at similar experimental conditions [38]. In this work a unique geometry for fuzzy W production is used, with a W wire wrapped around an alumina tube and exposed to radio frequency (RF) He plasma. It is reported in the study that the flux of ions is different across the wire surface, while there is no recording of a real time temperature measurement during the experiment. It is possible that this result of a much larger incubation fluence is erroneous due to either the temperature reading method or flux measurement, as at similar ion energies ($\sim$ 60 eV) and surface temperatures (1120 K) in [38] an incubation fluence of $\sim$ 2.5 x 10^{24} m^{-2} was found. Overall, it is implied by the observations in [64] and [68] that fuzzy W growth can be initiated at larger He ion energies, and this should be investigated further.

2.1.4 Erosion Limits to Fuzzy Tungsten Growth

For fuzzy W layers, the thickness of the layer has been shown to be reduced if the incident ion energy is greater than the threshold for sputtering on W [63], [69]. In Equation 2.2 the observed dependency of the fuzzy layer thickness on the fluence of He ions is described, however this equation does not account for any inherent erosion that could occur during the plasma exposure. This erosion may be caused by impurity species within the plasma (air leaks can lead to N_2 and O species) or the He ions themselves.

A saturation in the thickness of layers of fuzzy W was shown in [63] by Doerner *et al.*,

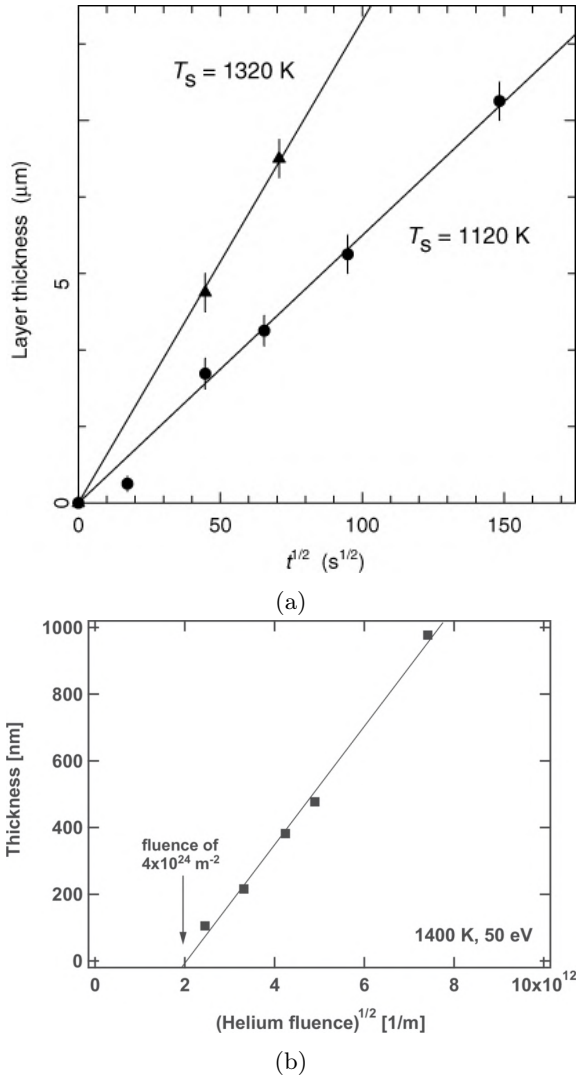

Figure 2.9: In a) a comparison of the fuzzy layer thickness against the square root of the exposure time ($t^{1/2}$) for two different surface temperatures (1120 and 1320 K)[43]. In b) a similar graph to a) howvever the He ion fluence is used in place of the exposure time, taken from [62].

where He ions with large energies (>250 eV), above the threshold for sputtering on W, were used. After a certain amount of time during the plasma exposure it was observed that a constant, non-changing fuzzy layer thickness was formed, any subequent increases in the exposure time did not enhance the layer thickness. Similar results were seen by Noiri *et al.* in [69], where a constant thickness or "equilibrium" thickness was produced after a balance between the fuzz growth rate and erosion rate by He ions was reached. An extension to the growth equation (2.2) was proposed in [38] to account for the erosion by of the fuzzy layer by ions, and is given as:

$$\mathrm{h}(\Phi) = \frac{\mathrm{C}}{2\epsilon_{\mathrm{fuzz}}}\Big(W\big[-\exp\big(-\frac{2\epsilon_{\mathrm{fuzz}}^2}{\mathrm{C}}(\Phi-\Phi_0)-1\big)\big]+1\Big) \tag{2.3}$$

where ϵ_{fuzz} is an erosion parameter equivalent to an erosion rate (E) divided by the He

ion flux (Γ), W is the Lambert function, and all other parameters are as defined earlier. Equation 2.3 has several useful features; when $\Phi \rightarrow \infty$, the exponential term approaches zero, meaning W[0] = 0, and h(Φ) $\rightarrow$ C/2ϵ_{fuzz} (the workings of the Lambert function are explained in more detail in [70]). As both C and ϵ_f are easily calculable, this implies that at high enough fluence, the thickness of fuzz will approach a constant value, i.e. an equilibrium thickness, agreeing with the experimental observations made in [38], [63], [69]. It is possible for the equilibrium thickness of the fuzzy layer to be produced after very large He ion fluence thresholds (x 10^{28} m^{-2}) like in [38] where the ion impact energy is low ($\sim$ 60 eV), or intermediate ion fluences (x10^{25}) like in [69] where the energy of the ions surpasses the sputtering threshold for He on W (see figure 2.10). The latter situation will be very relevant during the transient events predicted in fusion reactors, where the energy of ions near plasma facing surfaces is likely to reach hundreds of eV.

2.1.5 Changes in Tungsten Properties After Fuzzy W Growth

Fuzzy W growth has been shown to cause various changes to the properties of the W it forms on including: the sputtering yield [71], [72], secondary electron emission [73]–[75], thermal conductivity [76]–[80], and optical reflectivity [46], [65], [81]. Specifically, the sputtering yield for fuzzy W surfaces has been shown to decrease relative to pristine W surfaces [71], [72]. In [71], Nishijima *et al.* showed the reduction in the yield from a fuzzy W surface is decreased for thicker layers of fuzz growth with line of sight redeposition of sputtered particles believed to be linked to the reduced loss of material. In [78], Kajita *et al.* observed the heat diffusion across the nanostructured W layer with short (1 ns) laser pulse heating, and found the thermal conductivity of the nanostructured layer to be $\sim$ 1.5 W/mK which is around 1 % of that of pure (ideal) W. As a result of this decrease in the thermal conductivity, there are concerns over the stability of W surfaces in operation in a fusion reactor if indeed fuzzy W can form on them.

In one case, melting traces were observed on a fuzzy W surface after treatment with a pulsed layer despite the surface temperature being beneath the melting point for W [76]. In [82], Kajita *et al.* investigated the annealing temperatures required for a fuzzy W layer. They produced fuzz at 50 eV and a fluence of 1 x 10^{26} m^{-2} in NAGDIS-II, and found that fuzzy layer thicknesses could be reduced between surface temperatures of 1300 - 1600 K, with nearly all the surface morphologies removed after the temperature exceeded 1600 K [82].

2.1.6 Other Aspects and Applications of Fuzzy W

Fuzzy W surface morphologies have been shown to vary with the underlying crystallographic orientation, for both low ion energy (< 100 eV) [83], [84] and high ion energy (> keV) [60], [68], [85] He ion exposures. In many of the studies given in [67], [68], [85], W crystals with (100) orientations were deemed to have the greatest resistance to He ion irradiation, as a reduced number of fuzzy W surface morphologies were observed. However, in the investigation by Parish *et al.* [84], surface morphologies were observed on the (100)

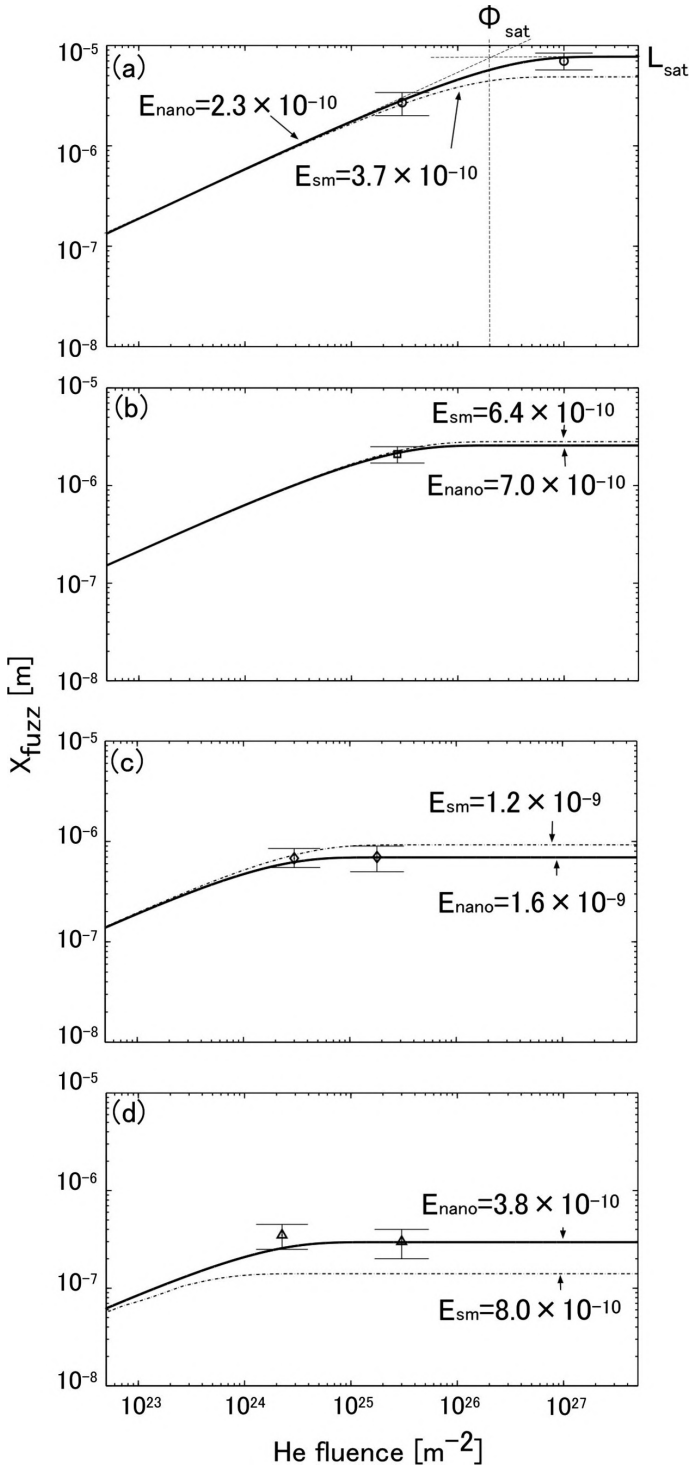

Figure 2.10: Fuzzy layer thickness (x_{fuzz}) reached at a constant sample temperature of 1300 K and for different He ion energies: (a) 200 eV, (b) 250 eV, (c) 400 eV and (d) 500 eV; the He fluxes ranged from 2.5 10^{21} m^2 s^1 at 500 eV to 10^{22} m^2 s^1 at 200 eV. In each case, the value of x_{fuzz} reaches a constant after some He ion fluence is reached, with an equilibrium thickness being reached in a shorter period as the He ion energy is increased.

planes after He irradiation on W surfaces after an incubation fluence of $\sim$ 4 x 10^{24} m^{-2}) was reached. Where fuzzy W was deemed not to be able to grow on (100) planes in the studies within [67], [68], [85], much lower He ion fluences (x 10^{22} to 10^{23}) were used. This

could imply that with enough exposure time, any resistance to fuzzy W growth is overcome. It should be noted that although fuzzy W formation was not observed initially on (100) W surfaces in [67], after a He ion fluences of 1.6 x 10^{25} m^{-2} was reached fuzzy W did grow, possibly due to a sufficient loading of the surface with He ions.

Fuzzy W surfaces have also been investigated for their applications outside of fusion research [86]–[88]. The reduction in the optical reflectivity of the surface of fuzzy W has led to investigation in the use of these layers toward solar thermophotovoltaic (TPV) cells, with fuzzy W layers estimated to absorb 98 % of solar light [86]. Oxidised fuzzy W layers (i.e fuzzy WO_3) were also observed to produced 5 x greater photocurrents compared to non fuzzy WO_3 surfaces [87], implying these nanostructured layers may have use in the process of solar induced water splitting for hydrogen production.

2.1.7 Formation Theories of Fuzz

Many mechanisms have been proposed to explain the initial formation of fuzz. Kajita *et al.* initially proposed a mechanism whereby He bubbles coalesce beneath the surface to produce larger high pressure bubbles, these are illustrated by the graphics in figure 2.11(a) and (b). As the bubbles increase in size, they are liable to rupture (c), which eventually will lead to the protrusions on the surface which resemble fuzz (d). However, this mechanism of fuzz growth would be unable to explain the continued growth of fuzz as tendrils become thicker (i.e. vertically away from the surface), as He would need to be able to reach the bulk of the metal to coalesce with other He and form bubbles. The mechanism described in figure 2.11 is therefore quite simplistic and would need more evidence to support it.

Alternative methods for fuzzy W growth typically include He bubble formation in the initial stages, with the later stages toward tendril/fiber formation through mechanisms of W adatom diffusion [89] or plastic flows of W [90]. In the report by Martynenko *et al.* [89], a model for fuzzy W growth showed how surface W adatoms are ejected from the surface layer and preferentially around He bubbles in the near surface region. The model produced the time ($t^{1/2}$) dependence for fuzz growth due to the kinetics of adatom diffusion over the metal surface, and the He ion energy threshold ($\geq$ 20 eV) for fuzz formation was produced in terms of the minimum energy for adatom formation ($\sim$ one-third of the sputtering threshold for He on W).

The model proposed in [90] by Krashennikov *et al.* (an illustration of which is shown in figure 2.12) describes the growth of tendrils through He accumulation beneath the surface, and a plastic flow of W around He bubbles to grow the fuzzy tendrils. Due to He bubbles coalescing beneath the W surface to form larger bubbles, W atoms will experience an asymmetrical force, caused by a reduction in the number of W atoms on each side. Nearer the surface side there are fewer atoms and far more atoms on the bulk side; hence a pressure gradient is formed which produces a net upward force on the W atoms. This force also exists for He bubbles that form, so He bubbles move upwards towards the surface in addition to W atoms. At large surface temperatures the effective viscosity becomes low and creep becomes important, allowing W to flow around He bubbles and begin the growth

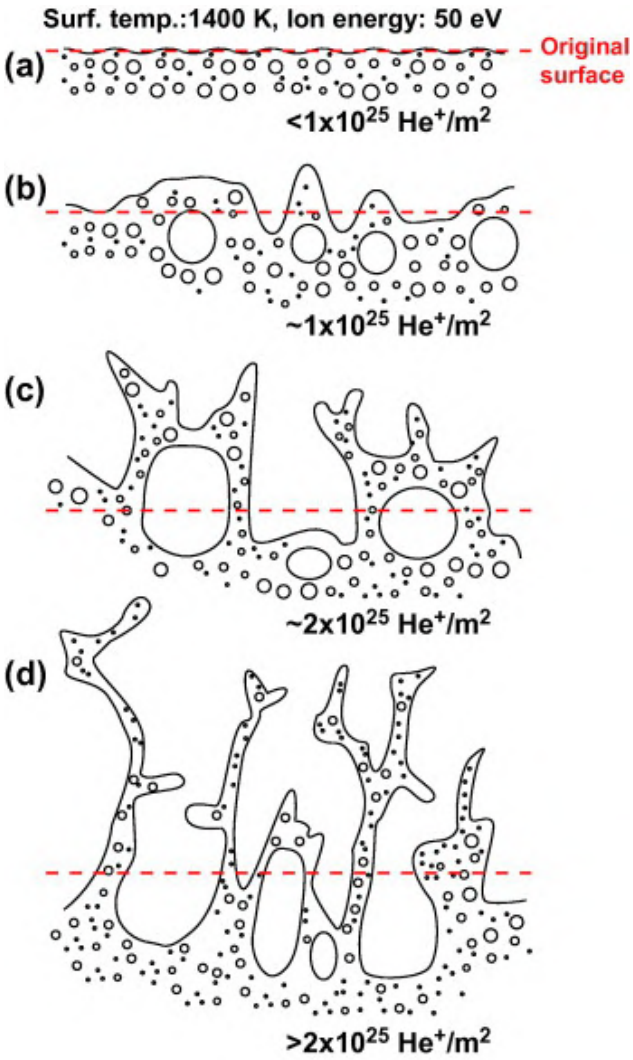

Figure 2.11: A theory for fuzz growth as described in [62] involving the growth and bursting of He bubbles.

of a tendril. The model shows many of the observations seen in experiments, such as $t^{1/2}$ dependence of the fuzz thickness, the saturation of fuzz growth with a He ion flux of 10^{22} m^{-2} s^{-1} (observed in experiments in [47]), the termination in fuzz growth at temperature $\sim$ 2000 K (upper bound of fuzz growth shown in figure 2.4), and the crystal orientation dependency on fuzzy W growth.

More recently a theory combining the mechanisms of adatom diffusion and viscoelastic flow was described by Trufanov *et al.* in [91]. The preferential movement of W atoms toward the tip of a tendril was explained by the increase in surface binding energy toward the tip. This difference in binding energy between the base and tip of the tendril produced a net force upward, explaining the growth of the tendri. Again the proposed $t^{1/2}$ dependence was found, and values for the diffusion coefficient D (see equation 2.1) were consistent with the experimentally found values for D at 1120 and 1320 K in [43].

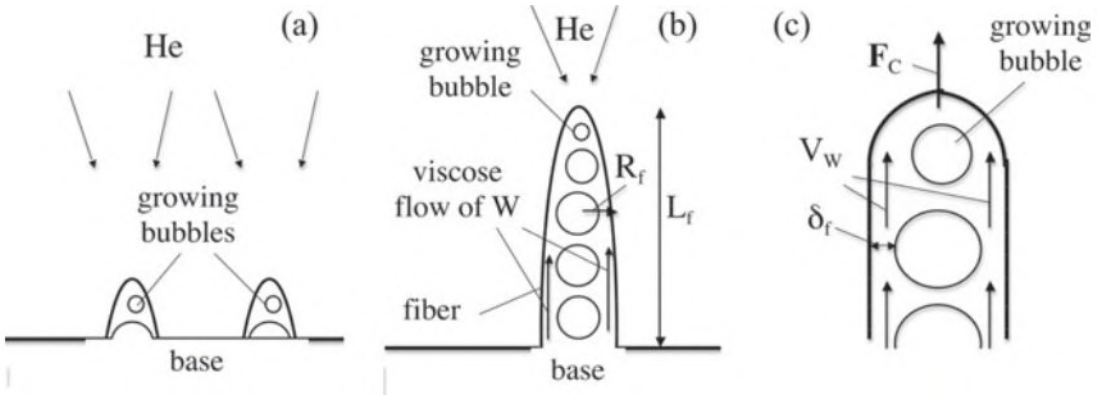

Figure 2.12: A proposed model for fuzz growth based on the viscoelastic flow of W atoms [90].

2.1.8 Relevance of Fuzzy Tungsten Growth For Nuclear Fusion Reactors

As a result of the choice for W components to replace CFCs in ITER, many experimental fusion devices (Alcator C-Mod, D-II-D, ASDEX-U, K-STAR, LHD) which were built in preparation for ITER have included W components in their design, particularly in the divertor regions of the reactor. With the possibility for fuzzy W production in certain sections of the ITER divertor, various studies within the aforementioned experimental reactors have investigated the evolution of fuzzy W layers under fusion like conditions.

Evidence of Fuzzy W Growth In Fusion Reactors

Although fuzzy W is regularly produced in laboratory experiments within linear plasma devices (LPD's such as NAGDIS II [37] and PISCES A [45])), small plasma devices (e.g. magnetrons [92], [93] and ion beam accelerators [84], [94]), fuzzy W formation has only been observed sparingly in fusion reactors [95], [96].

Wright *et al.* reported fuzzy W growth on W Langmuir probes situated in the Alcator C-Mod W divertor [95], for He ion fluences of $\sim 10^{26}$ m^{-2} and ion energies estimated to be in the range 50 - 250 eV. Surprisingly, the fuzzy layer that had formed showed little to no signs of melting in the SEM imaging of the W probes, which was significant as large heat loads ($\sim$ 40 MW/m^{-2}) were produced during the eleven 2s discharges. No observations of unipolar arcing were made across the fuzzy W surfaces in [95], something which has previously been observed on fuzzy W surfaces in both experimental LPD [72], [97]–[99] and fusion reactor devices [96], [100]–[102].

Unipolar arcing on fuzzy W surfaces has been shown to induce small mass losses ($\sim$ 10 % of the fuzzy W layer) on the surfaces they form across, with deep arcing trails also being observed to reach the bulk surface [99]. In [97] laser pulses with energies of 0.01 MW m^{-2} were sufficient enough to initiate arcing on a fuzzy W surface, with these laser energies being far lower than those expected during transient edge localised mode (ELM) events in ITER ($\sim$ 20 MW m^{-2}). The fuzzy W layers were imaged using transmission electron microscopy pre and post laser exposure and the reduction in the fuzzy layer was clear from their imaging, given in figure 2.13 a) and b). In a separate study by De Temmerman *et*

al. [103] where far larger laser pulse energies (0.5 MJ m^{-2}) than in [97] were used, fuzzy W layers were observed to reduce in thickness and in some cases completely disappear. It is likely that this reduction in the fuzzy thickness is due to annealing, which has been observed to to occur for fuzzy W layers in the temperature range 1300 to 1600 K [82].

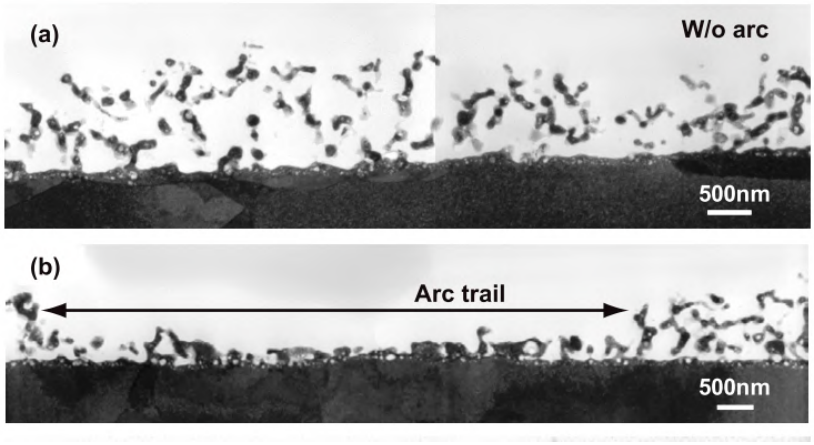

Figure 2.13: In a) the original fuzzy W layer and in b) the same fuzzy layer but post arc ignition across the surface. Adapted from [97].

In what may seem a confusing result by comparison, exposure of fuzzy W samples to far larger heat loads (20 MW m^{-2}) by Wong *et al.* in the DIII-D tokamak divertor for 2 - 4 s discharges showed no measurable mass loss, with only partial surface arcing observed after SEM imaging [104]. In a similar study at the COMPASS tokamak [102], pre-prepared fuzzy W samples were held in position in the divertor regions and subjected to an ELM plasma to test their stability under large fluxes of high energy ions. Melting of the fuzzy layer was observed in some small areas (shown in figure 2.14) however for the most part the fuzzy W surface was preserved. In addition, mass loss measurements did not show any loss of mass had occurred, which questioned whether material was removed during the melting but had instead annealed back into the surface. It is also important to note that mass measurements would have to be very precise to measure a mass difference after any small removal of a fuzzy W layer. Typical fuzzy layer masses have been reported to be tens of μg for $\sim 1\mu$m thick layer on a 1 cm diameter disc [105]. One question unanswered is why fuzzy W has only been observed so sparingly in fusion reactors so far, with multiple tokamaks using W materials as well as, on occasion, He or D/T plasma exposures. In current tokamaks it is necessary for material surface conditioning between plasma exposures to remove the build up of any organic or oxide films on the chamber walls. To condition the wall surfaces, glow discharges are generally used to sputter clean away any impurity deposits on the wall area. It may be that during this sputtering any fuzzy W which may have formed is actually removed, hence why fuzz growth has been notably absent from any major fusion reactors D-T/He campaigns.

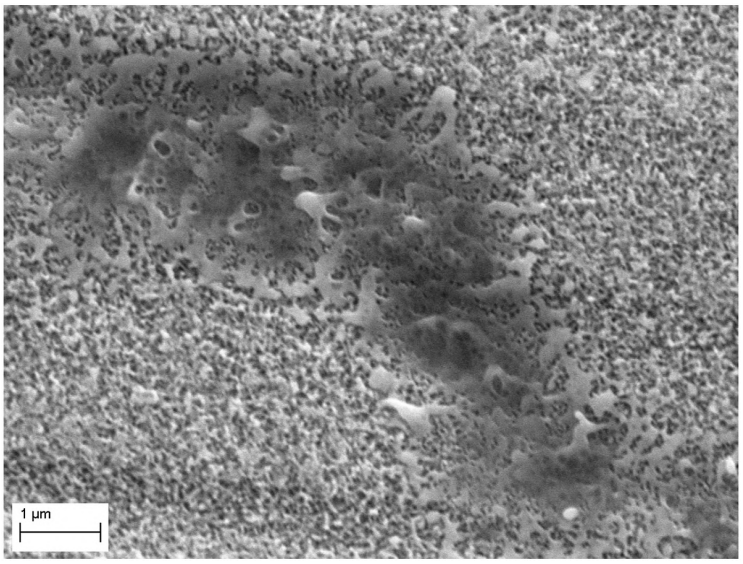

Figure 2.14: Localized fuzz melting inside an arc trace on a fuzzy W sample placed in the COMPASS tokamak divertor taken from [102].

The Effects of Fuzz Growth on Hydrogen Retention

The retention of hydrogenic fuels (in particular tritium) is a concern in the safe operation of fusion devices. Although some level of T retention is likely to occur, it is important to limit this where possible. The are limits to the physical amounts of tritium that can be held on a nuclear site at any time, as well as to preserve the fuel within the fusion plasma as possible [106]. It is still a matter of ongoing research as to whether He gases can encourage the retention of hydrogen (H) in W surfaces. In some cases, H retention has been reduced by the growth of He bubbles in W [35], [107]–[110], whereas other investigations have suggested that He bubbles attract H and enhance its retention in the metal [111], [112]. The study by Roth *et al.* in [113] explained that as hydrogen diffusion in W is relatively fast, but hydrogen's solubility in W is relatively low, He can trap H in the near surface region rather than deep within the material. This should, in effect, reduce hydrogen retention by trapping most of it near the surface regions. This conclusion was also reached by Wampler and Doerner as well [114]. A similar reduction in D retention was also shown by Reinhart *et al.* [115] where they used a small percentage of He impurity (5%) in a D plasma. At low surface W surface temperatures (380 K) and ion energies of 40 eV, the deuterium retention was reduced by a factor of three. In the same studyusing a small percentage of argon in place of He was found to increase D retention by 30 %.

2.1.9 Fuzz on Other Materials

Although the focus of this thesis is on W fuzz growth, other fuzzy nanostructures can also be formed on other metal surfaces. Small nanostructures have been observed for H irradiation of W in [25], but fuzzy nanostructure growth is an effect unique to He plasma. Kajita *et al.* have recently provided a summary on the production of nanostructures on a wide variety of metals [116]. The formation of nanostructures after helium irradiation

had already been observed through SEM imaging in previous works including those on titanium [117], tantalum [118]–[120], iron [118], [121], [122], rhenium [120], niobium [123], molybdenum [124]–[127] nickel [121], alloys such as stainless steel and silicon carbide [128] and alloys of tungsten including tungsten rhenium [44] and tungsten-tantalum [129]. Figure 2.16 shows the dependence on the growth of the nanostructures, which can vary from the typical tendril to nano/micro pillar structures (see figure 2.15), on the surface temperature and melting point of the metal. Kajita *et al.* had previously proposed that the temperature window for fuzz formation was a function of the melting temperature, T_m, and the surface temperature T_s [130]. The ratio of both T_s and T_m was found to be equivalent to a window for fuzz growth such that if $T_s/\ T_m \sim 0.25$ - 0.55, fuzz can be formed on the surface [130].

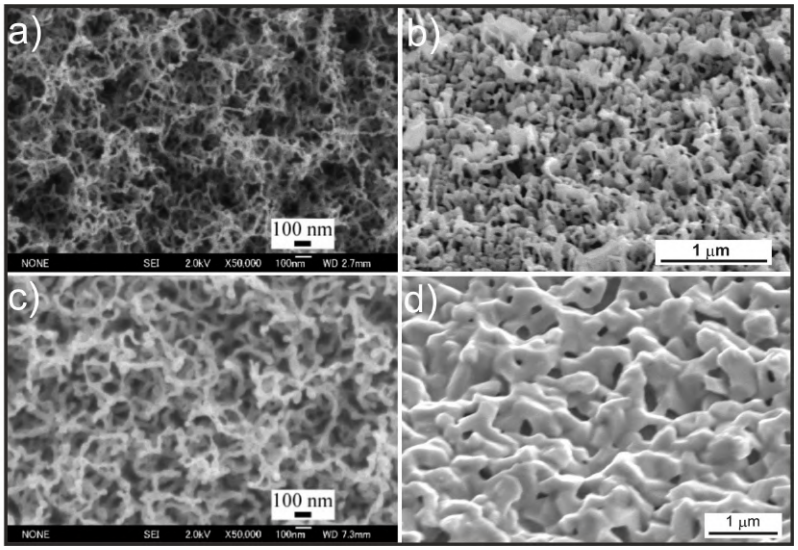

Figure 2.15: Comparison of the nanostructure formations formed on surfaces of a) W [125], b) Mo [125], c) Pt [116] and d) Ti [117] after treatment with He plasma

For W, fuzz generally grows for surface temperatures in the range 1000 and 2000 K, which corresponds to $T_s/\ T_m = 0.27$ - 0.54, whereas Mo fuzz has been shown to grow in a much narrower window than in figure 2.16 of 800 - 1073 K [120], [126]. In addition, the He ion energy is likely to be more important as the threshold energy condition for sputtering by He may decrease as the surface type changes. At energies of < 100 eV, the sputtering yields for He on W or Mo can be low ($< 10^{-4}$) [131], however for other metals, Fe for example, the yield can be considerably larger ($\sim 10^{-2}$ at 48 eV). As the threshold energy for sputtering deceases, the competition between the fuzz growth rate and sputtering becomes more important. Therefore although fuzz growth can occur on other metals in addition to W, if the He ions are energetic enough to cause significant sputtering, then it is likely that no nanostructures would be visible on the surface. Therefore, without a proper consideration of the incident He ion energy, the temperature window shown in figure 2.16 should be viewed with some caution.

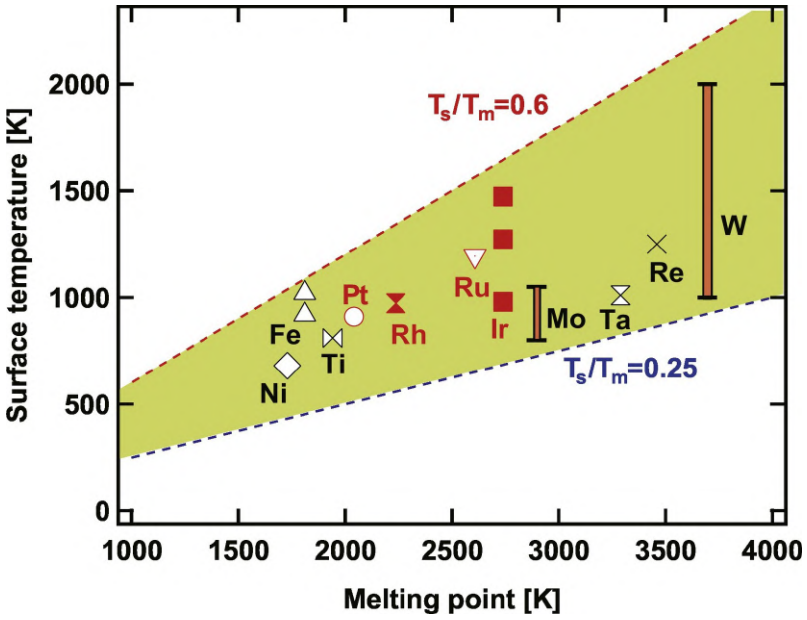

Figure 2.16: Comparison of the surface temperature and melting point for a range of metals which have been shown to demonstrate fuzzy formation. The yellow shaded region indicates the temperature window (between $0.25t_m$ and $0.5T_m$ where T_m is the melting temperature) for fuzzy nanostructure production on each metal. Taken from [116]

2.1.10 Mixed Helium and Impurity Plasma Exposures of Tungsten

In the divertor regions of ITER, it is likely that the plasma will be a mixture of many different species including H and He. It is also possible that wall material (Be, C, W) can be removed due to physical sputtering, transported from other areas of the reactor, and be deposited upon PFCs in the divertor. To date, there has been little research investigating the effects these kinds of deposition could have on fuzzy W growth. He ion beams mixed with small percentages of impurity were exposed to W surfaces by Baldwin *et al.* [47] and Al-ajlony *et al.* [132]. In [132], a He ion beam was mixed with C impurity, and for a W surface temperature of 1173 K and an ion energy of 300 eV, no fuzzy W was formed despite the relative percentage of C being decreased from 0.5 % to 0.05 %. When the impurity percentage of C in the He beam was $\sim$ 0.01%, fuzzy W was not observed to across the whole of the surface but instead small "islands" of fuzzy W structures (figure 2.17) were observed with a seemingly random distribution. There was a large variation in the shape and size of these islands, and SEM analysis showed He bubble formation was not present beneath the surfaces where the islands were observed. This implied that the islands may have grown elsewhere on the surface and been transported to their final position, although this was not confirmed.

Similar structures to the fuzzy W islands described in [132] were observed to form on W surfaces exposed to He plasma and ion energy modulation [94], [133]. In the study by Woller *et al.*, Nano-Tendril Bundles (NTBs) were observed on W surfaces treated with a helicon plasma source (see figure 2.18). The formation of NTBs were initially believed to be due to an RF-modulation effect on the He ion impact energy on a timescale consistent

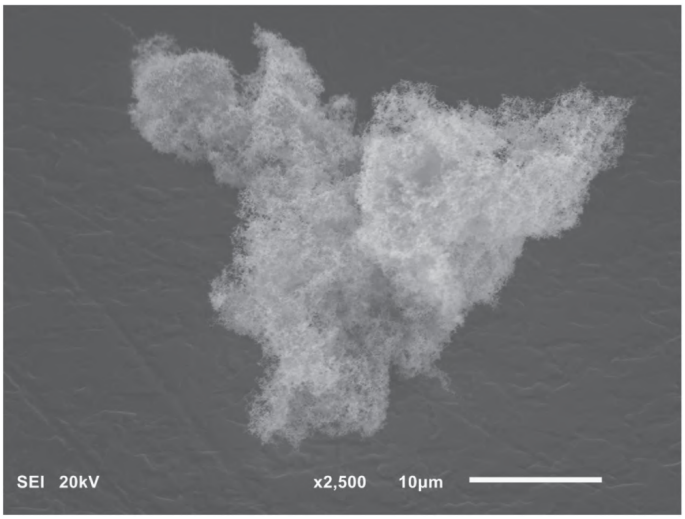

Figure 2.17: Islands of isolated fuzzy W structures observed using SEM imaging, from [132].

with surface-adatom diffusion time [94]. However, subsequent findings by Woller *et al.* showed NTB formation using much lower ion energy modulation frequencies (by a factor of 1000) [133], with NTB formation still yet to be fully understood.

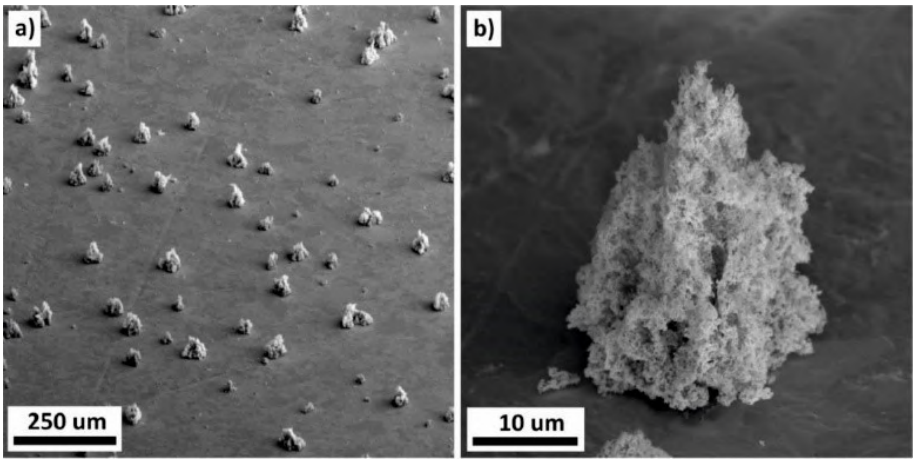

Figure 2.18: The observation of Nano Tendril Bundles (NTBs) on W surfaces in [133].

2.1.11 Devices For Fuzzy W Research

To summarise the plasma devices that have been described in the literature review so far, a large amount of fuzzy W research is carried out in two main research groups at Nagoya University and the University of California at San Diego (USCD). In the Nagoya group, the linear plasma device (LPD) NAGDIS II is predominantly used for fuzzy W research, and in USCD the PISCES laboratory, which house the LPDs PISCES A and B, is used for investigations of He interactions with W. Research into the interactions of He with W surfaces is also carried out by research groups at the DIFFER institute in the Netherlands using the LPDs Magnum-PSI and Pilot-PSI. LPDs are unique experimental devices for the purposes of nuclear fusion research in that the plasma densities ($\sim 10^{20}$ m^{-2}) and

particles fluxes (10^{23} m^{-2} s^{-1}) that can be produced within them are comparable to those predicted for the ITER divertor. Generally, LPDs consist of vacuum vessels (several metres in length), with plasma sources in the upstream regions and a magnetic field configuration designed to transport the plasma to the downstream. In each LPD, the plasma source can vary, with LaB_6 cathode (NAGDIS-II, PISCES A and B) or cascaded arc sources (Magnum-PSI, Pilot-PSI) being used to generate plasma. Discharge currents of 100s of A and magnetic fields on the order of 0.1 T are easily created in these devices These devices act primarly as a simulator of divertor conditions within a fusion reactor. Excess power entering divertor areas will radiated away by impurity gas seeding, ultimately producing divertor plasma detachment. Electron temperatures, expected to be tens of eV in a fusion reactor divertor, can be recreated in these machines.

In addition to LPDs, smaller scale experimental investigations into He irradiations of W surfaces have been carried out using magnetron sputtering devices [65], [93]. These devices are capable of producing He plasma at much lower densities ($\sim 10^{15}$ - 10^{16} m^{-2}) and fluxes ($\sim 10^{20}$ m^{-2} s^{-1}) than in the aforementioned LPDs, however the relatively cheap and simple set up of magnetron sputtering systems make them an interesting alternative to conduct fuzzy W research.

2.2 Magnetron Sputtering Devices

Up to now, the research that has been described for fuzzy W has been conducted on large LPD's. Recently, new approaches to fuzzy W research through the use magnetron sputtering devices have been demonstrated [65], [93]. Magnetron sputtering devices are capable of producing plasma densities of $\sim 10^{14}$ - 10^{16}, when operating in direct current (DC) modes, however larger densities have been shown to be produced through high power pulsed modes [134]. Due to the lower density in the DC mode, low fluxes of He ions are produced, and this can allow lower He ion fluence ranges to be probed, an area often overlooked in fuzzy W research. By their nature, magnetrons can produce metallic deposition during the plasma exposure via sputtering of a metal target. Because of this, magnetron devices are typically used in the production of thin film production for industrial applications [135], [136]. This production of metallic deposition also offers an interesting way to simulate a fusion like environment where co-deposition of metallic material may occur. This thesis consists of experiments using a DC magnetron sputtering system, so a description of the processes involved in magnetron sputtering devices will now be given.

2.2.1 Magnetron Sputtering Devices Concepts

Fusion plasmas are often described as thermal plasmas due to the large temperatures of both the ions and electrons (many keV) which are produced within them. Laboratory plasmas by comparison typically have cold ions (room temperature) and hot electrons (a few eV), and ionisation rates can be very small, meaning only a small percent of the neutral gas is actually ionised. A way to maximise the ionisation rate of the neutral gas is to

introduce magnetic fields which can confine electrons, and therefore increase the likelihood of interactions of electrons with neutrals. Magnetron sputtering devices (MSDs) utilise this process [137].

In direct current (DC) MSDs, a cathode plate has a metallic target placed in front of it. Behind the cathode, i.e. on the non - plasma facing side, permanent magnets are arranged in such a way that one pole is positioned at the centre axis of the metal target, with a ring of magnets producing a second pole at the outer edge. Through the application of an electric field on the cathode, the plasma discharge is initiated where ions in the plasma are accelerated towards the cathode/target surface. These ions bombard the metallic target surface producing secondary electrons. The emitted electrons are confined in front of the target by the presence of the magnetic field, with electrons following Larmor orbits centred around these field lines. In the areas where these electrons are confined and their density increases, more ionisation of the neutral gas will occur. As more ions are produced and accelerated toward the target, ion bombardment can lead to the removal of atoms from the target surface, a process known as sputtering. In sputtering, the material ejected from the target surface is able to diffuse through the vacuum chamber and deposit on to the chamber walls or other surfaces placed in their path. This process is a widely used technique to produce deposition of thin film layers or coatings with these layers having applications in engineering and industrial fields.

For DC magnetrons, the typical ranges of cathode potential (100s of volts) mean that ions have energies which, when they bombard atoms on the target surface, will produce a single knock-on regime of sputtering. The energy threshold (E_{th}) required to remove an atom from its surface can be considered in terms of the conservation of momentum in the interaction, where $\mathrm{E_{th}}$ is given by,

$$E_{\mathrm{th}} = \frac{(M_i + M_t)^2}{4 M_i M_t} E_s \tag{2.4}$$

where M_i and M_t are the ion mass and target atom mass, and E_s is the surface binding energy. The most common choice for the surface binding energy is to use the sublimation energy [21] and this is given to be in a range 8.68 to 8.80 eV for W [138]). As can be seen from equation 2.4, where $M_i \ll M_t$, E_{th} is large; this is the case for He sputtering of W. For He ion irradiations on W a value of E_{th} is found to be $\sim$ 100 eV assuming the earlier stated values of E_s. Comparative gas species, such as argon (Ar), which are also used in magnetron sputtering devices have much lower energy threshold values for sputtering threshold on W ($\sim$ 15 eV). Given that the typical DC voltages on MSD cathodes are usually on the scale of 100s of volts [137], He ions are still likely to have enough energy to sputter a W target in a magnetron system. In sputtering events, the measure of sputtered particles or yield of the surface is given by the ratio of ejected particles to the incident flux of particles. The sputtering yield can be defined as,

$$Y = \frac{\text{number of particles removed}}{\text{incident number of particles}} \tag{2.5}$$

with sputtering yields known to depend on the type of target atom and the incident ion energy. In practice, the sputtering yield of a surface can also be found if the mass change, Δm, during the plasma exposure is known, An expression for the experimentally measured sputtering yield is given in [21] to be,

$$Y = \frac{\Delta m}{M_2 n_1} N_0 \tag{2.6}$$

where M_2 is the target atomic mass, n_1 is the number of particles reaching the surface, and N_0 is Avogadro's number. Sputtered material will leave the surface with some energy (E), and this energy has been shown to be represented by a distribution described by the Sigmund-Thompson theory

$$f(E)dE = \frac{E}{(E + E_s)^3} dE \tag{2.7}$$

where f(E) is the energy distribution as a function of the sputtered particle energy (E), and E_s is the surface binding energy. An example plot of equation 2.7is the Thompson distribution, shown in figure 2.19. In this plot a W surface was assumed, thus for sputtered W the maximum point on figure 2.19 corresponds to a particle energy of $E_s/2 = 4.34$ eV. MSDs can also operate with different magnetic field configurations, determined by the

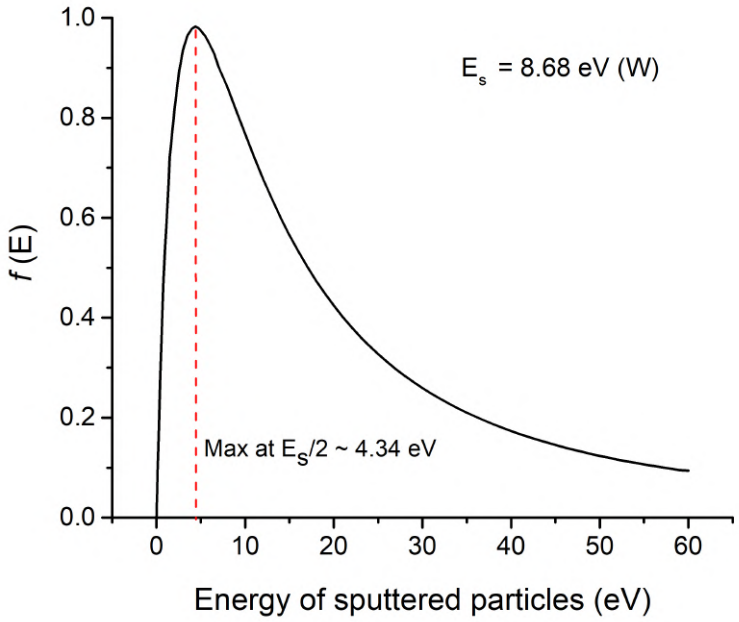

Figure 2.19: A Sigmund-Thompson energy distribution of sputtered particles for a W case where $E_s = 8.68$ eV, normalised to 1. The maximum point of the curve is seen to occur at 4.34 eV.

balance in strength between the central magnet and the outer ring of magnets. In an unbalanced configuration, the outer ring of magnets is strengthened relative to the central pole. In this case not all field lines are closed between the central and outer poles, with field lines generally extending toward substrate surfaces placed inside the magnetron system.

This allows secondary electrons to propagate a greater distance into the chamber, increasing the plasma density closer to the substrate surface. This operation of the magnetron in an unbalanced mode therefore acts to increase the ion flux density to the substrate surface [137]. This increase in ion flux density at the substrate can enhance the ion bombardment of it, improving properties (hardness, density) of the thin film layers [139].

2.2.2 Plasma Physics Concepts

Plasmas must meet certain requirements to be classified as a plasma and not a gas. A fundamental characteristic of a plasma is its capability to "screen" out any electrical potentials that are applied to it. Assuming a floating (i.e. non-electrically biased) surface is inserted into a plasma, a negative charge will build up on its surface due to the higher mobility of electrons compared to ions. As a result, an electric field is established which acts to decelerate electrons and accelerate ions toward the surface. This field acts to increase the ion flux to the surface to match the electron flux, such that zero net current leaves the plasma. Around the surface the density of ions increases, creating a positive region of space charge (or cloud), while the density of electrons is reduced. At the edge of this cloud region the electrostatic field produced can be weak. The thermal energy of particles is sufficient to allow them to escape the electrostatic potential well. The thermal energy is given as,

$$eV = k_{\mathrm{B}}T \tag{2.8}$$

where e is the electron charge, V is the potential at the surface placed in the plasma, k_{B} is the Boltzmann constant and T is the particle's temperature. As described in [140], a measure of this shielding distance, known as the Debye Sheath, is given by the Debye length λ_{D}, defined as,

$$\lambda_{\mathrm{D}} = \left(\frac{\epsilon_0 k_{\mathrm{B}} T_{\mathrm{e}}}{ne^2}\right)^{\frac{1}{2}} \tag{2.9}$$

where ϵ_0 is the permittivity of free space, T_{e} is the electron temperature, n is the plasma density and e is the electron charge. In equation 2.9 it can be seen how for an increase in the plasma density n, λ_{D} will decrease. Conversely, as T_{e} increases, so does λ_{D}. It is the electron temperature which is used in λ_{D} due to the increased mobility of electrons, allowing them to move to create decreases or increases in the electron density within the sheath during the shielding process. For Debye shielding to be sufficient to shield away charges placed inside the plasma the number of particles, N_{D}, required for this is,

$$N_{\mathrm{D}} = n\frac{4}{3}\pi\lambda_{\mathrm{D}}^3 \tag{2.10}$$

Using these two quantities λ_{D} and N_{D}, Chen summarises the necessary criterion for a plasma as follows [141]. Firstly, the Debye length $\lambda_{\mathrm{D}} \ll$ L, where L is the dimensions of the system. Secondly, $N_{\mathrm{D}} \ll 1$. The third requirement is related to the collisions of ions with neutral particles within the plasma. If ions collide too frequently with neutrals, their

motion is controlled by ordinary gas kinetics, and not electromagnetic forces. In plasmas, it is required that the product of the frequency of the plasma oscillations ω and the mean time between collisions with neutral atoms τ is greater than one, i.e. $\omega\tau > 1$. In the case of the magnetron sputtering system when W surfaces are used to grow fuzz on, a sheath will be produced around its surface after it is placed in the plasma. The energy of ions impinging on the surface will depend on both the plasma potential V_p (the ions initial energy) and the bias applied to the surface (V_b) on which fuzz is growing. The energy of ions (E_i) can be found using:

$$E_i = V_p - V_b \tag{2.11}$$

with the units of the ion energy given in eV. The ions will have this energy if they do not collide with other neutrals within the sheath regions, so the collisionality of the sheath is also important to consider. This can be verified by comparing the cross section for a collision between ions and neutral with the mean free path of a He ion. Low temperature plasmas like those produced in magnetrons are known to be weakly ionised [137] but collisions between charged particles and neutral species can still occur. The mean free path, λ_m, is calculated as,

$$\lambda_m = \frac{1}{n_n \sigma} \tag{2.12}$$

where n_n is the density of the neutral gas atoms and σ is the cross sectional area of the neutral atoms [141] For the case where $\lambda_m > \lambda_D$, the sheath can be assumed to be collisionless and the ion energy is given by calculation of equation 2.11. A calculation is made in appendix A to show that the sheath at a fuzzy W surface in the magnetron system can be considered collision-less.

2.2.3 Mechanism of formation of He bubbles in W

Due to its low solubility in metals, helium is present in metals only implantation, with displacement damage within the lattice being necessary to allow He accumulation. During He irradiation, He diffuses through the metal, clustering together with other He atoms, a result of their strong repulsion by W atoms [34], and strong attraction to He (amongst other defects such as vacancies or impurity atoms [142]. The predominant positions for He atoms in the lattice are interstitial and substitutional sites (where a He atom occupies a vacancy (V)).

The likelihood of finding a He atom in a particular position and its dominant migration type depends on both the surface temperature and presence of defects (both intrinsic and radiation-induced), which act as traps for He atoms. As He accumulates, producing more massive clusters, the pressure within the cluster increases, forcing nearby W atoms to be "pushed" from their lattice sites to interstitial positions. The removal of W atoms produces a vacancy in the lattice, otherwise known as a Frenkel pair. The He cluster is now effectively bound to a vacancy (so-called He-vacancy complexes), with interstitial W prevented from recombining by He atoms, which then occupy the vacancy. This process,

known as trap mutation or self-trapping [143], [144], allows the production of larger He clusters (commonly called bubbles) to form. The critical size of a cluster to produce this effect is known to vary with temperature, a result of the pressure of the gas inside the cluster/bubble and the activation energy for self interstitial formation [145]. However, a threshold of 6 or 7 He interstitials appear to be required to trigger a spontaneous trap mutation in bulk W [146], with lower numbers being sufficient nearer the surface [147].

Bubbles will grow as they accumulate more mobile He clusters, causing a further repetition of the trap mutation process, releasing more interstitial W. As bubbles become larger interstitial loops of individual interstitials are formed (loop punching), migrating to the surface, and forming adatom islands of W [148]. Bubbles cause plastic deformation of the near-surface region, creating small craters visible on the surface [145]. Together this loop-punching mechanism and trap mutation form the basis of the retention behavior of He in metals, implying that He trap sites can incorporate a near limitless supply of He [149], while also being a key driver behind vacancy and interstitial generation in the material [48].

In the case of He ion bombardment of a metal surface, two regimes exist; those where the ions have enough energy to produce displacement damage within the lattice and those which do not. Assuming an elastic collision between incident ions and metal atoms, equation 2.4 can be used to calculate a value for the displacement energy of a W atom due to He ion bombardment. With the displacement energy for tungsten given to be 40 eV [150], a He ion would require roughly 480 eV to form a vacancy in the W lattice. This value for the displacement energy agrees well with previous calculations of this energy in the literature [150], [151]. Therefore, assuming the incident ion energy is above the threshold for displacement damage, ion bombardment can produce defects, which then, in turn, allows He to accumulate at these sites. With more vacancies present in the lattice, He clustering is likely to occur at a higher rate, enhancing bubble formation rates [151]. In the case where lower ion energies are expected ($<$ 500 eV), He bubbles will form but without internal displacement damage due to the initial ion bombardment. For He clustering to lead to bubble formation, defects form through the processes described earlier (i.e., trap mutation and loop punching). These are both dependants on sample temperature, with the He diffusion rate, thermal vacancy concentration, and inter-bubble fracture (a method of He bubble coalescence [152]) sensitive to the material's temperature [151].

In the conditions expected in the ITER divertor, surface temperatures will be sufficient to produce thermal vacancy migration. However, atomic displacement due to ion bombardment may not be produced (see figure 1.9. Despite this, helium bubble formation is observed within metals under ion bombarding energies of less than 500 eV, with bubble formation known to precede fuzzy tungsten growth. A combination of the processes that cause He bubble growth, i.e., the migration of W atoms to the surface, adatom surface diffusion, are all assumed to be integral to the growth of fuzzy nanostructures. For this reason, an understanding of the behaviour of He bubble formation within tungsten will be critical to a complete understanding of how the nanostructure forms.

Chapter 3

Experimental Method

In this chapter, the experimental methods that were used in this thesis will be described. This will include an overview of the experimental magnetron system, the custom built sample heater, and the methods used to make temperature measurements of fuzzy surfaces. The plasma diagnostic techniques used to characterise the plasma environments will also be introduced, with the experimental results from these studies presented in Chapter 4. The surface analysis processes which were used to characterise the fuzzy W surfaces are also summarised. Finally, experimental results shown in both Chapter 5 and 6 were produced using the linear magnetised plasma device NAGDIS II; therefore, a brief description of this device is provided at the end of the current chapter.

3.1 Magnetron Sputtering System

Fuzzy W experiments conducted at the University of Liverpool (UOL) were made using a magnetron sputtering system, shown in figure 3.1. The system consists of a cylindrical, stainless steel rig (Gencoa Ltd), 600 mm in length and 388 mm in internal diameter. A vacuum was produced and maintained inside the chamber using a two stage pumping process; first using a rotary pump (Edwards E2M40) and then a turbomolecular pump (LEYBOLD Turbovac 1000). Both pumps were connected in series. The ultimate base pressure that could be achieved in the vacuum chamber was of the order of 10^{-4} Pa (10^{-6} Torr). Helium gas (99.9995% purity supplied by BOC) flow was maintained using a mass flow controller (MKS instruments), with flow rates into the chamber of 156 sccm being sufficient to reach a working pressure of 2.67 Pa (2 x 10^{-2} Torr). The gas pressure inside the chamber was measured using three different pressure gauges, with each gauge monitoring a different pressure range during the vacuum pumping stages. A Pirani gauge (BOX Edwards APG100) measured the pressure change during the initial pumping of the vacuum vessel with the rotary pump. During this phase, the pressure could decrease from atmospheric pressure to around 10^{-1} Pa ($\sim 10^{-3}$ Torr). After reaching a pressure close to 6 Pa, the turbomolecular pump was operated using the Turbotronik NT 1000 controller unit, with the pressure inside the system decreasing further toward the ultimate base pressure of $\sim 10^{-4}$ Pa (10^{-6} Torr) that could be achieved in the system. An inverted magnetron

gauge (AIM BOC Edwards) was used to measure pressures inside the chamber from 10^{-1} to 10^{-4} Pa (10^{-3} – 10^{-2} Torr). A capacitance manometer (MKS Baratron Type 627) was used predominantly used to monitor the gas pressure during the plasma experiments inside the magnetron system, with experiments (in the main) carried out at gas pressures in the range 2.6 to 5.3 Pa (10^{-3} to 10^{-6} Torr). During the venting process of the system, nitrogen gas was leaked into the chamber using a needle and globe valve (shown on figure 3.2 in series to regulate the flow of gas. Nitrogen was preferred during the venting process as venting with air can lead to water vapor adsorbing to the chamber walls, which was likely to extend the evacuation time during subsequent pumping.

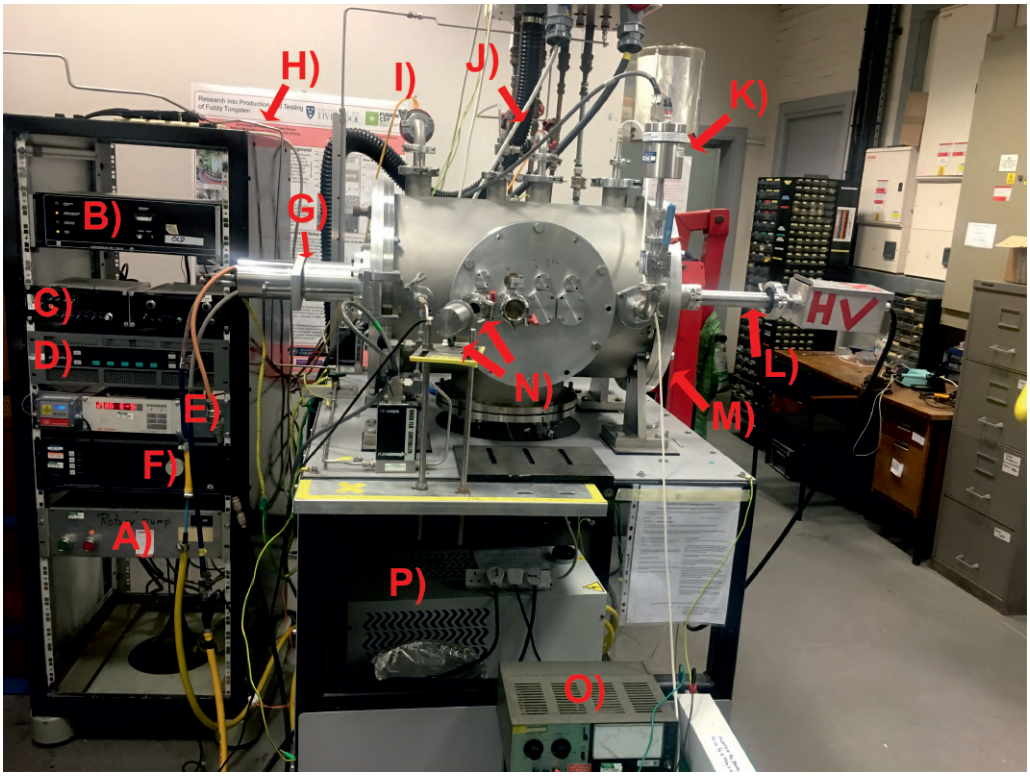

Figure 3.1: Image showing the experimental magnetron sputtering system used at the UOL. Each part is labelled as follows: A) is the rotary pump controller, B) is the Turbotronik NT 1000 controller unit, C) shows the mass flow controller and Baratron pressure gauge visual readouts, D) is the DC magnetron power supply, E) is the visual readout for the Pirani and Penning pressure gauges, F) is the sample heater power supply, G) the magnetron, H) is the He gas line leading to the mass flow controller, I) the Penning gauge, J) the Pirani gauge, K) the Baratron gauge, L) the feedthrough for the heating supply unit, M) the vacuum vessel, N) the IR pyrometer and saphire window, O) the DC bias power supply and finally P) the water chilling unit for the magnetron.

The magnetron source (a V-Tech^{TM} magnetron supplied by Gencoa Ltd) was mounted on one side of the chamber (shown as G on figure 3.1). The magnetron source is powered by a DC power supply (Advanced Energy Pinnacle Plus^{+}) capable of producing 5 kW of output power. The sample holder and heater were attached to a cylindrical arm (indicated by L on the same figure) which allowed the position of the holder to be changed, if needed. Heating of the sample was created using a HEAT2-PS power supply (PREVAC) connected

to a thoriated W filament held close to metal samples that were used to grow fuzz on. The temperature of the samples was monitored with type K thermocouples or by an IR pyrometer (CTLM-3H1CF4-C3, Micro-Epsilon UK Ltd.)

3.1.1 V-Tech^{TM} Magnetron Sputtering Source

The magnetron source used in this thesis was an unbalanced, circular planar magnetron. The metal target, positioned in front of cathode, had a diameter of 150 mm and thickness of 6.35 mm. The target material could be changed depending on the type of metallic deposition that was required in each experiment. Behind the target, permanent magnets form a ring which creates a magnetic field in front of the target, acting to trap electrons and enhance ionisation of the neutral gas. The target is held in position by a stainless steel ring (with a thickness of 5 mm) screwed into position on the face of the target. The stainless steel ring is kept in constant contact with the water cooling system (P on figure 3.1) which in turn cools the magnetron target. Surrounding the target and steel ring is a grounded aluminium ring, which acts as the anode.

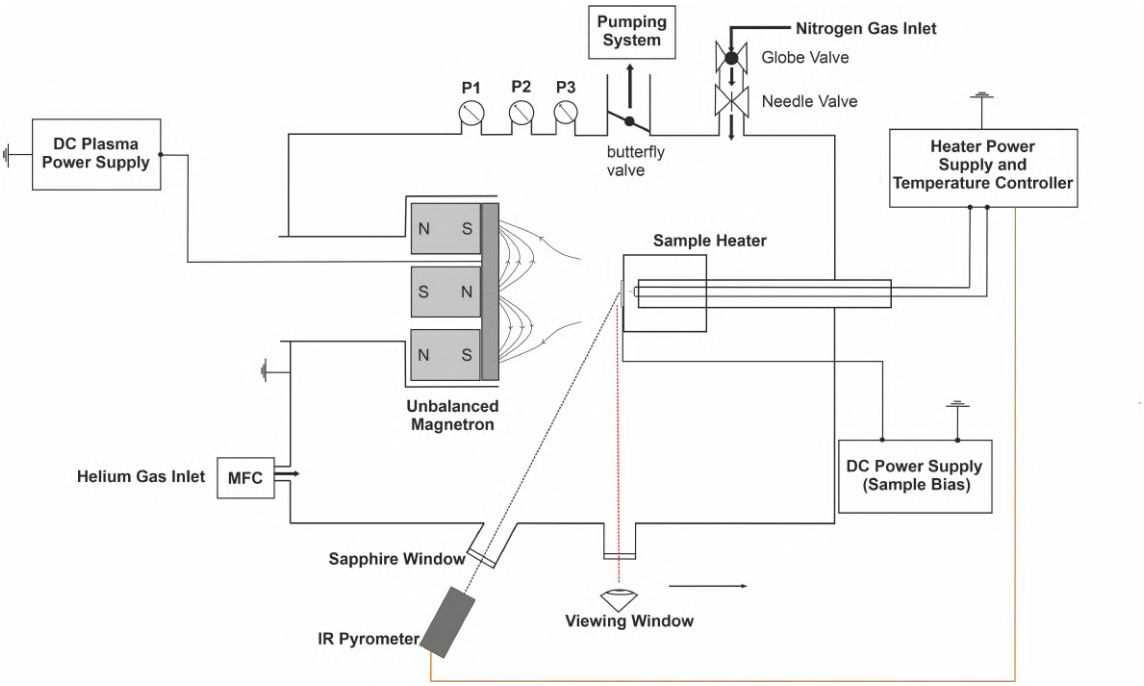

Figure 3.2: Diagram of the magnetron sputtering system used in this thesis. On the system, P1 is the Pirani pressure gauge, P2 is an inverted magnetron and P3 is the Baratron capacitance monometer. All three gauges are used to monitor the pressure inside the chamber. The nitrogen gas inlet was used during the venting process of the chamber, with the flow of nitrogen regulated using a needle and globe valve. He gas flow into the chamber was regulated by a mass flow controller, and a viewing window was positioned on the near side of the chamber so the plasma igntion could be confirmed during each experiment.

3.1.2 The Sample Heating Unit

To heat metal samples placed in the sample holder, an electron beam produced from thermionic emission of a thoriated W filament is accelerated toward the samples. The thoriated W filaments were powered by a HEAT2-PS power supply, with the power supply working principle was as follows. The cathode current, I_c, is passed through the filament due to a cathode potential U_c. An emission potential, U_e is applied between the filament and the metal sample, which in turn creates an emission current of electrons, I_e, from the filament toward the sample. When the power supply was operated, it could run in two modes manual or automatic. To have a greater precision over the surface temperature of the heated samples, the unit was generally used in automatic mode where a surface temperature could be chosen. The user has control over the value of I_c which is set at the

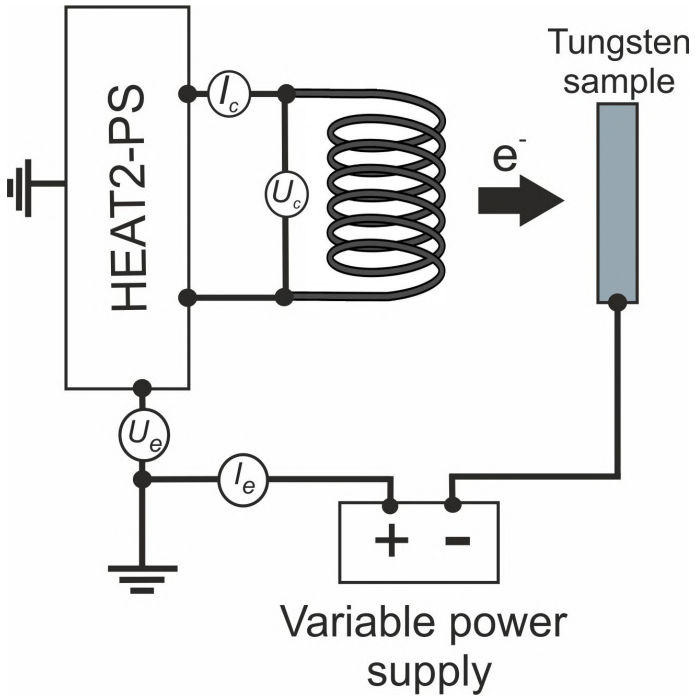

Figure 3.3: Diagram showing the heating unit operation. Each component measured by the heater, the cathode current I_c, the emission potential U_e, the cathode potential U_c and the emission current is labelled in the image.

start of the heating, once this is set U_c is established, and the power supply automatically varies U_e which can give rise to a sufficient value of I_e to heat the sample to the chosen temperature. Generally as the surface temperature is increased the value of I_e required increases, therefore the user can either increase I_c or the box will automatically increase U_e. The surface temperature was measured by the power supply using a type-k thermocouple input, with the temperature of the samples measured by either thermocouples or an IR pyrometer. Where the IR pyrometer was used, an emulating output from the IR pyrometer allowed the temperature to be passed to the thermocouple input on the HEAT-2PS power supply. In practice, values of I_c were increased at a rate of 0.1 A/min, and it was observed that the lifetime of filaments could be extended if the heating process was more gradual.

Table 3.1: Typical operational values of the HEAT-2PS power supply to reach a W surface temperature of 1150 K.

Parameter	Value
I_c (A)	1.90
U_e (V)	300
I_e (mA)	30
U_c (V)	3

Generally, sample heating could take up to 20 minutes to reach a surface temperature of 1150 K, and the typical operational parameters of the HEAT2-PS supply are summarised in table 3.1.

3.1.3 The Sample Holder

A custom built sample holder was used to house the samples and heating elements during plasma exposure inside the magnetron sputtering system. A breakdown of the sample holder is given in figure 3.4, with a) showing the front of the holder with a sample held down by three clamps, b) shows the back of the face of the holder, where the two power cables and the biasing wire (3.4b) part i)) are shown, c) shows the thoriated W filament which heats the samples, as well as the three clamps which secure the samples in place. The holder itself is a small stainless steel box containing insulating Macor sheets (3.4d) part iii)) in which the sample is placed.

The filament used to heat the sample were shielded within the box (3.4c) part ii)), so as to avoid large radiative heating of the inner components of the holder. To do this, a small Macor cylinder and disc (figure 3.4e) part vi) and vii)) are placed around the filament, with the cylinder and disc sitting and supported in a stainless steel crucible (figure 3.4e) part ii)) . Metal samples (e.g in (figure 3.4e) part iv)) then sit on a small sapphire ring (figure 3.4e) part v)) which separates the Macor shield (figure 3.4e) part vi) and vii)) and the metal sample. The use of the Macor shield required that temperatures of the samples were maintained beneath 1200 K as above this temperature the insulating properties of the Macor degrade, with a maximum operating temperature for the Macor shield advised to be $\sim$ 1270 K. The sapphire ring has a much higher melting point of 2310 K, so there may be head room to increase the temperature ranges of the sample holder in the future if the Macor shield is upgraded to a higher melting point material.

3.2 Plasma Diagnostic Equipment

Various plasma diagnostic techniques were used throughout the thesis to measure and characterise different plasma parameters. Each of these will be described here.

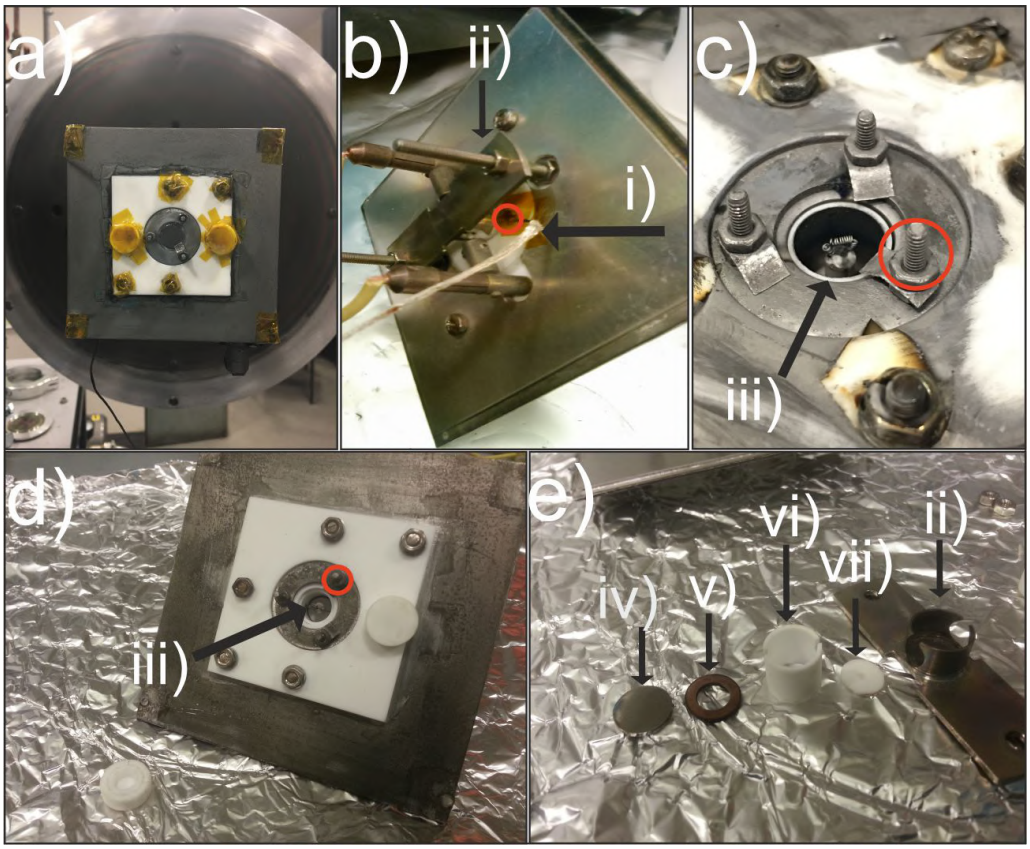

Figure 3.4: An image summarising the components of the sample holder. In a) a fully equipped sample holder is shown, with Kapton tape covering conducting surfaces from being coated during the plasma exposure. Image b) shows the back side of the face of the holder with the biasing wire which connects the DC bias power supply to the sample surface indicated by i). In the same image a steel crucible (labelled ii)) is shown which was used to shield the filament away from the inside of the holder. In c) the filament, labelled iii), is shown, and in the same image a red ring indicates the screw which the bias wire is attached to the on the reverse of the face of the holder. In d), the face of the holder is shown, with the filament labelled iii) in the centre, with the Macor shield. labelled in image e) as vi) and vii), visible around the filament. In e), a W sample iv), the sapphire ring v), the Macor cylinder vi) & disc vii), and the stainless steel crucible are shown.

3.2.1 Langmuir Probes

In plasma physics certain tools can be utilised to help gain knowledge of the plasma and its characteristics. These characteristics, which will be discussed in more detail shortly, include the plasma potential, the floating potential, the electron temperature, the plasma density and electron & ion saturation currents. These quantities can then be used to give insights into other elements of the plasma environment. A key parameter for work in this thesis was the He flux of ions (units of m^{-2} s^{-1}) incident to the sample, but to calculate this the quantities mentioned above were required to be measured. To do this, an electrical probe known as a Langmuir probe was used.

The Langmuir probe, first introduced by Mott-Smith and Langmuir [153] in 1926, allows a measure of the current in a plasma to be made, measured as a function of the bias voltage applied to the surface of the probe. Basic Langmuir probes consists of a bare wire (a material with a high melting point like W is often chosen) inserted into a plasma. The

wire itself is housed in a probe stem (but with isolation from it) and the wire is then fed from the plasma to a power supply where a variable bias can be applied to. A current (I) will be drawn as the bias is applied, and by sweeping the voltage (V) an I-V characteristic is attained. An example of an ideal IV characteristic is shown in figure 3.5.

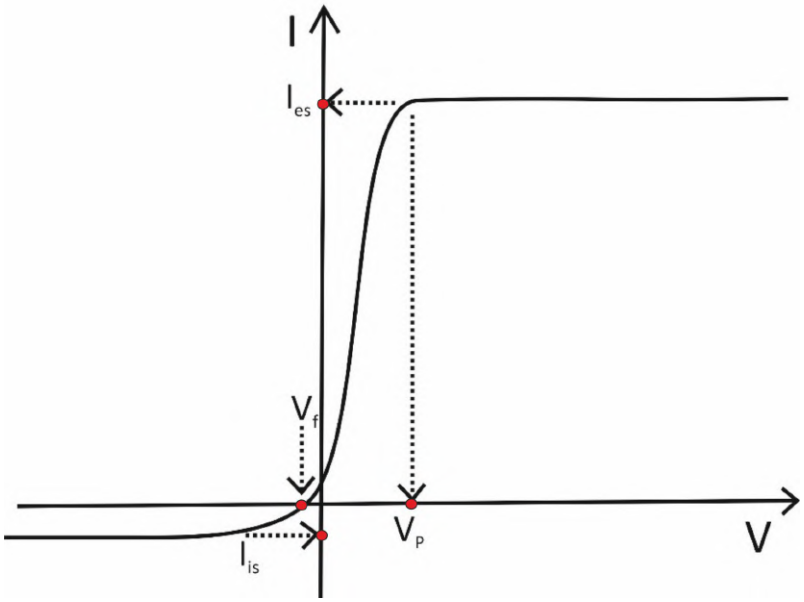

Figure 3.5: An example of an ideal I-V curve, showing the electron saturation current (I_{es}), plasma potential (V_{p}), floating potential (V_f) and the ion saturation current (I_{is}). The y-axis is current (I) and the x axis is voltage (V).

Returning to figure 3.5, multiple features can be described. If a Langmuir probe is inserted into a plasma with zero electrical bias applied to it, the bias voltage produced on the probe, $\mathrm{V_b}$, is equivalent to the floating potential, $\mathrm{V_f}$. At $\mathrm{V_f}$, the probe is said to be drawing no net current. In plasmas, both electron and ion components will contribute toward the current drawn by the probe, but at $\mathrm{V_f}$ these ion and electron components are matched, resulting in no net current being collected by the probe. This feature of an I-V curve is generally the simplest characteristic to measure, as this is where the I-V curve crosses the x-axis. As the bias on the probe becomes more negative ($\mathrm{V_b} \ll \mathrm{V_f}$) the current drawn will consist of mainly ions, repelling even the most energetic electrons from being captured by the probe surface. Eventually a stage is reached where only ions are collected by the probe, and the current drawn to it is known as the ion saturation current I_{is}. As the bias on the probe is made more positive than the floating potential ($\mathrm{V_p} > \mathrm{V_f}$), ions will then begin to be repelled and instead electrons are now attracted to the probe surface. Over this region of the I-V curve, called the transition region, the temperature of electrons ($\mathrm{T_e}$) inside the plasma can be found. Increasing the bias to very positive probe voltages ($\mathrm{V_b} \gg \mathrm{V_f}$) results in a similar saturation of the electron current as was the case for the ions when very negative biases were applied. This current is therefore known as the electron saturation current I_{es}. It is important to notice that the relative sizes of the currents drawn by electron and ions are considerably different, with electrons producing far larger currents. This is due to a greater mobility of electrons relative to ions, as a result of their lower masses. Where I_{es}

is labelled on figure 3.5, in the I-V curve a characteristic "knee" is visible, and this defines the plasma potential V_p, the average potential at which the bulk plasma is said to be at. By sweeping the voltage on the probe from negative to positive voltages, the full I-V characteristic in figure 3.5 will be produced. In practice, real Langmuir probe I-V curves are slightly different to the example shown in figure 3.5. In figure 3.6 an experimental I-V curve collected during experiments in the magnetron system is shown.

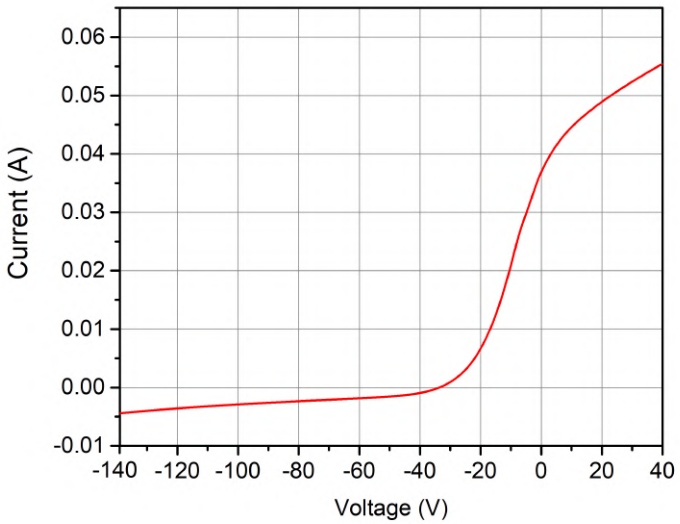

Figure 3.6: An experimental I-V curve obtained in a He plasma, with a DC power of 700 W and a neutral pressure of 2.6 Pa. The probe was positioned $\sim$ 115 mm, on the centre line, facing the magnetron target.

The experimental I-V curve has noticeable differences to the ideal curve. The rounded knee is no longer as distinct, making a measure of V_p less straight forward, and the electron and ion currents do not saturate completely for positive and negative voltage extremes on the probe. The reason for this is the presence of the plasma sheath at the probe surface, which can continue to expand, thus allowing more current to be collected by the probe. In effect, the area for particle collection is the sheath area, and not the geometric probe area. It is generally accepted that to find the V_p and I_{is}, two approaches are taken toward the experimental I-V curve analysis. Firstly, by plotting a semi log graph of I against V (shown in figure 3.7b), V_p is more easily identified, although some small error will still exist in its determination. Other approaches to find V_p include taking the second derivative of the I-V curve (d^2I/dV^2) and finding where this is equal to zero. In the same figure, the electron temperature T_e can be found by taking the gradient of the linear section (i.e the slope) of the graph. A conventional method for calculating the ion saturation current is to linearly extrapolate the slope of the ion saturation region of the I-V curve with respect to V_p [154]. This method is shown in figure 3.7a.

Langmuir probe measurements taken using a planar probe from within the magnetron system are presented in figure 3.8. The probe geometry chosen was equal to with the area

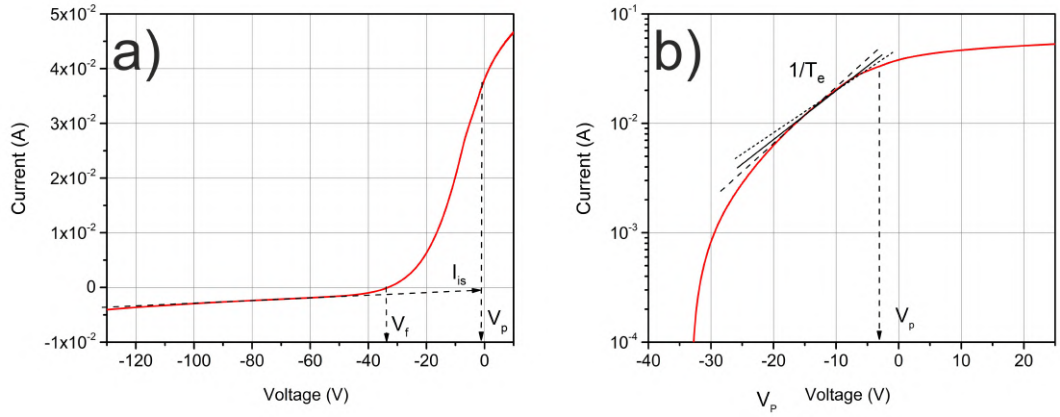

Figure 3.7: In figure a), an I-V curve showing the extrapolation of the ion saturation region back to V_p is shown, as well as the labelling of V_f where I = 0. In b), the I-V curve is represented on a semi log plot, where the characteristic "knee" of the I-V curve is clearer to see, indicating the potential where V_p is. Also shown in b) is the gradient of the downward slope which can be used to find T_e.

of metal samples where fuzz is grown on. The probe itself consisted of a steel disc of 10 mm diameter and 2 mm thickness, with a small hole drilled into its side, allowing the insertion of a thin conducting W wire. This wire, wrapped in electrically insulating Kapton tape and a metallic sheath, is connected to an electrical feedthrough on the top of the vacuum chamber. The feedthrough is attached via a BNC cable to an automatic Langmuir probe acquisition system (ALP - 150 Impedans), allowing fast analysis and recording of currents given a voltage range. To calibrate the ALP system, a known resistance was attached to its output, allowing the electrical offset to be measured. To ensure stray currents were not drawn from the plasma, the small steel clamps, labeled in figure 3.8b), were insulated from the probe by covering them with Kapton tape.

The added magnetic field of the magnetron system also complicates the interpretation of Langmuir probe results. Due to the gyro-orbit of electrons being much smaller than ions, electron collection is affected much more than ion collection. That in mind, the measurement of plasma characteristics using electron or ion saturation currents can cause discrepancies in the measurement made. Ion saturation currents are generally accepted to be more reliable than electron currents when measuring plasma density [154].

3.2.2 Quartz Crystal Microbalance

Magnetron devices are able to deposit metallic material via sputtering of the cathode target, so it was beneficial to know the rate at which material would be deposited on to a surface placed in the magnetron system. To measure this rate, a crystal quartz microbalance (QCM) was used inside the magnetron sputtering system. The basic principle of the QCM is that by applying an alternating voltage to the surface of two electrodes, a piezoelectric quartz crystal then positioned between these two will begin oscillate at its resonant frequency. As a layer of deposition is made on the crystal, the effective mass of

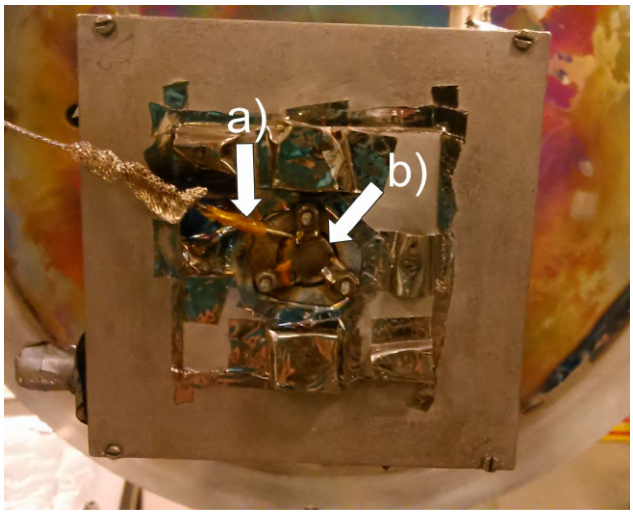

Figure 3.8: An image of the planar Langmuir probe used in this work. a) indicates the wire (insulated from the plasma with Kapton tape and a metallic sheath) used to insert into the side of the stainless steel sample, the sample is indicated in b).

the crystal will increase. The frequency of the oscillation of the crystal will then vary as a result of the mass change, and it is possible to determine the mass change during the deposition through using the Sauerbrey equation [155],

$$\Delta \mathrm{f} = \frac{2f_0^2}{A\sqrt{\rho_\mathrm{q}\mu_\mathrm{q}}}\Delta \mathrm{m} \tag{3.1}$$

where Δf is the change in the resonant frequency, f_0 is the initial resonant frequency, A is the area between the electrodes, ρ_q is the quartz crystal density, μ_q is the shear modulus of the quartz crystal and Δm is the mass change of the crystal after deposition occurs.

The QCM consisted of a gold plated quartz crystal mounted on a water cooled stainless steel holder, and was held in the vacuum vessel facing the magnetron target as shown in figure 3.9. Water cooling was used to maintain the operating temperature of the device in the correct temperature range (0 °C - 50 °C). The QCM electrodes were electrically connected to a mass microbalance (Maxtek TM-400), and this unit applied the alternating current. The microbalance was also able to display the time averaged deposition rate in units of Å/sec, and measurements were taken over a 45 minute plasma exposure time. Each measurement of the deposition rate required the density of the material being deposited to be input into the microbalance monitor. W and molybdenum targets were used in this work, so separate densities of 19.25 g cm^{-2} and 10.28 g cm^{-2} were entered respectively.

3.2.3 Gencoa Optix Spectrometer

The Optix spectrometer (Gencoa Ltd) was used used for the identification of both the type and relative amount of gases present in the magnetron vacuum vessel. The sensor, which was attached using a flange on the top of the chamber, works by generating a small plasma using an ionisation gauge. A high voltage is applied to two electrodes inside the gauge, ionising the gas species, and a permanent magnet (placed behind the anode in the

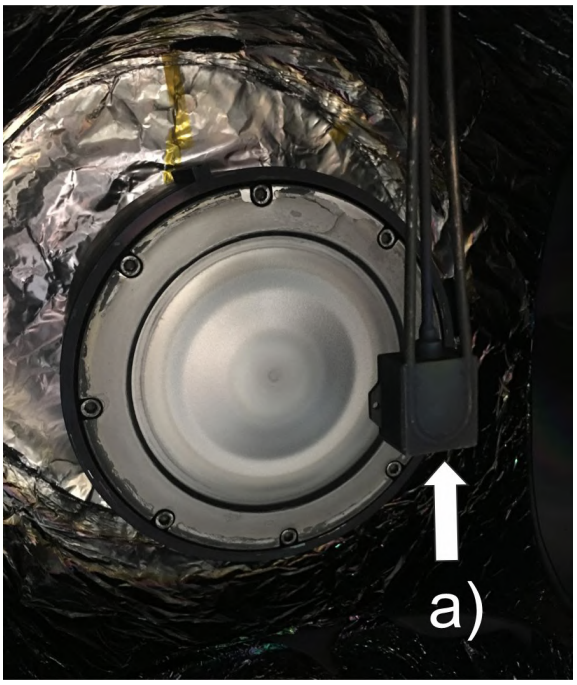

Figure 3.9: The QCM (a) positioned in the magnetron sputtering system, facing the magnetron target

gauge) produces a magnetic field which confines electrons and enhanced ionisation of the neutral gases. As ionisation occurs and the subsequent plasma glows, the emitted light characteristic to each plasma species (a result of the discrete energy levels in each gas type) is collected by the spectrometer. The system allows identification of the species present based on the detected wavelength. The instrument is not absolutely calibrated so offers only qualitative information, with the peak heights demonstrating approximately the relative abundances of the species. The spectrometer had a spectral range from 200 to 900 nm wavelengths, and was operated across a neutral pressure range of $\sim$ 1 x 10^{-4} to 2.6 Pa. As a result of the location of the spectrometer, metallic material sputtered from the magnetron target was not detected by the gauge. This is likely due to the deposition of this material within the vacuum vessel before reaching the gauge.

3.2.4 Temperature Measuring Methods

The formation of fuzzy W is heavily dependent on the temperature of the metal surface, therefore it was important to have correct surface temperature readings during the He plasma exposure. In this thesis, two methods of heat measurement were used to produce these readings; these were type-k thermocouples and an infra-red (IR) pyrometer. The IR pyrotmeter was predominantly used for experiments in this thesis (it is also used in much of the literature on fuzzy W growth e.g. in [37], [117], [156]), although thermocouples were used in some cases such as during the calibration of the IR pyrometer. A description of the thermocouple and IR pyrometer equipment is given below.

Thermocouples

Type-k thermocouples (made of chromel and alumel) were used to measure the surface of heated metal samples. Thermocouples consists of two different metals joined together to form two junctions. When one junction is heated relative to the other (cold) junction, the change in temperature at the heated junctions causes a current to flow through the wires which in turn produces a voltage potential (on the order of mV). The voltage produced is then measured from the circuit of the thermocouple, and can be converted to a temperature measurement using the principle of the Seebeck effect [157]. Thermocouples used in this work were either connected to an electronic readout (Thermosense) or the HEAT 2-PS power supply so the temperature could be monitored in real time.

IR Pyrometer

For the majority of temperature measurements in this thesis, an IR pyrometer was used, in conjunction with the heating power supply, to measure the temperature of the fuzzy W samples during He irradiation. The IR pyrometer was held in position outside of the vacuum chamber (approximately 400 mm away from the sample of interest), with the pyrometer directed through a sapphire window. Prior to plasma exposure, the pyrometer was aligned to the sample surface using two built-in guiding lasers, allowing correct positioning of the pyrometer so as to correctly measure the temperature of each sample. The spot size of the pyrometer was given to be 1.4 mm at the distance at which the IR pyrometer was held, and this was sufficient for the diameter of the samples used here (10 mm discs).

The IR pyrometer has a temperature range of 420 - 1270 K, and measures IR radiation at wavelengths of 2.3 μm, with the sapphire window used in this thesis (supplied by Kurt J. Lesker) known to have a transmittance of 87 % at 2.3 μm. The transmittance of the window was later verified through calibration in section 4.4.

3.3 Surface Analysis Techniques

After He plasma irradiation of the metal samples, various surface analysis techniques were used to image and characterise the surface morphologies that were formed. An outline of each analysis technique will be provided here.

3.3.1 Sample Preparation

In preliminary fuzzy W layers that were produced in the magnetron system, the base of the layer was found to be uneven across the W surface, presumably due to the uneven nature of W samples as bought from the manufacturer (supplied by Future Alloys). In addition to this, the roughness and reflectivity of each W surface was likely to differ between each sample. This could possibly lead to erroneous temperature measurements as a result of the change in emissivity. A process of electro-polishing was used to produce a more even and mirror-like finish of the W surfaces.

In figure 3.10 a, a schematic of the experimental set up used to electro-polish the W samples is shown, comprising a DC variable power supply, cathode (tweezers + sample) and anode (steel rod), potassium hydroxide (KOH) electrolyte and magnetic stirring plate. A beaker containing 150 ml of purified water (Purite DC7) mixed with 3 g of KOH was used as the electrolyte source during the polishing, and the beaker was placed on a magnetic plate. A magnetic stirrer was used to aid the mixing process. In the circuit in figure 3.10a, a pair of steel tweezers holds a W sample. This acts as the anode of the circuit when it submerged inside the KOH electrolyte, with a steel rod behaving as the cathode. If the anode and cathode are connected to the positive and negative terminals on the DC power supply respectively, applying a voltage ($\sim$ 15 V) across the electrodes allows a current ($\sim$ 2 A) to be passed through the circuit. When the circuit is completed, metal atoms on the surface of the W samples would be oxidised and dissolved in the electrolyte, leaving the surfaces with a visibly more reflective appearance.

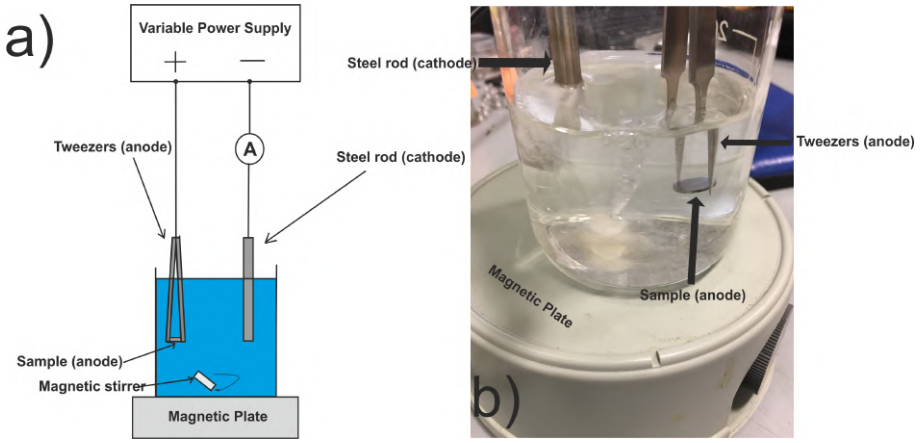

Figure 3.10: Experimental apparatus used to electro-polish W samples. In a) the schematic of the set up is shown and b) shows the beaker holding the KOH electrolyte, with the tweezers, steel rod, W sample and magnetic stirring plate highlighted.

It was observed that if the electro-polishing was carried out in excess of 30 second intervals, distortions near the edges of each sample were visible. The polishing was generally completed in 30 second intervals, with the DC power supply switched off after 30 seconds. This process was repeated over a 3 minute period, after which the circuit was switched off and the sample was re-adjusted in the tweezers. In total, the polishing times were generally around 20 minutes. After a mirror finish was deemed to have been produced on the sample surface, each sample was cleaned with isopropanol. In figure 3.11, the surfaces of two W samples, one non-polished and one polished, are shown using SEM imaging. It is clear from the imaging that the electro-polished sample has more visible grain structures on its surface, which indicates any surface contamination has been removed during the cleaning.

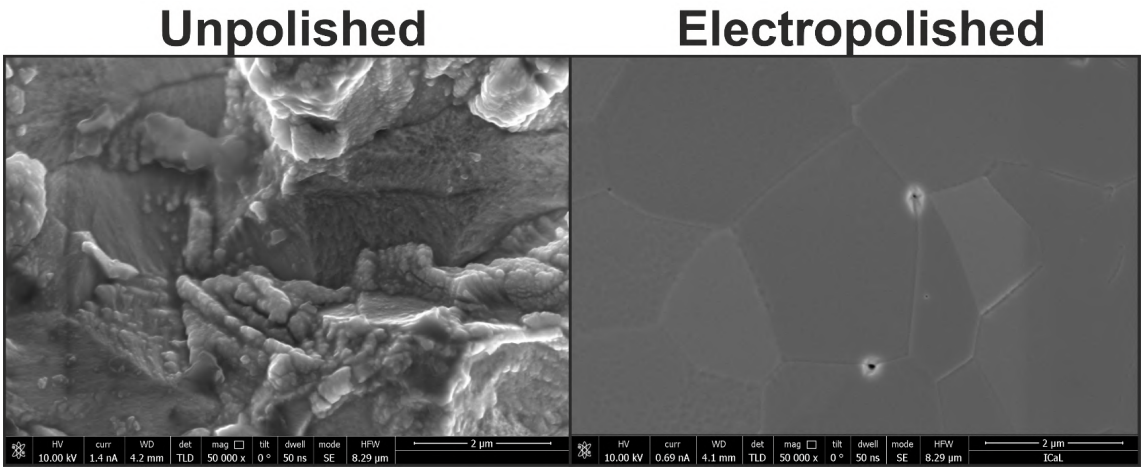

Figure 3.11: A comparison of the surface of an unpolished (left) and electro-polished (right) W sample as viewed under SEM imaging.

3.3.2 Scanning Electron Microscopy

Scanning Electron Microscopy (SEM) was used to image all fuzzy W surfaces produced in this thesis, with the aim being to acquire focused images of the structures that had been formed after He irradiation inside the magnetron system. Although SEMs are capable of resolving surface features down to tens of nm, the method of electron beam production in each model (JEOL 6610 and JEOL 7001) used in this thesis differed slightly. Specifically, the JEOL 6610 contained a heated W hairpin which emits electrons via thermionic emission, whilst the JEOL 7001 contained a zirconium oxide tip which is also heated and emits electrons via thermionic emission. In the JEOL 7001 however, a strong negative electric field was applied to the tip to lower the work function of the surface, and increase the emission of electrons, a process known as the Schottky effect. In figure 3.12 a), the JEOL 7001 SEM used at the UOL is shown, and in 3.12 b) a schematic summarising the features of an SEM is provided. As a rough summary the main components of the SEM are the electron gun, electromagnetic lenses, scanning coils, detectors which collect emissions from the sample and a digital imaging system.

A description of the working principle of an SEM can be made as follows. After the emission of electrons from a heated W hairpin/zirconium oxide tip, the electrons are accelerated by two electrodes. The final electrode is grounded, with the difference in potential between the filament and this electrode defining the both the energy of the electrons and their penetration depth into the sample being viewed. This electron energy could be defined during the operation of the computer interface of each SEM. It should be noted that the entire electron column is under a high vacuum (x 10^{-10} to x 10^{-11} Torr) so as to protect the electron beam source from any contamination. This is also to reduce the effects of electron beam scattering from other atoms or molecules which may degrade the image quality. The electromagnetic lenses control the path of the electrons, and generally two lenses are seen in SEMs. The condenser lens first converges the electron beam to define its size, the cone of the beams expands to then be converged again by the objective lens which

focuses the beam on to the sample. Scanning/deflector coils are used to raster the beam across the sample, and apertures control the size of the beam and refocus any defocused electrons. The stage that holds the samples can be moved in the x, y and z directions and even tilted up to 70°, with each manipulation of the stage changing the focus of the images. Usually the working distance (i.e the distance at which the beam is focused) changes for each movement of the stage in the Z plane, so refocusing of the beam is required to produce a sharp image.

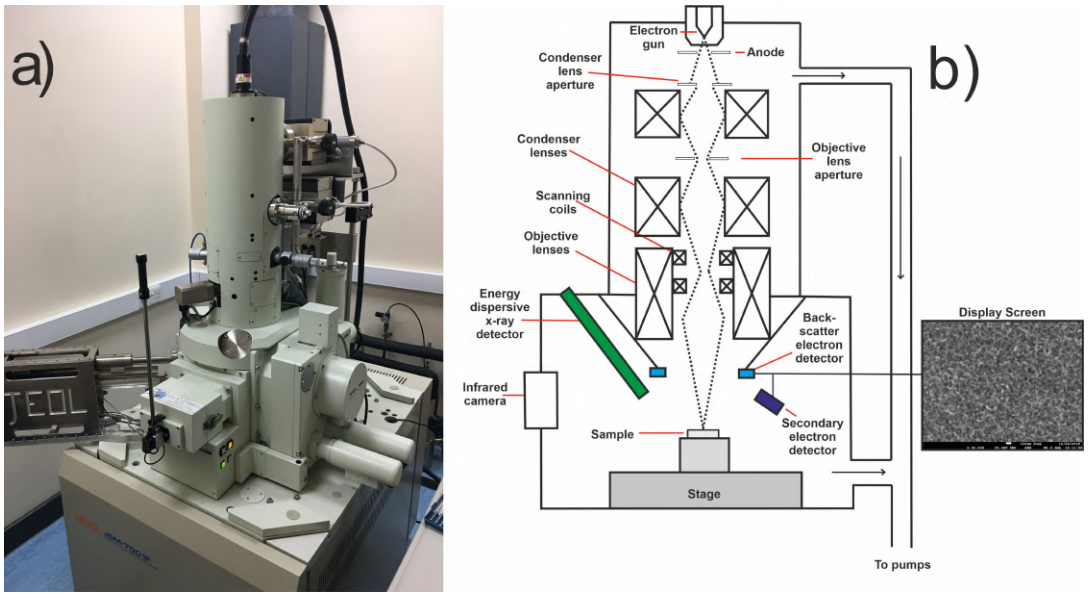

Figure 3.12: a) The 7001 JEOL SEM at the University of Liverpool and b) a schematic of an SEM

When the incident ion beam interacts with the sample surface, many different types of interactions can occur which scatter the electrons, and this leads to various signals being produced. In figure 3.13, the possible interactions of electrons within the near surface region of the sample are shown. In SEMs, the signals produced are due to inelastic and elastic scattering of the incoming beam, and these are used to form images of the sample surface. Secondary electrons (SE) are produced by the inelastic scattering of an incoming electron with an electron in a surface atom (figure 3.13 a), with SEs typically having energies of tens of eV. After the production of this SE emission, a higher energy level electron can de-excite and occupy the vacancy. This process will produce x-rays characteristic of the energy transition the electron undergoes. These x-rays can be used to chracterise the type of surface that is being analysed, which is also another form of analysis possible in SEMs.

Back scattered electrons (BSEs) are formed when an incoming electron's path is perturbed slightly due to the nuclei of surface atoms. With continued perturbations, the electrons path can be diverted such that it leaves the surface (figure 3.13 b). The energy of the original incoming electrons is not largely changed by this interaction, and can be considered elastic, with BSEs having energies in a range of tens of eV to (near) the original electron beam energy.

In figure 3.13 c), the origin depth for each type of signal (i.e. SE, BSE etc) from within

the sample is shown. For SEs their escape depth is approximately 5 - 50 nm, whereas BSEs can escape from a depth 100x greater than this, and X-rays even further. The chosen technique of imaging can therefore give rise to different levels of spatial resolution. As fuzzy W layers are generally 100s of nm in thickness, the detected signal used to produce the images was generally SEs.

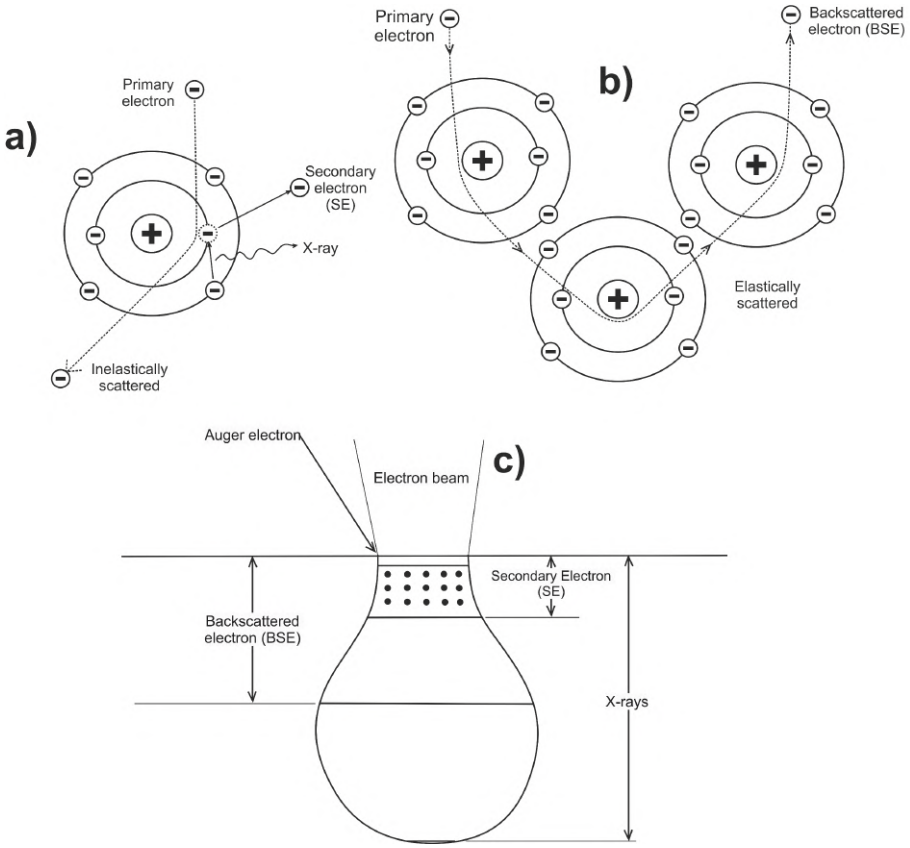

Figure 3.13: The interaction processes of incident electrons on sample surfaces inside the SEM. In a) secondary electrons (SE) and characteristic x-rays are produced due to inelastic scattering. In b), elastic scattering can lead to backscatter (BSE) electrons. In c), the relative penetration depth of each signal (SE, BSE, x-ray etc) is illustrated.

3.3.3 Focused Ion Beam Scanning Electron Microscopy

In many fuzzy W research studies the focused ion beam (FIB) SEM is used as a technique for acquiring fuzzy W layer thicknesses [65], [132], [158]. In this thesis, many of the thicknesses measured were taken using a FEI Helios Nanolab 600i FIB/SEM. The FIB-SEM works as follows: a fuzzy W layer (figure 3.14 a)) is deposited on using sources of carbon (C) and platinum (Pt) (figure 3.14 b) layer deposition. These layers provide the necessary protection of the underlying fuzzy surface from melting during the ion beam milling process.

A high energy gallium (Ga) beam is used to mill out the sample surface and acquire thickness measurmements (figure 3.14 c)). The high energy (tens of keV) Ga beam can be optimised in terms of the current used to provide the necessary depth measurement.

Generally, the initial milling can be produced with around 30 keV and 1 - 2 nA of current. Polishing can be carried out in addition to milling, and typically a much lower current (0.2-0.4 nA) would be used for this. The dimensions of the region for milling were 10 x 5 x 4 μm, and this was sufficient to take around 100 measurements of the thickness at 0.1μm intervals across the fuzzy W layer. Overall, milling and polishing times could take up to 1 or 2 hours depending on the size of layer that was required to be milled out. The thickness of each layer was generally taken with the sample tilted to a 52 ° angle. Therefore, each thickness measurement was multiplied by 1/sin52° to give the true layer thickness (figure 3.14d)). In figure 3.15a) - d), a real example of the FIB milling process (observed through

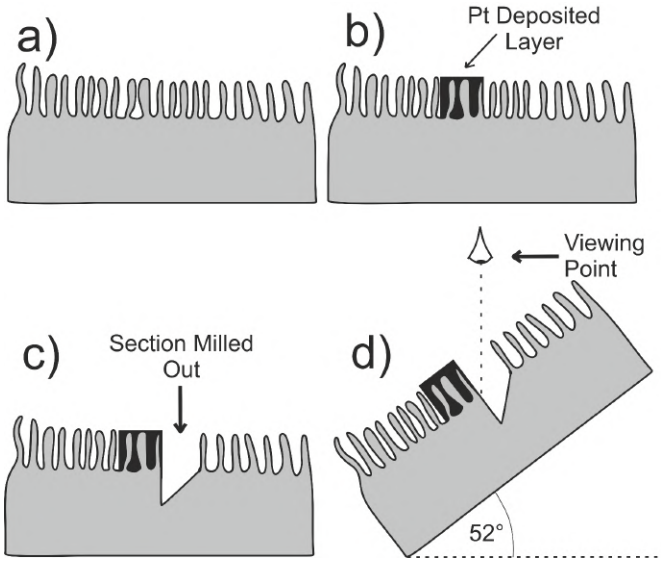

Figure 3.14: The focused ion beam (FIB) milling process, shown in diagrams a) to d). In image a) a fuzzy layer, in b) a Pt layer is deposited over a small proportion of the layers to provide protection for c) where the Ga ion beam is used to mill out a section of the fuzzy layer. In d) the layer is tilted to 52° during the measurement.

SEM imaging) described above is shown. In images a), b) and c) the deposited Pt layer is visible on the surface. In d) a fuzzy W layer is shown after FIB milling was performed. In image d) each transition in the layer is labelled, with the centre region of the image indicating the fuzzy layer, which can be characterised by the He bubble formation visible.

3.3.4 Transmission Electron Microscopy

Transmission electron microscopy (TEM) is a method for studying the underlying crystallographic and electronic structure, as well as morphologies of materials at a very high resolution ($\sim$ 0.19nm). The operation of the TEM is similar to SEM in that a high voltage electron source at the top of the microscope emits electrons that are guided through a vacuum column. Electromagnetic lenses focus the electrons to a thin beam to be directed toward the sample surface of interest. Whereas in the SEM secondary electrons or back scattered electrons can be used to image the surface, in the case of the TEM, the electrons that pass through the sample are used to create an image. The samples that are used for TEM are therefore typically much thinner than those used in the SEM, and would usually

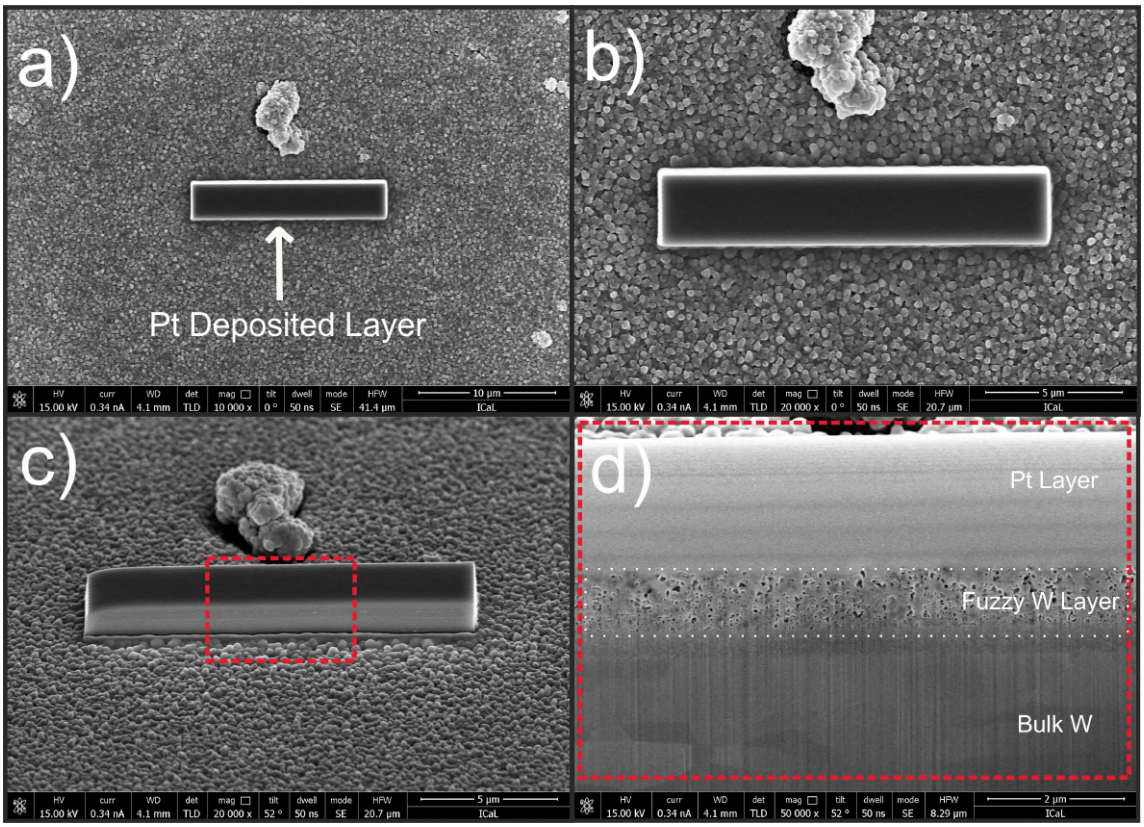

Figure 3.15: The focussed ion beam (FIB) milling process, shown in diagrams a) to d). In image a) a fuzzy layer, in b) a Pt layer is deposited over a small proportion of the layers to provide protection for c) where the Ga ion beam is used to mill out a section of the fuzzy layer. In d) the sample layer is tilted to 52° so as to allow a cross-sectional measurement to be made.

have thicknesses in the range of 100 – 200 nm to allow transmission of electrons through them. The standard bright field (BF) imaging involves incident electrons being scattered as a result of the the density and crystal orientation of the sample. The intensity of the beam that transmits through the material un-scattered is then refocused and magnified by an electromagnetic lens system consisting of two lenses. After the beam passes through the sample, it is projected onto a phosphor screen charge coupled device (CCD) camera to convert the electron image information to a visible form.

When electrons transmit through the sample they interact with the arrangement of atoms within the lattice structure, causing them to scatter. This can lead to either constructive or destructive interference between the transmitted electrons, with the condition for each type of interference being described by Bragg's law

$$\mathrm{n}\lambda = 2dsin\theta \tag{3.2}$$

where n is an integer, λ is the wavelength of electrons, d is the distance between atomic planes and θ is angle of scattering between the incident beam and atomic scattering planes. According to this law if the path length difference between two electron waves is an integer number of wavelengths then constructive interference will occur. This is represented in

electron diffraction patterns as maxima spots i.e spots of intense light. Where destructive interference occurs dark minimas are formed. The areas of constructive interference and hence the production of light spots are directly related to the scattering angle, θ, which allows information about the interatomic spacing and arrangements to be found. By calculating the angle of diffraction and knowing the wavelength of the electrons incident to the sample, the interatomic spacing of the crystal can be measured. As it conventional to

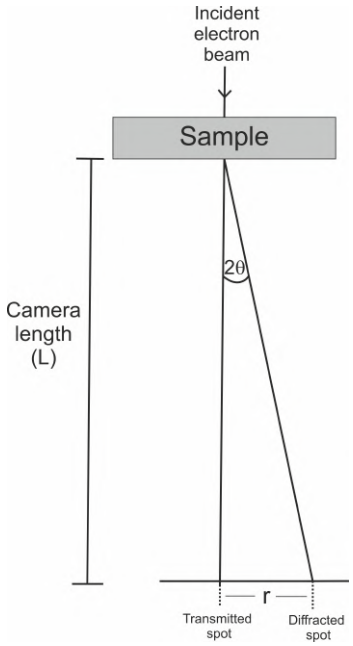

Figure 3.16: Illustration of electron diffraction in a TEM

deal with first order diffraction (i.e n = 1) in electron diffraction, this gives,

$$d = \frac{\lambda}{2sin\theta} \tag{3.3}$$

As the scattering angles θ can be considered small, a result of the short wavelengths of incident electrons used in TEM ($\sim$ 3 pm at 200 keV) and standard lattice spacings (e.g. a common d-spacing in W is 1.129 Å), equation 3.4 can be rewritten as,

$$d = \frac{\lambda}{2sin\theta} = \frac{\lambda}{2\theta} \tag{3.4}$$

Close inspection of figure 3.16 shows how d can be measured from the diffraction pattern produced. Using the reciprocal lattice vector r that is measured on the diffraction pattern and the camera length L which is known, it is found that

$$\frac{r}{L} = tan2\theta \approx 2\theta \tag{3.5}$$

By substitution of equation 3.5 into equation 3.4 the d spacing can be calculated using,

$$d = \frac{\lambda L}{r} \tag{3.6}$$

The camera length L is known for the TEM system used here as well as the wavelength λ. By measuring the reciprrocal lattice vector r from the diffraction pattern, d can be calculated. This in turn allows identification of the crystal lattice being analysed.

3.3.5 Energy-Dispersive X-ray Spectroscopy

Energy-dispersive X-ray spectroscopy (EDS, EDX, EDXS, or XEDS) is an analytical technique which is used for the identification of compositions of different elements in a specific sample. It relies on an interaction between the surface atoms in a material and a source of excitation (in this case, the electron beam within an SEM). The electron beam from the SEM excites near surface atoms in the material it interacts with, leading to the emission of characteristic wavelengths of X-rays (see figure 3.13a)) related to the atomic structure of each surface element.

In an EDS detector (a solid-state device that discriminates among X-ray energies) the elements present can be identified, and their relative abundance can also be calculated. In quantitative analysis, the concentration of a specific element present in a sample can be measured using the intensities of peaks. The SEMs (JEOL 6610, 7001) and FEI Helios Nanolab 600i FIB/SEM used in this thesis were all equipped with an EDX detector, thus allowing the elemental composition of fuzzy surfaces to be found using these devices. The Helios Nanolab 600i FIB/SEM used the EDAX Octane Pro EDX detector, with spectra produced and analysed using the EDAX EBSD DigiView with integrated EBSD EDS TEAM analysis software. Where EDS was performed in the JEOL 6610 or 7001, an Oxford Instruments INCA X-act EDX detector was used.

3.3.6 Surface Reflectivity

The reflectivity of samples was measured to confirm the production of fuzz on a sample surface, with fuzzy W surfaces known to have a reduced optical reflectivity [65]. Measurements in this work were made using a USB2000 + spectrometer (Ocean Optics), which was used in conjunction with a DH-2000-BAL deuterium halogen light source. A bifurcated fibre-optic probe was housed into a metallic sheath at one end, while the two ends of the bifurcated optic cable were connected to the light source and spectrometer respectively. The metallic sheath was held above the sample (90° to the surface), and reflected light is then collected and transmitted back toward the spectrometer to be analysed. A reference scan was performed first with a mirror surface so as to calibrate the device for a 100 % reflective surface.

The spectrometer was capable of measuring across the UV-Vis and NIR range, and for the purposes of the measurements in this thesis the spectrometer was used in the range 300 - 900 mm. In the results sections of this work, the measurement of the reflectivity at 632.8 nm was used for comparison between fuzzy W samples. This is consistent with other works where reflectivity is compared [65], [159].

3.4 Other Plasma Devices

The experiments carried out in Chapters 5 and 6 included those made using the linear plasma device NAGDIS II, a device built to simulate divertor conditions within future fusion tokamak reactors. A description of this device will be provided here.

3.4.1 NAGDIS II

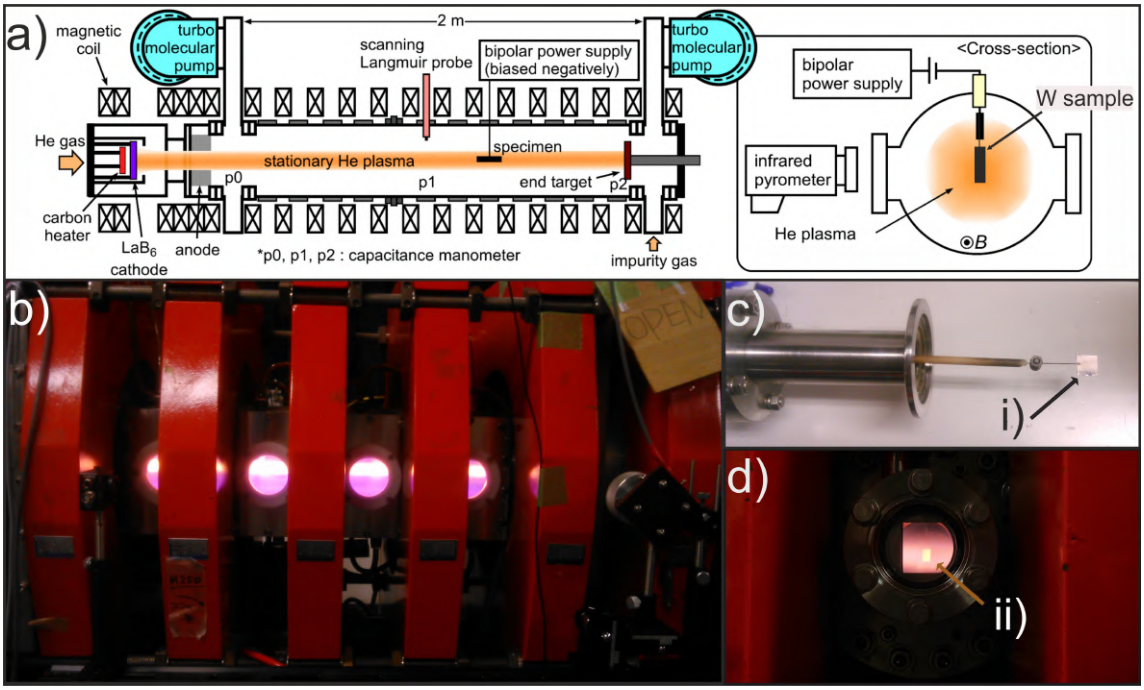

Figure 3.17: The NAGDIS II linear plasma device. In a) a schematic of the experimental device is shown, with the set up for fuzzy W experiments also illustrated [160]. In b) the production of a plasma as viewed through viewing ports on the device is shown. The rig used to hold the W samples (labelled i) is shown in c), and in d) the W sample (now labelled ii) is exposed to the plasma inside NAGDIS II (as viewed through a viewing port).

NAGDIS II contains a water cooled vacuum chamber, 2.5 m in length and 0.18 m in diameter, with 21 solenoidal magnetic coils positioned around the body of the vessel. The magnetic field strengths that can be reached with the current magnetic coil set up is believed to be 0.25 T. Due to the high magnetic fields, the device is capable of producing plasma with large electron densities, measured to be up to 10^{20} m^{-2} in steady state operation. These densities make this machine a relevant plasma device for the edge conditions in fusion devices. The plasma discharge region consists of 108 mm diameter lanthanum hexaboride (LaB_6) disc cathode.

Heating to the cathode is supplied by a carbon heater with typical heating powers of 3 kW. This external heating of the cathode induces an initial creation of the discharge and maintains a discharge voltage of less than 100 V for helium plasma and 200 V in hydrogen plasmas. A molybdenum cylinder surrounds the cathode, improving confinement of heat from the carbon heater and the efficiency of gas. A cuso magnetic field is created

to provide confinement of the plasma discharge. Generally, ionisation fractions are low in DC discharges ($\sim$ 1%) so in order to produce a high density plasma using this DC system, neutral pressures in the discharge region are typically tens of Pa. The neutral pressure in the plasma test region (i.e the downstream of the device) is kept at much lower pressures (on the order of 0.1 Pa) due to the pumping system, consisting of two 2000 L/s turbomolecular pumps (TG200M Osaka Vacuum Ltd). The discharge current, supplied to the LaB_6 cathode, can also be increased to further increase the neutral pressure in the discharge region. As well, an increase in discharge current produces an increase in the plasma density.

The plasma plume is terminated on a target plate located at the end of the vacuum chamber. Secondary gases can be supplied to the downstream region of the chamber via mass flow controllers located in these regions. The plasma properties are measured using three Langmuir probes. The probes are positioned at three different locations moving radially away from the discharge region. In order, probes are located at 0.25 m (entrance), 1.06 m (upstream), 1.39 m (midstream) and 1.72 m (downstream) away from the anode of the discharge region.

Chapter 4

Characterisation of the Magnetron Sputtering System

In this chapter, a characterisation of the magnetron sputtering system is made. These investigations included using a Langmuir probe to measure the He ion flux inside the device for various neutral pressures, DC plasma powers and probe positions inside the device. The sputtering target deposition rate is calculated by use of a quartz crystal microbalance (QCM), and the impurity species and concentrations within the vacuum vessel are interpreted using a residual gas analysis (RGA). A calibration for the IR pyrometer is provided, allowing the transmittance of a sapphire window and the emissivity of the metal surfaces used to grow fuzz to be measured. The calibration of the IR pyrometer was verified through a short investigation on fuzzy W growth across a surface temperature range (900 - 1200 K). This investigation was bench marked against the known temperature range for fuzzy W to grow at (1000 - 2000 K) as an indication that the surface temperatures measured by the IR pyrometer were calibrated correctly.

4.1 Langmuir Probe Diagnostic Measurements

In experiments on fuzzy W formation, the He ion flux is an important parameter to have knowledge of. This is due to the known dependence of the fuzzy W growth rates on the He ion fluence. To take a He ion flux measurement, the sample probe (see section 3.2.1) was positioned along the centre line of the magnetron target. With the probe facing the magnetron target, a DC He plasma was ignited. The He ion flux measurements were made for a range of experimental parameters: the neutral pressure was varied in the range 2.67 to 6.67 Pa, the DC plasma power was varied between 400 to 800 W, and the distance of the probe was varied along the centre line of the magnetron device from 95 - 105 mm away from the target.

To calculate the He ion flux, first the plasma parameters described in section 3.2.1 were measured. The probe used to make the measurement was connected to a Langmuir probe acquisition system (ALP 150 Impedans), and a current voltage (I-V) scan from -140 to 50 V, with steps of 0.1 V, was taken.

Previous attempts to produce fuzzy W using this experimental rig were made at a pressure of 5.33 Pa [65], so the measurements produced in this chapter were taken to show the variation in He ion flux as the neutral pressure was changed. A knowledge of the He ion flux at different pressures would allow fuzzy W experiments to be conducted in new pressure ranges.

4.1.1 Plasma Parameter Measurement

To calculate the He ion flux, certain plasma parameters were required. These parameters included the floating potential V_f, the plasma potential V_p, the electron temperature T_e, the ion I_{is} & electron I_{is} saturation currents, and the plasma density n. The process to find each parameter is summarised below.

Floating Potential

To identify V_f on a typical current-voltage (I-V) curve, the region where the current to the probe is equivalent to zero ($I = 0$) should be identified. On the plot, this is the region where the I-V curve intersects the x-axis.

Plasma Potential

Finding a value for V_p can be determined in a number of ways. By plotting the I-V on a semi log plot, the characteristic "knee" of the I-V curve is more clearly identified, and can give an indication of V_p. A more precise determination of V_p can be found by taking the first or second derivative of the IV curve. By identifying the voltage where dI/dV is a maximum point, or d^2I/dV^2 is zero, V_p is found.

Ion Saturation Current

To calculate I_{is} the gradient of the ion saturation region is recorded, and extrapolated to V_p.

Electron Temperature

To calculate a value for T_e, a semi log I vs V graph is plotted. An example of this was given in figure 3.7. The region of interest is known as the transition region, where the bias on the probe v_b is made more positive relative to V_f, slowly increasing toward V_p. In this region (i.e $V_b \leq V_p$), electrons are drawn to the probe and ions are repelled, and assuming a Maxwellian electron velocity distribution, the inverse slope of the probe current with respect to the bias voltage can be used to find T_e. When calculating T_e the value for I_{is} is subtracted from the I-V characteristic. The current drawn to the probe (I_p) will be due to contributions of both electron and ion currents, so subtracting the ion contribution from the total current before measuring T_e is necessary. The method for obtaining T_e in the region of $V_b \leq V_p$ on an I-V curve is given below.

$$I_{\mathrm{p}}(V_{\mathrm{b}}) = I_{\mathrm{es}}\exp(e(V_{\mathrm{b}} - V_{\mathrm{p}})/k_{\mathrm{B}}T_{\mathrm{e}}) + I_{is} \tag{4.1}$$

$$I(V_{\mathrm{b}}) = I_{\mathrm{es}}\exp(e(V_{\mathrm{b}} - V_{\mathrm{p}})/k_{\mathrm{B}}T_{\mathrm{e}}) \qquad \text{(Subtract } I_{is}\text{)} \tag{4.2}$$

$$\ln(I(V_{\mathrm{b}})) = \ln(I_{\mathrm{es}})\exp(e(V_{\mathrm{b}} - V_{\mathrm{p}})/k_{\mathrm{B}}T_{\mathrm{e}})) \qquad \text{(Take the natural log)} \tag{4.3}$$

$$\ln(I(V_{\mathrm{b}})) = \frac{e(V_{\mathrm{p}} - V_{\mathrm{b}})}{k_{\mathrm{B}}T_{\mathrm{e}}} + ln(I_{\mathrm{es}}) \qquad \text{(To be compared with)} \tag{4.4}$$

$$\mathrm{y} = \mathrm{mx} + \mathrm{c} \qquad \text{(equation of a straight line)} \tag{4.5}$$

The gradient (m) was obtained using the OriginPro software package by applying a linear fit over the transition region. By rearrangement of the expression in equation 4.5, and using the known values for electron charge e, the plasma potential V_{p}, bias voltage V_{b} and the Boltzmann constant k_{B}, a value for T_{e} can be found.

Plasma Density

In plasmas where $T_e \gg T_i$, the ion saturation current is given by the Bohm ion current, $\mathrm{I_{Bohm}}$,

$$I_{\mathrm{is}} = I_{\mathrm{Bohm}} = en_{\mathrm{sheath}}\sqrt{\frac{k_{\mathrm{B}}T_{\mathrm{e}}}{m_i}} \tag{4.6}$$

where e is the electron charge, k_B is the Boltzmann constant, m_i is the mass of the ions, A is the area of the probe face and n_{sheath} is the plasma sheath density. As a Maxwellian distribution is assumed for the electrons in the plasma, their density at the entrance to the sheath n_{esheath} is described by the Boltzmann relation,

$$n_{\mathrm{esheath}} = n_{\mathrm{e}}e^{-\Phi/T_{\mathrm{e}}} \approx 0.61n_{\mathrm{e}} \tag{4.7}$$

where n_{e} is the electron density in the bulk plasma and Φ is the potential relative to the $\mathrm{V_p}$ at the location of n_{es}. The plasma is quasi-neutral, thus $n_{\mathrm{e}} \approx n_{\mathrm{i}} = n$, allowing equation 4.8 to be written as,

$$I_{\mathrm{is}} = I_{\mathrm{Bohm}} = 0.61en\sqrt{\frac{k_{\mathrm{B}}T_{\mathrm{e}}}{m_i}} \tag{4.8}$$

The electron saturation current $\mathrm{I_{es}}$ can be expressed as

$$I_{\mathrm{es}} = \frac{1}{4}en_e\bar{v}_eA \tag{4.9}$$

where $\overline{v}_e$ is the mean electron speed, and the other parameters are as previously defined. The mean electron speed is given by,

$$\overline{v}_e = \left(\frac{8eT_\mathrm{e}}{\pi m_e}\right)^{\frac{1}{2}} \tag{4.10}$$

Equation 4.9 can also be used to find n, however in magnetised plasmas the radius of orbit (known as the gyroradius) of charged particles is affected by the presence of a magnetic field, and this can lead to differences in the measured plasma density from both saturation currents [154]. The gyro-radius of an electron is much smaller than an ion, hence the collection of electrons is more affected by the field, therefore depending on the position of the probe an under/over representation of the plasma density could be made if $\mathrm{I_{es}}$ is used in the calculation of n. Generally $\mathrm{I_{is}}$ is used to calculate the plasma density.

4.1.2 Calculating the Particle Flux

The flux to the sample surface, Γ, can be calculated from the formula below,

$$\Gamma = \frac{\mathrm{I_p}}{\mathrm{eA}} \tag{4.11}$$

where e is the electron charge, I_p is the probe current, and A is the probe area. However a more accurate measurement of Γ will account for the combination of electron and ion components of the probe current. The probe current I_p can be expressed in terms of both electron, I_e, and ion currents, I_i such that,

$$\mathrm{I}_p = I_e - I_i \tag{4.12}$$

The ion flux, Γ_i, can now be written in terms of the total plasma and electron current where,

$$\Gamma_i = \frac{1}{eA}(I_e - I_p) \tag{4.13}$$

An expression for the electron component of the total probe current is given in [140] to be,

$$I_p + I_i = I_e = \frac{1}{4}en_o\overline{v}_e\mathrm{Aexp}\left(\frac{V_\mathrm{b} - V_\mathrm{p}}{T_\mathrm{e}}\right) \tag{4.14}$$

where V_b is the bias voltage applied to the probe, V_p is the plasma potential, $\mathrm{T_e}$ is the electron temperature and $\overline{v}_e$ is the mean electron speed.

Now, by substitution of equation 4.14 into equation 4.13, an expression for the ion flux Γ_i is left as,

$$\Gamma_i = \frac{1}{4} n_o \bar{v}_e \exp\left(\frac{V_b - V_p}{T_e}\right) - \frac{I_p}{eA} \tag{4.15}$$

From equation 4.15 it can be seen that when the difference in potential between the probe and the plasma is much less than zero (ie. V_b - V_p « 0), the electron component will be significantly reduced, with the flux to the probe dominated by ions.

4.1.3 Ion Flux Measurements

The probe was first used to attain I-V characteristics across a bias voltage range of - 140 to 50 V, for different neutral pressures (2.67 Pa - 5.33 Pa), DC plasma powers (400 - 800 W) and distances of the probe from the magnetron target (95 - 105 mm). The measurements were taken using the automatic Langmuir probe acquisition system (ALP 150 Impedans) and the pressure inside the chamber was regulated using a mass flow controller (MKS Instruments) calibrated for He. In figure 4.1, the flux (Γ_i) measurements calculated at a probe bias of - 100 V over these experimental parameter ranges are shown. In figure 4.1 a) - c) each figure represents the results for each neutral pressure used: a) 2.67 Pa, b) 4.00 Pa and c) 5.33 Pa. It is clear from the trend in figures 4.1 a) - c) that an increase in the DC power consistently produces a greater measured ion flux to the probe surface, with a near 2x increase in the flux when the DC plasma power is increased from 400 to 800 W.

An increase in the neutral pressure does not produce a noticeable increase in the flux. A closer inspection of the difference in the flux measured by the probe across the pressure range (2.67 - 5.33 Pa) here is shown in figure 4.2. In figure 4.2, the measures of Γ_i at a probe distance from the target of 97 mm for the three different operating pressures are shown. The increase in He neutral pressure does appear to increase the measured flux by a small amount; at a DC power of 700 W, probe bias of -100 V and probe-magnetron distance of 97 mm, the ion flux measured by the probe increases from 1.17 x 10^{20} to 1.25 x 10^{20} m^{-2} as the neutral pressure is increased from 2.67 to 5.33 Pa.

As the ion flux does not change considerably with the change in neutral pressure, the lower boundary of the pressure range was investigated further. A lower neutral pressure would not only conserve the He gas longer in the experiments, but (as will be discussed in section 4.3) at lower pressures the deposition rates from the magnetron target are increased, something desired for the fuzzy W experiments used in this thesis. In addition, fuzzy W research on LPDs is typically conducted at lower neutral He pressures ($\sim$ 1 Pa in [37], [97], [160]), therefore operating the magnetron sputtering system at a lower pressure will allow a better comparison between the fuzzy W grown in each environment.

A more thorough set of Langmuir probe measurements were made using the operating pressure of 2.67 Pa and a DC plasma power of 700 W, with the distance of the probe from the magnetron target being varied in a larger range from 89 to 125 mm. The minimum distance at which the probe was positioned ($\sim$ 89 mm) was chosen as the closest distance that the probe could be placed and still, if it was heated, be able to have its surface

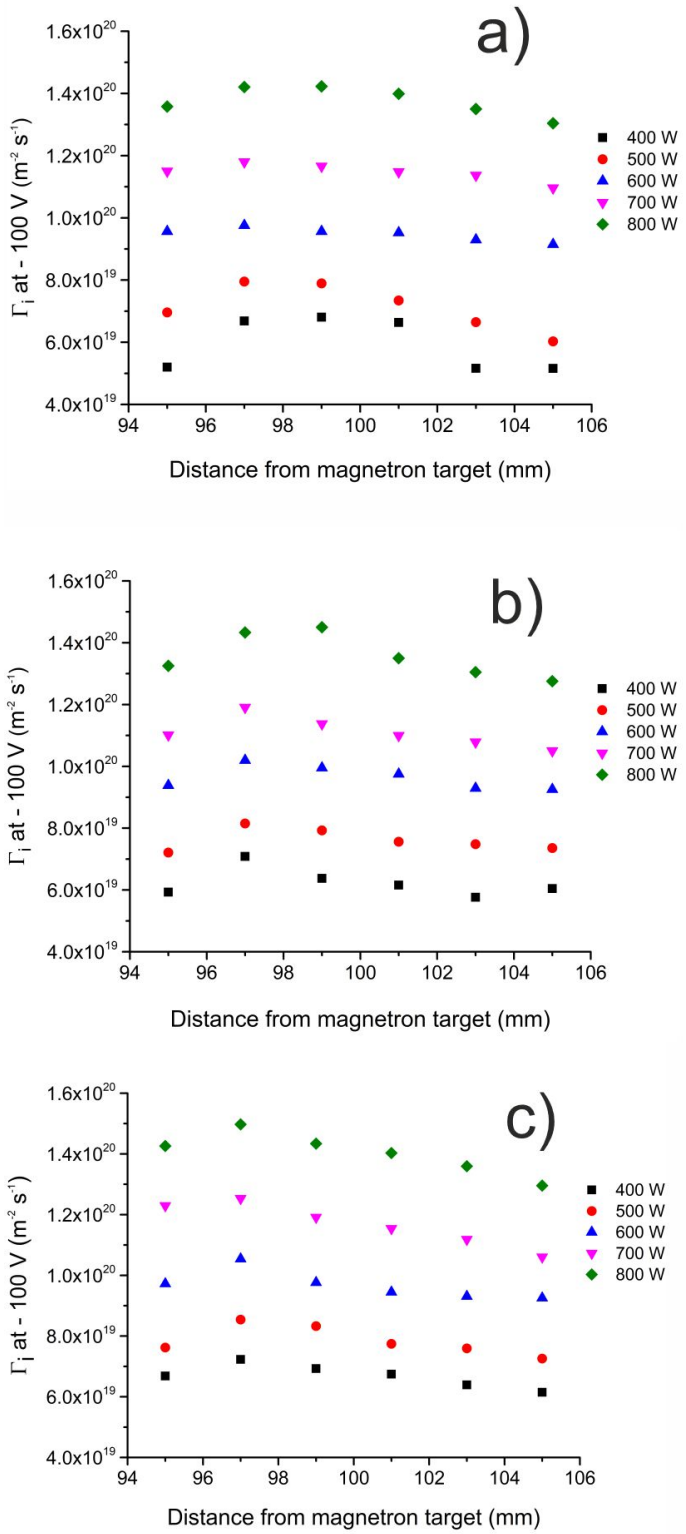

Figure 4.1: Flux measurements for a He plasma at 3 different pressures (a) 2. 67 Pa, b) 4.00 Pa and c) 5.33 Pa) whilst varying the DC plasma power in the range 400 - 800 W and the position of the probe along the centre line of the magnetron target.

temperature measured by the IR pyrometer. Due to the angle of sapphire window port for the IR pyrometer, at distances $<$ 89 mm away from the magnetron target the IR pyrometer

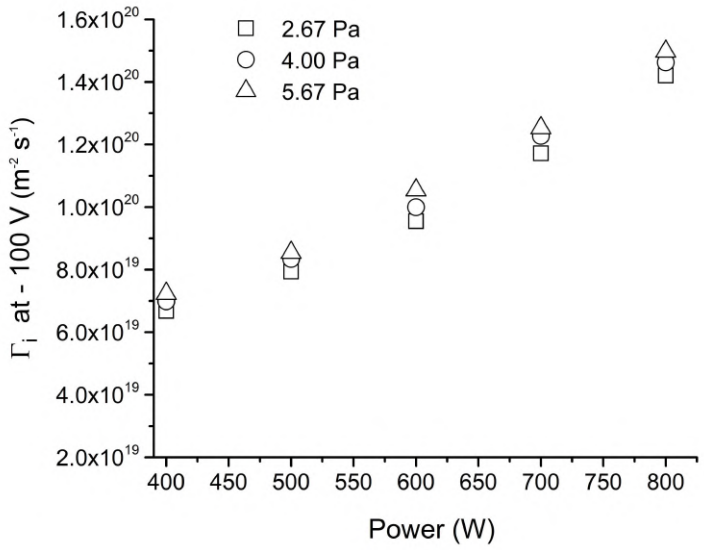

Figure 4.2: Flux measurements for a He plasma at 3 different pressures (2. 67 Pa, 4.00 Pa and 5.33 Pa) whilst varying the DC plasma power in the range 400 - 800 W. The probe was held at 97 mm away from the magnetron target at a bias voltage of - 100 V.

would no longer "see" the sample surface, thus a temperature measurement would not be possible. It was decided the distances of the probe 89 mm or more away from the centre of the magnetron target would be investigated as these were the distances a sample at which fuzz was grown would reasonably be positioned inside the magnetron system.

The results of the probe measurements for V_f, V_p and T_e are shown in figure 4.3. The measurements were taken at a pressure of 2.67 Pa, while the position of the probe was varied along the centre line of the magnetron target. In 4.3 a, the evolution in V_f shows a maximum value in the range 95 to 98 mm. This can indicate the null point of the unbalanced magnetron configuration inside the system. The errors for parameter V_f, V_p and T_e were calculated by taking an average of three separate probe measurements, and using twice the standard deviation between measurements for the error. In previous studies on the same experimental rig, the null point was identified to be in the range of $\sim$ 80 to 100 mm away from the centre of the target [65], [161], agreeing with the trend of V_f shown here. Additionally, the electron temperature T_e shows a minimum in the range 95 - 100 mm away from the magnetron target, which is likely to correlate with the region of the null. The electron temperature T_e was found to be $\sim$ 8 eV during the probe measurements. The plasma density n was calculated from a measurement of the ion saturation current I_{is}, which was found to be $\sim$ 3 to 4 mA. Using equation 4.8, n was calculated to be $\sim$ 5 x 10^{15} m^{-3}.

Closing the butterfly valve during the operation of the magnetron vacuum system produced an increase in the base pressure of the system. In practice, with the valve open, the combination of the rotary and turbomolecular pumps was sufficient to produce a base pressure of $\sim$ 6 x 10^{-4} Pa inside the magnetron system. By closing the butterfly valve, the

pumping speed of the system decreased, raising the base pressure to 5.33 x 10^{-3} Pa. In addition, the flow rate of He gas required to reach the operating pressure of 2.67 Pa decreased from 192 sccm to 164 sccm with the valve closed. As a result of the background pressure increase, the background impurity level (see section 4.2), as well as the target sputtering rate (see section 4.3), was increased. A separate set of Langmuir probe measurements, examining the effects of operating the butterfly valve on the ion flux to the probe, were taken under these new conditions. The flux measurements made with and without the operation of the butterfly valve are presented in figure 4.4 a) and b), respectively. The distance of the probe from the magnetron target was varied over the range of distances from 89 - 130 mm. In both cases, the optimum distance (highlighted in red) for the highest ion flux was generally found to be at 97 mm. Figures 4.4 a) and b) also indicate that as the probe bias V_b reaches larger negative biases, the ion flux measured by the probe increases. As V_b becomes more negative, the sheath around the probe expands, enhancing the collection area of charged ions and, therefore, the measured flux.

In figure 4.4 a) and b), the ion flux measured at a probe bias of - 100 V is shown for a range of distances along the centre line of the magnetron target, at two different base pressures. The maximum of the ion flux at a distance of $\sim$ 97 mm is observed in both figures, with the maximum ion flux measured to be (1.17 $\pm$ 0.04) x 10^{20} m^{-2} when the butterfly valve is operated and (1.10 $\pm$ 0.05) x 10^{20} m^{-2} when it is not. As a way of comparison, previous ion flux measurements made using the same magnetron system were compared to the current results. In previous investigations where a neutral He pressure of 5.34 Pa and 700 W of DC power was used, Langmuir probe measurements showed an electron temperature of around 7 eV and a He flux on the order of 1 x 10^{20} m^{-2} s^{-1} [65]. These measurements agree well with the findings in the current work. As the He ion flux was found to be largest at a probe distance of 97 mm away from the magnetron target, the samples were held at this position inside the magnetron system during plasma treatment.

4.1.4 Probe Error

As a result of the clamps used to hold the sample probe in place, parts of the probe surface were shaded from the plasma (illustrated in figure 4.5). Therefore a calculation was made to find this missing area covered by the clamps. The area of the probe, used in equation 4.15, was corrected in the final calculation of the ion flux. The formula used to find the area A in figure 4.5 is,

$$\mathrm{A} = A_{\text{sector}} - A_{\text{isosceles triangle}}$$

$$\mathrm{A} = \frac{1}{2}r^2\theta - \frac{1}{2}r^2 sin\theta$$

where r is the radius of the probe surface (0.005 m) and θ is the angle of the sector in radians. The length of the chord, a, was found to be 0.035 m after measuring the small

holder clips. By using trigonometry, a value for θ can now be found using:

$$\frac{a}{2} = \mathrm{rsin}\left(\frac{\theta}{2}\right) \tag{4.16}$$

A value for θ was calculated to be 0.72 radians, and by using equation 4.16 the area of the probe surface clips is found to be 7.84 x 10^{-7} m^2. Subtracting this value from the total area of the probe (7.85 x 10^{-5} m^2) results in an area of 7.70 x 10^{-5} m^2 exposed on the probe surface. This area was used in the calculation for the ion flux.

4.2 Residual Gas Analysis

Here the Optix spectrometer supplied by Gencoa Ltd, described in section 4.2, was used to perform a residual gas analysis (RGA) to attain the species of impurity gases inside the vacuum chamber. It was observed that by operating (i.e. closing) the butterfly valve inside the chamber during the initial vacuum pumping of the chamber, the base pressure of the system rose from 6.67 x 10^{-4} and 5.33 x 10^{-3} Pa. See figure 3.2 for a schematic of the butterfly valve in relation to the vacuum pumps connected to the chamber. This increase in base pressure implied that closing the butterfly valve slowed down the overall pumping speed to the vacuum vessel, increasing the amount of air impurity within it.

As the gas species type can affect the sputtering rate of the magnetron target when a plasma is produced, it was important to understand the changes in impurity type and amount during the operation of the butterfly valve. Operating with and without the butterfly valve, the Optix spectrometer was used to gather data on the gas impurity species within the chamber after a night of vacuum pumping (a total time of 9 hours). Figures 4.6 a) and b) show RGA spectra for the two chosen base pressures of 6.67 x 10^{-4} and 5.33 x 10^{-3} Pa. The main species identified are those derived from air (e.g. N_2, O, O_2, H and OH). With an increased base pressure, the main N_2, O and O_2 peaks increase in intensity by five or six times, consistent with an eight fold increase in the backing pressure. These species are considered the main species that can sputter the magnetron target.

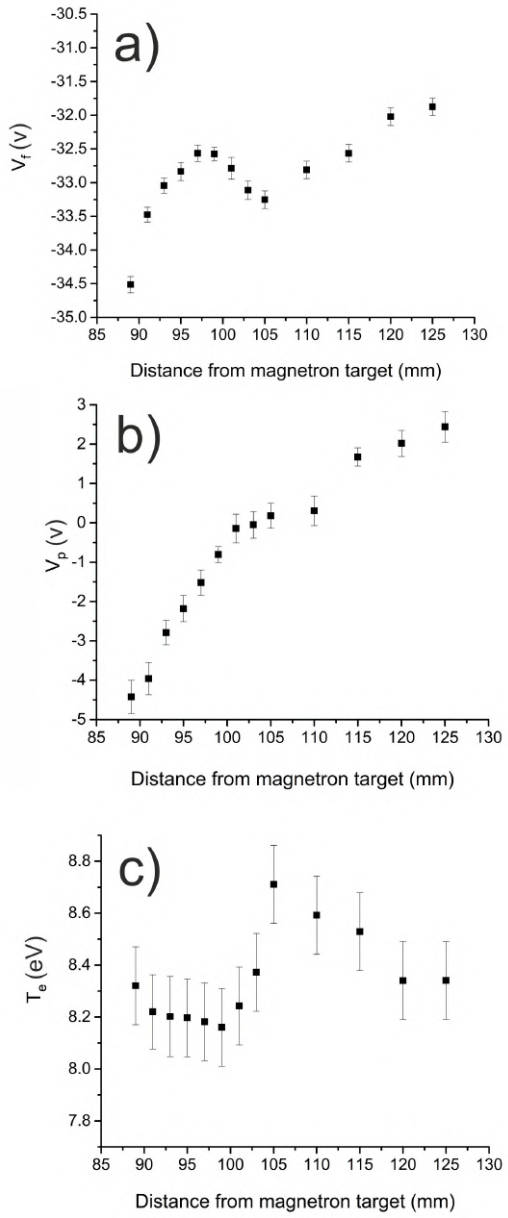

Figure 4.3: Langmuir probe data taken at 2.67 Pa and a DC power of 700 W, for a range of probe distances from the magnetron target. In a), the measurements of V_f are given, in b) the measurements of V_p are shown and in c) the calculations of T_e are provided.

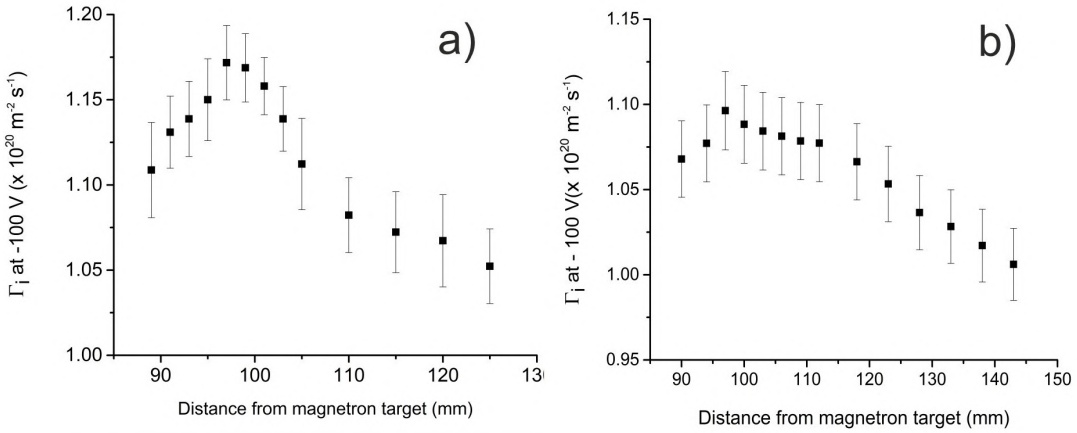

Figure 4.4: Flux measurements for a neutral pressure of 2.6 Pa with the butterfly valve closed (a) and the butterfly valve open (b), while holding the probe bias at - 100 V and varying the probe distance from the target.

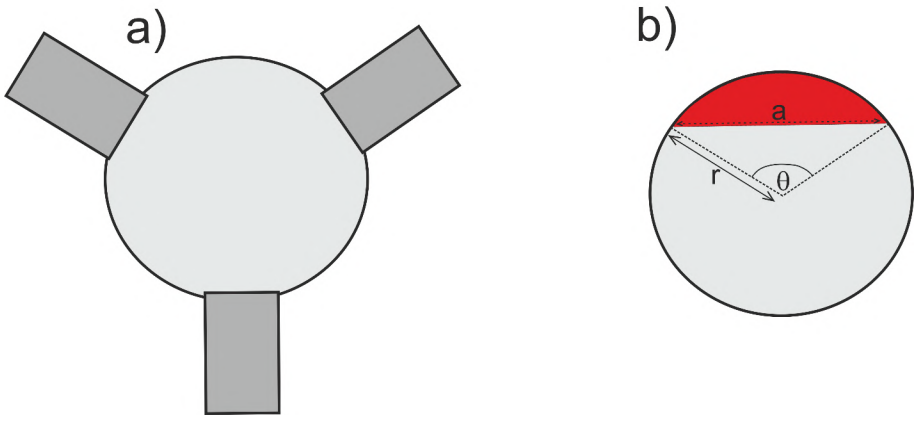

Figure 4.5: In a), an illustration of the three clips covering small sections of the probe/sample surface, and in b) an image describing the process of finding the area covered by each small clip by calculating the area of a segment of a circle.

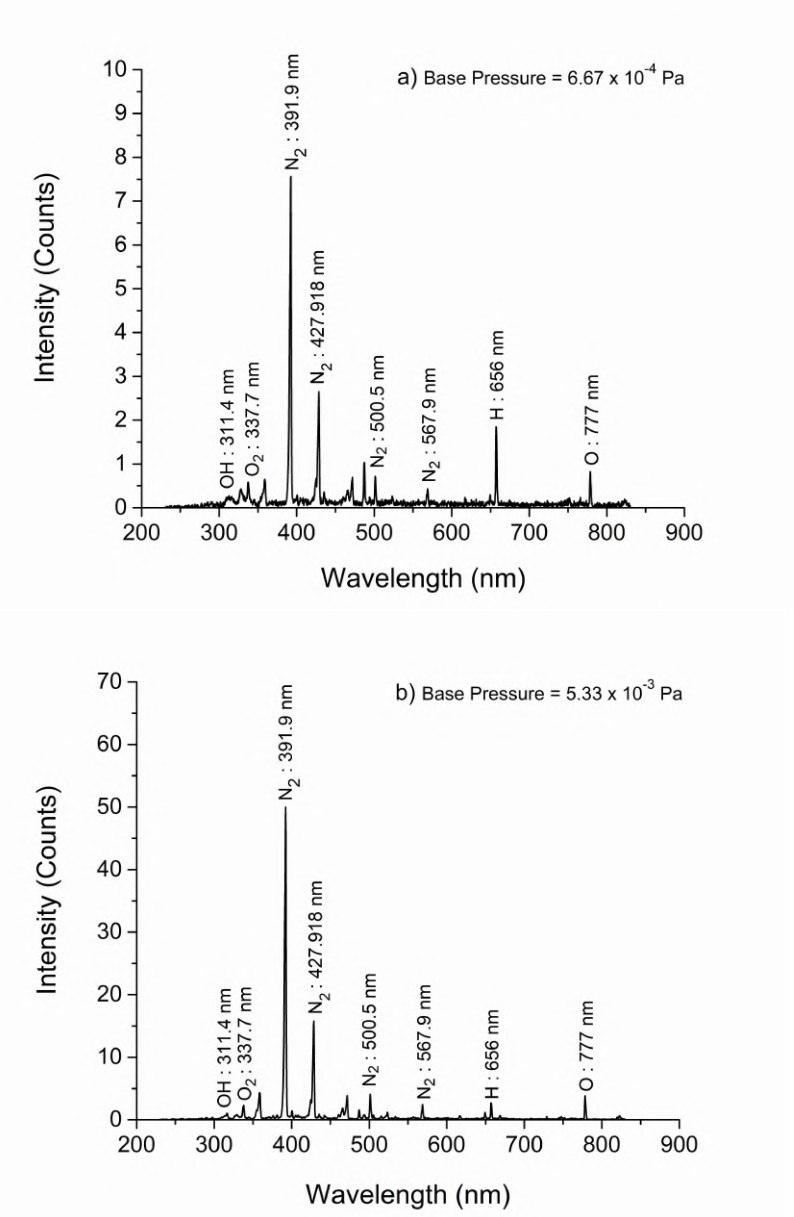

Figure 4.6: RGA (optical emission spectra) results obtained in the magnetron system for the two different base-pressures a) and b).

Further RGA measurements were used to investigate the evolution of species type as the magnetron system was in operation. The neutral pressure was maintained at 2.67 Pa, and the DC power was 700 W. Again the butterfly valve was varied in its operation so as to raise the base pressure of the system. In figure 4.7 the results of the RGA with the magnetron in operation at 700 W are shown. Figures 4.7 a) and c) show the spectra produced at each base pressure, one minute after the plasma was ignited. Figures 4.7 b) and d) show the RGA results after six hours of He plasma irradiation inside the magnetron.

It can be seen from figure 4.7 a) and c) that a small increase in the height of the N_2 (391.4 nm) peak is visible for the higher base pressure of 5.33 x 10^{-3} Pa relative to the lower base pressure. This is likely due to the higher concentration of N_2 that was measured for the larger base pressure, shown in figure 4.6. The magnetron target may also contribute to the increase in concentration of N_2 as a result of nitride removal from its surface during sputtering. A large number of peaks visible figure 4.7 correspond to He for all four spectra, although a H peak is visible at 656 nm. As the plasma exposure was increased, the intensity of this peak was seen to decrease in both figure 4.7 b) and d). It is likely that over the course of the plasma exposure, the heating supplied by the plasma can remove H trapped within the walls, and gradually this will be pumped out of the system.

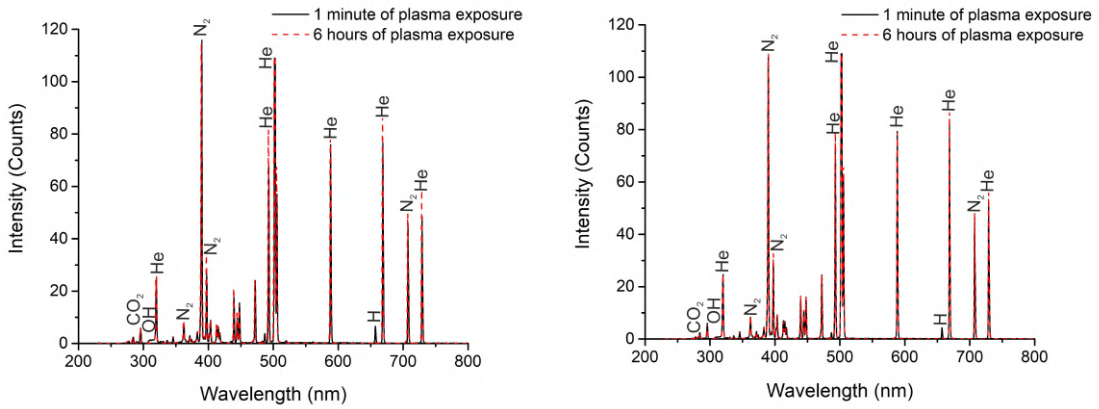

Figure 4.7: RGA for an operational neutral pressure of 2.6 Pa and 700 W of DC plasma power, at two different base pressures inside the magnetron system.

4.3 Deposition Rate Measurements

A QCM was used to gain an understanding of the deposition rates in the magnetron system, with the QCM placed around 140 mm away from the centre of the magnetron target. As it was useful to know for later experiments, two different magnetron targets types, W and Mo, were used to take deposition rate measurements. During both sets of deposition rate measurements, the magnetron system was maintained at a neutral He pressure of 2.67 Pa with a DC plasma power of 700 W. For the W target, the deposition rate measurements were taken for different neutral pressures (2.67, 4.00 or 5.33 Pa), different base pressures (6.67 x 10^{-4} or 5.33 x 10^{-3} Pa)) and different DC powers (600 or 700 W). For Mo, only

700 W and a neutral pressure of 2.67 Pa was used.

The results from the QCM measurements found using a W target and Mo target are presented in figure 4.8 a) and 4.8 b) respectively. As the results in figure 4.8 show, the apparent thin film of deposition formed on the QCM depends on the neutral pressure inside the vacuum chamber, as well as the DC power applied to the cathode. As the neutral pressure increases the deposition rate is observed to decrease, and as the power increases to the plasma so does the deposition rate if a constant pressure is maintained. Similar patterns of the deposition rate for variations in the gas neutral pressure and plasma power have been seen in previous studies in DC magnetron systems [162], [163].

As He produces a greater sputtering yield on Mo relative to W for the same ion energy, the sputtering yield on an Mo target would be expected to be larger, which is the case for the data in figure 4.8. Given the cathode bias was measured to be $\sim$ 300 V during the plasma exposure, the typical yields for W and Mo surfaces by He ion bombardment at 300 eV would be 8.61 x 10^{-3} and 8 x 10^{-1} respectively [21]. A summary of the deposition rates measured by the QCM for a range of neutral pressures and background pressures are shown in table 4.1

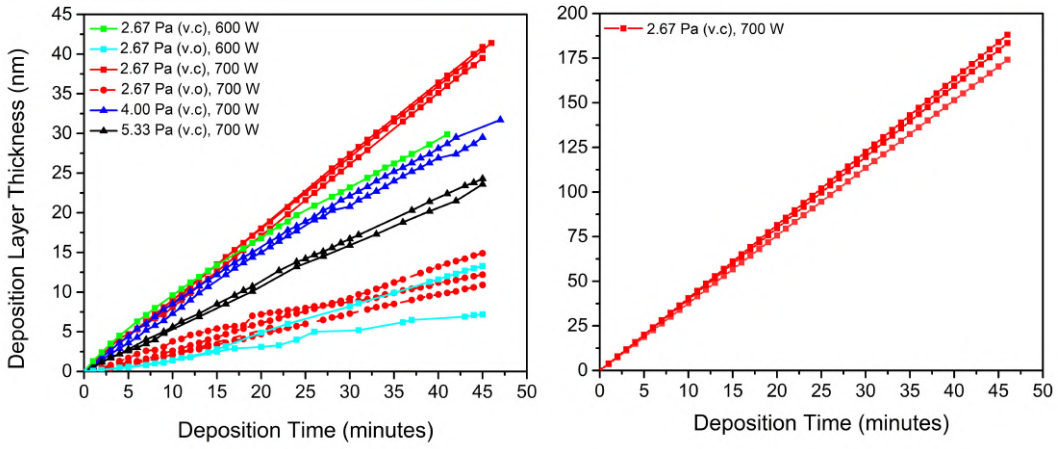

Figure 4.8: The thickness of a layer of deposition measured by the QCM for He sputtering of a a) W target and b) Mo target, for various neutral pressures and DC plasma powers. The abbreviations v.c. and v.o. stand for (butterfly) valve closed and (butterfly) valve open respectively.

4.4 Calibration of the IR Pyrometer

The IR pyrometer in this work was used to give a measure of the surface temperature of the metal sample throughout the initial heating stage and plasma exposure. The IR pyrometer analyses the emitted infrared radiation from the surface and yields a voltage signal which corresponds to the temperature of the surface. Two inputs, the transmittance of radiation (τ) and emissivity (ϵ), are needed to be found so as to calibrate the IR system correctly. To calculate the emissivity, samples were heated inside the chamber using the

Table 4.1: Deposition rates of a W and Mo target for a range of neutral pressures and plasma powers.

Plasma Conditions	Target Type	Butterfly Valve	Deposition Rate (nm/hr)
2.67 Pa, 600 W	W	Closed	30
2.67 Pa, 600 W	W	Open	14 ± 6
2.67 Pa, 700 W	W	Closed	54 ± 4
2.67 Pa, 700 W	W	Open	17 ± 3
4.00 Pa, 700 W	W	Closed	41 ± 4
5.33 Pa, 700 W	W	Closed	32 ± 2
2.67 Pa, 700 W	Mo	Closed	251 ± 11

electron beam heater described in section 3.1.2.

For a black body, the spectral radiant emittance (R) can be expressed using Planck's law as [164],

$$R = \frac{2hc^2/\lambda^5}{\exp(hc/\lambda k_B T) - 1} \tag{4.17}$$

where h is the Planck's constant, c is the speed of light, λ is the radiation wavelength and k_B is Boltzmann's constant. When considering surfaces like the samples used in this work, the emissivity is taken into account. The spectral radiant emittance for the samples (R_sample) used here is related to R as follows [165],

$$R_\mathrm{sample} = \epsilon R \tag{4.18}$$

The radiation emitted from the sample surface and measured by the IR pyrometer must pass through the sapphire window before it reaches the detector, so when calculating the incident spectral irradiance (I) the transmission of this window is considered: [166]

$$I = \tau R_\mathrm{sample} = \tau \epsilon R = \tau \epsilon \frac{2hc^2/\lambda^5}{\exp(hc/\lambda k_B T) - 1} \tag{4.19}$$

4.4.1 Transmission Calibration

First the transmission of the sapphire window was verified. A small calibration rig was assembled to calibrate the transmission of the window, and this comprised of an aluminium plate with two type-k thermocouples attached to it, with the IR pyrometer focused on an area on the plate between the two thermocouples. At this stage, there was no window in front of the IR pyrometer.

Heating was then applied to the plate via two soldering irons, and the temperatures of the thermocouples and IR pyrometer were recorded. The small aluminium sheet used to perform the calibration could reach a surface temperature of ($\sim$ 150°C) using the two

soldering ions to heat it up. At this point, the emissivity setting on the IR pyrometer was changed until the average of the two thermocouples agreed with the pyrometer. Once agreement was found, the window was then placed in the way of the pyrometer. The transmittance of the window was then set by changing the transmittance of the IR pyrometer, and τ was found to 0.78. According to the data sheet supplied with the sapphire window, it has an 87 % transmittance at a wavelength of 2.3 μm. Previous measurements of τ using the same sapphire window were found to be 0.8, implying a slight degradation in the transmittance in the window has occurred. This presumably due to deposition on to its surface during operation of the plasma.

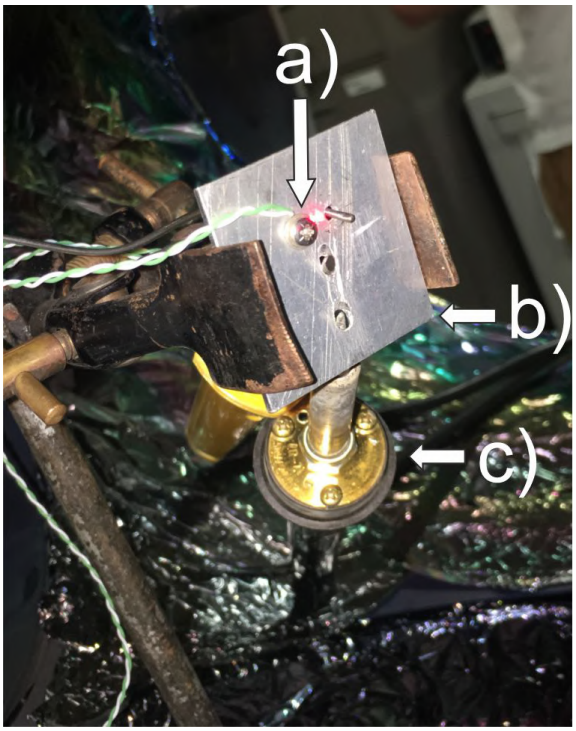

Figure 4.9: Experimental rig used to calibrate the transmission of the IR pyrometer. Each part of the rig is labelled, a) shows two thermocouples with the IR pyrometer (red beam) focussed between these two points. The aluminium sheet is labelled b) and the soldering irons are each labelled c).

Emissivity Calibration

To calculate the emissivity ϵ polished metal samples (W or Mo) were placed individually in the sample heater, held in place on the retractable arm inside the magnetron system. All samples were polished using the methods outlined in section 3.3.1 which supplied a near mirror finish to each surface. To measure the surface temperature of the W sample, two thermocouples were attached to the samples surface using the small clamps of the sample holder. The IR pyrometer was aligned on the W sample at a position equidistant from the centre of the sample (shown in figure 4.10). The thoriated W filaments which supply heating to the samples are held beneath the centre of the sample, so all temperature sensing methods were positioned at similar distances from this point. The heating of the

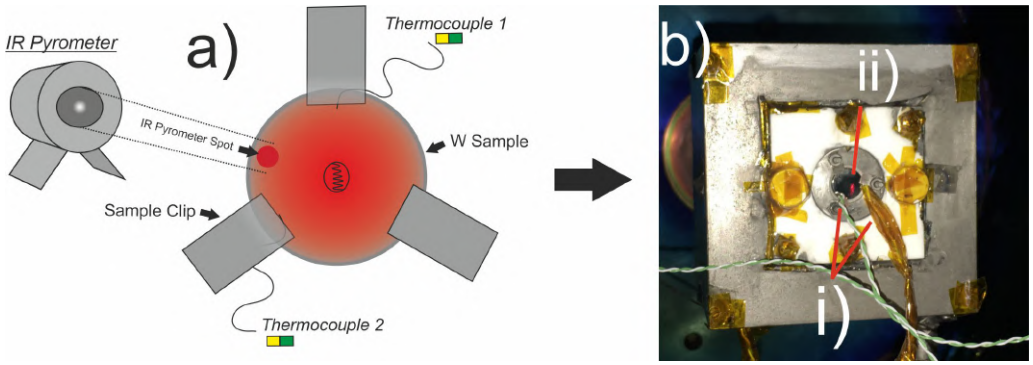

Figure 4.10: Figure showing an illustration of the emissivity calibration process. In a) a diagram illustrates the set up of the two thermocouples and an IR pyrometer on the W sample. Two thermocouples are placed underneath the sample clips, and the IR pyrometer is reading from a spot equidistant from the centre of the sample. The filament (shown beneath the centre of the sample) supplies the heating. In b), the emissivity calibration set up used in the magnetron sputtering system is shown. The thermocouples (i) and IR pyrometer (ii) temperature sensing locations are labelled accordingly.

metal surfaces was conducted after vacuum pumping the system for $\sim$ 5 hours to reach a base pressure of 6.67 x 10^{-4} Pa. As the HEAT2-PS power supply was operated in automatic mode, a temperature reading was supplied to the power supply by using a type K thermocouple, with this thermocouple being defined as thermocouple 1 (T_1). The second thermocouple (T_2) and IR pyrometer will have no baring on the feedback loop which controls the heating, but these temperature measurements were used to calibrate ϵ

The process of heating the samples was carried out as follows. The temperature of the sample was initially raised to 240°C and maintained at this temperature for several minutes, in this time the temperature was allowed to stabalise to a constant reading. All temperatures from T_1, T_2 and IR pyrometer were then recorded. The temperature was then increased by 50 ° C sequentially before reaching a maximum temperature of 940°C , the operational temperature limit of components of the sample heater. After each 50°C increase in the surface temperature, the readings of T_1, T_2 and IR pyrometer were all recorded. This process was then repeated for three different W samples, as well as two Mo samples.

The values for temperature measured by each different temperature sensing method were then used to calculate a value for emissivity from the metal surfaces. ϵ was initially chosen to be 0.63, and this was chosen arbitrarily so as to demonstrate the need for correct calibration of the emissivity of the samples. Using the temperature value output by the IR pyrometer (and $\epsilon = 0.63$ and $\tau = 0.78$) a value for I could be calculated using equation 4.19. Using this value for I just found, and the thermocouple temperatures T_1, T_2 and T_{av} (the average of T_1 and T_2), a value for ϵ was found by rearranging equation 4.19 for ϵ. Now, the value for ϵ which gives the recorded temperature values (T_1, T_2 or T_{av}) can be calculated by using the value for I measured earlier. Figures 4.11 and 4.12 show the values of ϵ that were found to correspond to each recorded temperatures T_1, T_2 or T_{av}. A linear line of best fit (green line) was used to give an averaged emissivity value of 0.28

$\pm$ 0.02 for polished W, and 0.35 $\pm$ 0.02 for polished Mo. This is in good agreement with previous articles using polished W samples where ϵ is quoted to be between 0.26 and 0.5 for polished W [65], [167].

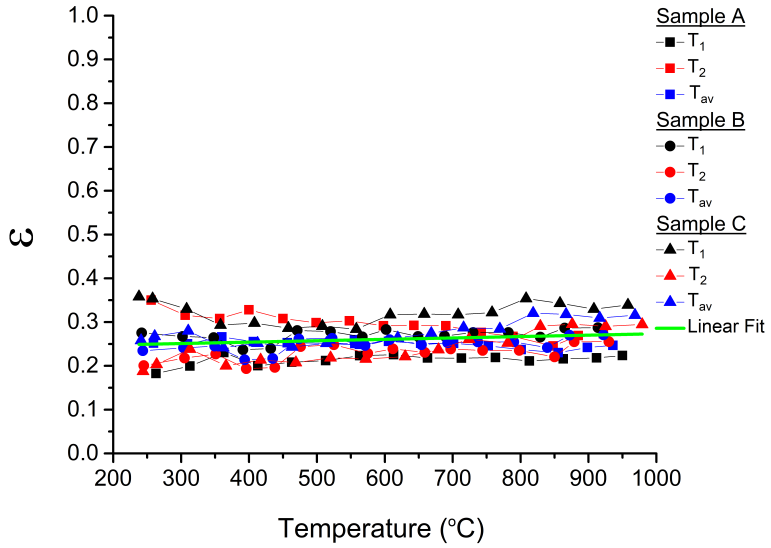

Figure 4.11: Values for ϵ calculated as a function of the sample temperature read by T_1, T_2 or T_av. Measurements made for polished W samples.

4.5 Temperature Threshold for Fuzzy Tungsten Growth

To verify the known temperature threshold for fuzzy W production ($\sim$ 1000 K), a short investigation was carried out in the magnetron sputtering system. Samples of W were exposed to He plasma over a range of surface temperatures (900 - 1200 K) encompasing the temperature threshold to produce fuzzy W. Each W sample was treated with He plasma for 7 hours of exposure time reaching a He ion fluence of 2.6 x 10^{24} m^{-2}. The ion energy was set at 80 eV by application of a DC bias to the W sample surface. The neutral pressure and DC plasma power were maintained throughout the plasma exposure at 2.67 Pa and 700 W respectively. To heat the W surfaces, each sample was heated using electron bombardment from the sample heater unit, and the surface temperature was monitored using an IR pyrometer. After the plasma exposure, each sample was analysed using the SEM to characterise the surface morphologies produced, and surface reflectivity measurements were taken to examine any reduction in the reflectivity from each surface.

In figure 4.13, the SEM observations from each W sample exposed to He plasma for a temperature range of 900 - 1200 K are shown. In figure 4.13 a) an untreated W sample is shown for a comparison to the plasma treated surfaces. It can be seen in figure 4.13 a change in the surface morphology on the surfaces is evident between the temperatures of 1000 (d)) and 1050 K (e)). This change appears to be characterised as a deviation from nodules on the surface to longer tendril structures. As the He ion fluence used in this

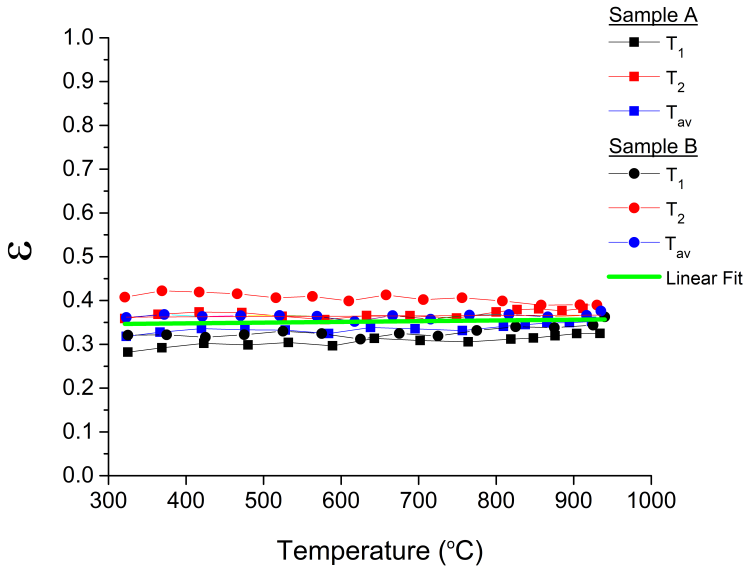

Figure 4.12: Values for ϵ calculated as a function of the sample temperature read by T_1, T_2 or T_av. Measurements made for polished Mo samples.

investigation exceeds the experimentally verified incubation fluence for fuzzy W growth ($\sim$ 2.4 x 10^{24} m^{-2} [38]), and the He ion energy is large enough to produce fuzz (as shown in figure 2.4), it can be assumed that the only limiting factor to fuzz growth should be the surface temperature. As a transition from nodules of fuzz (presumably an early stage of growth) to fully formed tendrils occurs in the range of surface temperatures from 1000 K to 1050 K, it implies that the threshold for fuzzy W formation in the magnetron lies within this range. This finding agrees well with the observed temperature threshold of 1000 K. Conswith the error found to be a maximum of $\pm$ 10 K when considering the variation in the emissivity for W surfaces found in section 4.4.1. To calculate a final reflectivity value for each fuzzy W surface, three measurements were made for each sample using the USB2000 + spectrometer (Ocean Optics) reflectivity probe. Results were taken over a wavelength range from 300 to 800 nm, and a background scan was subtracted from each scan before the final value was found. To compare between each sample the reflectivity value measured at a light wavelength of 632.8 nm was used. This is consistent with other comparisons of reflectivity of fuzzy W surfaces that have been made in the literature [65], [98], [159].

The results of the reflectivity for each fuzzy W surface shown in figure 4.13 are presented in figure 4.14. A reduction in the reflectivity is clear in the range 1000 - 1100 K, with a significant decrease in the reflectivity of the W surface from $\sim$ 40 % at 1000 K to $\sim$ 15 % at 1050 K. This indicates a transition which is likely related to the development of fuzzy W on the surface. The reflectivity measured for each subsequent surface decreased further to 2 % for a surface temperature of 1200 K. These results, coupled with the SEM imaging in figure 4.14, indicates that fuzzy W is produced in the magnetron in the expected temperature range, and that the IR pyrometer is calibrated correctly. Considering the error on the temperature measurements which was taken to be $\pm$ 10 K given the variation in

ϵ for measured in section 4.4.1), the temperature threshold for fuzzy W to form is in the range 1000 - 1050 K in the magnetron. The minimum/maximum ranges for the surface temperature would therefore be 990 - 1060 K. This would give a boundary condition for fuzzy W growth in the magnetron system to be 1025 ± 35 K.

4.6 Conclusions

In this chapter an investigation was carried out in the magnetron sputtering system using a Langmuir probe, resulting in measurements of the plasma parameters (V_f, V_p, T_e) and the ion flux to the probe surface for a range of neutral pressures (2.67 - 5.33 Pa), DC plasma powers (400 - 800 W) and distances from the magnetron target (results taken over a range of 89 - 143 mm). The ion flux to the probe surface was found at a bias of -100 V, DC power of 700 W and He neutral pressure of 2.67 Pa to be on the order of 1 x 10^{20} m^{-2} s^{-1}. A comparison of the ion flux measurements produced with and without operating the butterfly valve, used to regulate the pressure inside the magnetron sputtering system, was provided. It was found there was a negligible difference between the ion fluxes measured when the valve was open or closed.

The deposition rates inside the magnetron system were quantified for a range of pressures (2.67 - 5.33 Pa), as well as the change in deposition rate when operating the butterfly valve or not. A calibration for the IR pyrometer was performed, with the transmission of the sapphire window (0.78) and the emissivity of W (0.28 ± 0.02) and Mo (0.35 ± 0.02) surfaces being measured. Finally, the temperature threshold for fuzzy W growth using the current experimental set up was found to be 1025 ± 35 K. This agrees well with the boundary conditions for the surface temperature of $\sim$ 1000 K [37], [159].

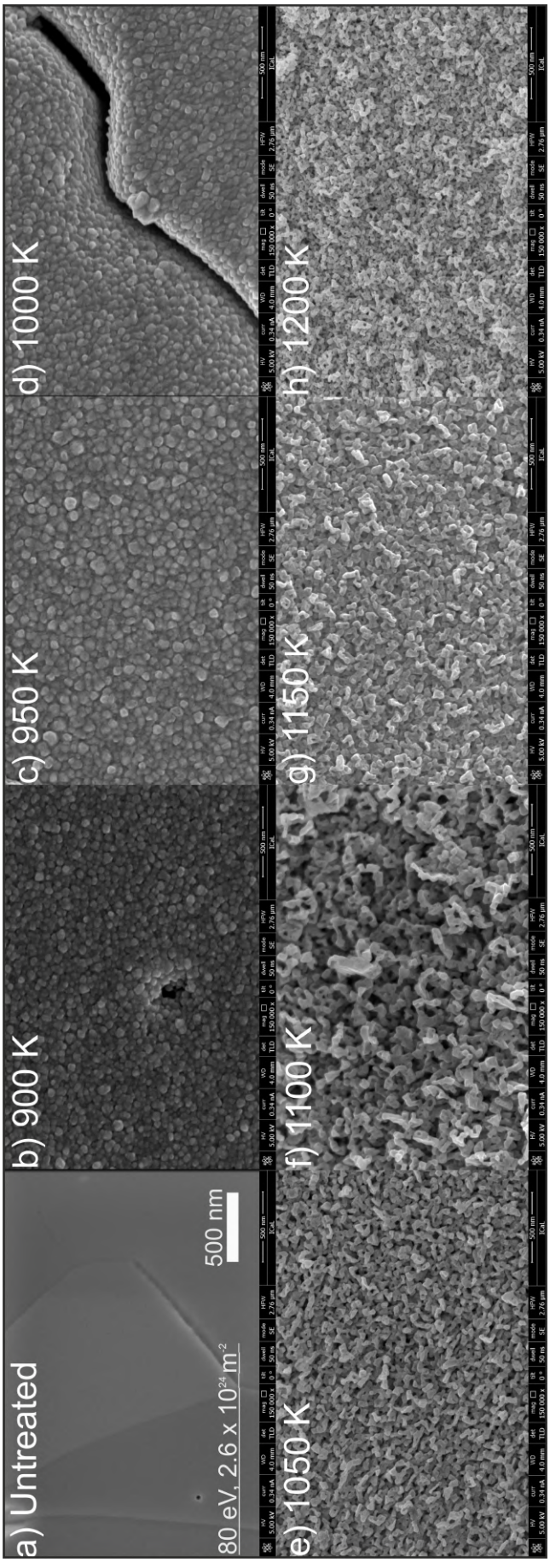

Figure 4.13: The surface morphologies of W samples after exposure to He plasma for a constant He ion fluence (2.6 x 10^{24} m^{-2}) and ion energy of 80 eV, over a temperature range of 900 - 1200 K. A scale bar is supplied in figure a).

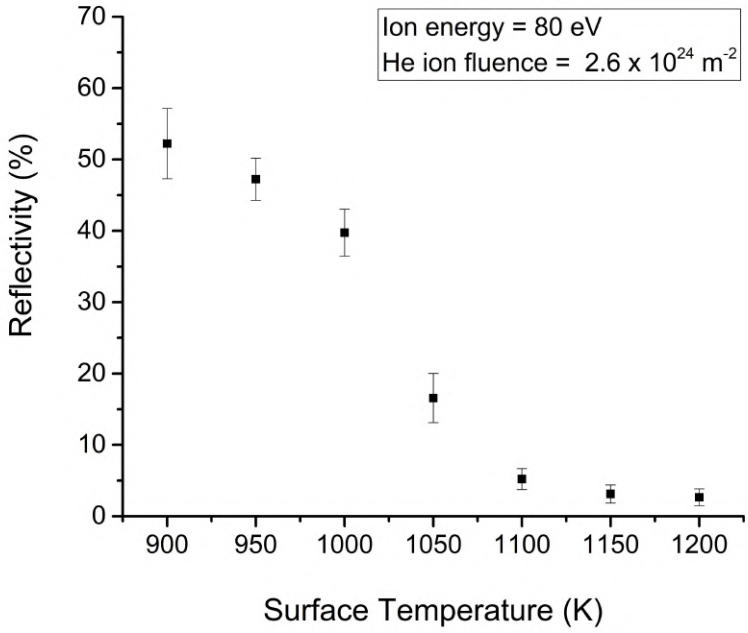

Figure 4.14: Reflectvity measurements for fuzzy W samples produced in the temperature range 900 - 1200 K , at a He ion fluence and energy of 2.6 x 10^{24} m^{-2} and 80 eV respectively. All reflectivity measurements were made at A 632.8 nm wavelength.

Chapter 5

The Effects of Impurity Gas Seeding On The Growth of Fuzzy Tungsten

In figure 1.9, the predicted temperature and ion energy profile for the ITER outer target is shown. This figure not only implies that conditions for fuzzy W formation could be met in ITER's divertor, but also that ion species may have sufficient energy to sputter plasma facing surfaces. This will be an important consideration for the operation of ITER, as impurity gas species (e.g. N_2, Ar, Ne) will be used to regulate heat and power loads on surfaces within the reactor. For the impurity species mentioned, ion energies greater than 40 eV will be sufficient to sputter W surfaces. If fuzzy W does form in ITER it may lower the sputtering yield of the surface it grows on [71], however it is currently unknown how impurity species alter the growths of fuzzy W. Therefore it useful to understand how, in the areas of the reactor where fuzzy W could grow, impurity gas species can affect, if at all, the growth of fuzzy W.

In this chapter, the results from experiments investigating the surfaces morphologies produced due to He + impurity plasma irradiations on W surfaces are shown. Parts of the results shown here contributed towards the publication within the study by Hwangbo *et al.* [160], which was one of the first studies to look at mixed He and impurity plasma exposures on W surfaces. The study showed observations of much larger fuzzy W structures, known as Nano-Tendril Bundles (NTBs), and a parameter space (surface temperature, sputtering yield) to observe the effects of the impurity gases on the growth of fuzzy W.

5.1 Introduction

In the steady state operation of plasma in the thermonuclear reactor ITER, an engineering limit for the permissible power loads on PFCs has been established at 10 MW m^{-2} [11]. This will increase for transient power loads, on a time scale of milli seconds, to 20 MW m^{-2}. For ITER, ions which are exhausted from the outer most regions of the plasma and transported to the divertor can have significant energies (hundreds of eV), so it is planned that impurity gas species will be pumped in front of divertor regions to reduce power

loads to PFCs [14], [33], [168], [169] as a way of enhancing PFC lifetimes. Without this mitigation, power loads could reach as high as 150 MW m^{-2} [170].

The power dissipation will be governed by charge exchange and radiation loss processes, with gas impurity seeding known to significantly increase the latter. As a consequence of the radiation losses, the electron temperature is reduced to tens of eV where atomic processes and recombination become significant. This decrease in electron temperature and plasma density in the divertor regions will produce the detachment of the divertor region plasma from the core. In preparation for ITER, there have been multiple studies on the testing of various impurity species (e.g. Ne, N_2, Ar) for divertor detachment in tokamak experiments at ASEDX Upgrade (AUG) , Alcator C - Mod, D-II-D and JET [169], [171], [172]. Similar impurity species are also predicted to be used in the future demonstration fusion power plant DEMO [173], [174]. Not only will the seeded impurity enhance radiation, but it also introduces a new sputtering species, with the impurities likely to be at a larger mass than the hydrogenic/helium ions already present in the reactor. Sputtering of PFCs due to the presence of impurities is therefore of a concern, as limiting the concentration of sputtered wall material is desired for long pulse operations of fusion plasma [175].

With W the proposed choice for the divertor materials in ITER, it is likely that He ash exhausted from the core plasma can produce fuzzy W formation as a result of the temperature and ion energy ranges predicted in these regions [33]. Here there will be a number of different species (H, N_2, Ne, Ar) in addition to He, and it is possible that these species may reduce the thickness of fuzz produced due to sputtering. It has has been shown by Nishijima *et al.* [71] that fuzzy W surfaces generally have a reduced sputtering yield relative to pristine W . In [71], pre-prepared fuzzy W surfaces were exposed to Ar plasma, and the mass loss was recorded giving an experimental fuzzy yield. However, there has been little to no research investigating the effects of mixtures of He + impurity plasma on W surfaces, with fuzzy W growing at the same time as sputtering is occuring. In ITER, fluxes of He and impurity species will be incident at the same to W plasma facing components, thus a study showing the effects of mixed He/impurity plasma effects on W would be useful in predictions for ITER's divertor.

In this chapter, He discharges mixed with different gas impurities (N_2, Ne or Ar) are exposed to W surfaces within the linear plasma device NAGDIS II. As was described in chapter 3.17, NAGDIS II is a device capable of re-producing the plasma densities expected for the ITER divertor, so the results obtained from this study will have a relevance for nuclear fusion research. The impurity levels were set at 5, 7.5 and 10 %, with bombarding ion energies maintained at 60 eV and W surface temperatures in the range 1320 to 1550 K. The surface temperatures, ion energies and impurity chosen were chosen to be consistent with those expected for the ITER divertor [33], [169]. After plasma irradiation within NAGDIS II, surface analysis of the fuzzy W layers is used to analyse the effect of the impurity and ion fluence on the fuzz growth, namely the surface morphologies produced, equilibrium thicknesses, the rate of sputtering of samples, their porosity and optical reflectivity.

5.2 Experimental Method

The plasma experiment and tools used to analyse the exposed W samples are described below.

The Plasma Rig

The experiments in this chapter were conducted using the linear magnetized plasma device NAGDIS-II described earlier in section 3.4.1. Langmuir probe measurements revealed typical electron density and temperature values of $\sim 10^{19}$ m^{-3} and ~ 5 eV respectively. Square sheets of W (purity 99. 95 % supplied by PLANSEE) with sides of 10 mm length and 0.2 mm thick were suspended on a conducting rod ~ 1.4 m downstream of the plasma source, with their surfaces orientated perpendicular to the magnetic field lines. W samples were biased negatively, using a DC power supply, to maintain an incident ion energy of 60 eV, taking into account the plasma potential (+ 5 V)

During the plasma exposure, the surface temperatures (T_s) were measured to be in the range 1320 - 1550 K using an infra-red pyrometer (KTL-PRO) sensitive to 1.6 μm wavelengths. The incident ion flux was calculated to be in the range of 2.5 x 10^{21} to 2 x 10^{22} and over the time intervals used in this study, He + impurity fluences corresponded to 2 x 10^{25} to 2 x 10^{27} m^{-2}. The base pressure of the system was of the order 1 x 10^{-5} Pa maintained by two turbo molecular pumps (TG 200M Osaka Vacuum Ltd), backed by rotary pumps and measured by a capacitance monometer gauge (Type 627 MKS Instruments). The He gas was supplied to the source region, whilst the impurity species of N_2, Ar or Ne were introduced at the far end of the device. With low base pressures and operating pressures between 0.6 - 0.7 Pa, any background impurity (residual air) could be ignored when considering the composition of the plasma species. To fix the percentage levels (i.e 5, 7.5 and 10 %) of the chosen impurities, He gas was first introduced into the system to a known pressure. Shortly afterwards the impurity gas was added until the required pressure increase was reached indicating the desired quantities of each in the system. In each case where a impurity percentage was estimated, the ionisation energy for each gas present in the plasma was not accounted for in the results of the ion flux or fluence. This may lead to an under estimation of the species percentage within the plasma; the first ionisation energies of Ne (22 eV [176]), Ar (16 eV [177]) and N_2 (47 eV [178]) all different to He (25 eV [179]), implying a different rate of ionisation may occur for each gas species mixture. The ratio of impurity (Ne, N_2, Ar) ions will not equal the impurity/He ration due to Penning ionisation of impurity species via He metastable states [180], [181].

Surface Imaging Analysis

After He plasma irradiation inside NAGDIS II, the fuzzy W layers were imaged using an SEM (JEOL 7001F Schottky field emission SEM). A thickness measurement was made for each layer by first mechanically fracturing each sample, allowing the cross section of the sample to be viewed. An average of 100 thickness measurements was taken, with

the specified error equivalent to twice the standard deviation. Optical reflectivity was measured for each W fuzz sample using the USB2000 + spectrometer (Ocean Optics) and corresponding DH-2000-BAL deuterium halogen light source, described in section 4.14. The measurement of the reflectivity at a wavelength of 632.8 nm was taken for the comparison between fuzzy W samples.

Mass loss Measurements and Determination of Sputter Yields

With the presence of impurity in the He plasma, and the ion energy range that was chosen for the experiments (60 eV), some level of sputtering of the W samples during plasma exposure was expected. To quantify this, mass measurements were made pre and post plasma irradiation using an A & D Co. BM-22 microbalance, with a precision of 1 μg. The mass of each W sample was recorded 20 times (both pre and post irradiation) and from this an average mass loss value Δm was found. Based on this mass loss Δm, the sputter yield Y_{fuzz} of a fuzzy W surface due to He-impurity plasma irradiation was calculated using the equation given in [21],

$$Y_{fuzz} = \frac{\Delta m}{A \Phi m_w} \tag{5.1}$$

where A is the area of the sample, Φ is the fluence of particles to the sample surface and m_w is the mass of a W atom.

Sample porosity measurements

The porosity of plasma exposed fuzzy W samples was calculated using a similar technique to that given by Doerner *et al.* in [105], [182]. In their method the surface fuzz is removed by wiping the surface, the resultant mass loss and volume of the removed layer are then calculated. The mass measurements were made using a XS205DU analytical balance manufactured by Mettler Toledo with a precision of 10 μg. In each case the mass of the sample was measured 10 times before and after the fuzzy W layer was removed. Fuzzy layers were removed by wiping with a paper cloth, and SEM imaging was used to show the layer of fuzz had been removed. Explicitly the porosity of the fuzzy layer p_{fuzz} is given as [71],

$$p_{fuzz} = 1 - \frac{\Delta m_{fuzz}}{\rho_w V_{fuzz}} \tag{5.2}$$

where, Δ m_{fuzz} is the measured mass difference between the fuzz removal, ρ_w bulk W density and V_{fuzz} is the volume of fuzz removed.

Analytical Model Describing Fuzzy Tungsten Growth In Erosive Plasmas

In the absence of any surface erosion the thickness h of the growing fuzzy W layer can be described by equation 2.2, which is reproduced here,

$$\mathrm{h}(\Phi) = (\mathrm{C}(\Phi - \Phi_0))^{1/2}$$

where C is a temperature dependent constant, Φ is the ion fluence, and Φ_0 is the incubation fluence. In the presence of impurity ions in the plasma or very high He bombarding energies, the fuzzy layer thickness can be reduced by physical sputtering. In this case, equation 2.2 is modified by inclusion of the erosion parameter ϵ_{fuzz} to give equation 2.3, which is rewritten here,

$$\mathrm{h}(\Phi) = \frac{\mathrm{C}}{2\epsilon_{\mathrm{fuzz}}}\Big(W\big[-\exp\big(-\frac{2\epsilon_{\mathrm{fuzz}}^2}{\mathrm{C}}(\Phi - \Phi_0) - 1\big)\big] + 1\Big)$$

where W is the Lambert function and ϵ_{fuzz} is an erosion parameter. The erosion parameter ϵ_{fuzz} is related to the sputter yield of the fuzzy surface $\mathrm{Y_{fuzz}}$ by [38],

$$\epsilon_{\mathrm{fuzz}} = \frac{\mathrm{Y_{fuzz}} \mathrm{m_W}}{\rho_{\mathrm{W}}(1 - p_{\mathrm{fuzz}})} \tag{5.3}$$

where $\mathrm{m_W}$ and ρ_{W} are the atomic mass and density of bulk W respectively and p is the fuzz layer porosity. Inspection of equation 5.4 and using the properties of the Lambert function [70] shows that for ever-increasing fluences ($\Phi \rightarrow \infty$) the fuzz layer thickness tends to a limiting value of $\mathrm{h}\ (\Phi) \rightarrow \mathrm{C}/2\epsilon_{\mathrm{fuzz}}$. This value can be calculated and indicates an estimation for the equilibrium thickness ($\mathrm{h_{eq}}$) of fuzz, a stage in the formation of fuzzy W where the growth and erosion rates are equal. In [38] the equations to calculate $\mathrm{h_{eq}}$ are given as,

$$\mathrm{h_{eq}} = \mathrm{C}\left(\frac{\rho_{\mathrm{w}}(1 - p_{\mathrm{fuzz}})}{2\mathrm{m_w Y_{fuzz}}}\right) \tag{5.4}$$

$$\mathrm{h_{eq}} = \mathrm{C}\left(\frac{\rho_{\mathrm{w}}}{2\mathrm{m_w Y_{bulk}}}\right) \tag{5.5}$$

5.3 Results and Discussion

A series of experiments have been performed in which W surfaces were exposed to He + impurity plasma bombardment for a variation of operation conditions. These were discharges containing He and small concentrations (5, 7.5 and 10 %) of Ne, Ar, N_2. The typical sample temperatures (T_s) were in the range 1320 to 1550 K, with incident ion energies of 60 eV, and the operating pressure in the range 0.6 - 0.7 Pa. Samples were exposed to He + impurity plasmas for a increasing amounts of time, providing ion fluence (Φ) ranges of 5 x 10^{24} to 2 x 10m^{27} m^{-2}. After plasma exposure, the samples were analysed by SEM to provide fuzz thickness measurements (h) and images of the surface morphologies produced. In addition to the surface microscopy, mass loss, optical reflectivity and porosity measurements were made.

5.3.1 Surface Morphologies

Initially, ten samples of W were exposed to He + impurity plasma within NAGDIS II to an ion fluence of $\sim$ 3 x 10^{25} m^{-2}, for increasing percentages of impurity (from 5 - 10%). The ion energies and surface temperatures used were as described earlier in the experimental method. In figure 5.1, the cross-sectional thickness (top row) and surface morphologies (bottom row) are imaged for W surfaces exposed to plasmas containing 100 % He (a) & e)), 95 % He + 5 % Ne (b) & f)), 95 % He + 5 % N_2 (c) & g)), and 95 % He + 5 % Ar (d) & h)). Where the surface morphologies (bottom row of 5.1) are imaged, samples were tilted to 45° from the surface normal.

It is clear from the images that with the introduction of a small amount of impurity into the He plasma, the thickness of the fuzzy W layer is reduced. A factor of 3 reduction in the thickness was observed for all three impurities (Ne, N_2 and Ar) compared to the case of pure He irradiation. There are also some changes in morphology observed, for instance with 5 % of Ne impurity where the surface structures appear to be more cone-like than tendril, as already reported in [160]. The effect of impurity on fuzzy W growth can be seen more readily for higher concentrations of impurity as shown in figure 5.2 for the same exposure parameters as in figure 5.1. The cross sectional and tilted images reveal that 10 % impurity level fuzzy W growth can be impeded if not almost terminated for higher atomic mass gases. The data obtained from the images in figure 5.1 and 5.2 is summarised in Table 5.1. The results and discussion will follow after the next page.

To understand the trends in table 5.1 it is was useful to measure the mass loss of each sample after irradiation, indicating the level of material erosion due to physical sputtering. Figure 5.3 shows the mass loss for the nine different combinations of impurity species and their concentrations, for a fluence of $\sim$ 5 x 10^{25} m^{-2} and ion energy of 60 eV. The mass loss of the sample is seen to increase with increasing impurity atomic mass and concentration demonstrating that sputtering is most likely the cause. Figure 5.3 also demonstrates a near linear dependency between the mass and impurity concentration and implies, from an extrapolation of the data back to the x-axis (level of impurity %) that there may

Table 5.1: A summary of W fuzz thicknesses and type of surface morphology produced for each different impurity species type and relative concentration.

	Impurity % Concentration			
Impurity Species Type	5%	7.5%	10%	100%
Ne	0.74 ± 0.08 μm	0.78 ± 0.12 μm	0.75 ± 0.09 μm	N/A
N_2	0.75 ± 0.05 μm	0.49 ± 0.12 μm	0.31 ± 0.12 μm	N/A
Ar	0.59 ± 0.09 μm	$\sim$ 0 μm	$\sim$ 0 μm	N/A
He	N/A	N/A	N/A	1.96 ± 0.43 μm

be a threshold impurity level below which erosion does not occur. It was observed that where the highest percentage of impurity was used (10%), W surfaces treated with N_2 and Ar had little fuzzy nanostructure growth on the surface, and still remained to the naked eye reflective. It was beneficial therefore to quantify the reflectivity of each surface to investigate this. Figure 5.4 shows the measured percentage reflectivity over a range of ion fluence, impurity species type and relative abundance in the plasma. There is little variation over the range of parameters, with most fuzzy W samples showing 1 - 2 % of reflectivity, agreeing well with previous reflectivity measurements for fuzzy W layers of similar thicknesses [46], [65], [98]. However, surfaces experiencing the highest mass loss (plasmas with 10% of N_2 and Ar impurities) and little fuzz growth were significantly more reflective (8 - 16 %).

5.3.2 Measured Sputtering Yields

A further ten W samples were exposed to 90 % He + 5 % impurity (N_2 and Ne) discharges inside NAGDIS II, with the exposure times increased gradually for each sample to produce a range of fluences of exposure (between x 10^{25} - 10^{27} m^{-2}). The ion energy was maintained at 60 eV, and T_s was measured to be in the range 1320 - 1465 K. Each sample was analysed using the SEM to determine the thickness of fuzz that had grown on each surface.

It has been shown in various studies [71], [72], [122] that fuzzy W surfaces produce a lower sputtering yield than pristine W surfaces (i.e. surfaces where no fuzz is present). Here it is investigated whether the fuzzy surfaces produced with 5 % of impurity (N_2 and Ne) exhibit the same lower sputtering yields compared to pristine surfaces. The bulk sputtering yields for Ne and N on W were given in [131]. In the case of the N_2 impurity species, it is known that molecular sputtering can enhance the sputtering yield of surfaces for low incident ion energies ($<$ 1 keV) [183], [184]. In addition, N_2 plasma has been shown to increase the sputtering yield of Au surfaces up to 4x larger than that predicted for N with ion energies $\sim$ 50 eV [184]. As a similar ion energy (60 eV) is used here, it could be assumed that the yield may be enhanced for sputtering with N_2, therefore bulk sputtering yields for N on W were quadrupled when comparing fuzzy (Y_{fuzz}) and bulk (Y_{bulk}) sputtering yields

In figure 5.5, the values for Y_{fuzz} calculated for each surface with 90 % He + 5 % impurity (N_2 and Ne) discharges are shown against the respective fuzzy W layer thickness. As the sputtering yield is known to decrease with increasing fuzzy W layer thicknesses [71], [72], this seemed an appropriate comparison to make. It is clear from the results that the sputtering yield does decrease as the fuzzy layer thicknesses increases. In addition, on figure 5.5, inset is a plot showing how the ratio of the measured yield Y_{fuzz} and the bulk yields Y_{bulk} (i.e. Y_{fuzz}/Y_{bulk}) decreases as the layer thickness increases. This implies that in this experiment, the fuzzy W surfaces had exhibited lower sputtering yields. This may also be related to the large surface temperatures ($T_s > 1320$ K) measured for each surface.

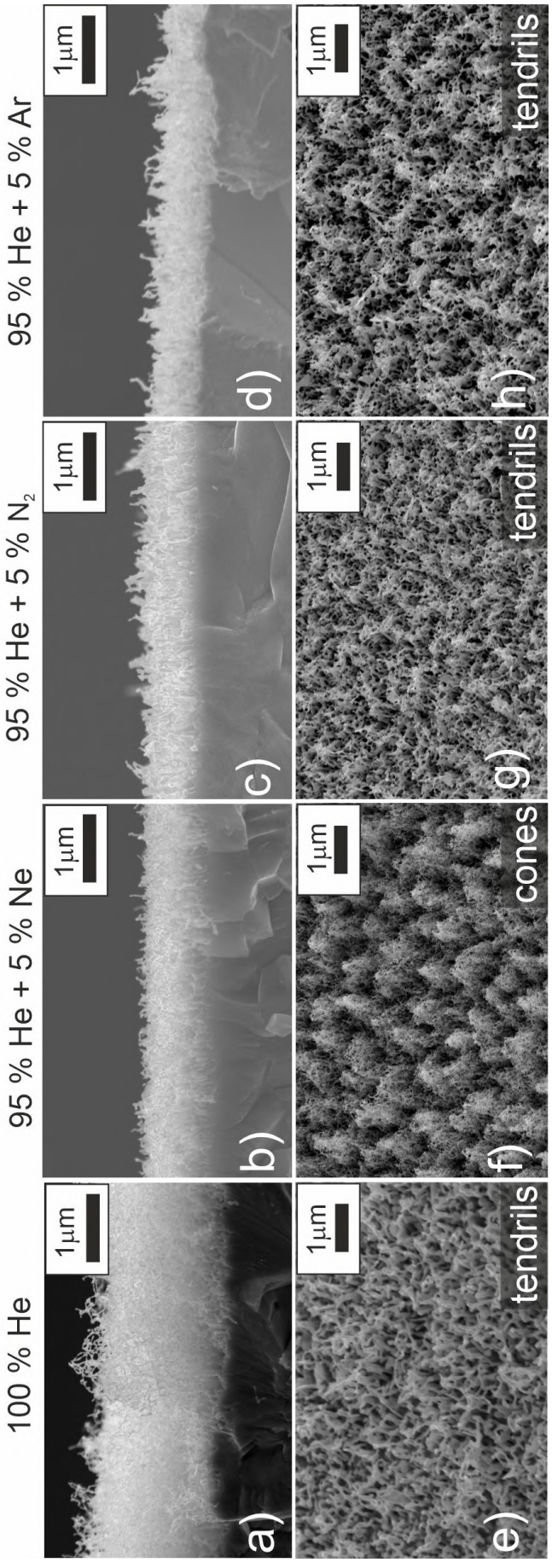

Figure 5.1: Cross-sectional SEM micrographs of irradiated samples (top row) and 45 ° tilted images (bottom row) for plasmas containing a) and e) 100 % He, b) and f) 5 % Ne, c) and g) 5 % N_2, and d) and h) 5 % Ar. The ion bombarding energy was 60 eV and the surface T_s was 1320 K. The ion energy and fluence were 60 eV and $\sim$ 4 x 10^{25} m^{-2} (corresponding to 3600 seconds exposure) respectively.

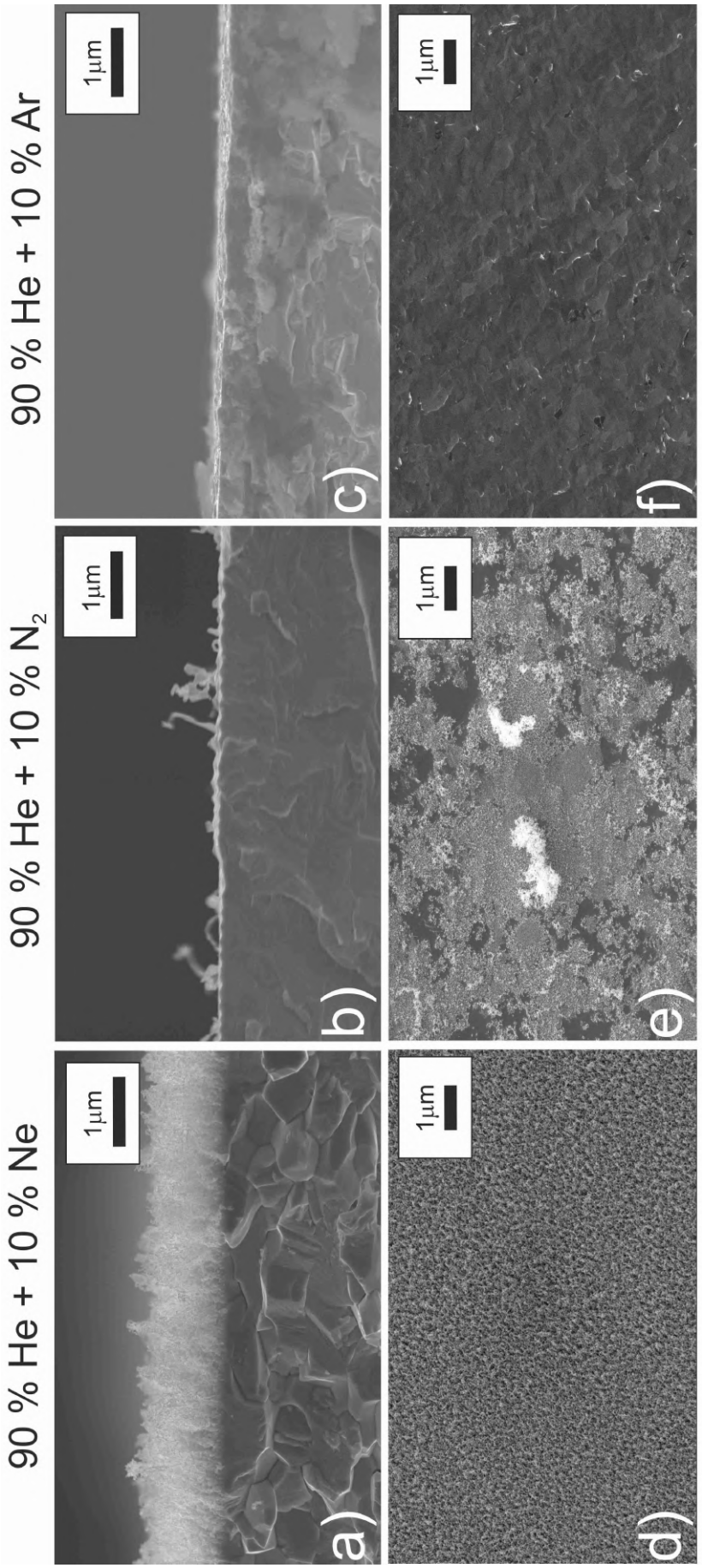

Figure 5.2: SEM micrographs similar to those in figure 2 but for 10% impurity levels. The plasma and sample conditions are the same as for those in figure 5.1.

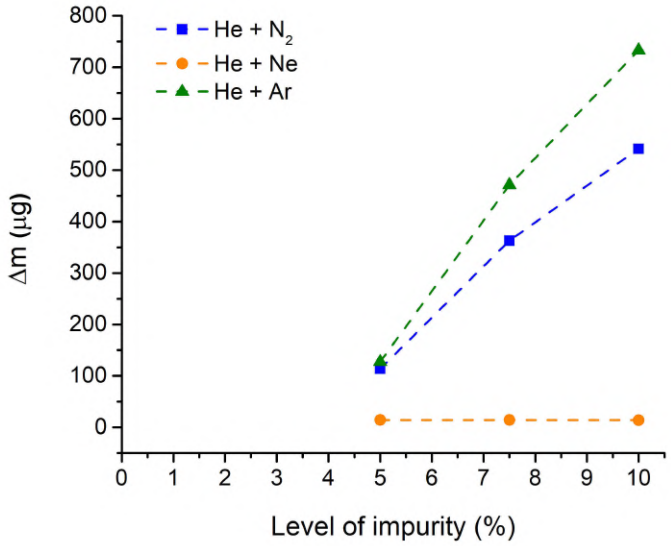

Figure 5.3: A plot of the mass loss Δm versus the relative level of impurity for Ne, N2 and Ar. The bombarding ion energy and fluences were 60 eV and $\sim$ 4 - 8 x 10^{25} m^{-2} (3600 s exposure) with T_s between 1320 - 1465 K. Errors in Δm were fixed at $\sim$ 20 μg for each measurement.

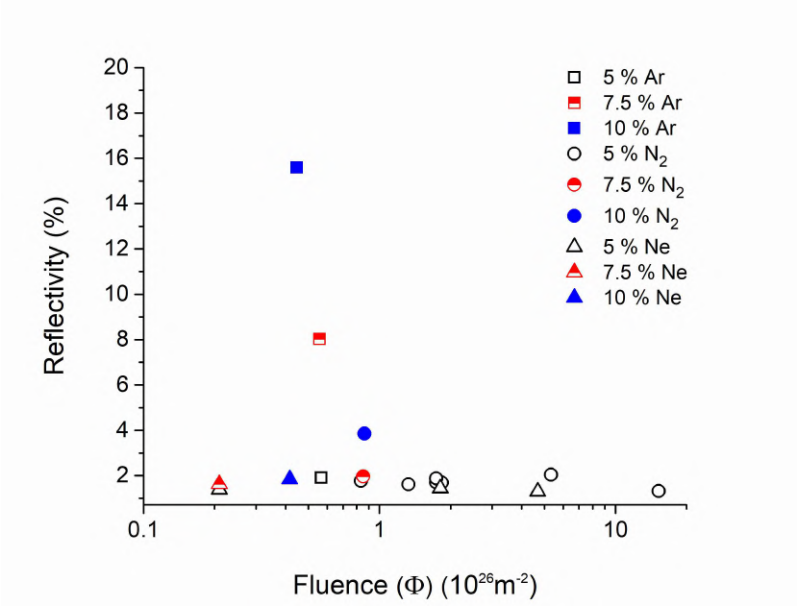

Figure 5.4: Reflectivity measurements for plasma exposed W samples plotted against ion fluence. Each impurity is labelled as circles for N_2, triangles for Ne and squares for Ar.

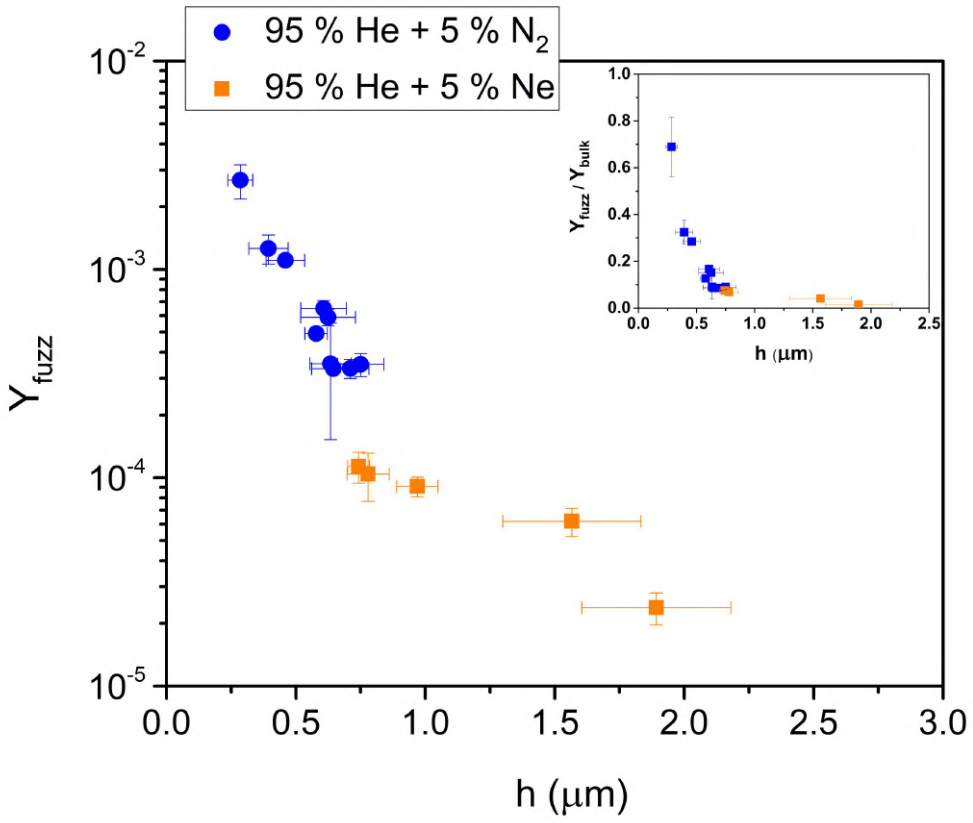

Figure 5.5: The measured sputtering yields against fuzz thickness for 5 % of N_2 and Ne impurity species in the He plasma.

5.3.3 Equilibrium Thickness Measurements from Tungsten surfaces

The fuzzy W layers produced under 95 % + 5% impurity (N_2, Ne) plasma exposures were further analysed for their development of an equilibrium thickness (h_{eq}) of fuzz, a process known to occur due to the balance of growth and erosion in erosive He plasmas [38]. The equations presented in section 5.2 allow predictions for the value of h_{eq} to be made, given certain experimental parameters (p and C) are known.

A 100 % He discharge was used to grow fuzzy W samples and allow the calculation of a temperature constant C at 1465 K; values for C had been previously calculated in the literature to be 0.8 x 10^{37} m^{-2} at T_s = 1320 K. For T_s = 1465 K, W fuzz samples were produced within NAGDIS II with their fuzz thicknesses h measured using SEM and plotted on figure 5.7 as black circles. These values for h were then used with equation 5.2 to calculate a temperature constant C which best represents the data. Previous investigations on NAGDIS II have established an incubation fluence of $\sim$ 4 x 10^{24} m^{-2} is necessary for fuzz formation, so here a similar value (Φ_0) of 5 x 10^{24} m^{-2} was used in the calculation of C. An average of the C values calculated for each value for in a 100 % was made, and C at 1465 K was found to be 1.15 x 10^{-37} m^{-4}. Previously it was thought that at surface temperatures above 1400 K, annealing due to desorption of He may reduce the temperature

Table 5.2: Comparison of temperature constants C calculated at a range of temperatures, available from the literature and found in the current work.

T_s (K)	Temperature Constant C (m^{-4})
1120 [43]	2.64 x 10^{-38}
1320 [43]	8 x 10^{-38}
1465 (current work)	1.15 x 10^{-37}

constant C, however here here the temperature constant C is larger than those previously calculated in the literature (see table 5.2). This increase in the growth rate as the W surface temperature increases has been seen in other studies where fuzzy W layers were measured over increasing surface temperature ranges [43], [44].

Equation 5.2 is represented as the black dashed line on figure 5.7, indicating a good agreement between the fuzzy W thicknesses grown in 100 % He and the predicted trend of growth given by equation 5.2. The porosity of two layers, produced for the largest fluence samples, was measured by removal of the fuzzy layer by wiping the surface clear of of the fuzzy surface. In figure 5.6, the surface is shown with half of its surface wiped off, and cross sectional SEM imaging shows the reduction in the fuzzy layer thickness after removal. It was difficult to confirm that all fuzz was removed during removal, therefore there is a chance that the fuzz layer was merely compressed in some regions, something that has been observed in other studies [105]. After the fuzzy layer was believed to be fully removed, a mass loss of $\sim$ 100 μg and $\sim$ 340 μg was measured for the 5 % N_2 and Ne samples respectively. This corresponded to a porosity of $\sim$ 0.7 for the fuzzy layer produced under 5 % N_2 (h = 0.65 μm), and 0.9 for the fuzzy layer produced under 5 % Ne (h = 1.89 μm).

Now the fuzz thicknesses produced on W samples using He and impurity plasma for a

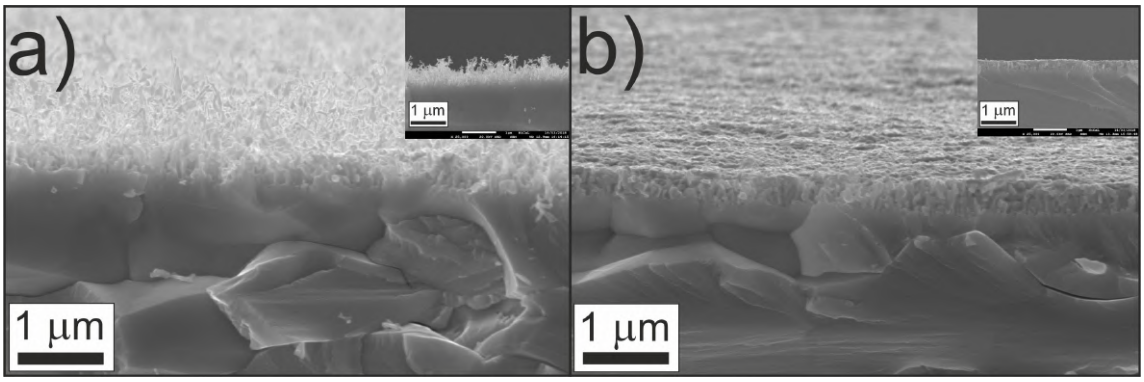

Figure 5.6: SEM images of the fuzzy W surface grown under 95% He + 5% N_2 plasma for an ion fluence of 1.5 x 10^{27} m^{-2}, with the surface before (a) and after (b) removal of the fuzzy layer. Inset is a cross-sectional SEM image of the fuzzy layer pre and post wiping.

range of fluences will be considered. The measurements of each fuzzy layer thickness (h) produced under fluences (Φ) of 95 % He + 5% impurity (N_2 or Ne) are shown in figure 5.3.3. In both cases (N_2 and Ne) the presence of impurity now reduces h relative to the

100 % He case. It is worth noting that the data for 5 % Ne in figure 5.7 were taken at T_s = 1320 K, which would result in a lower temperature constant C, equivalent to 8 x 10^{-38} m^{-4} (calculated using data given in [43]). This lower value of C will in turn mean the expected trend of equation 2.2 at 1320 K will be different, however it was found that the presence of 5 % Ne still results in a lower growth rate of fuzz when this calculation is made.

Comparing the trend of the growth of fuzz for each different impurity in figure 5.3.3, the heavier atomic mass impurity (N_2) leads to lower fuzz growths compared to the lower atomic mass impurity (Ne). Specifically the highest fluence samples for the 5 % Ne and N_2 discharges in figure 5.7 show a reduction in fuzz length of around 3 times from Ne to N_2. It is likely that this is due to an increased sputtering effect of N_2 compared to Ne, and this agrees with the results in figure 5.3 where an enhancement in mass loss was seen when comparing the one hour discharges containing 5 % Ne or N_2. As well as mass effects, the temperature of the surfaces where N_2 was used as the impurity species were sometimes close to 1465 K, which is hotter than the surfaces where Ne was used as the impurity during irradiation. It is has been shown in previous investigations that an increased erosion rate can occur for higher surface temperatures [185], similar effects may have occurred here. Overall, the thickness of fuzzy layers grown in plasma where impurity

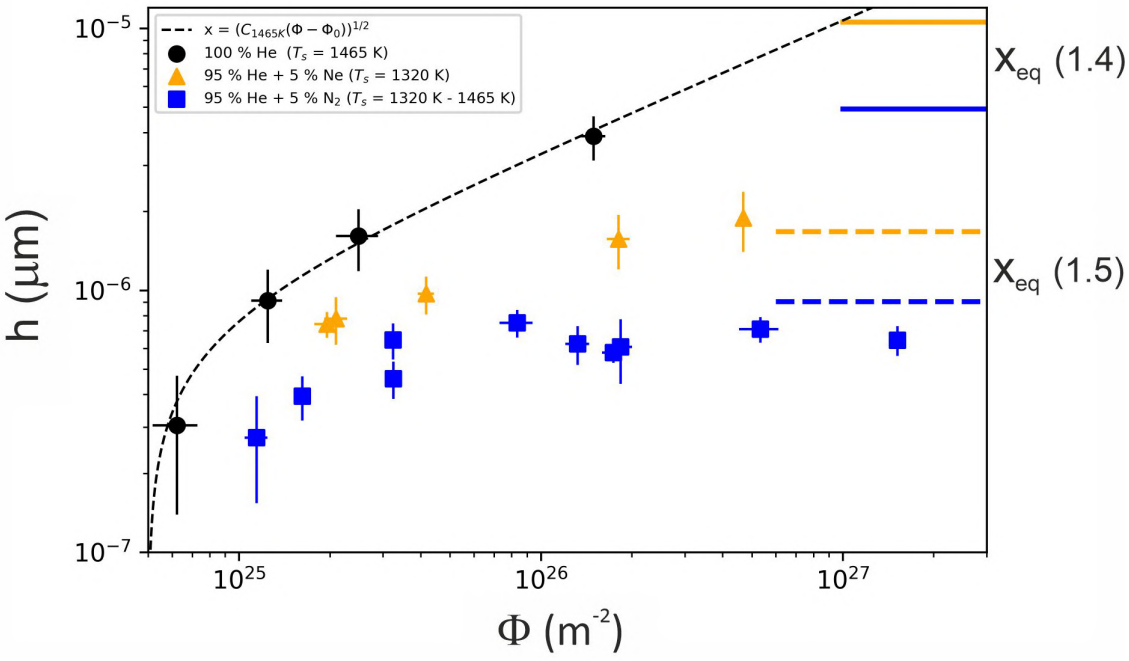

Figure 5.7: The W fuzz thicknesses produced in a 100 % He plasma (black points), 95 % He + 5 % N_2 plasma (blue squares) and 95 % He + 5 % Ne plasma (yellow triangles). The horizontal dashed lines represent the equilibrium thickness calculated using equation 5.5 for N_2 (blue dashed) and Ne (yellow dashed). The horizontal full lines show the results of equation 5.4 using the calculated sputter yield and porosity values for both N_2 and Ne.

is present are reduced relative to the 100 % He case over the fluence range given in figure

5.7.

It is noticeable that the measured fuzz thicknesses are no longer changing as rapidly as fluence increases, particularly in the case of N_2 where the fuzz thicknesses are very similar above 8 x 10^{25}. A balance has been reached between growth and erosion of fuzz, resulting in the equilibrium fuzz growth [38], [63], [69]. In section 5.2, the equations introduced were used to calculate a value for the equilibrium thickness (h_{eq}) based on bulk sputtering yields given in [131] or using calculated values for porosity and sputtering yield using methods described in section 5.2 and 5.2 respectively.

Plotted on figure 5.7 are the values for h_{eq} using equation 5.4 (represented with a horizontal dashed line) and equation 5.5 (plotted as a shorter, full line). Greater agreement between results of the irradiations from NAGDIS II and the predictions of the analytical model is found when bulk sputtering yields are used. In the case of Ne, the sputtering yield (Y_{bulk}) given in [131] was reduced by a factor of three in line with the known discrepancy that exists under low mass projectile species in high flux experiments [186], and taken to be $\sim$ 1 x 10^{-3}. To verify this assumption, a pristine W sample was treated with a pure Ne plasma for an ion fluence of 5 x 10^{24} m^{-2} within NAGDIS II. After the plasma exposure, the mass change of the sample resulted in a sputtering yield of $\sim$ 1.3 x 10^{-3}, a factor of three lower than the theoretical yields predicted in [131], and agreeing well with the findings in [186]. In the case of N_2, it has been shown that molecular sputtering is up to 4x as great on surfaces compared to atomic sputtering, so yields have been adjusted accordingly [184].

The largest discrepancy was seen when using the measured fuzzy sputtering yields and porosity measurements, with predicted x_{eq} values for both N_2 (full blue line) and Ne (full yellow line) are both much greater than the apparent equilibrium thicknesses from the raw data in figure 5.3.3. It has been mentioned in [38] that a better accuracy in the prediction of fuzz thicknesses is found when using bulk yields over measured yields and porosity values, which is seen here.

5.3.4 Nano-Tendril Bundle Growth

On closer inspection of the fuzzy W surfaces produced in NAGDIS II under He + impurity irradiation, larger nanostructures which were different to typical fuzzy W morphologies were observed to have grown. These larger nanostructures did not show any uniformity in their shape or distribution across the surface, but were in some cases as great as 20 times greater thickness ($\sim$ 20 μm) than the typical fuzzy W growth on observed on the surface. These structures appeared to be similar to typical fuzz growth, with tendril diameters equivalent to tens of nm, and resembled similar larger fuzz growths known as nano-tendril bundles (NTBs) reported by Woller *et al.* in [94], [133]. These have subsequently been observed in other studies by Hwangbo *et al.* in [160], [187]. After thorough SEM analysis of the fuzzy W samples was performed, NTB structures were observed to grow on a number of the samples that were imaged. Each W surface which was observed to have produced NTBs are indicated in table 5.3, which provides a full summary of the characteristics (T_s,

h etc) for all the fuzzy W samples produced in this study.

In figure 5.8, examples of NTBs that were formed on W surfaces exposed to He + N_2 plasma are shown through SEM imaging. In figures 5.8 a) - c), the NTBs were produced after treatment with 92 .5 % He + 7.5 % N_2 plasma for an ion fluence of 6 x 10^{25} m^{-2}, and in d) - e) NTBs were formed after exposure to a plasma with 90 % He + 10 % N_2 for an ion fluence 8 x 10^{25} m^{-2}. These surface morphologies are near randomly distributed across the surface, and their average heights are difficult to measure due to the large quantity of NTBs that were observed to form. In figure 5.8 d) and e), two NTBs were found to have average heights of $\sim$ 20 μm, which may not be representative of all NTBs formed under a 90 % He + 10 % N_2 plasma, but it does give an indication of the scale that NTBs can grow to. Typical fuzzy W can grow to 100s of nm to several μm depending on the exposure conditions [43], and given that the fuzzy layer was found to be 311 $\pm$ 120 nm in thickness, the NTBs have a near 50x larger thickness from the surface. Figure 5.9 shows the results of EDX analysis for two regions (labelled in a)) on a He + N_2 sample, with spectrum 1 indicating a normal fuzz region and spectrum 2 indicating a region including an NTB on the surface.

An estimation of the spatial resolution x (μm) provided by EDX analysis is given in [188] to be

$$\mathrm{x} = \frac{0.064\left(\mathrm{E}_0^{3/2} - E_\mathrm{c}^{3/2}\right)}{\rho_\mathrm{w}}$$

where E_0 is the accelerating voltage (keV), the E_c is the critical excitation energy (keV), and ρ_w is the density of the material. The density of fuzzy W layers should also be considered, with fuzzy layer densities having been shown to be as low as 10 % of the bulk [71], therefore the implantation depth may be in fact enhanced relative to bulk W. Assuming this deviation in the density, with the incident electron beam energy at 20 keV the depth the EDX measurement can usually inspect depths of 0.5 - 5 μm. With the fuzzy layer thickness being 0.4 μm for this sample and NTBs having thicknesses from the surface of $\sim$ 8 μm, the penetration depth is sufficient enough to probe the usual fuzz and NTB structures. The results of the analysis show characteristic peaks for W in the spectra (see the inset figure on figure 5.9a)), indicating the two areas consist of an identical chemical composition in the near surface region. Hence the larger structures that resemble NTBs on the surface can reasonably be confirmed as having a very similar elemental composition to W fuzz.

Table 5.3: A summary of W fuzz thicknesses and type of surface morphology produced for each different impurity species type and relative concentration

Gas Mixture	Φ (x 10^{26} m^{-2})	T_s (K)	h (μm)	Y_{fuzz} (x 10^{-4})	NTB
He (95 %) + N_2 (5 %)	0.32 ± 0.04	1320	0.46 ± 0.07	11.1 ± 0.51	Yes
He (95 %) + N_2 (5 %)	1.32 ± 0.12	1320	0.62 ± 0.11	5.90 ± 0.54	Yes
He (95 %) + N_2 (5 %)	1.83 ± 0.16	1320	0.61 ± 0.16	6.50 ± 0.60	Yes
He (95 %) + N_2 (5 %)	0.11 ± 0.01	1465	0.29 ± 0.04	27.61± 5.92	N/A
He (95 %) + N_2 (5 %)	0.16 ± 0.02	1465	0.39 ± 0.08	12.62 ± 2.10	N/A
He (95 %) + N_2 (5 %)	0.32 ± 0.03	1465	0.63 ± 0.08	3.52 ± 0.9	N/A
He (95 %) + N_2 (5 %)	0.73 ± 0.10	1465	0.75 ± 0.09	3.51 ± 0.44	No
He (95 %) + N_2 (5 %)	1.74 ± 0.15	1465	0.58 ± 0.03	4.92 ± 0.25	Yes
He (95 %) + N_2 (5 %)	5.33 ± 0.80	1465	0.71 ± 0.07	3.35 ± 0.31	Yes
He (95 %) + N_2 (5 %)	15.23 ± 1.00	1465	0.65 ± 0.08	3.34± 0.15	No
He (92.5 %) + N_2 (7.5 %)	0.63± 0.62	1465	0.49 ± 0.62	9.84± 0.71	Yes
He (90 %) + N_2 (10 %)	0.83± 0.55	1465	0.31 ± 0.12	15.05 ± 1.84	Yes
He (95 %) + Ne (5 %)	0.19 ± 0.02	1320	0.74 ± 0.16	1.13 ± 0.20	No
He (95 %) + Ne (5 %)	0.21 ± 0.02	1320	0.79 ± 0.08	1.04 ± 0.27	No
He (95 %) + Ne (5 %)	0.42 ± 0.02	1320	0.97 ± 0.08	0.91 ± 0.1	No
He (95 %) + Ne (5 %)	1.81 ± 0.16	1320	1.57 ± 0.46	0.62 ± 0.10	No
He (95 %) + Ne (5 %)	4.67 ± 0.12	1320	1.89 ± 0.48	0.23 ± 0.04	No
He (92.5 %) + Ne (7.5 %)	0.23 ± 0.02	1320	0.77 ± 0.06	1.14 ± 0.21	No
He (90 %) + Ne (10 %)	0.42 ± 0.03	1320	0.92 ± 0.06	0.98 ± 0.07	Yes
He (95 %) + Ar (5 %)	0.36 ± 0.02	1320	0.59 ± 0.08	3.78 ± 0.20	No
He (92.5 %) + Ar (7.5 %)	0.55 ± 0.08	1320	~ 0	N/A	No
He (90 %) + Ar (10 %)	0.44 ± 0.04	1320	~ 0	N/A	No

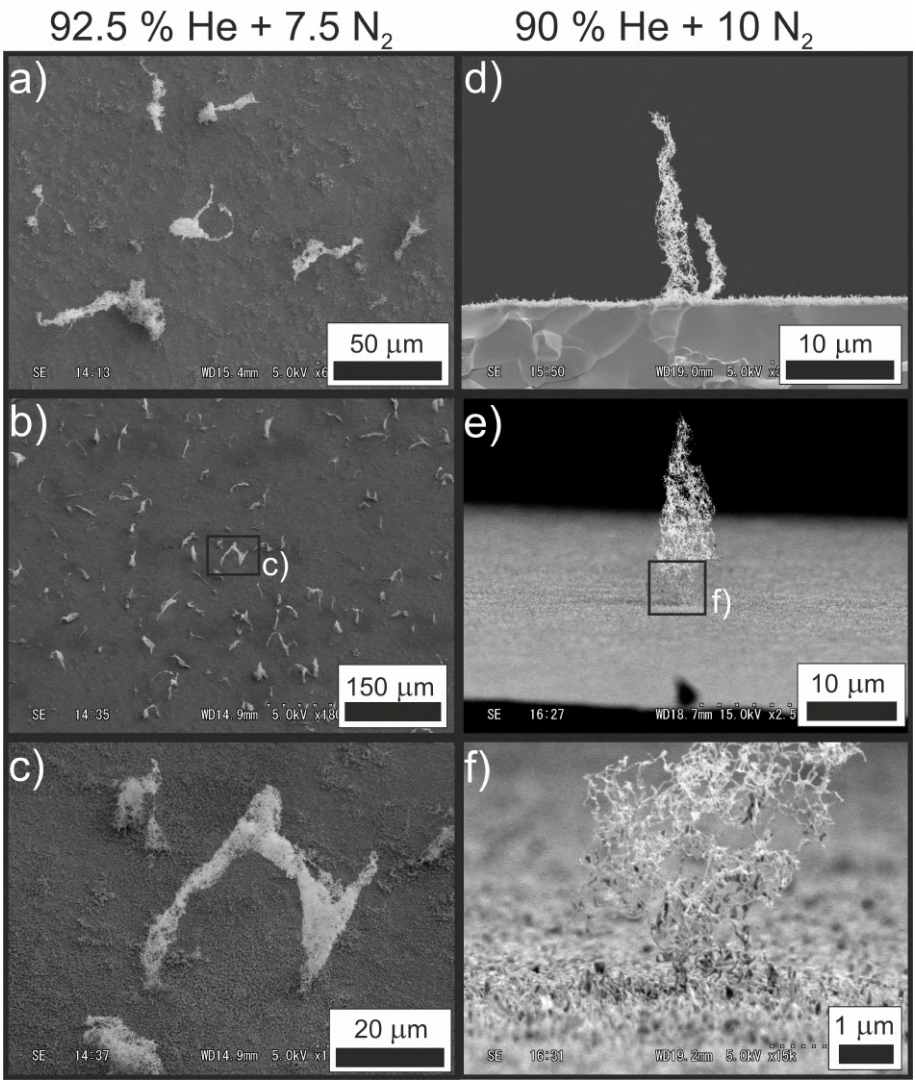

Figure 5.8: Images of NTBs produced on the W surfaces exposed to He + N_2 impurity plasmas. In a), b) and c), NTBs are visible as the whitish areas on the fuzzy surface, with the grey regions representing typical fuzzy W growth. Image c) is an expanded view of the surface shown in b). NTBs are viewed at 90 and $\sim 80°$ to the surface normal, with the cross sectional thickness of the NTBs in the images estimated to be 16 - 21 μm. In f), the base of the NTB in e) is inspected closer, with the SEM imaging showing that NTBs appear to grow out of the surface they form on.

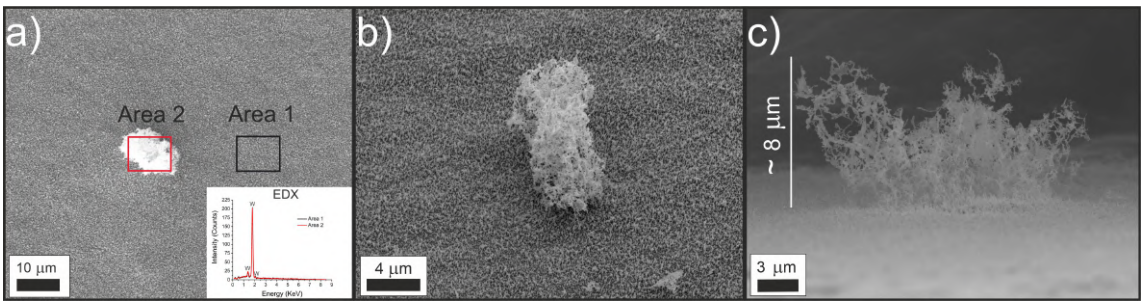

Figure 5.9: Images of an NTB produced on a sample exposed to 95 % He + 5 % N_2 plasma to a total ion fluence of 1.83 x 10^{26} m^{-2}. In a), a top down view of the NTB is shown, in b) the surface was tilted to 45°, and in c) the NTB is viewed at $\sim 90°$ to the surface normal. Inset of a) is an EDX analysis graph showing the fuzzy layer and NTB both consist of elemental W.

5.3.5 Potential Mechanisms of NTB Growth

In the previous reports of "islands" of fuzzy W or NTBs in the literature [94], [132], [133] Woller *et al.* initially observed that NTBs were formed with an RF modulation on the He ion energy, varying between 25 - 100 eV [94]. A subsequent study showed that NTBs were formed at much lower frequencies of ion energy modulation (20 kHz in [133]), implying that RF modulation was not required to produce an NTB, however some variation in the ion energy was needed. In their findings, Woller *et al.* state the impurity % level in their device (the DIONISOS linear plasma experiment [189]) was roughly $\sim$ 0.1 %, and this would be likely to include air impurity (N_2, O_2 etc), which if ionised would be sufficiently energetic enough to produce some level of sputtering. In addition, at the upper limit of the energy range in their study ($\sim$ 100 eV), He ions would roughly have enough energy to sputter a W surface as well. It is clear from the findings in [133], that only when a wider ion energy range distribution (from $\sim$ 20 eV to $\sim$ 100 eV) is used, and He ion energies can actually reach 100 eV, do NTBs form. At a more narrow ion energy range ($\sim$ 50 - 70 eV), NTBs are not formed on the surface, but typical fuzz is formed instead. This indicates that the ion energy is important, and that the higher the ion energy, the more likely NTBs are to form.

In the only other observations of NTB-like structures in the literature made by Al-Ajloni *et al.* in [132], a He ion beam was mixed with increasing percentages (0.01 - 0.5 %) of carbon (C), with fuzz growth observed to be terminated at the higher percentages but small islands of fuzz visible on the surface when 0.01% of C was used. At the ion energies used in their study (300 eV), it is likely that with higher concentrations of C the surface sputtering rate is too large for fuzz to grow, but at lower concentrations some threshold is met where the sputtering of the surface and growth processes involved in fuzz formation balance in some way, to allow pockets of fuzz to form.

In each case of NTB formation in [132] or in [94], [133], larger nanostructures similar to fuzzy W were observed where the condition for the sputtering threshold on W was met by the ion species present in the plasma, and it seems reasonable to assume this could be linked to NTB growth.

In the current study, NTBs have been observed when some impurity is present in the plasma, with impurity ions having sufficient energy (60 eV) to sputter W. It is not yet clear how sputtering of the fuzzy W surface could lead to areas where NTBs are produced, but a possible mechanism was outlined by Hwangbo *et al.* in [160] . As fuzzy W formation is known to have a grain orientation dependency [83], [190] and also reduce the sputtering yield from the surface, it may be that on grains where fuzzy W growth is accelerated relative to other grains, any sputtered material from the surroundings areas could be trapped (in a similar way to the line of sight deposition described in [71]) by fuzz that is already forming. This could perhaps explain the formation and seemingly random distribution of NTBs on the W surfaces in [133] and [160], as the grain orientation of surfaces was not kept constant across the surface according to the experimental information available.

Prompt Redeposition

For the first time prompt redeposition is considered as a possible production mechanism for NTBs. Prompt redeposition is a process where sputtered material can return to the surface in one gyro-radius if the ionisation mean free path (λ_{ion}) is smaller than the Larmor radius (R_{L}). The condition for prompt redeposition ($\mathrm{P_{prompt}}$) given in [191] is,

$$\mathrm{P_{prompt}} = \frac{\lambda_{\mathrm{ion}}}{R_{\mathrm{L}}} = \frac{\mathrm{QB}}{\mathrm{m_w} < \sigma_{ion} v > n_e} \tag{5.6}$$

where Q is the electron charge, B is the magnetic field density, m_W is the mass of a W atom, $< \sigma_{ion} v > n_e$ is an ionising rate coefficient and n_e is the electron density.

In NAGDIS II, the experimental parameters are as follows. The magnetic field B = 0.1 T, typical electron densities n_e are 4.5 x 10^{18} m^{-3}, $< \sigma_{ion} v >$ is an ionizing rate coefficient of 8.81 x 10^{-14} m^3 s^{-1} [192], and Q and m_W are already known. It is found that in NAGDIS II, the ratio is < 1 implying that for these conditions prompt redeposition can occur. However, if the width of the sample surface is much smaller than $\mathrm{R_L}$, in reality the ionised W will not be returned to the surface. The Larmor radius can be calculated using quantities established earlier, as well as the velocity of a sputtered W particle. Assuming that the sputtered particles leaves with an energy equivalent to 1/2 of the binding energy (taken to be 8.68 eV), the velocity of the particles can be estimated to be 2.12 x 10^3 ms^{-1}, giving R_{L} to be ~ 4 cm. As this is larger than the width of the sample, it is unlikely for these particles to be returned to the surface, however lower energy particles ($\sim$ 0.3 eV) would have Larmor radii comparable to the width of the sample. If the sputtered particles have an energy distribution given by the Thomson distribution (described in section 2.2.1, there is a possibility for low energy particles to have small orbits which may permit redeposition. Although the percentage of particles with this energy is likely to be small, it presents a potential mechanism for NTB growth through redeposited W.

Using the conditions predicted for ITER and its divertor regions, with a B field of 11 T, n_e 10^{19} m^{-3}, $<\sigma_{\mathrm{ion}}\mathrm{v}>$ found to be of 4.53 x 10^{-14} m^3 s^{-1}, $\mathrm{p_{prompt}}$ is also found to be less than 1. If redeposition is a precursor for NTB growth then NTBs could feasibly be produced in the areas of the divertor where fuzzy W is likely to grow.

5.3.6 Threshold Conditions for NTB Formation

The work in this chapter contributed toward the findings in the study by Hwangbo et al., and in that study a temperature and sputtering yield window was observed for NTB formation. Specifically, for $\mathrm{T_s}$ in the range 1400 - 1600 K and $\mathrm{Y_{fuzz}}$ between x 10^{-3} - 10^{-2} NTBs were formed after He + impurity exposures. The findings in this chapter show that there is an extension to both ranges of $\mathrm{T_s}$ and $\mathrm{Y_{fuzz}}$ which can produce NTBs. In figure 5.10 the ranges of $\mathrm{T_s}$ which were observed to produce NTBs in NAGDIS II from the study in [160] and the current chapter are shown. Also included is a temperature range observed by Woller et al. that was sufficient to produce NTBs in their experiments [94].

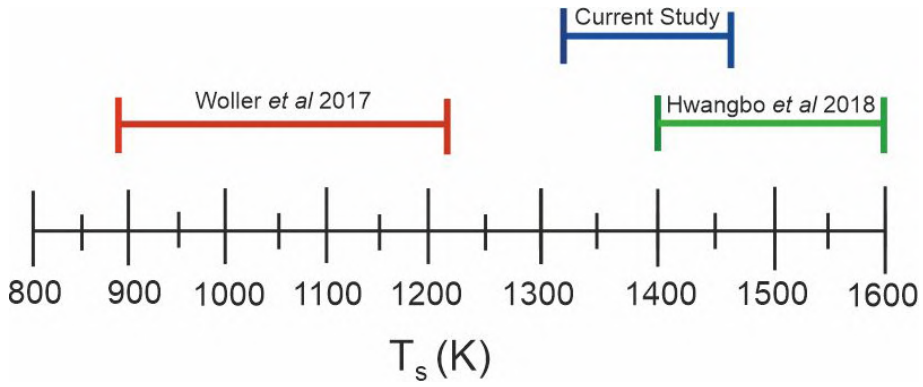

Figure 5.10: Temperature range established for NTB production from the literature [94], [160] and current study.

It can be seen from figure 5.10 that there was a significant difference between the observed temperature range for NTB found in [94], [160]. The study in this current chapter essentially provides a bridge between the two literature temperature ranges for NTB growth, expanding the temperature range for NTB from 870 to 1600 K. In addition, the sputtering yield window for NTB production would now be in the range x 10^{-4} to 10^{-2} by merging the findings summarised in table 5.3 with the work in [160]. This provides new insights into the formation for NTBs on W surfaces.

It should be noted that there was difficulty in decreasing T_s much lower than 1300 K in NAGDIS II. Surface heating is supplied by the plasma, therefore changes to current within the plasma itself would be required, however this would in turn change the flux of particles. A cooling system can be used in NAGDIS II to reduce T_s to temperatures as low as 1200 K, however this wasn't attempted during the experiments. In future experiments it would be useful to probe the apparent gap in the temperature range for which NTBs (in figure 5.10) can be formed.

5.4 Conclusions

In this chapter a systematic study has been carried out to find the effect of impurity species (N_2, Ne and Ar) and their concentrations (5 %, 7.5 % and 10 %) on the growth rates and structures of fuzzy W produced in a high density He linear plasma device (NAGDIS II). It was found that the growth rate of fuzz was reduced for higher impurity atomic masses and higher concentrations. Mass loss measurements showed that for higher percentages of impurity in the He plasma, the heavier species resulted in more sputtering from those surfaces if the fluence was similar during plasma exposure. Surface microscopy revealed for N_2 (5 % and 7.5 %) and Ar (5 %) W fuzz tendrils were seen, and for Ne (5 %, 7.5 % and 10 %) fuzzy W cones were noticed. For 10 % of N_2 the W fuzz surface was sputtered to reveal areas of little to no fuzz growth, and some areas of the surface where He pinholes were visible. For 7.5 % and 10 % of Ar in He, no fuzz was created, indicating heavy sputtering from the impurity source.

For long He plasma exposures (fluences up to 10^{27} m^{-2}), equilibrium thicknesses of fuzz were attained due to the combined effect of fuzz growth and sputter erosion caused by the impurity species in the plasma. The measured equilibrium thicknesses were found to be consistent with an analytical model developed for the simultaneous growth and erosion of fuzz given in [38]. From mass loss measurements the ratios of fuzzy sputter yield to bulk sputter yield (Y_{fuzz}/Y_{bulk}) were determined for each W fuzz sample, where it was found ratios of Y_{fuzz}/Y_{bulk} deg decrease strongly with increasing fuzz thickness. Assuming these impurity gases (N_2, Ne and Ar) will be present in fusion reactors, and with W fuzz likely to be formed, it is seen in this work that heavier species produce lower equilibrium thicknesses. This should be a consideration for the W plasma facing components in future reactors. In addition, as the impurity species for seeding in ITER is not yet confirmed, the results here imply that using Ne would reduce the fuzzy W layer thickness at a slower rate than the other candidate species (N_2 , Ar) which should be beneficial for lower the sputtering yield from W surfaces.

The observations of nano-tendril bundles NTBs have been made through SEM imaging, with comparisons made to previous studies where similar structures were observed. The formation of NTBs have been characterised in terms of their temperature and measured sputter yield ranges, with new insights from this chapter expanding the temperature window from 1320 - 1600 K and sputtering yield in a range from 10^{-4} to 10^{-2}. Two potential mechanisms for NTB growth through line of sight deposition and/or prompt re deposition of sputtered W have been described. In ITER, prompt redeposition fractions will be $\sim$ 50 % during normal operation [175], and close to 99.9 % during high energy transient events [33]. This will lead to a significant return to the surface of any sputtered material. If NTBs are grown due to the coalescence of sputtered W being deposited in a line of sight method with growing tendrils, or through prompt redeposition, sputtered material that is redeposited could possibly lead to NTB or similar larger fuzzy structures if it it reaches areas where fuzzy W grows.

Chapter 6

Enhanced Fuzzy Tungsten Growth in the Presence of Tungsten Deposition

In this chapter, an investigation into the effects of W deposition on the growth rates of fuzzy W was carried out. This chapter included experiments carried out on the linear plasma device NAGDIS II as well as the magnetron sputtering system at the UOL.

6.1 Introduction

In section 2.1.3, the growth law that fuzzy W has been observed to follow was described, with equation 2.1 being recast later by Petty *et al.* in equation 2.2 to incorporate the He ion fluence and an incubation period necessary for fuzzy W to form. In practice, equation 2.2 can be used to predict the thickness of a fuzzy layer given the He ion fluence and surface temperature reached during an experiment. Typically, one would expect for say surface temperatures of 1120 K, He ion energies of 100 eV and fluences of 10^{25} m^2 a W fuzz layer to have grown to a height of h $\sim$ 500 nm [38].

Recently, however, it has been found that fuzzy W can grow at much higher rates than that predicted by equations 2.1 and 2.2 when He ion irradiation is in the presence of W deposition (for example from an external W source) [192]–[194]. This may be important with respect to ITER's operation since a not insignificant flux of ablated or sputtered W is expected to deposit on W first wall components that are meeting the conditions (of temperature, He ion fluence and ion energy) for fuzz to form [33], [195].

To simulate the effects of downstream deposition in a fusion reactor, Kajita *et al.* exposed W samples to deposition flux densities in the range 2.5 x 10^{18} - 1.75 x 10^{19} m^{-2} s^{-1} during fuzz growth in the NAGDIS II linear plasma device [192], [193]. The presence of this auxiliary W source gave rise to super-fast growth rates of fuzz, producing millimeter-scale fuzzy structures on the irradiated W surfaces. The produced W morphologies were given the name Large Fuzzy Nanostructures (LFNs). In their findings, Kajita *et al.* showed that for surface temperatures between 1200 and 1700 K and W deposition flux densities between 2.5 x 10^{18} and 1.75 x 10^{19} m^{-2} s^{-1} LFNs could be formed [192]. In ITER, W

Table 6.1: A comparison of the experimental parameters for the magnetron and NAGDIS II plasma devices, with the expected conditions within the ITER divertor [33], [195] also included.

Device	T (K)	E_{ion} (eV)	Γ_{He} (m^{-2} s^{-1})	Γ_w (m^{-2} s^{-1})
Uol Magnetron	1050 - 1150	80 - 100	1 x 10^{20}	3.0 - 9.4 x 10^{17}
NAGDIS II	1200 - 1220	70	5 x 10^{21}	~ 0
ITER	300 - 1200	1 - 100	$\sim 10^{21}$	0.4 - 1.1 x 10^{18}

deposition flux densities (at W plasma facing surfaces) are predicted to be around 0.4 to 1.1 x $10^{18} m^{-2}$ s^{-1} [195]. Despite these values being slightly lower than those used in [192]–[194] to observe LFN production, one may expect some enhancement in fuzz growth in ITER due to W deposition.

In this chapter, the magnetron sputtering system is used to deposit W atoms at a controlled rate on to W samples as they transition to fuzzy W. The surface temperatures, He ion energies and W flux densities were chosen to be relevant to those expected at the ITER divertor [33], [195], which gives results here a relevance to the future operation for ITER. During experiments He ion fluences produced in the magnetron were in the range of 4 x 10^{23} – 1 x 10^{25} m^{-2}. The magnetron grown fuzzy W surfaces were then compared and contrasted with those produced in a deposition-free environment of the linear plasma device NAGDIS II (across a similar ion fluence range). Surfaces of Mo were also exposed within the magnetron to investigate whether a similar enhancement in fuzzy Mo growth could be observed. For this investigation the magnetron target was equipped with an Mo target.

6.2 Experimental Method

In this study, fuzzy W samples were grown in two plasma systems, a magnetron sputtering source at the University of Liverpool and a magnetized linear plasma device (NAGDIS II) at Nagoya University. Both systems sustain DC He plasmas as a source of ion irradiation; however the magnetron, by its nature, is equipped with a metal target cathode, capable of providing an auxiliary source of sputtered atoms for in situ deposition on the growing fuzzy layer. Most of the results in this chapter are relevant to W, however a Mo target was also used in cases where fuzzy Mo was produced.

The fuzzy W samples produced in NAGDIS II were considered to be deposition-free during their formation. A summary of the operational parameters (He ion flux density Γ_{He}, W atom flux density Γ_w, He ion energies E_{ion} and surface temperatures T_s) of the magnetron and NAGDIS II systems (as well as those predicted for the ITER divertor) are shown in table 6.1.

Magnetron Sputtering Device

The magnetron sputtering system consisted of a V-Tech^{TM} 150 unbalanced planar magnetron source, described earlier in section 3.1.1. For the purposes of this investigation, the magnetron was equipped with a 6" diameter x 0.25" thick W (purity 99.95 %) or Mo (purity 99.95 %) target for sputter deposition. Through manipulation of a butterfly valve situated between the chamber and the pumping system the base pressure could be raised from 6.67 x 10^{-4} to 5.33 x 10^{-3} Pa. During plasma operation the DC plasma power was maintained at 700 W.

Discs (10 mm diameter and 1 mm thickness) used to grow fuzzy nanostructures were W and Mo (99.95 % purity) and supplied by Future Alloys. Each disc was positioned on the centre line of the system, 97 mm downstream from (and facing) the magnetron target, held in place by the sample holder described in section 3.1.3. The samples were electrically biased (by a DC power supply) to provide ion bombarding energies between 80 and 100 eV. The sample temperatures were measured using an IR pyrometer (Micro-Epsilon UK Ltd, wavelength = 2.3 μm) situated outside the vessel and viewed via a vacuum window, with the emissivity of the W samples determined to be 0.28 $\pm$ 0.02. This resulted in an error of $\pm$ 10 K in surface temperature readings.

Langmuir probe measurements in the magnetron system were shown in section 4.1, and at the chosen operating chamber pressure (2.67 Pa) and discharge power (700 W) used in this investigation the electron density and temperature were 5 x 10^{15} m^{-3} and $\sim$ 7 eV respectively. From ion saturation current measurements with the probe it was determined that over the ion energy range used in this chapter the He flux density (Γ_{He}) was of the order 1 x 10^{20} m^2 s^1. With plasma - sample exposure times up to 23 hours, He ion fluences Φ_{He} up to 10^{25} m^2 were achieved.

NAGDIS II

The linear magnetized plasma device NAGDIS-II (NAGoya DIvertor Simulator) was used to produce fuzzy W samples in a deposition-free environment [196]. The device has been described in section 3.4.1, and here the relevant details for the experiments carried out in this chapter will be given.

The plasma operating pressure was chosen to be 0.67 Pa, regulated using a mass flow controller (HORIBA STEC), and measured using a capacitance manometer gauge (Type 627 MKS Instruments) located in the downstream region of the sample position. Square W samples (purity 99.95%) with sides of 10 mm length and 0.2 mm thickness were suspended on a conducting rod 1.4 m downstream of the plasma source, with the normal to their surfaces orientated parallel to the magnetic field lines. Samples were biased negatively, using a DC power supply, to maintain incident ion energies of 70 eV. The plasma itself (through particle bombardment) was used to heat the W samples in the range 1200 - 1220 K. The surface temperatures were measured using an infra-red pyrometer (KTL-PRO), sensitive to 1.6 μm wavelengths.

Langmuir probe measurements close to the sample position had revealed typical electron density and temperature values of 7 x 10^{17} m^3 and $\sim$ 5 eV respectively, providing incident He ion flux densities (Γ_{He}) of 4.7 x 10^{21} m^2 s^1. Over plasma - sample exposure times of tens of minutes, He ion fluences of 3 x 10^{24} - 1 x 10^{25} m^{-2} were produced.

Residual Gas Analysis (on the magnetron system)

A residual gas analysis (RGA), performed using the Optix spectrometer (described in section 4.2), allowed the identification of impurity species type inside the magnetron vacuum chamber, for a variation of base pressures from 6.67 x 10^{-4} to 5.33 x 10^{-3} Pa. The technique is based on the production of an optical emission spectrum using a remote plasma discharge. Spectra were obtained at each base pressure in the vacuum chamber (shown in figure 4.6) prior to operation of the magnetron plasma.

Deposition Rate Measurements (in the magnetron system)

To obtain the deposition rate of sputtered material from the magnetron target during plasma operation, a quartz crystal microbalance (QCM) with a gold foil was used. The results measured by the QCM were summarised in section 4.3 for both W and Mo targets inside the magnetron sputtering system. When a W target was used, the data yielded deposition rates for the two different base pressures chosen in the study. In the low density DC magnetron, it is assumed that the deposition flux consisted mostly of sputtered W atoms, with a low proportion of plasma post-ionized metal species [197]–[199]. Ionized impurity air species in the plasma are deemed to be responsible for the sputtering of the W magnetron target, since sputter rates due to He bombardment are known to be very low [131].

Fuzzy Tungsten Surface Microscopy and Analysis

Surface analysis was performed on W fuzz samples using a FEI Helios Nanolab 600i focused ion beam scanning electron microscope (FIB-SEM) (described in section 3.3.3). A Ga ion beam milled and polished surface cross-sections, which were then imaged and measured to obtain fuzzy layer thicknesses. For each sample, protective coating layers of platinum were first deposited on the fuzzy surface and then length cross-sections of approximately 30 μm were milled out. Each FIB-SEM cross sectional image was taken at a tilt of 52° so to read exact lengths, image scale bars should be multiplied by a factor of $1/\sin(52°)$.

To gain high-resolution information of the fuzzy structures, a lamella for S/TEM analysis was prepared using FIB milling and analysed using a JEOL 2100F Cs-corrected (200 kV) analytical FEG scanning/transmission electron microscope (S/TEM). Crystallographic information was obtained through selected area electron diffraction (SAED) and coupled with imaging by TEM, bright-field (BF) STEM and high-angle annular dark-field (HAADF) STEM. The optical reflectivity was measured for each W fuzz sample using the USB2000

+ spectrometer (Ocean Optics) and corresponding DH-2000-BAL deuterium halogen light source, as described in section 3.3.6. The measurement of the reflectivity at a wavelength of 632.8 nm was used for the comparison between fuzzy W and Mo samples.

6.3 Results and Discussion

In figure 6.1, a summary of the deposition rate measurements shown in figure 4.8 for a W target with a neutral pressure of 2.67 Pa and plasma power of 700 W is presented. Figure 6.1 shows the thickness of W thin films produced in the system at these experimental conditions for the two different base pressures (6.67 x 10^{-4} and 5.33 x 10^{-4} Pa) as a function of time (for a 45 minute exposure). For these plots, deposition rates of 17 $\pm$ 5 nm/hr and 54 $\pm$ 4 nm/hr were calculated respectively. Since the plasma operating pressure was the same in each case, the three-fold increase in deposition rate at the higher backing pressure can be attributed to extra sputtering of the magnetron target due to an increased concentration of heavy air impurities.

In section 4.2, an RGA was performed in the magnetron sputtering system. The results of this investigation showed that as the butterfly valve was operated, the main impurity species identified were those derived from air (e.g. N_2, O, O_2, H and OH) (see figure 4.6). With an increased base pressure, the main N_2, O and O_2 peaks increased in intensity by five or six times. These species are considered the main species that can sputter the magnetron target

To allow clear comparison with the deposition conditions expected in ITER (see table 6.1), these deposition rates were converted to a W atom bombarding flux density, Γ_w, assuming a thin film density of 19,250 kg m^{-3} corresponding to a fully dense coating. It has been shown in previous reports that thin films of W produced by DC magnetron sputtering can have densities which are a few percent less than the density of bulk W [199], [200]. In the calculation of Γ_w the small difference between bulk and thin film densities was ignored, and the deposited W layers produced on the QCM were assumed to have densities consistent with bulk W.

In figure 6.1, the W atom fluence is also plotted, equivalent to the product of Γ_w and the measurement time in seconds. For the two base-pressure cases used in the magnetron system, the flux of W deposition was found to be Γ_w = 3.0 x 10^{17} m^{-2} s^{-1} and 9.4 x 10^{17} m^{-2} s^{-1} respectively. These values are less than 1 % of the bombarding He ion flux Γ_{He} ($\sim$ 1 x 10^{20} m^{-2} s^{-1}), yielding effective W atom-to-He ion arrival rate ratios Γ_w/Γ_{He} of 0.003 to 0.009. To confirm the QCM results, W samples were weighted before and after W deposition, allowing a calculation of the deposition rate to each sample to be made. It was found that from the mass increase measured for each sample, a deposition rate consistent with the QCM measurements was made to these W samples during the plasma exposure. The measurements of the samples masses are included in table B.1 in appendix B .

To compare fuzzy structures grown in deposition and non-deposition conditions, a combination of four SEM images of fuzzy layers produced in the magnetron and NAGDIS II

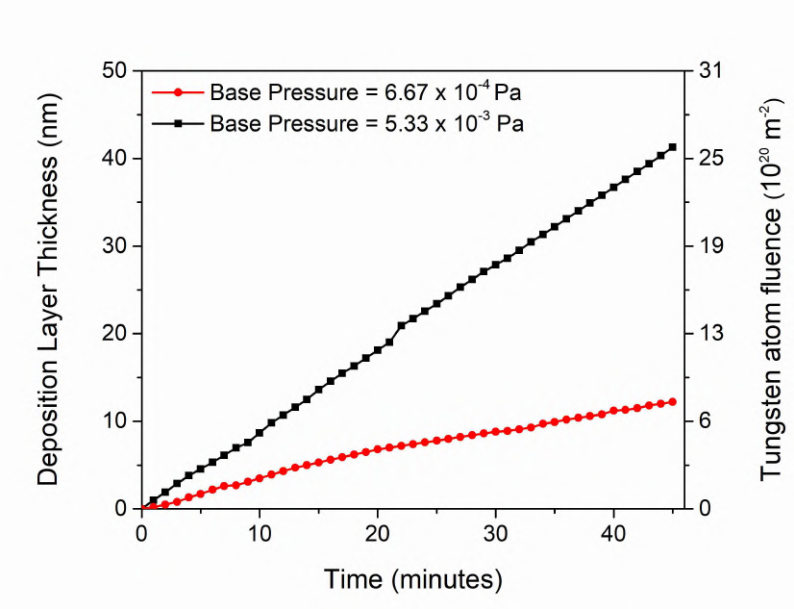

Figure 6.1: A plot of the W deposition thicknesses and corresponding W atom fluences versus time at the two chosen base pressures for an operating pressure of 2.67 Pa and plasma power of 700 W. In calculating the W atom fluence a thin film density of 19,250 kg m^{-3}, corresponding to a fully dense coating of W, was assumed.

for two different He ion fluences ($\Phi_{He} \sim 3$ x 10^{24} m^{-2} and ~ 6 x 10^{24} m^{-2}) and W flux densities ($\Gamma_w = 0$ and 9.4 x 10^{17} m^{-2} s^1) are displayed in figure 6.2. The ion bombarding energies and surface temperatures were similar across the different experiments, being 70 eV and 1200 - 1220 K in the NAGDIS II and 80 eV and 1150 K in the magnetron system. It is clear from the images that a substantially thicker fuzzy layer is produced in the depositing system. The magnetron created fuzz, produced with simultaneous deposition of W (shown in figures 6.2 b) and d)) are roughly four times thicker than the corresponding layers produced with no deposition (in figure 6.2 a) and c)).

Close inspection of the fuzzy layer thicknesses in figure 6.2 reveals that, for these He ion fluences, the difference in thickness between the depositing and non-depositing cases is approximately equal to the thickness that a W thin film would attain in non-fuzz conditions. For example, in the high ion fluence cases ($\Phi_{He} = 6$ x 10^{24} m^2), the fuzzy layer produced in NAGDIS II (figure 6.2 c) has a thickness of 332 $\pm$ 68 nm, whereas that produced in the magnetron (figure 6.2 d) is 1.17 $\pm$ 0.11 μm, the difference being 838 $\pm$ 189 nm. Over the $\sim$ 13 hours of exposure of the sample to the plasma in the magnetron, at a nominal deposition rate of 54 m/hr , this would yield a 710 nm thin film, close to the measured difference in the fuzz thicknesses of 838 $\pm$ 189 nm. In figure 6.3, the SEM was used to image the top of fuzzy structures surface, using the same four fuzzy samples as used in figure 6.2.

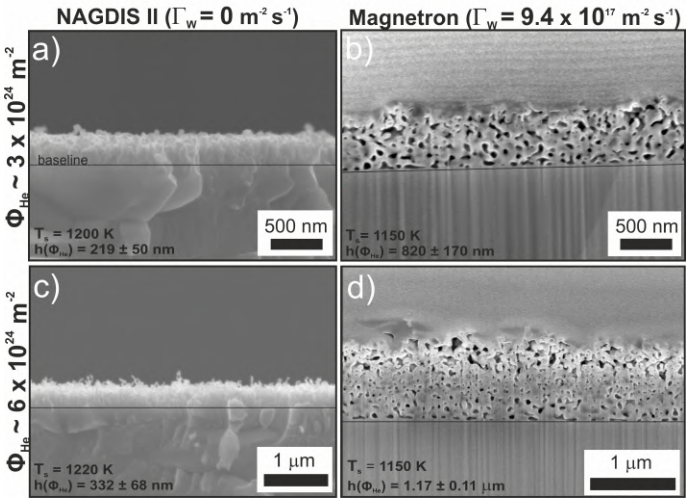

Figure 6.2: FIB-SEM cross-sectional images of fuzzy W grown in deposition-free (a, c) and deposition (b, d) environments, for two different He ion fluences. A black horizontal line laid over each image indicates the fuzz baseline. Samples in b) and d) are viewed at a 52° tilt angle.

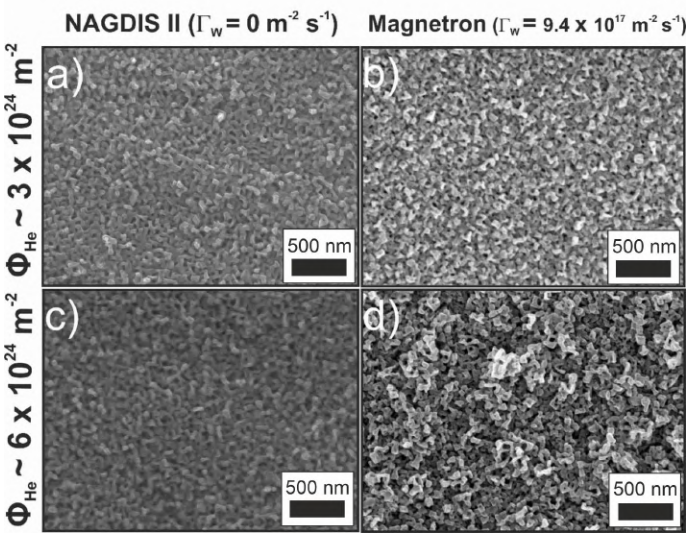

Figure 6.3: SEM images of the top of fuzzy W surfaces grown in deposition-free (a, c) and deposition (b, d) environments, for two different He ion fluences. The same four fuzzy surfaces that were used in the FIB-SEM cross sectional images of figure 6.2 are imaged here.

Interestingly, when the tendril widths on each surface (figures 6.3a) to d)) are compared, there is little difference to be found between those grown in deposition (figure 6.3b) and d)) and deposition free (figure 6.3a) and c)) environments. In both cases, the tendril width was measured to be on the scale of tens of nanometres, implying deposition does little to increase the width of tendrils, but instead increases their height vertically from the surface.

To determine how the growth of the fuzzy W layer is affected by a wider range of plasma exposures, samples were irradiated with He ion fluences from 4 x 10^{23} to 9 x 10^{24} m^{-2} in the magnetron and NAGDIS II systems. In the case of the magnetron, fuzz growth was produced under W deposition conditions with a W atom flux density ranging from 3.0 x 10^{17} to 9.4 x 10^{17} m^2 s^{-1}. This was done for a range of surface temperatures from 1100 to 1150 K. Figure 6.4 shows the fuzzy layer thicknesses (h) over the range of He ion fluences (Φ_{He}), in the different deposition conditions. Clearly, the presence of co-deposition of W greatly increases the thickness h. In these cases, there appears to be three phases of fuzzy growth: at low He ion fluences ($\Phi_{He} < 2$ x 10^{24} m^{-2}) h is consistent with non-deposition conditions, for intermediate fluences ($\sim$ 2 x 10^{24} m^{-2} $< \Phi_{He} <$ $\sim$ 6 x 10^{24} m^{-2}) h is increased by an amount consistent with the effective W thin film layer that would form, at high fluences ($\Phi_{He} > 6$ x 10^{24} m^{-2}) h increases very steeply with Φ_{He} to produce fuzzy layers up to $\sim$ 8 μm in thickness.

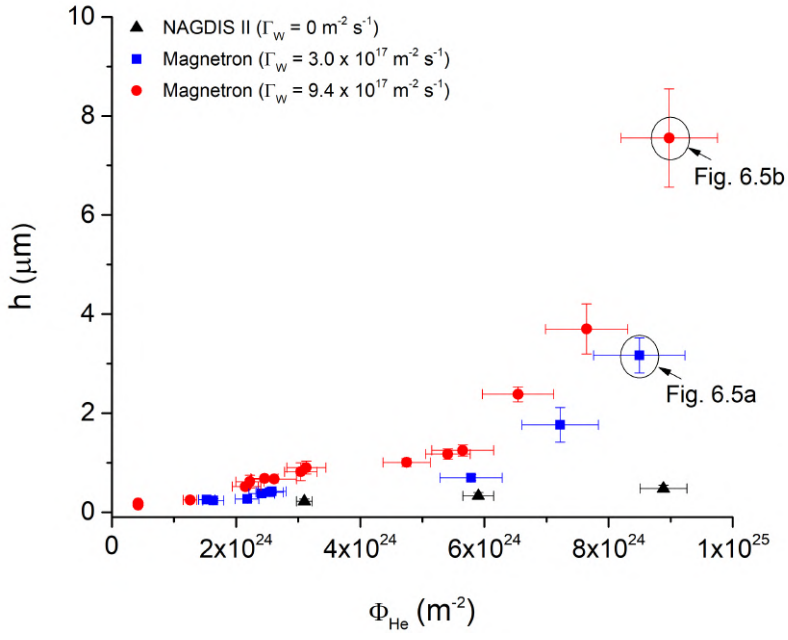

Figure 6.4: A plot of fuzz thickness versus He ion fluence for each deposition rate flux density.

In figure 6.4, the two largest fuzzy layers (indicated with black circles) that were produced for similar ion fluences ($\Phi_{He} \sim$ 9 x 10^{24} m^{-2}) but different W atom flux densities (Γ_w = 3.0 x 10^{17} m^{-2} s^{-1} and 9.4 x 10^{17} m^{-2} s^{-1}) are highlighted. By maintaining a He ion fluence of $\sim$ 9 x 10^{24} m^{-2} and increasing the W atom-to-He ion arrival rate ratio (Γ_w/Γ_{He}) from 0.003 to 0.009, h increased by just over a factor of two (increasing from 3.17

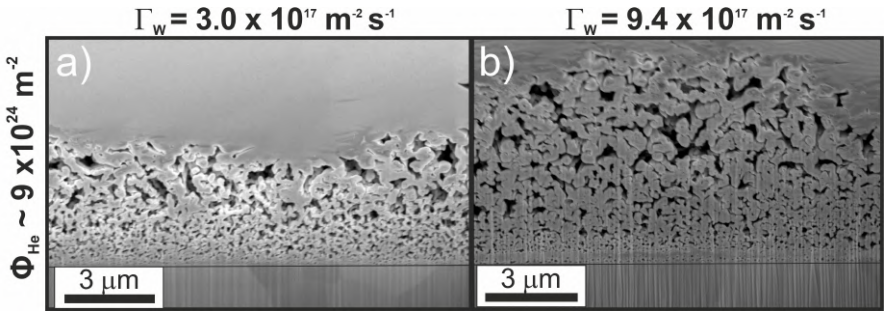

Figure 6.5: FIB-SEM cross-sectional images of fuzz samples grown for the same He ion fluence of $\sim$ 9 x 10^{24} m^{-2}, surface temperature of 1150 K, and different W deposition flux densities of a) 3.0 x 10^{17} m^{-2} s^{-1} and b) 9.4 x 10^{17} m^{-2} s^{-1}.

$\pm$ 0.36 μm to 7.56 $\pm$ 1.00 μm). In figures 6.5 a) and b), FIB – SEM cross sectional imaging of these two particular layers shows clearly that a thicker fuzzy layer is grown under the larger deposition flux density condition.

In figure 6.6, the surface morphology changes over a fluence range (4 x 10^{23} to 9 x 10^{24}) is shown using three magnetron grown fuzzy W samples. All three samples were produced with ion energies of 100 eV and surface temperatures of 1150 K. The fluence for each sample is labelled on the figure, and surfaces are viewed at a 52° tilt angle in b), d) and f). As the fluences increases from the lower range, nodules on the surface (a,b), which presumably indicate an early stage of fuzz growth, progress to thicker tendrils (c,d), then finally to fine fibres (e,f). In e) particularly, the porosity of the layer can be inferred from the dark regions of the SEM images. To show the evolution in the tendril width across the fluence range, the tendril width in each image was measured using ImageJ. One hundred measurements were taken in total to give an average value for the width, with the error prescribed to each measurement being two times the standard deviation. Figure 6.7 shows the results from these measurements. It was found that as the fluence increased from the lowest fluence ($\Phi_{He} \sim 4$ x 10^{23}) to the higher fluence sample ($\Phi_{He} \sim 9$ x 10^{24}), the tendril width decreased by a factor of two from 76 $\pm$ 16 nm to 35 $\pm$ 16 nm.

To better understand the effects of surface temperature on the onset of faster fuzz growth (circled cases in figure 6.4), additional fuzz surfaces (to those shown in figure 6.4) were grown in the magnetron under constant deposition conditions (Γ_w = 9.4 x 10^{17} m^{-2} s^{-1}) for He ion fluences between 2 x 10^{24} and 1 x 10^{25} m^{-2} and a range of surface temperatures T_s between 1050 K to 1150 K. Figure 6.8 shows FIB - SEM images of three fuzzy samples with T_s equal to 1050, 1100 ,1120 and 1150 K for the same He ion fluence ($\Phi_{He} \sim 9$ x 10^{24} m^2) and ion bombarding energy (100 eV). In figure 6.8 there is a large increase in the thickness of the fuzz layer from 1.32 $\pm$ 0.13 μm to 7.56 $\pm$ 0.39 μm for only a 100 K increase in T_s. This finding agrees well with previous reports where fuzzy W layers were observed to grow at faster rates when the surface temperature was raised from 1120 K to 1320 K for a constant He ion fluence [43].

To show clearly the three-phase growth of the fuzzy layer in deposition conditions and the dependency of surface temperature, it is convenient to plot the measured fuzzy layer

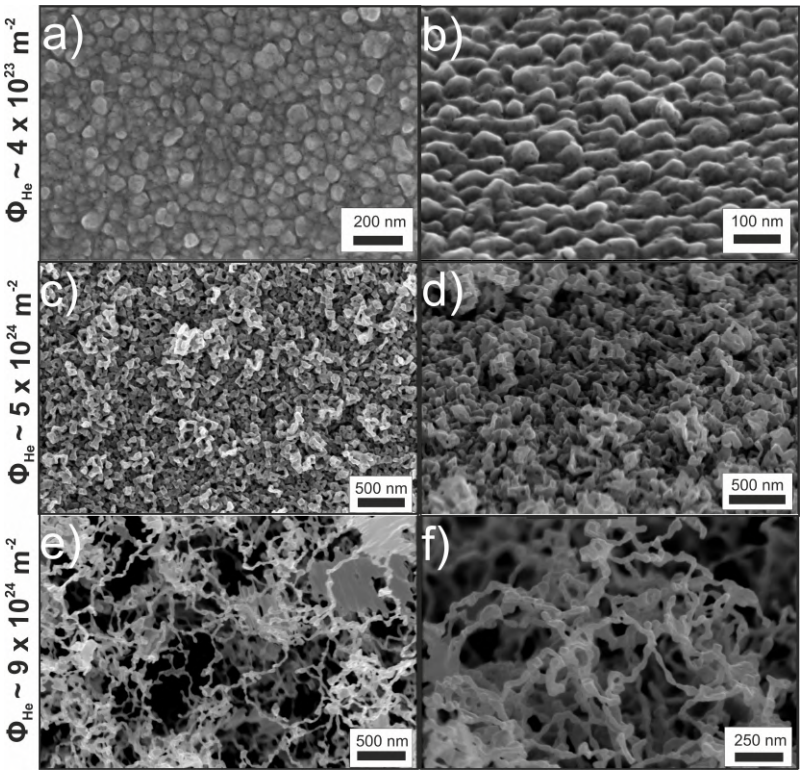

Figure 6.6: FIB-SEM images showing the surface morphologies from the top down (a,c,e) and at a 52° tilt (b,d,e) for three samples across a fluence range (4 x 10^{23} to 9 x 10^{24} m^{-2}. All fuzzy W samples shown here are produced under the higher deposition flux density (9.4 x 10^{17} m^{-2} s^{-1}).

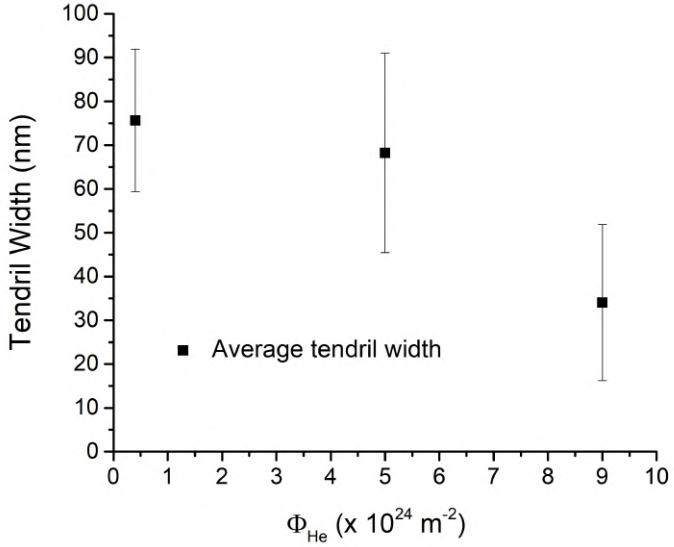

Figure 6.7: The average tendril width of the three fuzzy samples shown in figure 6.6. Each error is two times the standard deviation

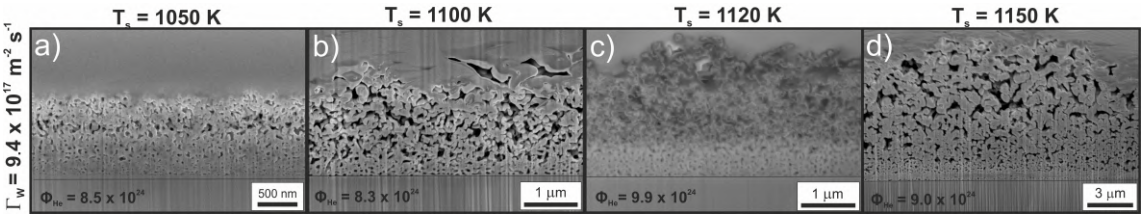

Figure 6.8: FIB-SEM cross-sectional images of fuzz grown in deposition conditions for a He ion fluence of $\sim$ 9 x 10^{24} m^2 across a surface temperature range from 1050 to 1150 K.

thicknesses against ion fluence on a plot with log-log axes. This is done in figure 6.9 for Γ_w = 9.4 x 10^{17} m^{-2} s^{-1} together with data obtained in this study for deposition-free conditions on NAGDIS II, as well as previous data compiled by Petty *et al.* on W fuzz growth in deposition-free linear plasma devices [38]. In the study by Petty *et al.*, the authors recorded the fuzz thicknesses produced for a range of He ion fluences ($\sim$ 2 x 10^{24} to 1 x 10^{28} m^{-2}), sample temperatures (1100 - 1200 K) and ion energies (60 - 80 eV). These experimental conditions are similar to the conditions at which fuzz was grown in this present study, thus allowing a comparison to be made between the data sets. Inspection of figure 6.9 shows that in deposition-free conditions at low He ion fluences ($\Gamma_{He} <$ 3 x 10^{24} m^{-2}) only small fuzzy thickness are obtained (h $\sim$ 5 x 10^{-2} μm), indicating that an incubation fluence is required to initiate fuzz growth. This behaviour can be represented by equation 2.2 (in section 6.1), in which the temperature-dependent constant C is found from a best fit from the deposition-free data (across the whole fluence range) to be 3.59 x 10^{-38} m^4 and with an incubation fluence Φ_0 = 2.5 x 10^{24} m^{-2} being appropriate. This relationship is shown as the dashed line in figure 6.9. However, this fit clearly does not hold for fuzzy surfaces grown with concurrent W deposition (i.e. the magnetron data in figure 6.9), which shows significantly elevated growth rates between fluences of $\sim$ 2 and $\sim$ 6 x 10^{24} m^{-2} and super-fast rates above 6 x 10^{24} m^{-2}. In addition, thicker fuzzy W layers were observed for increases in T_s, as demonstrated by the data points around $\Phi_{He} \sim 10^{25}$ m^{-2} representing measurements at temperatures of 1050, 110, 1120 and 1150 K.

It is also clear that there is no (or at least a much reduced) incubation fluence when fuzz forms with deposition present. In this case, Φ_0 can be taken to be $\sim$ 0 in equation 2.2, which is represented by the solid line in figure 6.9. It may be the case that an incubation fluence is still required in deposition conditions, however from this work Φ_0 would be less than the incubation fluence reported in [38] to be $\sim$ 2 x 10^{24} m^{-2}. It has been shown in previous studies that the early stages of fuzz growth can occur at fluences of close to 10^{23} m^{-2} [64], [65]. SEM imaging shown in figure 6.6 a) revealed that small fuzz-like nodules are present on the W surface once a He ion fluence of 4 x 10^{23} m^{-2} was reached, indicating a much lower incubation fluence in our magnetron system. All remaining FIB-SEM measurements which contributed to figure 6.9 are left to appendix C.

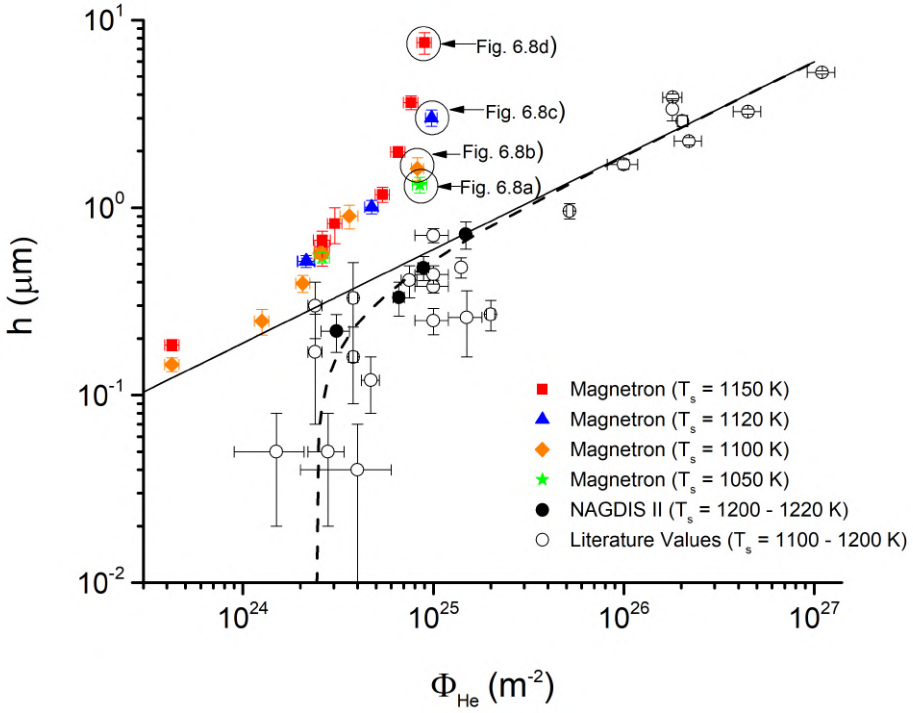

Figure 6.9: A log-log plot of the fuzzy layer thickness versus He ion fluence for fuzz grown with simultaneous deposition (inside the magnetron) and in deposition-free conditions (inside NAGDIS II and from the literature [38]). The black dashed and solid lines represent analytical fits of the data to a diffusive growth law with and without an inferred incubation fluence respectively.

6.3.1 High Resolution Imaging of Magnetron Grown Fuzz

The analysis by S/TEM was carried out by using the same magnetron fuzz sample as in fig.6.2b. The S/TEM images in fig.6.10 show the inner structure of the fuzzy tendrils formed on the sample's surface. Z-contrast in the HAADF images clearly shows porosity within the tendril structure, which is likely attributed to the presence of implanted He bubbles, and bears a strong resemblance to previous HAADF imaging of fuzzy tendrils [44], [59], [97], [201]. Size variability of the implanted bubbles ranges from $<$ 10 nm to 100 nm (approx.), and it is noticeable that the shape of the bubbles within the tendrils is varied, with no favoured bubble shape visible from the base toward the tip of a tendril, although larger bubbles tend to exist at the base. It can be seen that a denser W region exists toward the base of tendrils, possibly where tendrils have merged or W deposition has occupied the voids between tendrils. TEM analysis by Kajita *et al.* [194] showed that membranes existed between tendrils if metallic precipitation of W occurred during fuzz growth, with the metal atoms occupying voids between tendrils. A similarly dense region at the base of tendrils is seen on figure 6.11 a).

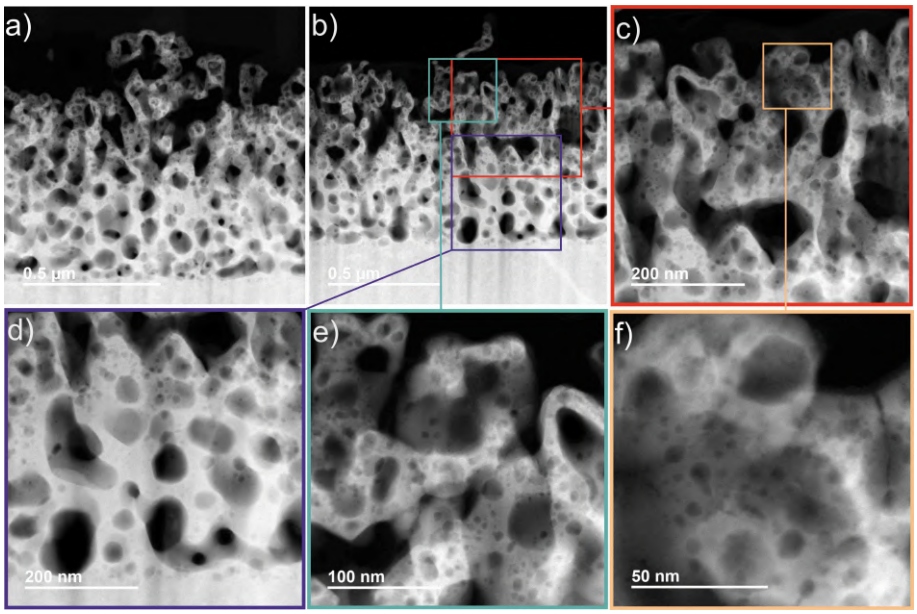

Figure 6.10: HAADF-STEM images (a) – f)) of the fuzz sample shown in figure 6.2b and 6.3b. Images a) and b) show low magnification images of the tendrils, and images c) - f) show magnified sections of the fuzzy layer shown in image b).

Crystallographic information of the same fuzzy sample was acquired through selected area electron diffraction (SAED) and is shown in figure 6.11. Three areas of interest were investigated; one from the bulk region of the sample where fuzz formation was deemed not to have occurred due to no visible He bubble formation (figure 6.11b) – c)), and two from the fuzzy W tendrils (figure 6.11 d) – g)). In figure 6.11 c) diffraction spots are attributable to single crystalline BCC W [202]. Diffraction rings for the fuzzy tendril regions suggest more polycrystallinity in the structure (figure 6.11e) and g)). Both fibril SAED patterns are also attributable to BCC polycrystalline W, with common d-spacing's of 2.258, 1.597, 1.129, 1.010 Å. Some of the diffraction spots in figure 6.11e) and g) are attributable to FCC platinum, which originate from the protective surface layer deposited during FIB milling preparation.

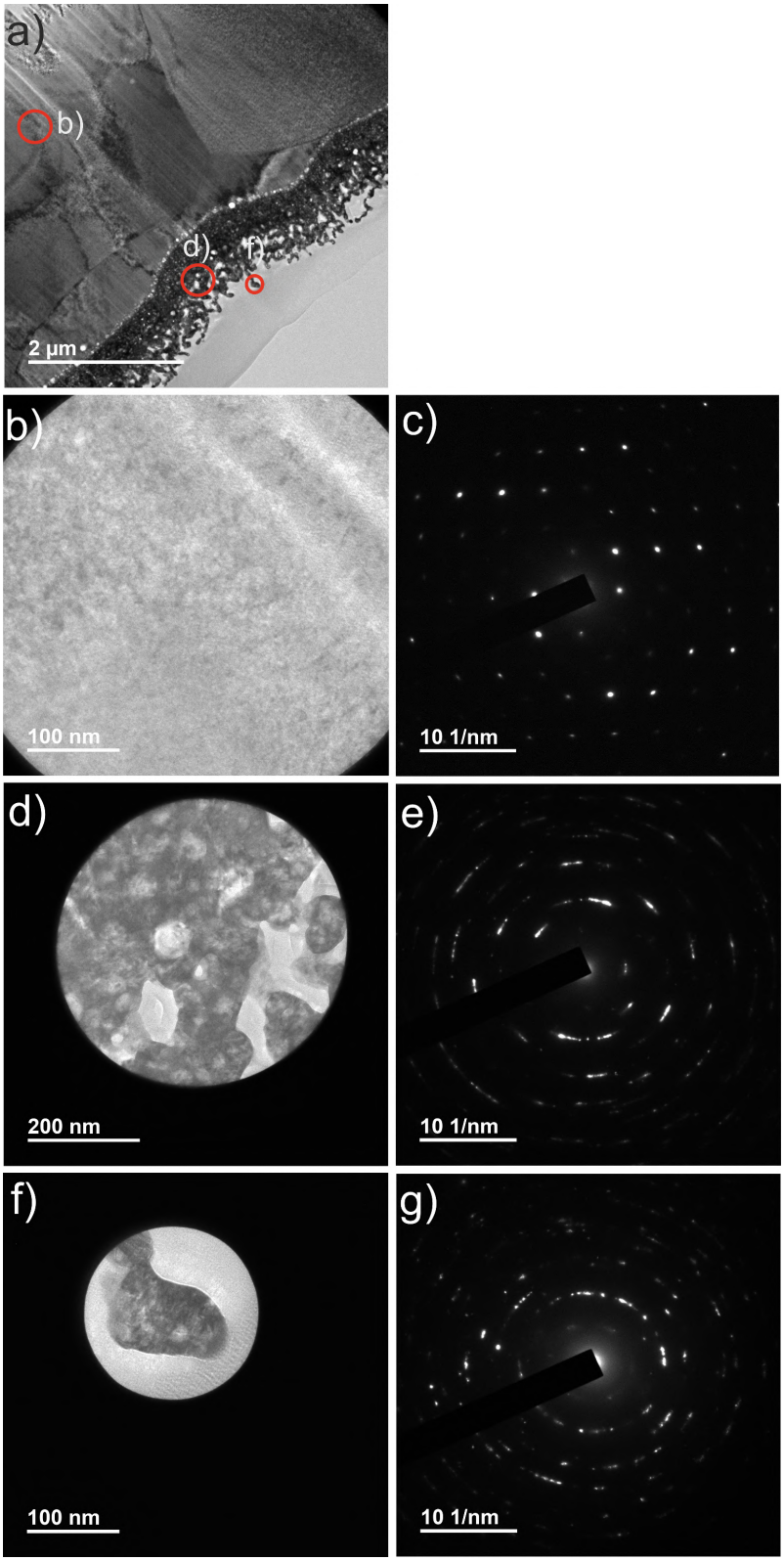

Figure 6.11: Cross-sectional TEM images and corresponding diffraction patterns, all produced using the same fuzz sample shown in figure 6.2b and 6.3b. Image a) shows a low magnification TEM image of the fuzzy surface cross-section. Images b), d) and f) are magnified regions as indicated on image a). Images c), e) and f) are the corresponding electron diffraction patterns produced from images b), d) and f) respectively.

6.3.2 Enhanced Fuzzy Tungsten Growth Mechanisms

Currently, the exact growth mechanisms which produce fuzzy W are unknown. It has been reported that fuzz forms due to He diffusion and bubble growth beneath the surface in the early stages [145], with W adatom diffusion [89], [91] or viscoelastic flows of W [90] describing the later stages of its formation toward tendril growth. In experimental [38] and theoretical [90] studies, the fuzzy layer thickness was shown to follow a $\sqrt{\Phi_{\mathrm{He}}}$ growth law, implying diffusion processes govern the growth rate of the nanostructures. In the current study and reports by Kajita *et al.* [192]–[194], it has been observed that when He ion irradiation is coupled with W deposition, the fuzzy layer thickness increases steeply with Φ_{He}. The processes which lead to the higher growth rates are not yet clear, however some possible mechanisms are outlined in [192] and [193], which are summarised below. When the fuzzy layer thickness h is comparable to or greater than the plasma sheath thickness λ_s (i.e. $\mathrm{h} \geq \lambda_s$), the sheath edge will not be flat but follow the shape of the fuzzy layer. As a result, an electric field would be formed around the tendrils, allowing He ions to be captured by the grown structures. This would enhance the ion capture due to the large surface area of the tendrils, which in turn would enhance He bubble formation and the fuzz growth rate. In [193], Kajita *et al.* demonstrated high growth rates even when $\mathrm{h} < \lambda_s$. In the current study, the debye length (λ_{D}) was calculated to give an estimation of the sheath thickness s, where λ_{D} is,

$$\lambda_{\mathrm{D}} = \left(\frac{\epsilon_0 k_B T_{\mathrm{e}}}{n e^2} \right)^{\frac{1}{2}} \tag{6.1}$$

where ϵ_0 is the permittivity of free space, k_{B} is the Boltzmann constant, n is the plasma density, and e is the electron charge. Using values calculated from the probe measurements at a neutral pressure of 2.6 Pa and 700 W of DC plasma power (in section 3.2.1), a value for λ_{D} was found to 7.6 μm. The Child Langmuir law [140] gives the sheath thickness s by,

$$\lambda_{\mathrm{s}} = \frac{\sqrt{2}}{3} \lambda_{\mathrm{D}} \left(\frac{2\mathrm{V}_0}{\mathrm{T}_{\mathrm{e}}} \right)^{3/4} \tag{6.2}$$

where V_0 is the potential drop across the sheath, and T_{e} is the electron temperature. As the sheath potential drop is determined by the plasma potential V_{P} (- 1 V) and the bias to the sample surface (- 100 V), V_0 was taken to be 100 V. The sheath thickness λ_{s} is found to be $\sim$ 40 μm, and this shows that high growth rates are produced under the condition $\mathrm{h} < \lambda_s$. In this regime ($\mathrm{h} < \lambda_s$), the growing tendrils are unlikely to perturb the shape of the sheath, with therefore no enhancement in the ion capture. In previous reports [38], [43] using deposition-free growth conditions, although thick fuzzy layers of several microns in height could be produced, the growth rates were not high. This rather implies that anomalously high growth rates are only associated with an auxiliary flux of W material. As such, growth rates are not limited by the diffusion law described by equations 2.1 and 2.2. In deposition enhanced growth, W atoms would arrive preferentially at the tips of

tendrils and possibly coalesce with a growing fuzz layer. This would relax the diffusion rate mechanism at the heart of current growth theories [89], [91] and [90] in which W is only transported from below the surface.

Recently, the team of Kajita have observed very high growth rates of fuzz on W surfaces exposed to He ion irradiation and simultaneous W deposition [192]–[194]. In [193], for a He ion fluence Φ_{He} of 1 x 10^{25} m^{-2}, fuzzy layers grew to thicknesses of 100s of microns to several millimeters. By a way of comparison, a maximum fuzzy layer thickness of 8 μm was observed in the current study for $\Phi_{He} \sim$ 1 x 10^{25} m^{-2}. The increased growth rate of fuzz in [193] relative to the conditions inside the magnetron is possibly due to the elevated range of surface temperatures and deposition flux densities used in [193]. Here, it has been observed that increasing both the W atom-to-He ion arrival rate ratio Γ_w/Γ_{He} from 0.003 to 0.009 and surface T_s temperature from 1050 to 1150 K can lead to a two-fold and six-fold increase respectively in the fuzzy layer thickness. By extrapolating to the experimental conditions in [193] (i.e $T_s \sim$ 1250 K, $\Gamma_w \sim$ 2.5 x 10^{18} m^{-2} s^{-1}, $\Phi_{He} \sim$ 1 x 10^{25} m^{-2}), and assuming the growth rate dependency for increases in Γ_w/Γ_{He} and T_s, it can be estimated that fuzz thicknesses of $\geq$ 100 μm would be formed within the magnetron system. In future experiments, increasing the range of sample temperatures and deposition flux densities within the magnetron system should be investigated to confirm the scale of fuzzy structures that can be produced. A method to grow samples of fuzz with large thicknesses ($\geq$ 100 μm) would be useful, considering the applications of fuzz outside of fusion research, such as in photo catalysis [121] or water splitting for hydrogen production [87].

Recrystallisation

As was observed in figure 6.8, the effects of a small increase in the surface temperature (from 1050 - 1150 K) produced a six-fold increase in the fuzzy layer thickness. As the surface temperature appears to be important to the enhancement in the fuzz growth rates observed, temperature effects will be considered on the W surface. Although the surface temperature range in this work is generally considered too low for recrystallisation on W to occur, fast rates of fuzzy W growth have also been demonstrated by Baldwin *et al.* on recrystallised W surfaces [45].

In the study a recrystallised W and pristine W surface were heated to 1120 K and treated with helium plasma for one hour to an ion fluence of 1.8 x 10^{26} m^{-2}. SEM imaging indicated a fuzzy layer thickness of at least 6.5 μm for the recrystallised W surface, while the non-recrystallised surface reached $\sim$ 3 μm for the same exposure conditions (shown in figure 6.12). It was not investigated further in their study, but the result implies that fuzz growth is accelerated on recrystallised W. Recrystallisation is a process where new crystals and grains are produced on metal surfaces, and through this process defects in the lattice would migrate to grain boundaries. It has been reported that defects in W are useful traps for helium atoms [57], [203], therefore it follows that having a higher proportion of defects together could result in a larger helium bubble accumulation, albeit at grain boundaries,

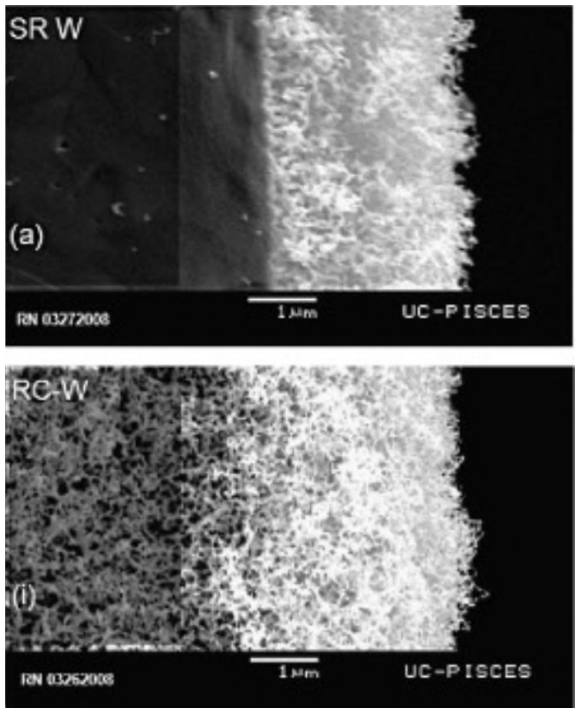

Figure 6.12: Fuzzy W produced by Baldwin *et al.* using a standard W surface (a) and a recrystallised W surface (i).

and fuzz formation could possibly be accelerated. It has been shown previously that grain boundaries can act as traps for He [150], which may support this argument. However it has also been shown that thin films of W containing large surface area to volume ratios can actively negate the growth of fuzzy W [204].

In W, recrystalisation thresholds are reported to be $\sim$ 1600 K [19], although recently much lower recrystallisation thresholds have been demonstrated. After around 60 hours of heating at 1373 K pure sheets of W were shown to reduce in hardness, implying recrystallisation processes had been initiated [205], with Tsuchida *et al.* observing in a seperate study that recrystallisation can begin at surface temperatures of $\sim$ 1373 K after 20 hours of consecutive heating [206]. In both reports, [205], [206], no surface temperatures were tested that were lower than 1373 K, so it is not possible to say whether recrystallisation can occur for lower temperatures (i.e. $<$ 1373 K). However, the findings in [205], [206] demonstrate that when W is heated for prolonged periods of time, recrystallisation can occur at lower temperatures than previously observed.

Recently a presentation given by Dr Thomas Morgan at The 17^{th} International Conference on Plasma-Facing Materials and Components for Fusion Applications reported observations of recrystallisation in tungsten monoblocks (see figure 6.13), at temperatures believed to be as low as 1123 K. In the findings that were presented, W monoblocks were exposed to high fluences ($\sim$ x 10^{30} m^{-2}) of deuterium plasma for 20 hour treatment times in the linear plasma device Magnum PSI. Although the plasma species used was different to He, it is interesting that for large fluences of plasma exposure and continued W heating, recrystallisation can occur in W at temperatures similar to the range used for

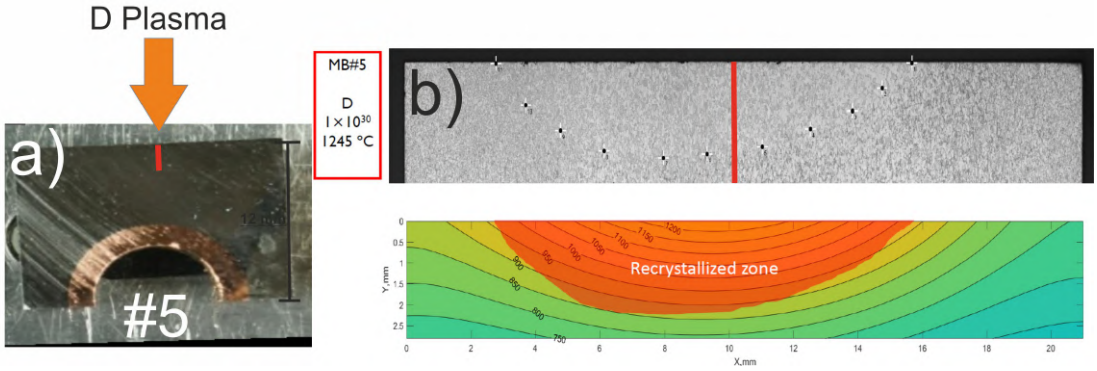

Figure 6.13: Image showing the reported recrystallisation of W monoblocks after 20 hours of consecutive D plasma exposure inside the linear plasma device Magnum PSI. The temperatures were measured using FEM analysis. The ion fluence was of the order x 10^{30} m^{-2}. Image a) shows a W monoblock, with a red line indicating the region over which recrystallisation was deemed to have occurred. In b) the estimated temperature beneath the W surface is estimated, with recrystallisation having occurred at surface temperatures of 850°.

the magnetron data in figure 6.9. To reach a He ion fluence Φ_{He} of $\sim$ 1 x 10^{25} m^{-2} in the magnetron, 20 + hours of plasma exposure is required. In figure 6.8, where $\Phi_{He} \sim$ 1 x 10^{25} m^{-2}, there is a clear enhancement in the growth rates of fuzz $\sim$ 1150 K, and it may be that recrystallisation has occurred due to the continued heating of W surfaces in the magnetron. This would therefore cause trapped He to migrate and collect at grain boundaries, which may enhance bubble formation. It has been shown previously that [207] that magnetron sputtered W films also contain signficant numbers of defects relative to pristine W layers. It is possible that the sputtered and deposited W inside the magnetron is able to produce He bubbles more readily due to the increased number of defect sites for He to be accumulated at.

6.3.3 ITER

For the conditions in the ITER divertor, it is likely that where the thresholds for fuzz growth are met, increases in the W atom-to-He ion arrival rate ratio (Γ_W/Γ_{He}) and surface temperature could produce enhanced fuzz growth rates. Assuming the values in table 6.1, Γ_W/Γ_{He} is estimated to be in the range 0.0004 to 0.001 for ITER. This is roughly the same order of Γ_W/Γ_{He} that was sufficient to show an enhance fuzz growth rate in the findings here, which implies that a small enhancement in the growth rate of fuzz in ITER may occur. In addition, the estimated temperature range of the ITER divertor (300 - 2000 K) is not only sufficient to allow fuzz to grow in some areas, but will also mean that in the hottest regions of the divertor, much larger fuzz growth rates could be possible. Transient events, such as ELMs, can increase both the wall surface temperature and the W deposition rate within a reactor, with deposition rates predicted to be five times larger during ELMs in ITER [195]. The subsequent increases in W surface temperatures and Γ_W/Γ_{He}, despite the short time scale of transient events, may ultimately produce an enhancement in fuzz growth rates in ITER.

6.3.4 Enhanced Growth on Fuzzy Molybdenum Surfaces

In section 2.1.9, the observations of fuzzy nanostructures on other metal surfaces, in addition to W, were described. Of these other metals where fuzz has been reported to grow, Mo will also feature in fusion reactors as a component of first wall mirrors used in diagnostic equipment [208]–[210]. Within the magnetron, it is possible to change the sputtering target. Hence it is possible to test whether the observed enhanced growth rates of fuzzy W will also be replicated on other materials. Here Mo samples are used to grow fuzzy Mo, while at the same time a Mo target was used to sputter and deposit on to the surface transitioning to fuzzy Mo.

The Mo surfaces were treated with He plasma for a constant He ion fluence (2.6 x 10^{24} m^{-2} and ion energy (100 eV), and after plasma exposure the FIB- SEM was used to image the surface morphologies and cross-sectional thicknesses of the fuzzy layer. In section 4.3, the deposition flux density from an Mo target at 2.6 Pa and 700 W of DC power was measured to be $\Gamma_{Mo} \sim 4$ x 10^{18} m^{-2} s^{-1} ($\sim$ 250 nm/hr). Assuming a similar He ion flux as found in 4.1.3, the Γ_{Mo}/Φ_{He} ratio is increased to $\sim$ 0.04, roughly 4x that which was calculated for the W magnetron target. The threshold conditions for Mo fuzz have not yet been well established, however in the studies where fuzzy Mo is observed to grow, a temperature window of 800 - 1073 K is sufficient to produce fuzz formation [124]–[126]. The fluence and ion energies required to grow fuzzy Mo are in the range of 2.6 x 10^{24} - 3 x 10^{25} m^{-2} and 50 - 100 eV respectively [125], [126]. As there is a large threshold window for each parameter, samples were produced across a large temperature range (923 - 1123 K) using the apparent upper limit for the ion energy (100 eV), so as to increase the chances of producing Mo fuzz. To reach an ion fluence of 1 x 10^{25} m^{-2} can take up to 23 hours inside the magnetron, so Mo samples were treated inside the magnetron sputtering device to a fluence of 2.6 x 10^{24} m^{-2} (6 hours). Each Mo surface was then analysed using FIB-SEM imaging, and reflectivity measurements provided information on the change of optical properties of the surface.

In figure 6.14, FIB-SEM images of the fuzzy Mo surfaces produced in the magnetron for a surface temperature range of 923 - 1123 K are shown. At the lower end of the temperature range (923 K), small nodules have grown on the surface which resemble images of W surfaces at Φ_{He} = 4 x 10^{23} m^{-2}. The cross-sectional images show porosity in each Mo fuzz layer, and all layers are similar to cross-sections of the fuzzy W layers produced in the magnetron shown in figures 6.2b) and d). This implies that the surface morphologies imaged here could be fuzz. The tenperature range of these samples is in the expected range for Mo fuzz formation described in [126], as well as the being in the range of T_s/T_s (see section 2.1.9). It is also noticeable that the thicknesses of each Mo fuzz layer are far greater than those produced in the magnetron with W. In figure 6.15 the fuzzy Mo thicknesses (red circles) produced in the magnetron are plotted against T_s. All Mo fuzzy layers had thicknesses of $\sim$ 1.5 μm, exceeding the thicknesses of fuzzy W produced at the same fluence (Φ_{He} = 2.6 x 10^{24} m^{-2}). This is likely due to the far higher deposition rates during the Mo fuzz experiments. Also plotted in figure 6.15 are the thicknesses of the Mo fuzzy layer when

the apparent thin film thickness of Mo deposition is subtracted from it. This measurement (shown as blue triangles) was compared to literature values for fuzzy Mo growth made by Tripathi *et al.* [126], using a He ion fluence of 2.6 x 10^{24} m^{-2} and an ion energy of 100 eV, with zero Mo deposition. It is clear from the figure that there is good agreement between the thicknesses of Mo grown under zero deposition and those produced in the magnetron, assuming the layer of deposition is removed. According to trends shown figure 6.4, for the ion fluence used to grow Mo fuzz in the magnetron (2.6 x 10^{24} m^{-2}), the thickness of the fuzzy layer produced under deposition conditions can be considered to be roughly equivalent to the predicted growth rate (given by equation 2.2) added to the thin film of deposition made. This appears to be the case for the Mo fuzz produced in the magnetron system, however it is not know currently whether fuzzy Mo formation follows the same growth law as W.

In figure 6.15 b), the reflectivity of Mo surfaces was measured. A sharp decrease in the reflectivity of Mo surfaces was observed in the temperature range 923 - 973 K, implying that a threshold for fuzz growth may be have met. As fuzzy surfaces typically show very low reflectivity measures, this decrease in the Mo surface reflectivity is presumably as a result of fuzz growth. This result also indicates a temperature threshold for fuzzy Mo formation of somewhere in the range of 923 - 973 K. When T_s was equal to 1123 K, the reflectivity had increased from $\sim$ 15 % to 25 %. Although this may only be a small increase, this could imply that the surface temperature window for fuzzy Mo production is in the range of 923 - 1073 K inside the magnetron system.

Further investigations into fuzzy Mo production using the magnetron system should aim to observe its growth under a lower deposition flux density, perhaps at similar level as for the W target. It may be that the high deposition rate of Mo is negating the growth of the Mo surfaces toward tendril formation, presumably due to a saturation of the surface with fresh Mo which would likely impede the formation of He bubbles. To lower the deposition rate the DC plasma power could be lowered, however this is likely to then decrease the He flux. The experimental exposure times will therefore have to increase, which may make the experiments unfeasible. Other approaches such as increasing the pressure may increase the He flux and decrease the deposition rate, so this should be tried in the future.

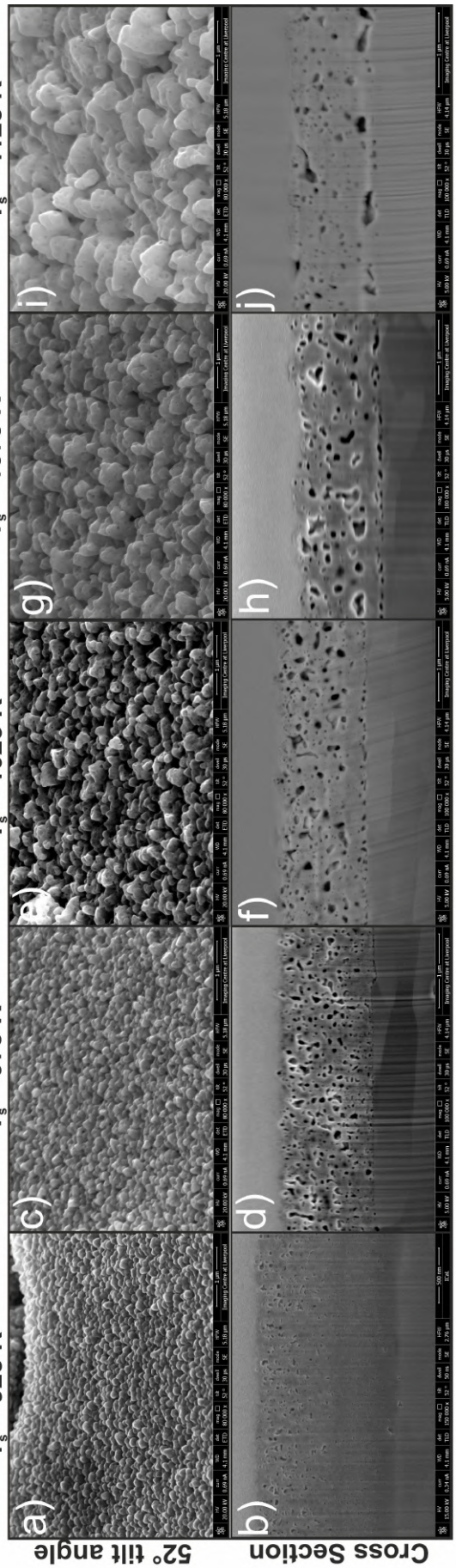

Figure 6.14: FIB-SEM images of fuzzy Mo surfaces produced in the magnetron across a surface temperature range (923 - 1123 K). The top row (a, c, e, g, h) shows the surface morphologies produced at a tilt angle of 52°, and in the bottom row (b, d, f, h, j) cross-sectional FIB images indicate the thickness of each fuzzy layer. In b), the magnification was decreased to 150,000x so as to allow the full layer to be imaged.

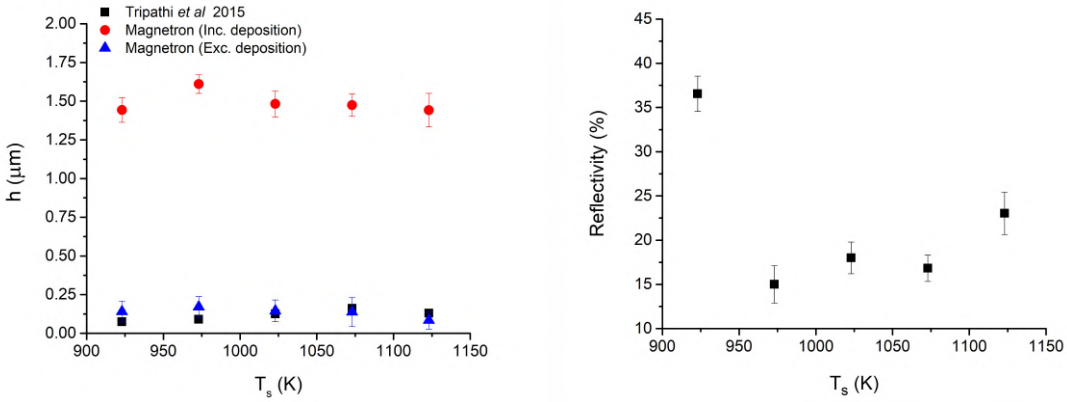

Figure 6.15: Figure showing the fuzzy Mo layer thicknesses measured from figure 6.14, as well as the layer produced if the thin film thickness of deposition is removed from the layer. In the figure experimental data collected by Tripathi et al. [126] is also plotted, showing the thickness of fuzz produced in [126] under similar experimental conditions (E_{ion} = 100 eV, Φ_{He} = 2.6 x 10^{24} m^{-2}) to the current study. In b), the reflectivity of the fuzzy Mo surfaces is shown.

6.4 Conclusions

In this chapter the magnetron sputtering system, operating in He, was used to grow fuzzy W samples with concurrent W deposition. The fuzzy layers were grown over a range of He ion fluences, Φ_{He}, (from 4 x 10^{23} to 1 x 10^{25} m^{-2}), sample temperatures, T_s, (from 1050 to 1150 K) and He ion energies (from 80 to 100 eV). The system allowed operator control over the W atom-to-He ion arrival rate ratio, Γ_w/Γ_{He}, at the sample (from 0.003 to 0.009). In the presence of W deposition, it appears that fuzz growth has three distinct stages: at low He ion fluences ($\sim \Phi_{He} <$ 2 x 10^{24} m^2) the height of the fuzzy layer, h, follows the expected h $\sim \sqrt{\Phi_{He}}$ diffusive law; at intermediate fluences ($\sim$ 2 x 10^{24} $m^{-2} < \Phi_{He} < \sim$ 6 x 10^{24} m^{-2}) h follows $\sqrt{\Phi_{He}}$ augmented by the "effective" thin film thickness of deposited W; at high fluences ($\Phi_{He} >$ 6 x 10^{24} m^2) h increases very steeply with Φ_{He}.

It was observed that the rate of growth in final stage was dependent on both T_s and the W atom-to-He ion arrival rate ratio. For the same He ion exposure ($\Phi_{He} \sim$ 9 x 10^{24} m^{-2}), raising T_s by 100 K from 1050 to 1150 K lead to a six fold increase in the fuzzy layer thickness, whilst increasing Γ_w/Γ_{He} from 0.003 to 0.009 produced a two-fold increase in the thickness. Microscopy and electron diffraction studies of the grown structures show He bubbles present within polycrystalline tendrils. The magnetron results were compared directly with fuzzy W layers grown in NAGDIS II, a deposition-free environment providing a similar range of ion fluences, ion energies and surface temperatures. The comparisons show that under simultaneous W deposition in the magnetron system, lower incubation fluences ($\sim$ 4 x 10^{23} m^{-2}) and enhanced growth rates of fuzz are produced. Our findings agree well with previous studies where enhanced growth rates can be attained through co-deposition of W from an auxiliary source.

An enhancement in the formation of fuzzy Mo was observed for a surface temperature range of 923 - 1123 K when Mo deposition was coupled with Mo fuzz growth. Mo fuzz samples produced in the magnetron were compared with literature values of Mo fuzz thickness formed under similar experimental conditions. This comparison inferred an enhancement in the fuzzy Mo layer thicknesses formed in the magnetron system. Reflectivity measurements of the fuzzy Mo surfaces indicated a decrease in the surface reflectivity down to 16 %, with the decrease in reflectivity of the surfaces likely caused by fuzz formation. Typical fuzzy W layers show reflectivity values as low as 1 - 2 % (see figure 4.14), although it may be that Mo fuzz has a higher incubation fluence, and the samples produced in this chapter are at an early stage of their growth. Thus the reflectivity values will not be as low for Mo fuzz in this study. Investigating higher ranges of He fluences may see a gradual decrease in the reflectivity to similar values as W fuzz layer.

On the likelihood of enhanced fuzz growth rates in ITER, the results presented in this chapter show that if W surfaces meet the conditions for fuzz growth, and this growth is coupled with some amount of W deposition, the fuzz growth rate could be enhanced. The growth of fuzz is also likely to be enhanced to a much higher rate during transient events like ELMs, where increases in the surface temperature and Γ_W/Γ_{He} ratio, due to larger fluxes of high energtic particles and W deposition respectively, are more likely.

Chapter 7

Conclusions

In this thesis, new results in the field of fuzzy nanostructure formation have been presented. An introduction in Chapter 1.1 provided background to nuclear fusion and relevant experimental fusion devices, as well as the necessity for W to be used in plasma facing components in these devices. The importance of research into the interactions between He plasma and W surfaces was explained due to the production of He ash as a by-product in the fusion reaction. The studies of He ion implantation into W surfaces were introduced in terms of their relevance for fusion research, with the conditions for ITER's divertor indicating the likelihood of fuzzy W formation in some areas.

In Chapter 2 a literature review of current fuzzy W research was introduced. The experimental parameters known to induce the growth of fuzzy W were described, and the observations of fuzzy W formation in experimental fusion reactors as well as the concerns for its growth were given. The current theories behind the growth process for fuzzy W growth were also described, with images provided from the literature used to aid their interpretation. The formation of fuzzy nanostructures on various metals through an experimentally observed temperature window was discussed. The research groups and experimental plasma devices predominantly used in fuzzy W research were introduced, with particular attention paid to the most prolific research groups on fuzzy W formation at Nagoya University and the University of California. The conclusion of this chapter discussed the main experimental device, the magnetron sputtering system, used at the UOL investigating fuzzy nanostructure formation. The plasma physics concepts important for this research were provided, highlighting the occurrence of surface sputtering and the classification of plasma.

The experimental methods used throughout this thesis were introduced in Chapter 3. This included a description of the experimental magnetron system, the sample heating unit and holder, and plasma diagnostic equipment used in this work. The analysis of fuzzy nanostructured layers was performed using various surface microscopy techniques which were all described. The plasma device used to grow fuzzy W samples at Nagoya University was also briefly introduced.

In Chapter 4, a characterisation of the magnetron sputtering system was made. Langmuir probe measurements found the variation in ion flux to the planar probe surface for a range of neutral pressures, DC plasma powers, and distances from the centre of the

magnetron target. Gas impurity species type were analysed using an RGA performed at two different base pressures inside the vacuum system. Similar analysis was performed during operation of the magnetron system, showing the gas species inside the system using a He neutral pressure of 2.67 Pa and 700 W of DC power. The deposition rate inside the magnetron system was found for different base and neutral pressures using a QCM, as well as the change in deposition rate for two different metallic targets. The IR pyrometer, used to provide real time measurements of the surface temperature, was calibrated for its transmission and emissivity coefficients. Finally, the temperature threshold for fuzzy W production was bench marked against the known surface temperature window shown to exist in the literature. The results from this investigation demonstrated a minimum temperature threshold for fuzzy W growth to be (1025 $\pm$ 35) K, agreeing well with the literature value of 1000 K.

In Chapter 5 new findings on the effects of He and impurity plasma mixtures on fuzzy W growth were presented. In this study, the impurity species (N_2, Ne and Ar) and other experimental parameters (surface temperature, incident ion energy, percentage of impurity) were chosen to mirror the conditions predicted for the ITER divertor, giving this investigation relevance to nuclear fusion research. The study investigated how the change in impurity species and concentration (5 , 7.5 and 10 %) changes the surfaces morphologies produced after He ion irradiation of W surfaces. At 5 % impurity (N_2, Ne and Ar), the fuzzy W layer thickness was reduced by a factor of 3 relative to a sample of fuzzy W produced under a 100 % He plasma at the same ion fluence. Fuzzy W growth was near terminated when higher percentages of Ar (7.5 and 10 %) were used in the He plasma, implying heavy sputtering had occurred on the surface at these impurity levels. Mass loss measurements showed that for each percentage of impurity level, the mass loss from the W surface due to sputtering was greatest for the heavier mass species.

Sputtering yields measured from surfaces exposed to 95 % He + 5 % N_2 or Ne showed a reduction in the measured sputtering yield with increasing thickness of the fuzzy layer. A reduction in the measured sputtering yield relative to bulk sputtering yields given by TRIM calculations was also observed. For long He + impurity plasma exposures ($5 > 10^{26}$ m^{-2}), the production of equilibrium thicknesses of fuzzy W were observed for 5 % of N_2 and Ne, with N_2 found to produce a lower equilibrium thickness than when using Ne. This was likely due to its heavier mass and larger sputtering yield on W. The equilibrium thicknesses that were measured for 5 % N_2 and Ne were compared to an analytical model predicting the scale of the equilibrium thickness based on bulk or measured sputtering yields. Using bulk sputtering yields provided a greater accuracy between experiment and the analytical model. Also observed were new larger nanostructures called Nano Tendril Bundles; a temperature and sputtering range was described for their formation.

Through results presented in Chapter 6 W surfaces were exposed to mixtures of He plasma and W deposition using a range of He ion fluences, Φ_{He}, from 4 x 10^{23} to 1 x 10^{25} m^{-2}, W atom-to-He ion arrival rate ratios from 0.003 to 0.009, surface temperatures from 1050 - 1150 K, and He ion energies of 80 to 100 eV. It was found that in the presence

of W deposition, the fuzz growth has three distinct stages: at low helium ion fluence the fuzzy layer thickness follows the expected $\sqrt{\Phi_{\mathrm{He}}}$ diffusive law; at intermediate fluences the thickness follows $\sqrt{\Phi_{\mathrm{He}}}$ but augmented by approximately the "effective" thin film thickness of deposited tungsten; at high fluences the fuzz thickness increases very steeply with Φ_{He}. During this third phase of fuzz growth the thickness was highly dependent on both the sample temperature and the tungsten atom-to-helium ion arrival rate ratio. For the same helium ion exposure, an increase in the sample temperature from 1050 to 1150 K lead to a six fold increase in the fuzzy layer thickness, whilst increasing the tungsten atom-to-helium ion arrival rate ratio over the full range produced a two-fold increase in the thickness. High resolution surface microscopy and electron diffraction studies of the grown structures showed clearly the presence of helium bubbles within polycrystalline tendrils.

The magnetron results were compared directly with fuzzy W layers grown in NAGDIS II, operating in completely deposition-free conditions, providing a similar range of helium ion fluences, ion energies and sample temperatures. The comparisons showed that a lower incubation fluence and an enhanced growth rate of fuzz was produced in the magnetron system. Enhancements in the growth rate of Mo fuzz were also observed in the magnetron when helium plasma treatment was coupled with Mo deposition. Magnetron grown fuzzy Mo results were compared to fuzzy Mo grown without inherent deposition but similar surface temperatures and ion fluences. The comparisons showed a clear enhancement in Mo fuzz grown under co-deposition. The findings in this study were extrapolated to ITER, with the implication being that as similar order of the W atom-to-He ion arrival rate are in parts of the divertor, enhanced fuzzy W growth could be possible.

Overall the aim of this thesis was to contribute to the body of knowledge regarding fuzzy nanostructure production and to help better understand its formation and growth under nuclear fusion like conditions. By recreating a fusion-like environment where mixed He + impurity plasma irradiate W surfaces, it has been shown how larger nanostructures called NTBs can be produced, as well as the benefits of fuzz growth to lower the sputtering yields of W surfaces. Deposition of sputtered W material has been shown to significantly enhance the formation rates of fuzzy W, implying fuzzy W growth could be accelerated in fusion reactors where deposition and fuzz growth occur simultaneously. Finally, the relatively simple and affordable methods employed here to produce fuzzy W (and other fuzzy materials) within the magnetron system should allow other research groups to carry out their own investigations into fuzzy nanostructure formation, for its application both in and outside of fusion research.

Chapter 8

Future Work

The experimental work presented here offers routes for future investigations into fuzzy nanostructure formation using the magnetron sputtering system . In chapter 6 insights into the enhanced growth rates of fuzzy W were observed after fuzzy W was grown in the presence of W deposition. As the results in that study had a maximum temperature range of 1150 K, it would be useful to extend this temperature range. A new heating system was built for this purpose, however due to a shortage of time new experiments were not carried out at a higher temperature. The new heating system works by resistively heating the sample after a large current is passed through it. In this way, many of the components of the sample heater used in this thesis are not needed, thus there are fewer concerns about the temperature tolerances of some materials used in the current holder (notably the macor shields used to house the filaments). This new heater was tested to produce surface temperatures of 1270 K across a W sheet, and this temperature was shown to be stable over 2 hours of constant heating. It is probable that through using the new heater and increasing the temperature range of the W surface, far greater thicknesses of fuzzy W could be produced in the magnetron system. In addition, the W atom-to-He ion arrival rate ratio should be increased to examine the effects this would have on the produced fuzzy thickness layer. Methods for changing the W atom-to-He ion arrival rate ratio would involve changing the neutral pressure inside the system or changing the DC plasma power.

The layers of fuzzy W should also be investigated further for their use in photocatalysis experiments. Currently, there is an ongoing collaboration with a chemistry group at the UOL investigating the measured photo-currents for increases in the thickness of fuzzy WO_3 layers. It has been shown previously that fuzzy WO_3 layers produce greater (upto 5x) photocurrents than non fuzzy WO_3 [87]. It is hoped that this work will contribute toward a publication in the near future.

Although ITER is planning for W to feature in the entirety of its divertor, it would be helpful for the fusion community to investigate fuzz formation on the alternatives proposed as plasma facing components in ITER. Research has shown alloying W with other materials such as rhenium (Re) and tantalum (Ta) can reduce the effects of thermal shocks and the retention of hydrogen [129], [211], therefore alloys of these materials could be investigated further within the magnetron to see the parameter ranges for fuzz to form, if it does at all.

In addition to the alloys mentioned, other materials are being investigated to accompany the use of W in divertors (such as Mo, Nb and Ta [212]), which could also be investigated in the magnetron system. It has already been investigated to an extent in this thesis the growth of Mo fuzz, however it would be useful to find ways of reducing the deposition rate during the exposure. This would allow a better comparison between the W and Mo fuzzy layers grown in the magnetron in Chapter 6 to be made. The deposition rate can be changed by varying the pressure or power, however this then affects the flux of He. From the findings in section 4.3 it seems the best way to maintain the He ion flux but reduce the deposition rate is to increase the He neutral pressure inside the system, so this could form a starting point for that investigation.

Ideally the temperature measurement method used in this work should be compensated in some way due to the change in emissivity of the surface during fuzz formation. This could involve having two infra-red pyrometers measuring from a fuzzy surface, one with a constant emissivity setting and the other being updated throughout the experiment. As the emissivity changes, the temperature the pyrometer reads will also change. Having two pyrometers, one which is kept at a constant emissivity (thus will show a temperature change over time), and one which emissivity is changed during exposure to maintain the same temperature, should give an estimation of the change in emissivity from the fuzzy surface. Alternatively, an integrating sphere could be used inside the magnetron, with the reflection measured from the surface of the sample. Calculating from Kirchoff's law would then give an estimation of the emissivity when fuzz grows.

The magnetron is a source of deposition so should easily be able to investigate the thinnest layer of fuzzy W possible to be produced, as well as material mixing of substrate layers. In a fusion reactor it is likely that sputtered material can be transported around a reactor and deposited in different areas, and it may be the case that material deposits mix with different materials. Therefore a study could be conducted on the magnetron system where substrates different to the sputtering target were used to produce fuzz. Analysis of the layers could use a surface sensitive method such Auger electron spectroscopy (AES) to probe the tips of fuzzy tendrils to investigate whether bulk material diffuses up a tendril, as is thought in some theories on fuzzy W formation [90], and has been alluded to in one previous experimental study [213].

Bibliography

[1] F. Paschen, "Ueber die zum Funkenübergang in Luft, Wasserstoff und Kohlensäure bei verschiedenen Drucken erforderliche Potentialdifferenz", *Annalen Phys*, vol. 273, no. 69, 1889.

[2] C. Tendero, C. Tixier, P. Tristant, *et al.*, "Atmospheric pressure plasmas: A review", *Spectrochimica Acta Part B: Atomic Spectroscopy*, vol. 61, no. 1, pp. 2–30, Jan. 2006.

[3] D. Mei and X. Tu, "Atmospheric Pressure Non-Thermal Plasma Activation of CO2 in a Packed-Bed Dielectric Barrier Discharge Reactor", *ChemPhysChem*, vol. 18, no. 22, pp. 3253–3259, 2017.

[4] G. McCracken and P. Stott, *Fusion*. Academic Press, Jan. 2013.

[5] I. Kirillov, I. Danilov, S. Sidorenkov, *et al.*, "Liquid lithium self-cooled breeding blanket design for ITER", *Fusion Engineering and Design*, vol. 39-40, pp. 669–674, Sep. 1998.

[6] A. J. H. Donné, "The European roadmap towards fusion electricity", *Philosophical Transactions of the Royal Society A: Mathematical, Physical and Engineering Sciences*, vol. 377, no. 2141, Mar. 2019.

[7] D. Reiter, H. Kever, G. H. Wolf, *et al.*, "Helium removal from tokamaks", *Plasma Physics and Controlled Fusion*, vol. 33, no. 13, pp. 1579–1600, 1991.

[8] J. D. Lawson, "Some Criteria for a Power Producing Thermonuclear Reactor", vol. 6, no. 70, pp. 6–10, 1956.

[9] Y. Xu, "A general comparison between tokamak and stellarator plasmas", *Matter and Radiation at Extremes*, vol. 1, no. 4, pp. 192–200, Jul. 2016.

[10] R. A. Pitts, S. Carpentier, F. Escourbiac, *et al.*, "A full tungsten divertor for ITER : Physics issues and design status", *Journal of Nuclear Materials*, vol. 438, S48–S56, 2013.

[11] T. Hirai, S. Panayotis, V. Barabash, *et al.*, "Use of tungsten material for the ITER divertor", *Nuclear Materials and Energy*, vol. 9, pp. 616–622, Dec. 2016.

[12] T. Loarer, C. Brosset, J. Bucalossi, *et al.*, "Gas balance and fuel retention in fusion devices", *Nuclear Fusion*, vol. 47, no. 9, pp. 1112–1120, 2007.

[13] T. Loarer, S. Brezinsek, V. Philipps, *et al.*, "Comparison of Fuel Retention in JET between Carbon and the ITER-Like Wall", no. 12,

[14] R. Neu and A. Kallenbach, "Overview on plasma operation with a full tungsten wall in ASDEX Upgrade", *Journal of Nuclear Materials*, vol. 438, S34–S41, Jul. 2013.

[15] J. Roth, E. Tsitrone, A. Loarte, *et al.*, "Recent analysis of key plasma wall interactions issues for ITER", *Journal of Nuclear Materials*, vol. 390-391, no. 1, pp. 1–9, 2009.

[16] R. Pitts, S. Carpentier, F. Escourbiac, *et al.*, "Physics basis and design of the ITER plasma-facing components", *Journal of Nuclear Materials*, vol. 415, no. 1, S957–S964, Aug. 2011.

[17] R. Pitts, S. Bardin, B. Bazylev, *et al.*, "Physics conclusions in support of ITER W divertor monoblock shaping", *Nuclear Materials and Energy*, vol. 12, pp. 60–74, Aug. 2017.

[18] S. Carpentier-Chouchana, T. Hirai, F. Escourbiac, *et al.*, "Status of the ITER full-tungsten divertor shaping and heat load distribution analysis", *Physica Scripta*, vol. T159, 2014.

[19] S. Mathaudhu, A. DeRosset, K. Hartwig, and L. Kecskes, "Microstructures and recrystallization behavior of severely hot-deformed tungsten", *Materials Science and Engineering: A*, vol. 503, no. 1-2, pp. 28–31, Mar. 2009.

[20] S. Panayotis, T. Hirai, V. Barabash, *et al.*, "Self-castellation of tungsten monoblock under high heat flux loading and impact of material properties", *Nuclear Materials and Energy*, vol. 12, pp. 200–204, 2017.

[21] R. Behrisch and W. Eckstein, *Sputtering by Particle Bombardment*. Springer International Publishing, 2007.

[22] M. Ye, H. Kanehara, S. Fukuta, *et al.*, "Blister formation on tungsten surface under low energy and high flux hydrogen plasma irradiation in NAGDIS-I", *Journal of Nuclear Materials*, vol. 313-316, pp. 72–76, Mar. 2003.

[23] V. Alimov, B. Tyburska-Püschel, S. Lindig, *et al.*, "Temperature dependence of surface morphology and deuterium retention in polycrystalline ITER-grade tungsten exposed to low-energy, high-flux D plasma", *Journal of Nuclear Materials*, vol. 420, no. 1-3, pp. 519–524, Jan. 2012.

[24] H. Xu, G. Luo, H. Schut, *et al.*, "Enhanced modification of tungsten surface by nanostructure formation during high flux deuterium plasma exposure", *Journal of Nuclear Materials*, vol. 447, no. 1-3, pp. 22–27, Apr. 2014.

[25] Y. Jia, W. Liu, B. Xu, *et al.*, "Nanostructures and pinholes on W surfaces exposed to high flux D plasma at high temperatures", *Journal of Nuclear Materials*, vol. 463, pp. 312–315, Aug. 2015.

[26] J. Condon and T. Schober, "Hydrogen bubbles in metals", *Journal of Nuclear Materials*, vol. 207, pp. 1–24, Dec. 1993.

[27] L. Buzi, G. De Temmerman, D. Matveev, *et al.*, "Surface modifications and deuterium retention in polycrystalline and single crystal tungsten as a function of particle flux and temperature", *Journal of Nuclear Materials*, vol. 495, pp. 211–219, Nov. 2017.

[28] D. Nishijima, M. Y. Ye, N. Ohno, and S. Takamura, "Incident ion energy dependence of bubble formation on tungsten surface with low energy and high flux helium plasma irradiation", *Journal of Nuclear Materials*, vol. 313-316, no. SUPPL. Pp. 97–101, 2003.

[29] S. Takamura, N. Ohno, D. Nishijima, and S. Kajita, "Formation of Nanostructured Tungsten with Arborescent Shape due to Helium Plasma Irradiation", *Plasma and Fusion Research*, vol. 1, pp. 051–051, 2006.

[30] H. Trinkaus and W. G. Wolfer, "Conditions for dislocation loop punching by helium bubbles", *Journal of Nuclear Materials*, vol. 122, no. 1-3, pp. 552–557, 1984.

[31] R. Behrisch and V. Prozesky, "Particle and power exhaust for a fusion plasma", *Nuclear Fusion*, vol. 30, no. 10, pp. 2166–2170, Oct. 1990.

[32] J. Hogan and D. Hillis, "Helium Transport and Exhaust in Tokamaks Report on the International Workshop on Helium Transport and Exhaust Experiments held at Gatlinburg, Tennessee, United States of America, 16–18 April 1991", *Nuclear Fusion*, vol. 31, no. 11, pp. 2181–2191, Nov. 1991.

[33] G. De Temmerman, T. Hirai, and R. A. Pitts, "The influence of plasma-surface interaction on the performance of tungsten at the ITER divertor vertical targets", *Plasma Physics and Controlled Fusion*, vol. 60, no. 4, p. 044 018, Apr. 2018.

[34] X. C. Li, Y. N. Liu, Y. Yu, *et al.*, "Helium defects interactions and mechanism of helium bubble growth in tungsten: A molecular dynamics simulation", *Journal of Nuclear Materials*, 2014.

[35] M. Miyamoto, D. Nishijima, Y. Ueda, *et al.*, "Observations of suppressed retention and blistering for tungsten exposed to deuterium–helium mixture plasmas", *Nuclear Fusion*, vol. 49, no. 6, p. 065 035, 2009.

[36] R. P. Doerner, D. L. Rudakov, C. P. Chrobak, *et al.*, "Investigation of He–W interactions using DiMES on DIII-D", *Physica Scripta*, vol. T167, no. 1, p. 014 054, 2016.

[37] S. Kajita, W. Sakaguchi, N. Ohno, *et al.*, "Formation process of tungsten nanostructure by the exposure to helium plasma under fusion relevant plasma conditions", *Nuclear Fusion*, vol. 49, no. 9, p. 095 005, 2009.

[38] T. Petty, M. Baldwin, M. Hasan, *et al.*, "Tungsten 'fuzz' growth re-examined: the dependence on ion fluence in non-erosive and erosive helium plasma", *Nuclear Fusion*, vol. 55, no. 9, p. 093 033, Sep. 2015.

[39] J. Brooks, J. Allain, R. Doerner, *et al.*, "Plasma–surface interaction issues of an all-metal ITER", *Nuclear Fusion*, vol. 49, no. 3, p. 035 007, Mar. 2009.

[40] H. Trinkaus and H. Ullmaier, "High temperature embrittlement of metals due to helium: is the lifetime dominated by cavity growth or crack growth?", *Journal of Nuclear Materials*, 1994.

[41] P. Fiflis, N. Connolly, and D. N. Ruzic, "Experimental mechanistic investigation of the nanostructuring of tungsten with low energy helium plasmas", *Journal of Nuclear Materials*, vol. 482, pp. 201–209, 2016.

[42] K. Wang, M. E. Bannister, F. W. Meyer, and C. M. Parish, "Effect of starting microstructure on helium plasma-materials interaction in tungsten", *Acta Materialia*, vol. 124, pp. 556–567, 2017.

[43] M. Baldwin and R. Doerner, "Helium induced nanoscopic morphology on tungsten under fusion relevant plasma conditions", *Nuclear Fusion*, vol. 48, no. 3, p. 035 001, Mar. 2008.

[44] A. Khan, G. De Temmerman, T. W. Morgan, and M. B. Ward, "Effect of rhenium addition on tungsten fuzz formation in helium plasmas", *Journal of Nuclear Materials*, vol. 474, pp. 99–104, 2016.

[45] M. Baldwin and R. Doerner, "Formation of helium induced nanostructure 'fuzz' on various tungsten grades", *Journal of Nuclear Materials*, vol. 404, no. 3, pp. 165–173, Sep. 2010.

[46] S. Kajita, T. Yokochi, N. Ohno, and T. Kumano, "Near Infrared Radiation from Heated Nanostructured Tungsten", *Japanese Journal of Applied Physics*, vol. 51, no. 1, 01AJ03, Jan. 2012.

[47] M. J. Baldwin, R. P. Doerner, D. Nishijima, *et al.*, "The effects of high fluence mixed-species (deuterium, helium, beryllium) plasma interactions with tungsten", *Journal of Nuclear Materials*, vol. 390-391, no. 1, pp. 886–890, 2009.

[48] H. Iwakiri, K. Yasunaga, K. Morishita, and N. Yoshida, "Microstructure evolution in tungsten during low-energy helium ion irradiation", *Journal of Nuclear Materials*, vol. 283-287, pp. 1134–1138, Dec. 2000.

[49] M. Ye, S. Fukuta, N. Ohno, *et al.*, "Modifications of Tungsten Irradiated by Low Energy and High Flux Helium Plasma", *J Plasma Fusion Res . . .*, vol. 3, no. January 2000, pp. 265–269, 2000.

[50] K. Tokunaga, R. Doerner, R. Seraydarian, *et al.*, "Surface morphology and helium retention on tungsten exposed to low energy and high flux helium plasma", *Journal of Nuclear Materials*, vol. 313-316, pp. 92–96, Mar. 2003.

[51] A. Al-Ajlony, J. Tripathi, and A. Hassanein, "Low energy helium ion irradiation induced nanostructure formation on tungsten surface", *Journal of Nuclear Materials*, 2017.

[52] S. Takamura, T. Miyamoto, and N. Ohno, "Effects of fibre-form nanostructures on particle emissions from a tungsten surface in plasmas", *Nuclear Fusion*, vol. 52, no. 12, 2012.

[53] K. Tokunaga, S. Tamura, N. Yoshida, *et al.*, "Synergistic effects of high heat loading and helium irradiation of tungsten", *Journal of Nuclear Materials*, vol. 329-333, no. 1-3 PART A, pp. 757–760, 2004.

[54] H. Ullmaier, "Review Paper the Influence of Helium on the Bulk Properties of Fusion Reactor", *Nuclear Fusion*, vol. 24, pp. 1039–83, 1984.

[55] M. Thompson, A. Deslandes, T. W. Morgan, *et al.*, "Observation of a helium ion energy threshold for retention in tungsten exposed to hydrogen/helium mixture plasma", *Nuclear Fusion*, vol. 56, no. 10, 2016.

[56] H. Greuner, H. Maier, M. Balden, *et al.*, "Investigation of W components exposed to high thermal and high H/He fluxes", in *Journal of Nuclear Materials*, 2011.

[57] F. W. Meyer, H. Hijazi, M. E. Bannister, *et al.*, "He-ion and self-atom induced damage and surface-morphology changes of a hot W target", *Physica Scripta*, vol. T159, p. 014 029, 2014.

[58] F. Meyer, L. Han, H. Hijazi, *et al.*, "Energy dependence of He-ion-induced tungsten nanofuzz formation at non-normal incidence angles", *Nuclear Materials and Energy*, vol. 12, pp. 366–371, Aug. 2017.

[59] K. Wang, R. P. Doerner, M. J. Baldwin, *et al.*, "Morphologies of tungsten nanotendrils grown under helium exposure", *Scientific Reports*, vol. 7, no. December 2016, pp. 1–9, 2017.

[60] M. E. Bannister, F. W. Meyer, H. Hijazi, *et al.*, "Surface morphologies of He-implanted tungsten", *Nuclear Instruments and Methods in Physics Research, Section B: Beam Interactions with Materials and Atoms*, vol. 382, pp. 76–81, 2016.

[61] S. J. Zenobia, L. M. Garrison, and G. L. Kulcinski, "The response of polycrystalline tungsten to 30 keV helium ion implantation at normal incidence and high temperatures", *Journal of Nuclear Materials*, vol. 425, no. 1-3, pp. 83–92, 2012.

[62] S. Kajita, N. Yoshida, R. Yoshihara, *et al.*, "TEM observation of the growth process of helium nanobubbles on tungsten: Nanostructure formation mechanism", *Journal of Nuclear Materials*, vol. 418, no. 1-3, pp. 152–158, 2011.

[63] R. Doerner, M. Baldwin, and P. Stangeby, "An equilibrium model for tungsten fuzz in an eroding plasma environment", *Nuclear Fusion*, vol. 51, no. 4, p. 043 001, Apr. 2011.

[64] F. W. Meyer, H. Hijazi, M. E. Bannister, *et al.*, "Flux threshold measurements of He-ion beam induced nanofuzz formation on hot tungsten surfaces", *Physica Scripta*, vol. 2016, no. T167, 2016.

[65] T. Petty, A. Khan, T. Heil, and J. Bradley, "Fuzzy tungsten in a magnetron sputtering device", *Journal of Nuclear Materials*, vol. 480, pp. 374–385, Nov. 2016.

[66] O. El-Atwani, S. Gonderman, M. Efe, *et al.*, "Ultrafine tungsten as a plasma-facing component in fusion devices: effect of high flux, high fluence low energy helium irradiation", *Nuclear Fusion*, vol. 54, no. 8, p. 083 013, 2014.

[67] S. Kajita, N. Yoshida, N. Ohno, *et al.*, "Helium plasma irradiation on single crystal tungsten and undersized atom doped tungsten alloys", *Physica Scripta*, vol. 89, no. 2, 2014.

[68] L. M. Garrison and G. L. Kulcinski, "Irradiation resistance of grains near {0 0 1} on polycrystalline tungsten under 30 keV He+ bombardment at 1173 K", *Physica Scripta*, vol. T159, 2014.

[69] Y. Noiri, S. Kajita, and N. Ohno, "Nanostructure growth by helium plasma irradiation to tungsten in sputtering regime", *Journal of Nuclear Materials*, vol. 463, pp. 285–288, 2015.

[70] R. M. Corless, G. H. Gonnet, D. E. Hare, *et al.*, "On the Lambert W function", *Advances in Computational Mathematics*, vol. 5, no. 4, pp. 329–359, 1996.

[71] D. Nishijima, M. J. Baldwin, R. P. Doerner, and J. H. Yu, "Sputtering properties of tungsten 'fuzzy' surfaces", *Journal of Nuclear Materials*, vol. 415, no. 1 SUPPL, pp. 96–99, 2011.

[72] D. Hwangbo, S. Kawaguchi, S. Kajita, and N. Ohno, "Erosion of nanostructured tungsten by laser ablation, sputtering and arcing", *Nuclear Materials and Energy*, vol. 12, pp. 386–391, 2017.

[73] H. Takamura, T. Miyamoto, and N. Ohno, "Deepening of Floating Potential for Tungsten Target Plate on the way to Nanostructure Formation", *Plasma and Fusion Research*, vol. 5, pp. 039–039, 2010.

[74] E. M. Hollmann, R. P. Doerner, D. Nishijima, and A. Y. Pigarov, "Observation of reduction of secondary electron emission from helium ion impact due to plasma-generated nanostructured tungsten fuzz", 2017.

[75] M. Patino, Y. Raitses, and R. Wirz, "Secondary electron emission from plasma-generated nanostructured tungsten fuzz", *Applied Physics Letters*, vol. 109, no. 20, p. 201 602, Nov. 2016.

[76] S. Kajita, S. Takamura, N. Ohno, *et al.*, "Sub-ms laser pulse irradiation on tungsten target damaged by exposure to helium plasma", *Nuclear Fusion*, vol. 47, no. 9, pp. 1358–1366, 2007.

[77] S. Kajita, G. De Temmerman, T. Morgan, *et al.*, "Thermal response of nanostructured tungsten", *Nuclear Fusion*, vol. 54, no. 3, p. 033 005, 2014.

[78] S. Kajita, T. Yagi, K. Kobayashi, *et al.*, "Measurement of heat diffusion across fuzzy tungsten layer", *Results in Physics*, vol. 6, pp. 877–878, 2016.

[79] S. Qu, Y. Li, Z. Wang, *et al.*, "Thermal conductivity measurement of the He-ion implanted layer of W using transient thermoreflectance technique", *Journal of Nuclear Materials*, 2017.

[80] S. Qu, H. Sun, A. Kreter, *et al.*, "Degradation of thermal conductivity of the damaged layer of tungsten irradiated by helium-plasma", *Fusion Engineering and Design*, vol. 137, no. August, pp. 97–103, 2018.

[81] S. Kajita, T. Saeki, Y. Hirahata, *et al.*, "Development of nanostructured black metal by self-growing helium bubbles for optical application", *Japanese Journal of Applied Physics*, vol. 50, no. 8 PART 2, 2011.

[82] S. Kajita, N. Ohno, M. Yajima, and J. Kato, "Growth annealing equilibrium of tungsten nanostructures by helium plasma irradiation in non-eroding regimes", *Journal of Nuclear Materials*, vol. 440, no. 1-3, pp. 55–62, Sep. 2013.

[83] N. Ohno, Y. Hirahata, M. Yamagiwa, *et al.*, "Influence of crystal orientation on damages of tungsten exposed to helium plasma", *Journal of Nuclear Materials*, vol. 438, no. SUPPL, S879–S882, 2013.

[84] C. Parish, H. Hijazi, H. Meyer, and F. Meyer, "Effect of tungsten crystallographic orientation on He-ion-induced surface morphology changes", *Acta Materialia*, vol. 62, no. 1, pp. 173–181, Jan. 2014.

[85] C. Li, H. Greuner, Y. Yuan, *et al.*, "Effects of temperature on surface modification of W exposed to He particles", *Journal of Nuclear Materials*, vol. 455, no. 1-3, pp. 201–206, 2014.

[86] S. Kajita, T. Saeki, N. Yoshida, *et al.*, "Nanostructured black metal: Novel fabrication method by use of self-growing helium bubbles", *Applied Physics Express*, vol. 3, no. 8, pp. 8–11, 2010.

[87] M. de Respinis, G. De Temmerman, I. Tanyeli, *et al.*, "Efficient Plasma Route to Nanostructure Materials: Case Study on the Use of m-WO 3 for Solar Water Splitting", *ACS Applied Materials & Interfaces*, vol. 5, no. 15, pp. 7621–7625, Aug. 2013.

[88] K. Komori, T. Yoshida, S. Yagi, *et al.*, "Application of Nanostructured Tungsten Fabricated by Helium Plasma Irradiation for Photoinduced Decolorization of Methylene Blue", *e-Journal of Surface Science and Nanotechnology*, vol. 12, no. July, pp. 343–348, 2014.

[89] Y. V. Martynenko and M. Y. Nagel', "Model of fuzz formation on a tungsten surface", *Plasma Physics Reports*, vol. 38, no. 12, pp. 996–999, 2012.

[90] S. I. Krasheninnikov, "Viscoelastic model of tungsten 'fuzz' growth", *Physica Scripta*, vol. T145, p. 014 040, Dec. 2011.

[91] D. Trufanov, E. Marenkov, and S. Krasheninnikov, "The role of the adatom diffusion in the tungsten fuzz growth", *Physics Procedia*, vol. 71, no. February, pp. 20–24, 2015.

[92] T. J. Petty and J. W. Bradley, "Tungsten nanostructure formation in a magnetron sputtering device", *Journal of Nuclear Materials*, vol. 453, no. 1-3, pp. 320–322, 2014.

[93] S. Iyyakkunnel, L. Marot, B. Eren, *et al.*, "Morphological Changes of Tungsten Surfaces by Low-Flux Helium Plasma Treatment and Helium Incorporation via Magnetron Sputtering", *ACS Applied Materials & Interfaces*, vol. 6, no. 14, pp. 11 609–11 616, Jul. 2014.

[94] K. Woller, D. Whyte, and G. Wright, "Impact of helium ion energy modulation on tungsten surface morphology and nano-tendril growth", *Nuclear Fusion*, vol. 57, no. 6, p. 066 005, 2017.

[95] G. Wright, D. Brunner, M. Baldwin, *et al.*, "Tungsten nano-tendril growth in the Alcator C-Mod divertor", *Nuclear Fusion*, vol. 52, no. 4, p. 042 003, 2012.

[96] M. Tokitani, S. Masuzaki, H. Kasahara, *et al.*, "Initial growth phase of W-fuzz formation in ultra-long pulse helium discharge in LHD", *Nuclear Materials and Energy*, vol. 0, pp. 1–5, 2016.

[97] S. Kajita, N. Ohno, N. Yoshida, *et al.*, "Arcing on tungsten subjected to helium and transients: ignition conditions and erosion rates", *Plasma Physics and Controlled Fusion*, vol. 54, no. 3, p. 035 009, 2012.

[98] D. Nishijima, R. Doerner, D. Iwamoto, *et al.*, "Response of fuzzy tungsten surfaces to pulsed plasma bombardment", *Journal of Nuclear Materials*, vol. 434, no. 1-3, pp. 230–234, Mar. 2013.

[99] D. Aussems, D. Nishijima, C. Brandt, *et al.*, "The occurrence and damage of unipolar arcing on fuzzy tungsten", *Journal of Nuclear Materials*, vol. 463, pp. 303–307, Aug. 2015.

[100] M. Tokitani, S. Kajita, S. Masuzaki, *et al.*, "Exfoliation of the tungsten fibreform nanostructure by unipolar arcing in the LHD divertor plasma", *Nuclear Fusion*, vol. 51, no. 10, 2011.

[101] D. L. Rudakov, C. P. Wong, R. P. Doerner, *et al.*, "Exposures of tungsten nanostructures to divertor plasmas in DIII-D", *Physica Scripta*, vol. 2016, no. T167, 2016.

[102] J. Matějíček, V. Weinzettl, M. Vilémová, *et al.*, "ELM-induced arcing on tungsten fuzz in the COMPASS divertor region", *Journal of Nuclear Materials*, vol. 492, pp. 204–212, 2017.

[103] G. De Temmerman, T. Morgan, G. van Eden, *et al.*, "Effect of high-flux H/He plasma exposure on tungsten damage due to transient heat loads", *Journal of Nuclear Materials*, vol. 463, pp. 198–201, 2015.

[104] C. P. C. Wong, D. L. Rudakov, J. N. Brooks, *et al.*, "Plasma Surface Interaction (PSI) studies at DIII-D", in *2013 IEEE 25th Symposium on Fusion Engineering, SOFE 2013*, 2013, pp. 1–6.

[105] R. P. Doerner, D. Nishijima, S. I. Krasheninnikov, *et al.*, "Motion of W and He atoms during formation of W fuzz", *Nuclear Fusion*, vol. 58, no. 6, 2018.

[106] J. Roth, E. Tsitrone, T. Loarer, *et al.*, "Tritium inventory in ITER plasma-facing materials and tritium removal procedures", *Plasma Physics and Controlled Fusion*, vol. 50, no. 10, p. 103 001, Oct. 2008.

[107] H. Iwakiri, K. Morishita, and N. Yoshida, "Effects of helium bombardment on the deuterium behavior in tungsten", *Journal of Nuclear Materials*, vol. 307-311, no. 1 SUPPL. Pp. 135–138, 2002.

[108] M. J. Baldwin, T. C. Lynch, R. P. Doerner, and J. H. Yu, "Nanostructure formation on tungsten exposed to low-pressure rf helium plasmas: A study of ion energy threshold and early stage growth", *Journal of Nuclear Materials*, vol. 415, no. 1 SUPPL, pp. 104–107, 2011.

[109] H. B. Zhou, Y. L. Liu, S. Jin, *et al.*, "Towards suppressing H blistering by investigating the physical origin of the H-He interaction in W", *Nuclear Fusion*, vol. 50, no. 11, 2010.

[110] R. P. Doerner, M. J. Baldwin, T. C. Lynch, and J. H. Yu, "Retention in tungsten resulting from extremely high fluence plasma exposure", vol. 9, pp. 89–92, 2016.

[111] N. Juslin and B. Wirth, "Molecular dynamics simulation of the effect of sub-surface helium bubbles on hydrogen retention in tungsten", *Journal of Nuclear Materials*, vol. 438, S1221–S1223, Jul. 2013.

[112] S. Markelj, T. Schwarz-Selinger, and A. Založnik, "Hydrogen isotope accumulation in the helium implantation zone in tungsten", *Nuclear Fusion*, vol. 57, no. 6, 2017.

[113] J. Roth and K. Schmid, "Hydrogen in tungsten as plasma-facing material", *Physica Scripta T*, vol. T145, 2011.

[114] W. R. Wampler and R. P. Doerner, "The influence of displacement damage on deuterium retention in tungsten exposed to plasma", *Nuclear Fusion*, vol. 49, no. 11, 2009.

[115] M. Reinhart, A. Kreter, L. Buzi, *et al.*, "Influence of plasma impurities on the deuterium retention in tungsten exposed in the linear plasma generator PSI-2", *Journal of Nuclear Materials*, vol. 463, pp. 1021–1024, Aug. 2015.

[116] S. Kajita, T. Nojima, Y. Tomita, *et al.*, "Fuzzy nanostructure growth on precious metals by He plasma irradiation", *Surface and Coatings Technology*, vol. 340, no. February, pp. 86–92, 2018.

[117] S. Kajita, D. Kitaoka, N. Ohno, *et al.*, "Surface modification of titanium using He plasma", *Applied Surface Science*, vol. 303, pp. 438–445, Jun. 2014.

[118] S. Kajita, T. Ishida, N. Ohno, *et al.*, "Fuzzy nanostructure growth on Ta/Fe by He plasma irradiation", *Scientific Reports*, vol. 6, no. 1, p. 30 380, Sep. 2016.

[119] T. J. Novakowski, J. K. Tripathi, and A. Hassanein, "Temperature-dependent surface modification of Ta due to high-flux, low-energy He+ ion irradiation", *Journal of Nuclear Materials*, vol. 467, pp. 244–250, 2015.

[120] S. Takamura and Y. Uesugi, "Experimental identification for physical mechanism of fiber-form nanostructure growth on metal surfaces with helium plasma irradiation", *Applied Surface Science*, vol. 356, pp. 888–897, 2015.

[121] S. Kajita, T. Yoshida, D. Kitaoka, *et al.*, "Helium plasma implantation on metals: Nanostructure formation and visible-light photocatalytic response", *Journal of Applied Physics*, vol. 113, no. 13, p. 134 301, 2013.

[122] I. Tanyeli, L. Marot, M. C. M. Van De Sanden, and G. De Temmerman, "Nanostructuring of iron surfaces by low-energy helium ions", *ACS Applied Materials and Interfaces*, vol. 6, no. 5, pp. 3462–3468, 2014.

[123] K. Omori, A. M. Ito, K. Shiga, *et al.*, "Comparison between helium plasma induced surface structures in group 5 (Nb, Ta) and group 6 elements (Mo, W)", *Journal of Applied Physics*, vol. 121, no. 15, 2017.

[124] G. De Temmerman, K. Bystrov, J. J. Zielinski, *et al.*, "Nanostructuring of molybdenum and tungsten surfaces by low-energy helium ions", *Journal of Vacuum Science & Technology A: Vacuum, Surfaces, and Films*, vol. 30, no. 2012, p. 041 306, 2012.

[125] S. Takamura, "Temperature Range for Fiber-Form Nanostructure Growth on Molybdenum Surfaces due to Helium Plasma Irradiation", vol. 9, pp. 1–4, 2014.

[126] J. Tripathi, T. Novakowski, G. Joseph, *et al.*, "Temperature dependent surface modification of molybdenum due to low energy He+ ion irradiation", *Journal of Nuclear Materials*, vol. 464, pp. 97–106, 2015.

[127] J. K. Tripathi, T. J. Novakowski, and A. Hassanein, "Tailoring molybdenum nanostructure evolution by low-energy He⁺ ion irradiation", *Applied Surface Science*, vol. 353, pp. 1070–1081, 2015.

[128] N. Yamashita, K. Omori, Y. Kimura, *et al.*, "Surface morphology changes of silicon carbide by helium plasma irradiation", *Nuclear Materials and Energy*, vol. 16, no. June, pp. 145–148, 2018.

[129] S. Gonderman, J. Tripathi, T. Novakowski, *et al.*, "Effect of dual ion beam irradiation (helium and deuterium) on tungsten–tantalum alloys under fusion relevant conditions", *Nuclear Materials and Energy*, vol. 12, pp. 346–352, Aug. 2017.

[130] S. Kajita, N. Yoshida, N. Ohno, and Y. Tsuji, "Growth of multifractal tungsten nanostructure by He bubble induced directional swelling", *New Journal of Physics*, vol. 17, no. 4, p. 043 038, Apr. 2015.

[131] W. Eckstein, *Calculated sputtering, reflection and range values*, 2002.

[132] A. Al-Ajlony, J. K. Tripathi, and A. Hassanein, "Role of carbon impurities on the surface morphology evolution of tungsten under high dose helium ion irradiation", *Journal of Nuclear Materials*, vol. 466, pp. 569–575, 2015.

[133] K. B. Woller, D. G. Whyte, and G. M. Wright, "Isolated nano-tendril bundles on tungsten surfaces exposed to radiofrequency helium plasma", *Nuclear Materials and Energy*, vol. 12, pp. 1282–1287, 2017.

[134] V. Kouznetsov, K. Macák, J. M. Schneider, *et al.*, "A novel pulsed magnetron sputter technique utilizing very high target power densities", *Surface and Coatings Technology*, vol. 122, no. 2-3, pp. 290–293, Dec. 1999.

[135] H. Zhang, J. Poole, R. Eller, and M. Keefe, "Cobalt sputtering target and sputter deposition of Co thin films for cobalt silicide metallization", *Journal of Vacuum Science & Technology A: Vacuum, Surfaces, and Films*, vol. 17, no. 4, pp. 1904–1910, 1999.

[136] D. Sinelnikov, D. Bulgadaryan, and V. Kurnaev, "Emission from Tungsten Nanostructured Tendril Bundles under Local Thermal Load", *2018 28th International Symposium on Discharges and Electrical Insulation in Vacuum (ISDEIV)*, vol. 1, pp. 31–34, 2018.

[137] P. Kelly and R. Arnell, "Magnetron sputtering: a review of recent developments and applications", *Vacuum*, vol. 56, no. 3, pp. 159–172, Mar. 2000.

[138] Y. Kudriavtsev, A. Villegas, A. Godines, and R. Asomoza, "Calculation of the surface binding energy for ion sputtered particles", *Applied Surface Science*, vol. 239, no. 3-4, pp. 273–278, 2005.

[139] M. Marinov, "Effect of ion bombardment on the initial stages of thin film growth", *Thin Solid Films*, vol. 46, no. 3, pp. 267–274, Nov. 1977.

[140] M. A. Lieberman and A. J. Lichtenberg, *Principles of Plasma Discharges and Materials Processing*, 2nd. John Wiley & Sons, Inc., 2005.

[141] F. F. Chen, *Introduction to Plasma Physics and Controlled Fusion*, Second. Springer International Publishing, 2010.

[142] H. Trinkaus and B. N. Singh, "Helium accumulation in metals during irradiation - Where do we stand?", in *Journal of Nuclear Materials*, 2003.

[143] L. Caspers, R. Pastenau, A. Van Veen, and W. Van Heugten, "Vacancies to Divacancies by Helium Trapping in Molybdenum", *Physica Status Solidi*, vol. 46, pp. 541–546, 1978.

[144] W. D. Wilson, C. L. Bisson, and M. I. Baskes, "Self-trapping of helium in metals", *Physical Review B*, vol. 24, no. 10, pp. 5616–5624, 1981.

[145] F. Sefta, K. D. Hammond, N. Juslin, and B. D. Wirth, "Tungsten surface evolution by helium bubble nucleation, growth and rupture", *Nuclear Fusion*, vol. 53, no. 7, p. 073 015, 2013.

[146] D. Perez, T. Vogel, and B. P. Uberuaga, "Diffusion and transformation kinetics of small helium clusters in bulk tungsten", *Physical Review B - Condensed Matter and Materials Physics*, vol. 90, no. 1, pp. 1–13, 2014.

[147] L. Hu, K. D. Hammond, B. D. Wirth, and D. Maroudas, "Molecular-dynamics analysis of mobile helium cluster reactions near surfaces of plasma-exposed tungsten", *Journal of Applied Physics*, vol. 118, no. 16, 2015.

[148] J. H. Evans, "The role of implanted gas and lateral stress in blister formation mechanisms", *Journal of Nuclear Materials*, 1978.

[149] E. V. Kornelsen and A. A. Van Gorkum, "A study of bubble nucleation in tungsten using thermal desorption spectrometry: Clusters of 2 to 100 helium atoms", *Journal of Nuclear Materials*, 1980.

[150] O. El-Atwani, K. Hattar, J. Hinks, *et al.*, "Helium bubble formation in ultrafine and nanocrystalline tungsten under different extreme conditions", *Journal of Nuclear Materials*, vol. 458, pp. 216–223, Mar. 2015.

[151] Y. Minyou, "Effects of Low Energy and High Flux Helium/Hydrogen Plasma Irradiation on Tungsten as Plasma Facing Material", *Plasma Science and Technology*, vol. 7, no. 3, pp. 2828–2834, 2006.

[152] J. Evans, "An interbubble fracture mechanism of blister formation on helium-irradiated metals", *Journal of Nuclear Materials*, vol. 68, no. 2, pp. 129–140, Oct. 1977.

[153] H. M. Mott-Smith and I. Langmuir, "The theory of collectors in gaseous discharges", *Physical Review*, vol. 28, no. 4, pp. 727–763, 1926.

[154] R. L. Merlino, "Understanding Langmuir probe current-voltage characteristics", *American Journal of Physics*, vol. 75, no. 12, p. 1078, 2007.

[155] G. Sauerbrey, "Use of Quartz Crystal Vibrator for Weighting Thin Films on a Microbalance", *Zeitschrift fur Physik*, vol. 155, pp. 206–222, 1959.

[156] S. Kajita, T. Saeki, N. Ohno, *et al.*, "Degradation of optical reflectivity of in-vessel mirror materials by helium bombardment", *Journal of Nuclear Materials*, vol. 417, no. 1-3, pp. 838–841, 2011.

[157] J. Jerhot and J. Vlcek, "Seebeck Effect in Polycrystalline Semiconductors", *Electronics and Optics*, vol. 92, pp. 259–271, 1982.

[158] F. W. Meyer, P. S. Krstic, H. Hijazi, *et al.*, "Surface-morphology changes and damage in hot tungsten by impact of 80 eV-12 keV He-ions and keV-energy self-atoms", *Journal of Physics: Conference Series*, vol. 488, no. SECTION 1, 2014.

[159] W. Sakaguchi, S. Kajita, N. Ohno, *et al.*, "Formation Condition of Fiberform Nanostructured Tungsten by Helium Plasma Exposure", *Plasma and Fusion Research*, vol. 5, S1023–S1023, 2010.

[160] D. Hwangbo, S. Kajita, N. Ohno, and P. McCarthy, "Growth of nano-tendril bundles on tungsten with impurity-rich He plasmas", *Nucl. Fusion*, vol. 58, p. 096 022, 2018.

[161] A. Mishra, P. J. Kelly, and J. W. Bradley, "The evolution of the plasma potential in a HiPIMS discharge and its relationship to deposition rate", *Plasma Sources Science and Technology*, vol. 19, no. 4, 2010.

[162] P. F. Cheng, "Directional deposition of Cu into semiconductor trench structures using ionized magnetron sputtering", *Journal of Vacuum Science & Technology B: Microelectronics and Nanometer Structures*, vol. 13, no. 2, p. 203, 1995.

[163] K. M. Green, D. B. Hayden, D. R. Juliano, and D. N. Ruzic, "Determination of flux ionization fraction using a quartz crystal microbalance and a gridded energy analyzer in an ionized magnetron sputtering system", *Review of Scientific Instruments*, vol. 68, no. 12, pp. 4555–4560, 1997.

[164] G. Rybicki and A. Lightman, *Radiative Processes in Astrophysics*. Wiley-VCH, 2008.

[165] K. Watson, "Spectral ratio method for measuring emissivity", *Remote Sensing of Environment*, vol. 42, no. 2, pp. 113–116, 1992.

[166] M. Ochs, T. Horbach, A. Schulz, *et al.*, "A novel calibration method for an infrared thermography system applied to heat transfer experiments", *Measurement Science and Technology*, vol. 20, no. 7, 2009.

[167] Y. Ozaki and R. H. Zee, "Investigation of thermal and hydrogen effects on emissivity of refractory metals and carbides", *Materials Science and Engineering A*, vol. 202, no. 1-2, pp. 134–141, 1995.

[168] D. Post, J. Abdallah, R. E. Clark, and N. Putvinskaya, "Calculations of energy losses due to atomic processes in tokamaks with applications to the International Thermonuclear Experimental Reactor divertor", *Physics of Plasmas*, vol. 2, no. 6, pp. 2328–2336, 1995.

[169] A. Kallenbach, M. Balden, R. Dux, *et al.*, "Plasma surface interactions in impurity seeded plasmas", *Journal of Nuclear Materials*, vol. 415, no. 1, S19–S26, Aug. 2011.

[170] M. Wischmeier, "High density operation for reactor-relevant power exhaust", *Journal of Nuclear Materials*, vol. 463, pp. 22–29, Aug. 2015.

[171] A. Kallenbach, M. Bernert, T. Eich, *et al.*, "Optimized tokamak power exhaust with double radiative feedback in ASDEX Upgrade", *Nuclear Fusion*, vol. 52, no. 12, p. 122 003, Dec. 2012.

[172] M. Bernert, M. Wischmeier, A. Huber, *et al.*, "Power exhaust by SOL and pedestal radiation at ASDEX Upgrade and JET", *Nuclear Materials and Energy*, vol. 12, pp. 111–118, 2017.

[173] a. Kallenbach, M. Bernert, R. Dux, *et al.*, "Impurity seeding for tokamak power exhaust: from present devices via ITER to DEMO", *Plasma Physics and Controlled Fusion*, vol. 55, no. 12, p. 124 041, Dec. 2013.

[174] R. Wenninger, F. Arbeiter, J. Aubert, *et al.*, "Advances in the physics basis for the European DEMO design", *Nuclear Fusion*, vol. 55, p. 063 003, 2015.

[175] G. Federici, C. Skinner, J. Brooks, *et al.*, "Plasma-material interactions in current tokamaks and their implications for next step fusion reactors", *Nuclear Fusion*, vol. 41, no. 12, p. 1967, 2001.

[176] E. B. Saloman and C. J. Sansonetti, "Wavelengths, Energy Level Classifications, and Energy Levels for the Spectrum of Neutral Neon", *Journal of Physical and Chemical Reference Data*, vol. 33, no. 4, pp. 1113–1158, Dec. 2004.

[177] I. Velchev, W. Hogervorst, and W. Ubachs, "Precision VUV spectroscopy of Ar I at 105 nm", *Journal of Physics B: Atomic, Molecular and Optical Physics*, vol. 32, no. 17, pp. L511–L516, Sep. 1999.

[178] E. Biemont, Y. Fremat, and P. Quinet, "Ionization Potentials of Atoms and Ions from Lithium to Tin (Z = 50)", *Atomic Data and Nuclear Data Tables*, vol. 71, no. 1, pp. 117–146, Jan. 1999.

[179] D. Z. Kandula, C. Gohle, T. J. Pinkert, *et al.*, "Extreme Ultraviolet Frequency Comb Metrology", *Physical Review Letters*, vol. 105, no. 6, p. 063 001, Aug. 2010.

[180] A. M. Hala and N. Hershkowitz, "Ion acoustic wave velocity measurement of the concentration of two ion species in a multi-dipole plasma", *Review of Scientific Instruments*, vol. 72, no. 5, pp. 2279–2281, 2001.

[181] N. Hershkowitz, "Sheaths: More complicated than think", *Physics of Plasmas*, vol. 12, no. 5, pp. 1–11, 2005.

[182] R. P. Doerner, M. J. Baldwin, M. Simmonds, *et al.*, "Quantitatively measuring the influence of helium in plasma-exposed tungsten", *Nuclear Materials and Energy*, vol. 12, pp. 372–378, 2017.

[183] Y. Yao, Z. Hargitai, M. Albert, *et al.*, "New molecular collisional interaction effect in low-energy sputtering", *Physical Review Letters*, vol. 81, no. 3, pp. 550–553, 1998.

[184] K. Dobes, P. Naderer, N. Lachaud, *et al.*, "Sputtering of tungsten by N + and N 2+ ions: Investigations of molecular effects", *Physica Scripta T*, vol. T145, 2011.

[185] R. P. Doerner, S. I. Krasheninnikov, and K. Schmid, "Particle-induced erosion of materials at elevated temperature", *Journal of Applied Physics*, vol. 95, no. 8, pp. 4471–4475, Apr. 2004.

[186] R. P. Doerner, C. Björkas, D. Nishijima, and T. Schwarz-Selinger, "Erosion of beryllium under high-flux plasma impact", *Journal of Nuclear Materials*, vol. 438, no. SUPPL, S272–S275, 2013.

[187] D. Hwangbo, S. Kajita, H. Tanaka, and N. Ohno, "Growth process of nano-tendril bundles with sputtered tungsten", *Nuclear Materials and Energy*, vol. 18, no. January, pp. 250–257, 2019.

[188] J. J. Friel, *X-ray and Image Analysis in Electron Microscopy*. Princeton Gamma-Tech, 2004.

[189] G. M. Wright, H. A. Barnard, L. A. Kesler, *et al.*, "An experiment on the dynamics of ion implantation and sputtering of surfaces", *Review of Scientific Instruments*, vol. 85, no. 2, p. 023 503, 2014.

[190] C. M. Parish, K. Wang, R. P. Doerner, and M. J. Baldwin, "Grain orientations and grain boundaries in tungsten nonotendril fuzz grown under divertor-like conditions", *Scripta Materialia*, vol. 127, pp. 132–135, 2017.

[191] D. Naujoks, K. Asmussen, M. Bessenrodt-Weberpals, *et al.*, "Tungsten as target material in fusion devices", *Nuclear Fusion*, vol. 36, no. 6, pp. 671–687, Jun. 1996.

[192] S. Kajita, S. Kawaguchi, N. Ohno, and N. Yoshida, "Enhanced growth of large-scale nanostructures with metallic ion precipitation in helium plasmas", *Scientific Reports*, no. August 2017, pp. 1–9, 2018.

[193] S. Kajita, S. Kawaguchi, N. Yoshida, *et al.*, "Morphologies of co-depositing W layer formed during He plasma irradiation", *Nucl. Fusion*, vol. 58, 106002 (9pp), 2018.

[194] S. Kajita, N. Yoshida, S. Kawaguchi, *et al.*, "Growth of membrane nanostructures on W co-deposition layer", *Nuclear Materials and Energy*, vol. 18, pp. 339–344, Jan. 2019.

[195] K. Schmid, K. Krieger, S. W. Lisgo, *et al.*, "WALLDYN simulations of global impurity migration in JET and extrapolations to ITER", *Nuclear Fusion*, vol. 55, no. 5, 2015.

[196] N. Ohno, D. Nishijima, S. Takamura, *et al.*, "Static and dynamic behaviour of plasma detachment in the divertor simulator experiment NAGDIS-II", *Nuclear Fusion*, vol. 41, no. 8, pp. 1055–1065, 2001.

[197] I. Petrov, A. Myers, J. E. Greene, and J. R. Abelson, "Mass and energy resolved detection of ions and neutral sputtered species incident at the substrate during reactive magnetron sputtering of Ti in mixed Ar+N 2 mixtures", *Journal of Vacuum Science & Technology A: Vacuum, Surfaces, and Films*, vol. 12, no. 5, pp. 2846–2854, Sep. 1994.

[198] C. Christou and Z. H. Barber, "Ionization of sputtered material in a planar magnetron discharge", *Journal of Vacuum Science & Technology A: Vacuum, Surfaces, and Films*, vol. 18, no. 6, pp. 2897–2907, Nov. 2000.

[199] I.-L. Velicu, V. Tiron, C. Porosnicu, *et al.*, "Enhanced properties of tungsten thin films deposited with a novel HiPIMS approach", *Applied Surface Science*, vol. 424, pp. 397–406, Dec. 2017.

[200] I. Prencipe, D. Dellasega, A. Zani, *et al.*, "Energy dispersive x-ray spectroscopy for nanostructured thin film density evaluation", *Science and Technology of Advanced Materials*, vol. 16, no. 2, p. 25 007, 2015.

[201] K. Zhu, Y. Xing, T. Liu, *et al.*, "Studies of He irradiated tungsten using transmission electron microscope", *Materials Letters*, vol. 213, pp. 362–365, 2018.

[202] K. Lejaeghere, V. Van Speybroeck, G. Van Oost, and S. Cottenier, "Error Estimates for Solid-State Density-Functional Theory Predictions: An Overview by Means of the Ground-State Elemental Crystals", *Critical Reviews in Solid State and Materials Sciences*, vol. 39, no. 1, pp. 1–24, Jan. 2014.

[203] S. I. Krasheninnikov, T. Faney, and B. D. Wirth, "On helium cluster dynamics in tungsten plasma facing components of fusion devices", *Nuclear Fusion*, vol. 54, no. 7, 2014.

[204] W. Qin, F. Ren, R. P. Doerner, *et al.*, "Nanochannel structures in W enhance radiation tolerance", *Acta Materialia*, vol. 153, pp. 147–155, 2018.

[205] A. Alfonso, D. Juul Jensen, G.-N. Luo, and W. Pantleon, "Thermal stability of a highly-deformed warm-rolled tungsten plate in the temperature range 1100–1250 °C", *Fusion Engineering and Design*, vol. 98-99, pp. 1924–1928, Oct. 2015.

[206] K. Tsuchida, T. Miyazawa, A. Hasegawa, *et al.*, "Recrystallization behavior of hot-rolled pure tungsten and its alloy plates during high-temperature annealing", *Nuclear Materials and Energy*, 2018.

[207] D. Choi, B. Wang, S. Chung, *et al.*, "Phase, grain structure, stress, and resistivity of sputter-deposited tungsten films", *Journal of Vacuum Science & Technology A: Vacuum, Surfaces, and Films*, vol. 29, no. 5, p. 051 512, Sep. 2011.

[208] V. S. Voitsenya, A. F. Bardamid, V. N. Bondarenko, *et al.*, "Some problems arising due to plasma-surface interaction for operation of the in-vessel mirrors in a fusion reactor", *Journal of Nuclear Materials*, vol. 290-293, pp. 336–340, 2001.

[209] T. Sugie, S. Kasai, M. Taniguchi, *et al.*, "Irradiation test of Mo- and W-mirrors for ITER by low energy deuterium ions", *Journal of Nuclear Materials*, vol. 329-333, no. Part B, pp. 1481–1485, 2004.

[210] A. Litnovsky, P. Wienhold, V. Philipps, *et al.*, "Diagnostic mirrors for ITER: A material choice and the impact of erosion and deposition on their performance", *Journal of Nuclear Materials*, vol. 363-365, no. 1-3, pp. 1395–1402, 2007.

[211] S. Wurster, B. Gludovatz, and R. Pippan, "High temperature fracture experiments on tungsten–rhenium alloys", *International Journal of Refractory Metals and Hard Materials*, vol. 28, no. 6, pp. 692–697, Nov. 2010.

[212] J. Brooks, L. El-Guebaly, A. Hassanein, and T. Sizyuk, "Plasma-facing material alternatives to tungsten", *Nuclear Fusion*, vol. 55, no. 4, p. 043 002, 2015.

[213] P. Fiflis, D. Curreli, and D. N. Ruzic, "Direct time-resolved observation of tungsten nanostructured growth due to helium plasma exposure", *Nuclear Fusion*, vol. 55, no. 3, 2015.

Appendices

Appendix A

Collision-less sheath calculation

During the experiments in this thesis, the incident ion energy at the sample surface was calculated using equation 2.11. For this calculation to be a valid interpretation of the ion energy, it is assumed that ions travel through the sheath adjacent to the sample surface without experiencing collisions with background gases. To verify this, the mean free path is compared to the sheath width. To find the mean free path, equation 2.12 can be used. As the background gas is predominately He ($\sim 99\%$), the radius of a He atom (3.1 x 10^{-11} m) is used to find σ through $\pi r^2 = \sigma$. This gives σ to be 3.02 x 10^{21} m^2.

The neutral density inside the chamber can be found from assuming the background gas behaves as an ideal gas (i.e. $P = n_{neutral}\ k_B T$). As the background gas is at a pressure of 2.67 Pa during plasma operation, and the gas can be considered at room temperature (293 K), the atomic density of the background gas is given by,

$$n_{neutral} = \frac{P}{k_B T} = \frac{2.67}{1.38\ \text{x}\ 10^{-23} \cdot 293} \approx 7\text{x}10^{20}\text{m}^{-3}$$

The mean free path for a collision is found using equation 2.12,

$$\lambda_m = \frac{1}{n_{neutral} \cdot \sigma}$$

This gives λ_m to be $\approx$ 50 cm. The sheath width λ_s was calculated in section 6.3.2 to be $\approx$ 40 μm. Therefore as the mean free path is much greater than the sheath width (i.e. $\lambda_m \gg s$) the sheath can be considered collision-less.

Appendix B

Mass measurements for magnetron grown fuzzy tungsten

Mass measurements were taken for many of the magnetron produced fuzzy W samples shown in figure 6.9. These are presented in figure B.1 as a function of the fluence of He ion exposure.

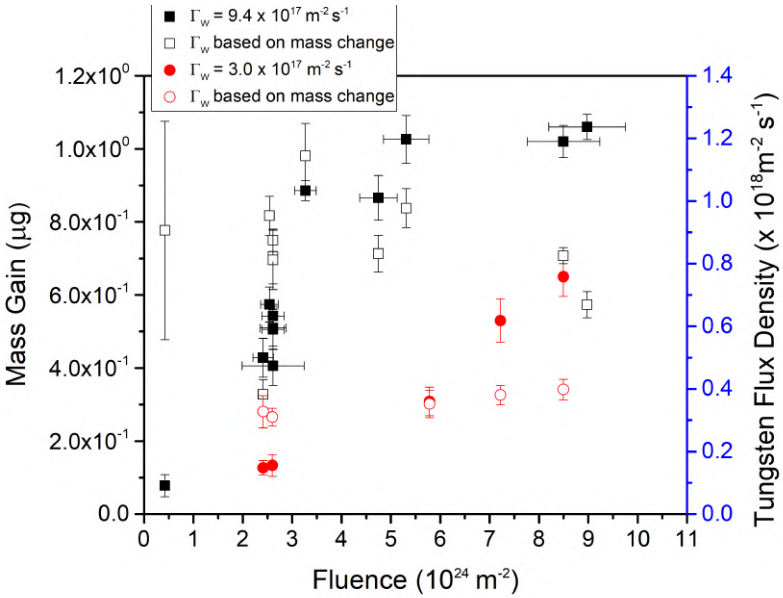

Figure B.1: The mass gain for magnetron produced fuzzy W samples as a function of the helium ion exposure. On the second y-axis (right) the mass gain has been converted to a W deposition flux density.

Two sets of data are labelled, those samples produced under the high (Γ_W = 9.4 x 10^{17} m^{-2} s^{-1}) and low (Γ_W = 3 x 10^{17} m^{-2} s^{-1}) deposition flux density. These masses were used to calculate an apparent flux density of W to the sample (shown on the 2nd y - axis on figure B.1), with each group of symbols as labelled in the legend in the figure.

It can be seen from the trends in the figure that as the fluence increases, the measured mass increase from samples under the higher deposition rate tend to "level off". It is likely that this is due to some level of erosion inside the system, which could take place as tendrils

grow to greater thicknesses and their growth rates slow down, as predicted in [38]. As a result of this the estimated flux density from the mass increases decreases (from $\sim 9 \times 10^{17}$ m^{-2} to 5×10^{17} m^{-2}) for the higher deposition flux density sample. For samples who were grown under the lower deposition flux density, their estimated flux densities inferred from the mass gain generally agree well with the QCM measurements. This indicates that the QCM results can reasonably be trusted.

Appendix C

Additional SEM Imaging

FIB-SEM cross-sectional images which were taken of the fuzzy W layers in figure 6.9 are included here. All images were viewed at a tilt of 52° to the surface, and scale bars are included in the right hand corner of each image. Also labelled on each image is the helium ion fluence Φ_{He}.

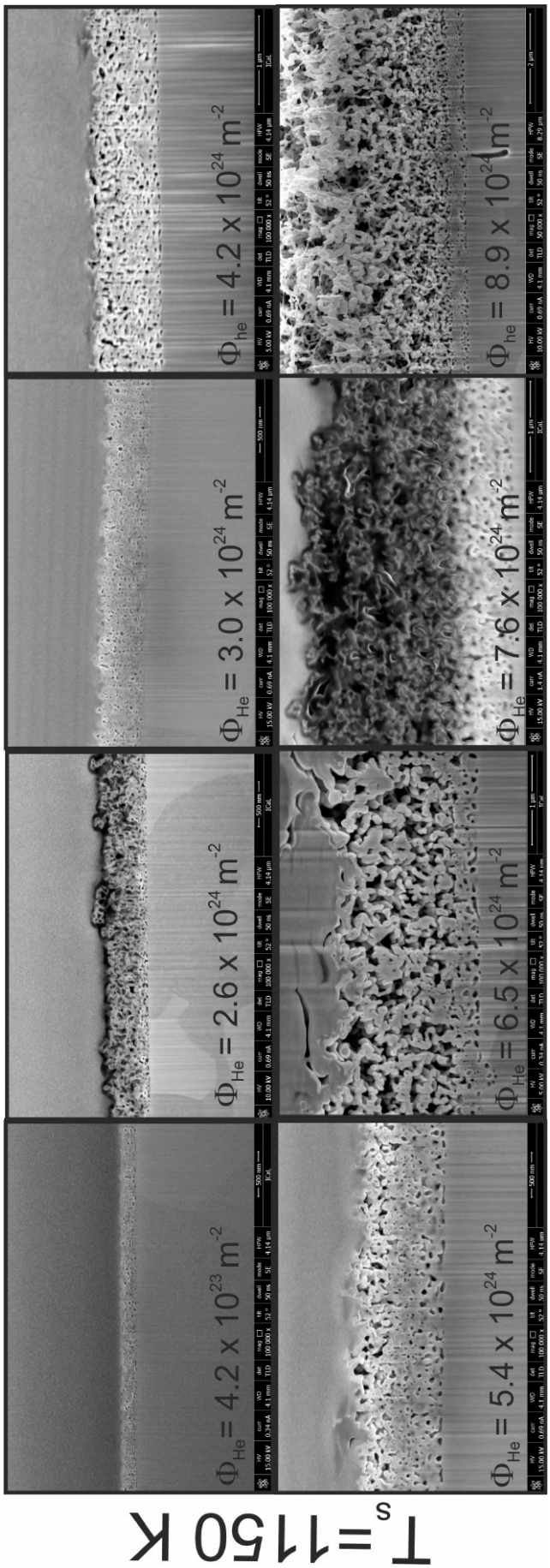

Figure C.1: Cross-sectional TEM images and corresponding diffraction patterns of fuzzy W samples grown in the magnetron for $T_s = 1150$ K across a fluence range (4×10^{23} - 9×10^{24} m^{-2})

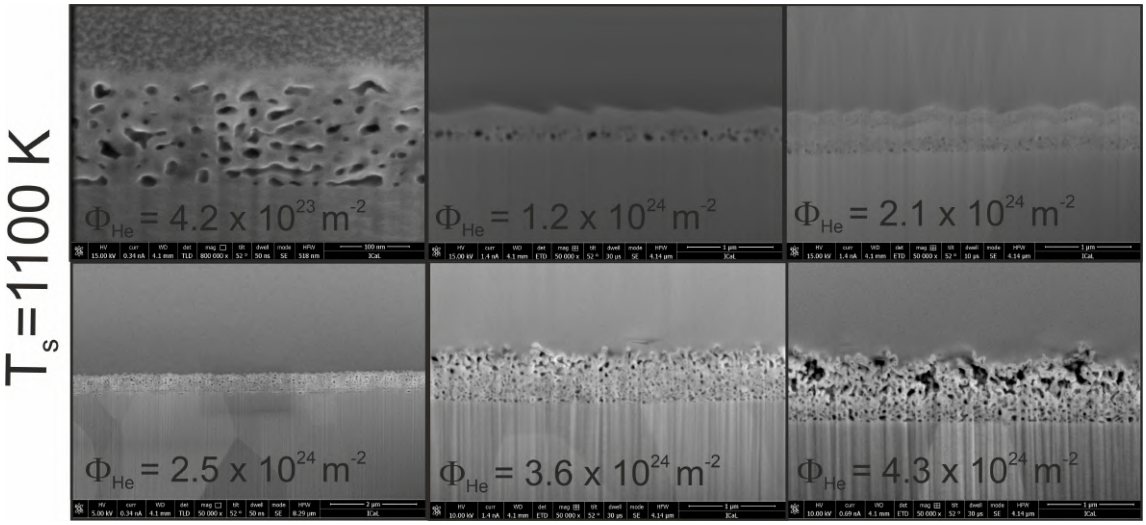

Figure C.2: Cross-sectional FIB-SEM images of fuzzy W samples grown in the magnetron for T_s = 1100 K across a fluence range (x 10^{23} - 5 x 10 ^{24} m^{-2})

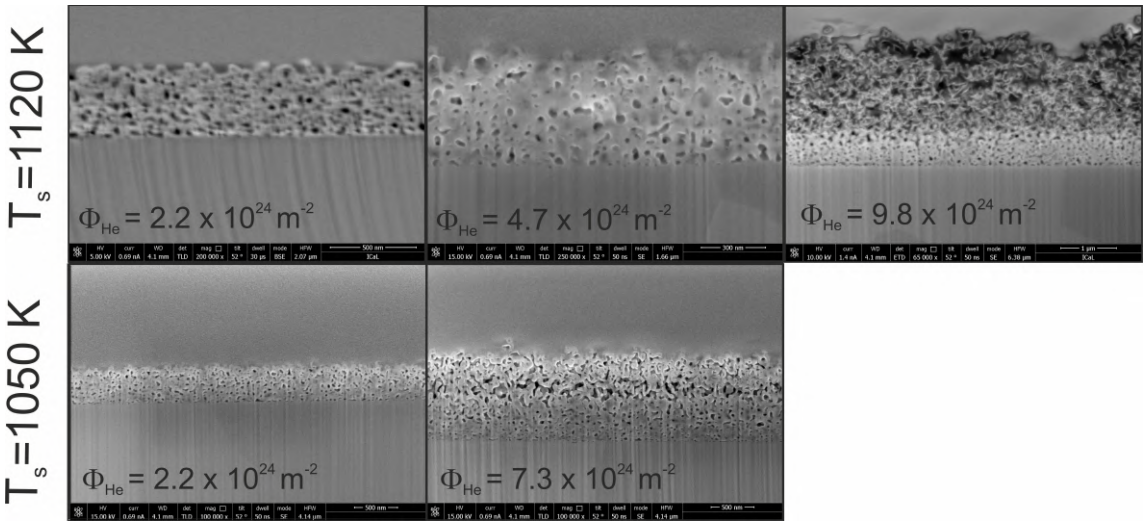

Figure C.3: FIB-SEM images of fuzzy W grown in the magnetron for T_s = 1120 and 1050 K across a fluence range (2 x 10^{24} - 1 x 10 ^{25} m^{-2})